Asymmetric infall beyond natal cores to protoplanetary disks: Observations and analysis of streamers toward embedded low-mass protostars

María Teresa Valdivia Mena

München 2024

Asymmetric infall beyond natal cores to protoplanetary disks: Observations and analysis of streamers toward embedded low-mass protostars

María Teresa Valdivia Mena

Dissertation
der Fakultät für Physik
der Ludwig-Maximilians-Universität
München

vorgelegt von
María Teresa Valdivia Mena
aus Santiago, Chile

München, den 28.02.2024

Erstgutachter: Prof. Dr. Paola Caselli
Zweitgutachter: Prof. Dr. Andreas Burkert
Tag der mündlichen Prüfung: 16.04.2024

Contents

List of Figures

List of Tables

Zussamenfassung

Die Masse eines Sterns wird während des protostellaren Stadiums festgelegt, in dem ein Protostern und die ihn begleitende Scheibe in ihren Geburtskern eingebettet sind. Die Mechanismen, die die Anhäufung von Masse innerhalb des Stern und Scheibensystems vorantreiben, sind jedoch nicht gut verstanden. Das klassische Bild der Sternentstehung geht davon aus, dass ein Protostern und seine planetenbildende Scheibe im Zentrum eines sphärisch symmetrischen Kerns akkretieren, der von äußeren Einflüssen isoliert ist. In Wirklichkeit ist die Verteilung des molekularen Gases auf allen Skalen asymmetrisch, von den parsec-großen Filamenten bis hin zu Asymmetrien in protoplanetaren Scheiben. Numerische Simulationen, die realistische Bedingungen in Sternentstehungsgebieten berücksichtigen, zeigen, dass der Einfall von Kernen in protostellare Scheiben durch lange und dünne Kanäle, sogenannte Streamer, erfolgt. Dank der Entwicklung leistungsfähiger Interferometer wie ALMA und NOEMA können wir nun diese Einfallkanäle in der Emission von molekularem Gas untersuchen. In dieser Dissertation untersuche ich die Eigenschaften von Streamers mit Hilfe von Submillimeter-Beobachtungen, wie zum Beispiel ihr Vorkommen und den Ursprung ihrer Massen.

Das erste Projekt zielt darauf ab, die Massenzufuhr zu einer protostellaren Scheibe durch einen Streamer zu verfolgen. Mit interferometrischen Daten des PRODIGE NOEMA Großprogramms habe ich die Hülle von Per-emb 50, einem eingebetteten Protostern im Perseus, untersucht. Ich finde einen Streamer, der mehr als genug Masse liefert, um die aktuelle Akkretionsrate von der Scheibe zum Protostern aufrechtzuerhalten, und so sammelt sich in der Scheibe selbst gas an, was in der Zukunft einen Akkretionsausbruch auslösen kann. Ich finde auch molekulare Emission, die mit einem Akkretionsschock in der Nähe des voraussichtlichen Landeplatzes des Streamers übereinstimmen, was auf eine chemische Veränderung aufgrund des Masseneinfalls hinweist.

Die Länge der beobachteten Streamer zeigt, dass sie Masse von außerhalb des Geburtskerns transportieren können, aber es ist nicht klar, woher die Masse kommt. Im zweiten Projekt verfolge ich den Massentransport von der größeren filamentären Struktur, die die Molekülwolken dominiert, hin zu einem einzelnen eingebetteten Protostern. Zu diesem Zweck untersuche ich die Gaskinematik in zwei verschiedenen physikalischen Größenordnungen, dem Gasfluss auf filamentärer Ebene ($\sim$ 10000 au) und der Hülle eines eingebetteten Protosterns (100 au). Dank dichtebasierter Clustering-Algorithmen, die auf die Molekülliniendaten angewandt werden, finde ich einen Streamer in Richtung eines eingebetteten Protosterns, den isolierten und dichten Barnard 5-Kern. Ich entdecke auch einen Zufluss aus der größeren umgebenden Wolke in Richtung der Filamentstrukturen, in die der Protostern eingebettet ist. Meine Analyse der Gaseigenschaften auf beiden Ebenen deutet darauf hin, dass der Zufluss aus der Wolke mit dem Streamer verbunden ist, was bedeutet, dass die protostellare Scheibe Zugang zu frischem Gas aus der umgebenden Wolke hat.

Fast alle Streamer wurden zufällig gefunden, und es ist unklar, ob sie in der Nähe von Protosternen häufig vorkommen oder nicht. Im Rahmen des Abschlussprojekts führe ich die erste systematische Suche nach Streamers unter Verwendung von NOEMA- und 30-m-Teleskopbeobachtungen. Ich stelle fest, dass im Süden von NGC 1333, der aktivsten Sternentstehungsregion in der Perseus-Molekülwolke, etwa 40 % der Protosterne Anzeichen

für einen asymmetrischen Einfall in Richtung ihrer Scheiben aufweisen. Ich stelle auch fest, dass das Gas aus der größeren umgebenden Molekülwolke stammt. Streamers sind also nicht nur häufig, sondern vergrößern auch das Massenreservoir, das nach dem klassischen Bild erwartet wird.

Ich schließe diese Arbeit mit einem Ausblick darauf, wie wir einige der offenen Fragen zu den Auswirkungen von Streamern bei der Stern- und Planetenentstehung klären können. Jetzt, da wir wissen, dass Streamer ein häufiges Merkmal sind, ist es unerlässlich, die Auswirkungen des asymmetrischen Einfalls auf die Struktur der protoplanetaren Scheiben zu erforschen. Hochauflösende Beobachtungen von Molekülen innerhalb der protostellaren Scheiben in frühen Entwicklungsstadien werden es Astronomen ermöglichen, die Streamers in das Rätsel der Sternentstehung einzuordnen.

Summary

The mass of a star is set during the protostellar stage, where a protostar and its accompanying disk are embedded in their natal core. However, the mechanisms that drive the accumulation of mass within the star and disk system are not well understood. The classical picture of star formation assumes a protostar and its planet-forming disk are accreting at the center of a spherically symmetric core, isolated from external influences. In reality, molecular gas distribution is asymmetric at all scales, from the parsec-sized filaments to asymmetries in protoplanetary disks. Numerical simulations that take into account realistic conditions within star forming regions find that infall from cores to disks proceeds through long and thin channels called streamers. Thanks to the development of powerful interferometers, such as ALMA and NOEMA, we can now study these infall channels in molecular gas emission. In this thesis, I investigate the properties of streamers using sub-millimeter observations, such as their occurrence and the origin of their masses.

The first project aims to follow the mass delivery to a protostellar disk through a streamer. Using interferometric data from the PRODIGE NOEMA large program, I investigated the envelope of Per-emb 50, an embedded protostar in Perseus. I find a streamer that delivers more than enough mass to sustain the current accretion rate from disk to protostar, and thus gas accumulates in the disk itself, which can produce an accretion outburst in the future. I also find molecular emission consistent with an accretion shock near the predicted landing site of the streamer, suggesting a chemical change due to the mass infall.

The length of observed streamers suggests that they can transport mass from outside the natal core, but it is not clear from where the mass comes from. In the second project, I follow the mass delivery from the larger filamentary structure that dominates molecular clouds toward an individual embedded protostar. For this, I study the gas kinematics in two different physical scales, the gas flow at filamentary scales ($\sim$ 10000 au) and the envelope of an embedded protostar ($\sim$ 100 au). Thanks to density-based clustering algorithms applied to the molecular line data, I find a streamer toward an embedded protostar in the isolated Barnard 5 dense core. I also detect inflow from the larger ambient cloud toward the filament spines where the protostar is embedded. My analysis of the gas properties at both scales suggests that the inflow from the cloud is connected to the streamer, implying the protostellar disk can access fresh gas from the ambient cloud.

Almost all streamers have been found serendipitously, and it is unclear if they are a frequent feature around protostars or not. In the final project, I lead the first systematic search for streamers, using NOEMA and 30-m telescope observations. I find that in the south of NGC 1333, the most active star-forming region in the Perseus Molecular Cloud, around 40% of the protostars show signs of asymmetric infall toward their disks. I also determine that the gas feeding the streamers comes from the larger ambient molecular cloud. Therefore, streamers are not only frequent, but also expand the mass reservoir expected from the classical picture.

I close this thesis with an outlook on how to resolve some of the open questions regarding the effects of streamers in star and planet formation. Now that we know streamers are a frequent feature, it is imperative to observe the effect of the asymmetric infall in the

structure of protoplanetary disks. High resolution observations of molecules within the protostellar disks in early stages will allow astronomers to place streamers neatly in the puzzle of star formation.

Chapter 1

Introduction

Stars have fascinated humankind since we have been able to look up and see the Milky Way above our heads. Breakthroughs in the XX century unveiled how the molecules essential for life and Earth's composition originate from the stellar life cycle, which transforms Hydrogen (H) and Helium (He) into larger atoms. Carl Sagan[1], in the first episode of his series *Cosmos*, famously said: "We are made of star stuff. We are a way for the cosmos to know itself". The formation of stars, in particular low-mass stars such as our own Sun, is of great interest in this context, as it can help understand how the Sun, Earth, and finally us, came to be.

Mass is the most important property of a star, as it determines its evolution. Stars are born within dense cores embedded in molecular clouds, from which they inherit the bulk of their mass. In the classical picture of star formation, the core is a spherically symmetric, collapsing reservoir of gas (Larson 1969; Shu 1977). During the collapse, a disk of gas and dust is formed around the protostar, which is the site for future planet formation. This disk is fed by the envelope until the latter dissipates, and the protostar is fed through accretion from the disk. In reality, the accretion process is much more chaotic, and the mechanisms that drive the mass accumulation can have significant impact in the subsequent star and planet formation process. Recent observations with powerful interferometers, such as the Atacama Large Millimeter/Submillimeter Array (ALMA), have revealed that gas travels through narrow channels called *streamers*, which transport mass from the natal core and even the larger molecular cloud, and deposit gas into the protostellar disk.

This introduction presents the main concepts and methods used in the analysis of star formation, low-mass protostars and streamers. Section 1.1 introduces the Interstellar Medium and the properties of molecular clouds, the sites of star formation. Section 1.2 briefly explains the classical picture of low-mass star formation and how it correlates with the observed properties of protostars. Section 1.3 introduces streamers, the main focus of this thesis, and summarizes their known properties. Section 1.4 provides an overview of the radiative processes in molecular clouds and how astronomers use them to gather information about matter in the universe. An overview of radio telescopes, the main tool

[1] Astronomer and science communicator, USA, 1934-1996

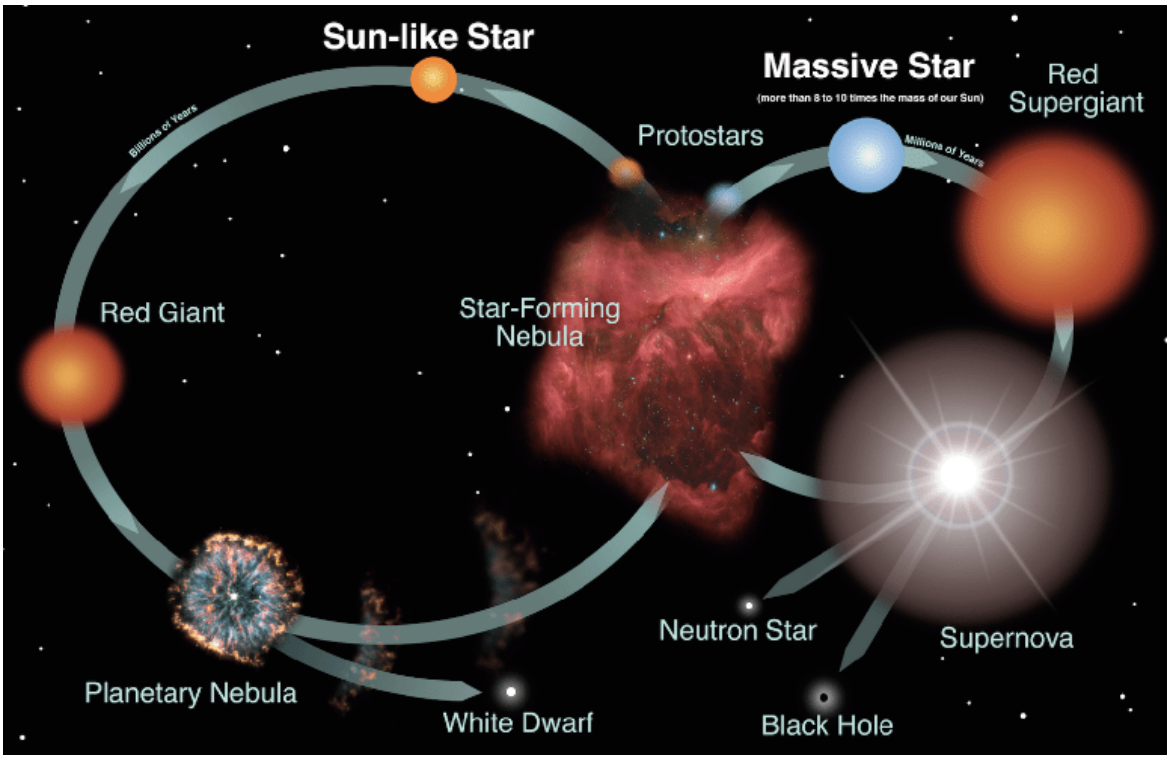

Figure 1.1: Diagram of the cycle of the ISM, showing the stages of a star's life. On the left is the cycle for a star with a similar mass to the sun (1 $M_\odot$). On the right is the cycle for a massive star ($\gtrsim$ 8 $M_\odot$). Figure credits: NASA, STScI, ESA.

used for this thesis, is given in Sect. 1.5. Finally, Sect. 1.6 describes the contents of the thesis.

1.1 The interstellar medium

The space in between stars is not at all empty: the interstellar medium (ISM) is all the matter and energy that is between the stars in a galaxy. The matter contained in the ISM is the fuel for new stars to form, and at the end of a star's life, much of the stellar matter may be returned to the ISM. The matter returned to the ISM at the end of a star's life is then used to form the next generation of stars. This is what is known as the Lifecycle of the ISM, and with each passing cycle, stars release more metals, enriching the ISM. This cycle is resumed in Fig. 1.1.

The majority of matter in the ISM is in the form of gas, and the most common element in the ISM is H, estimated to compose about 70% of the ISM by mass. Next is He, which composes about 28%, and the rest are all the other elements heavier than He, such as Carbon (C), usually referred to as "metals" by astronomers (although chemists will disagree with this naming convention, Spitzer 1978; Ferrière 2001). These atoms can combine to

form molecules: which ones form depend on the atoms available and the physical conditions that surround them (Yamamoto 2017). There are ~ 300 different molecules found in space, and this number is bound to continue growing in coming years (McGuire 2022; Ceccarelli et al. 2023).

Although the ISM is mostly gas, there are solid particles in the form of *interstellar dust*, in a proportion of 1-to-100 with respect to gas mass (Kennicutt & Evans 2012). Dust in the ISM is mostly composed of carbonaceous species and silicates (Draine 2003) and absorbs light coming from background stars, obscuring stellar light efficiently for wavelengths smaller than their size (~ 0.1 μm), which it then re-emits in the infrarred (Stahler & Palla 2004; Kennicutt & Evans 2012). Although less abundant than gas, dust plays a vital role in regulating the chemistry and energy balance in the ISM (Ferrière 2001). In particular for star formation, dust allows the formation of molecular H (H_2) together with many other molecular species in its surface, and further protects them from UV radiation (Draine 2004; van Dishoeck 2014).

Star formation is the process in which the diffuse gas in the ISM turns into stars by cooling, condensation, and eventual gravitational collapse of H_2 into a self-gravitating sphere of plasma. The details of star formation and the ISM are mostly known for our own galaxy, the Milky Way (also known as the Galaxy). The Milky Way is a barred spiral galaxy, which consists of a stellar disk with spiral arms, which concentrate most of the star forming regions, and a dense concentration of stars near the middle, in what is known as the central bulge. The Sun is located at approximately 8.5 kpc from the centre of the Galaxy, at about 1/3 of the galactic disk radius.

1.1.1 Phases of the ISM

The gaseous ISM has a wide range of temperatures and densities constituting different phases, where H can be in the form of molecules (H_2), as neutral atoms (atomic H, also called H I) or ionized (H^+, also called H II). Based on their temperature and density, the ISM is divided into the following phases: the hot ionized medium (HIM, also known as the hot intercloud medium), warm ionized medium (WIM), the warm and cold neutral medium (WNM and CNM), and molecular gas (McKee & Ostriker 1977; Ferrière 2001). The largest of the ISM phases by volume is the HIM, with an estimated temperature of $\sim 10^6$ K and a number density $n \approx 0.003$ cm^{-3}. The WIM has an estimated temperature of about 8000 K and $n \approx 0.3$ cm^{-3} (Stahler & Palla 2004). The ionized regions are a result of supernova explosions, that can drag ionized matter thousands of parsecs (pc) away, but as hinted by their low densities, they are a minimal fraction of the H in the ISM (McKee & Ostriker 1977). The neutral phases (H I) coexist in pressure equilibrium (Field et al. 1969): the WNM has temperatures and densities similar to the WIM, whereas the CNM has much higher densities ($n \sim 50$ cm^{-3}) and much lower temperatures ($T \sim 100$ K Stahler & Palla 2004). The highest densities and lowest temperatures are found in molecular clouds, which are central to star formation and therefore are described in more depth in the following.

1.1.2 Molecular clouds

H_2 is found within molecular clouds, which are the "stellar nurseries" of the Galaxy as these are the places where young stars are observed. Molecular clouds are the coldest regions of the ISM, with temperatures between $10 - 20$ K, and have the highest densities in comparison with the other phases, $n \geq 10^2$ cm^{-3} (Stahler & Palla 2004). About 80% of molecular H_2 mass of the Galaxy lies within Giant Molecular Clouds (GMCs), which are dust and gas complexes that have linear sizes of approximately 50 pc and contain around 10^5 $M_\odot$, even up to 5×10^6 $M_\odot$ (Heyer & Dame 2015). Examples of GMCs in the Galaxy include Orion and Taurus. The rest of the molecular mass is found within smaller molecular clouds and more isolated structures, called Bok globules, which are small condensations of molecular gas (about 1 pc, and containing $\sim 2 - 50$ $M_\odot$) surrounded by hot gas (Stahler & Palla 2004).

1.1.2.1 Observed structure of molecular clouds

The first descriptions of molecular clouds were based in observations of visible light, where voids of emission were seen in the sky. Dust in Molecular clouds blocks starlight in visible wavelengths, generating dark patches that contrast with the starry sky, which earned these objects the name *dark clouds* (Ferrière 2001; Bergin & Tafalla 2007). First described by William Herschel as "holes in the heavens" (Houghton 1942), the first catalog of these dark clouds was done by E. E. Barnard at the beginning of the XX century (Barnard 1919).

Thanks to the observations of absorption from interstellar dust and emissions from atoms and molecules in space, we now know that these dark patches are actually abundant with cold gas and dust which fuel star formation. Molecular clouds can be spatially resolved, and their properties such as masses and velocities studied, through millimeter and sub-millimeter emissions that come from the molecules and dust particles within them (Sect. 1.4). Astronomers have found that the molecular phase of the ISM consists of nested structures, of which molecular clouds are the top level of the hierarchy. With increasing spatial resolution, smaller sub-units appear within larger structures in a self-similar fashion, until we get to the star-forming structural unit, the *dense core* (Bergin & Tafalla 2007).

Molecular clouds are filled with elongated structures that concentrate the gas and dust within them, known as *filaments*. These structures cover around 0.1 to a few pc in length and concentrate the majority of dense gas within a cloud (André et al. 2014; Pineda et al. 2023). In dust emission, filaments within nearby Molecular clouds (less than 500 pc away) seem to have a typical width of ~ 0.1 pc, but seem to be thinner in other, dense gas tracers (Arzoumanian et al. 2011; André et al. 2014). An example of observed filaments toward the Taurus Molecular Cloud is shown in Fig. 1.2. Filaments are dynamic structures that are fed from the larger, more diffuse gas within the cloud and they serve as routes to feed matter into regions of clustered star formation (André et al. 2014). The self-similar nature of gas is reflected in the structure of filaments, where usually we find *filaments within filaments* through several spatial scales (e.g. Schneider et al. 2011; Suri et al. 2019; Hacar

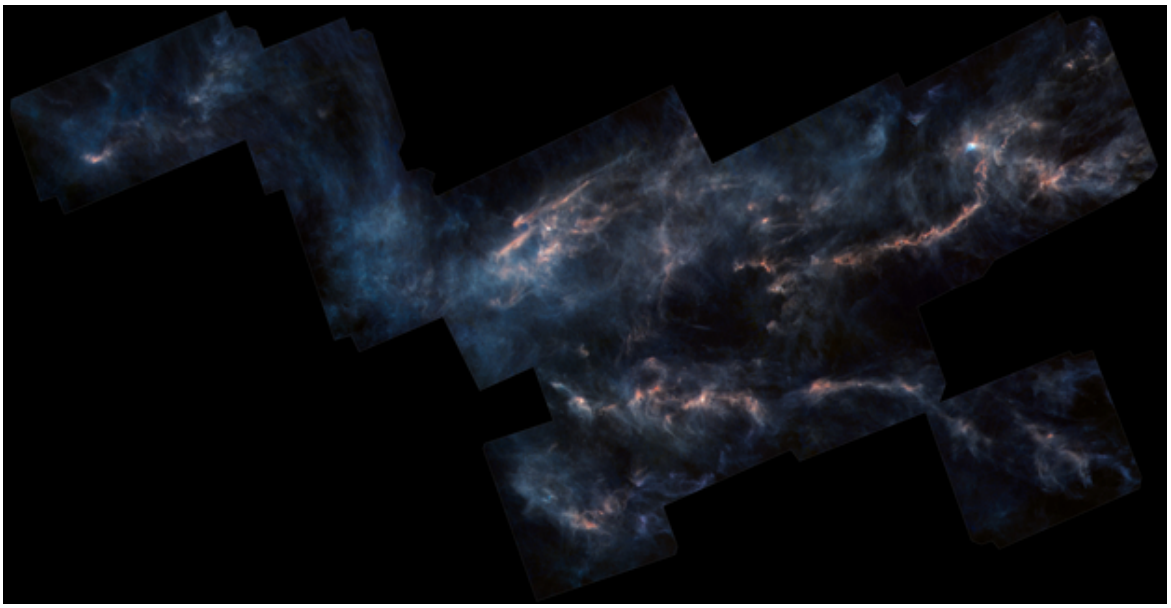

Figure 1.2: Taurus Molecular Cloud as seen by Herschel Space Observatory, an example of a molecular cloud consisting of filamentary structures. The image combines observations at 160 microns (blue), 250 microns (green), 350 microns (split between green and red) and 500 microns (red). Figure credits: ESA/Herschel/NASA/JPL-Caltech, R. Hurt (JPL/Caltech)

et al. 2023). The smallest filamentary substructure is called a *fiber,* with sub-pc lengths and masses between 5-10 $M_\odot$ (Hacar et al. 2023). They are defined as a velocity-coherent structure within a filament, and as such, are observed in molecular gas observations (e.g. Hacar et al. 2017, 2018).

Dense cores, the smallest structure in the hierarchy, are mostly found within filaments (e.g. André et al. 2010). Cores are structures with diameters around ~ 0.1 pc and average densities of $10^4 - 10^5$ cm^{-3}, and as individual protostars and stellar binaries form within them, they have been extensively studied (Bergin & Tafalla 2007). Usually, cores are divided into three categories: *protostellar*, which host a protostar; *prestellar*, where there is no protostar but the core shows signs of contraction, suggesting it will form a protostar; and *starless*, a core which has no signs of contraction (André et al. 2014; Kennicutt & Evans 2012). Cores contrast with their ambient cloud because the gas motions within them have subsonic velocity dispersion, unlike the supersonic motions of gas of the ambient cloud (Goodman et al. 1993; Pineda et al. 2010).

1.2 The classical picture of low-mass star formation

When we talk about "low-mass" star formation, we refer to the processes involved in the build-up and birth of stars that have masses $\lesssim 2$ $M_\odot$, i.e. similar and lower than the mass of the Sun. This regime of star formation is of great interest as it informs about the birth

of our own solar system. In this section, I explain the physical models of star formation and how they compare with the observed properties of protostars.

1.2.1 Cloud stability and fragmentation

The mathematical expressions of cloud stability and collapse, although simplified, help us to understand why clouds fragment into dense cores and form stars. I first discuss how we mathematically understand the fragmentation of molecular clouds into smaller, dense cores, and then how the accumulation of mass is theoretically described for a protostar.

1.2.1.1 Virial equilibrium

Molecular clouds' dynamics are regulated by gravity, unlike the atomic phases of the ISM which are sustained by pressure equilibrium. To understand why this is so, we use the virial theorem: it relates the energy within a system of particles with the moment of inertia I of the system (following the nomenclature of Stahler & Palla 2004):

$$\frac{1}{2}\frac{\partial^2 I}{\partial t^2} = 2U + \mathcal{W} + 2\mathcal{K} + \mathcal{M}, \tag{1.1}$$

where U is the thermal energy (related to the internal pressure of the gas), $\mathcal{K}$ is the kinetic energy (given by the bulk velocity within the cloud), $\mathcal{W}$ is the gravitational energy (i.e. the self-gravity of the cloud) and $\mathcal{M}$ is the energy associated to the magnetic field. A stable cloud, i.e. a cloud in *virial equilibrium*, will have $\frac{\partial^2 I}{\partial t^2} = 0$.

Assuming a spherical cloud made up of ideal gas, with mass M, constant temperature T and radius R, the gravity and thermal energy terms can be written as:

$$\mathcal{W} \approx -\frac{GM^2}{R},\ U \approx \frac{Mk_BT}{\mu m_H}, \tag{1.2}$$

where k_B is the Boltzmann constant, G is the gravitational constant, m_H is the mass of the H atom and μ is the mean molecular weight of the gas. The terms $\mathcal{M}$ and $\mathcal{K}$ are positive like U, which means they are repulsive energetic terms (i.e. they tend to expand the cloud). Therefore either of these terms or the sum of them must be similar to $\mathcal{W}$, which is negative and therefore attractive, for the cloud to be stable (Stahler & Palla 2004).

If gravity dominates over all terms in Eq. 1.1, the molecular cloud will collapse. Simplifying the moment of inertia as $I = MR^2$, a dimensional analysis gives us the *free-fall time* of the cloud:

$$t_{ff} \approx \sqrt{\frac{R^3}{GM}} \approx 7 \times 10^6\,\mathrm{yr}\left(\frac{M}{10^5\,\mathrm{M}_\odot}\right)^{-1/2}\left(\frac{R}{25\,\mathrm{pc}}\right)^{3/2} \tag{1.3}$$

(Stahler & Palla 2004). Choosing $M = 10^4$ $\mathrm{M}_\odot$ and $R = 10$ pc, this gives a timescale of a few times 10^6 yr.

So, does gravity dominate the other terms? Lets consider first the thermal pressure support. The thermal energy with respect to the gravitational energy in a cloud is given by:

$$\frac{U}{|\mathcal{W}|} \approx \frac{\frac{Mk_BT}{\mu m_H}}{\frac{GM^2}{R}} = \frac{3k_BTR}{2GM\mu m_H} \approx 0.03\Big(\frac{T}{20\,\mathrm{K}}\Big)\Big(\frac{R}{10\,\mathrm{pc}}\Big)\Big(\frac{M}{10^4\mathrm{M}_\odot}\Big)^{-1}. \tag{1.4}$$

For typical values of $M \sim 10^3 - 10^4$ $\mathrm{M}_\odot$, $T \approx 10$ K and $R \approx 10$ pc (Bergin & Tafalla 2007), $\frac{U}{|\mathcal{W}|} \ll 1$, so molecular clouds cannot be supported by thermal pressure alone. Polarization studies throughout the galaxy have proved that magnetic fields permeate molecular clouds (e.g. Planck Collaboration et al. 2016; Soler et al. 2016), so $\mathcal{M}$ is a non negligible term. However, it seems that in most cases its still lower than necessary to stabilize the cloud (Crutcher 2012). The kinetic energy $\mathcal{K}$, unlike U and $\mathcal{M}$, could be high enough to stabilize a cloud. GMCs contain strong non-thermal motions, caused by supersonic *turbulence* (Heyer & Brunt 2004; Dobbs et al. 2014). These non-thermal motions translate into a measured velocity dispersion $\sigma_v > c_s$, where c_s is the speed of sound in the gas:

$$c_s = \sqrt{\frac{k_BT}{\mu m_H}}. \tag{1.5}$$

Larson (1981) found that velocity dispersion and cloud size correlate through a power law, consistent with a turbulent velocity spectrum across several scales. The term $\mathcal{K}$, therefore, is usually regarded as the main force supporting the cloud against collapse (Larson 2003).

However, it is currently unclear if GMCs are in a global state of equilibrium. It is difficult to assess if a cloud is in virial equilibrium or in a state of global collapse because the expected σ_v for both cases are similar (e.g. Ballesteros-Paredes et al. 2011). The lifetimes of GMC are a matter of debate, with GMC lifetimes measured between a few Myr to more than 100 Myr (see Dobbs et al. 2014; Heyer & Dame 2015, and references within). Moreover, the environment where a GMC is embedded in influences its equilibrium and therefore must be taken into account (see Chevance et al. 2023, and references within). Usually, molecular clouds live long enough to form several stars and are dissipated after the formation of a massive star, which destroys the cloud from within (Palla & Stahler 1993a). Although molecular clouds as a whole are turbulent, the dense cores within them present subsonic velocities (Goodman et al. 1993; Pineda et al. 2010; Choudhury et al. 2020). Therefore, star formation must then occur in unstable structures *within* the molecular clouds.

1.2.1.2 Jeans length and Jeans mass

At which scales does gas collapse to form stars? Using the virial theorem, considering gravity and thermal pressure first, virial equilibrium implies $-W = |W| = 2U$. Then, the condition for collapse is that gravity is stronger than thermal motions, that is, $|W| > 2U$, which replacing with U and W reads:

$$\frac{GM}{R} > 3\frac{k_BT}{\mu m_H} \tag{1.6}$$

Assuming a spherically symmetric configuration, the total mass within the cloud can be written as $M = \frac{4\pi}{3}\rho R^3$, where ρ is the density. Usually, the density in molecular clouds is described through the *number density* $n = \rho/(\mu m_H)$. Isolating R with respect to T and n, Eq. 1.6 defines a maximum radius of stability:

$$R > \sqrt{\frac{9k_BT}{4\pi G(\mu m_H)^2 n}}. \tag{1.7}$$

This means that an isothermal gas with a radius larger than this value will *not* be sustained by thermal pressure and will therefore collapse. We call this scale the *Jeans length* λ_J, and in relevant T and n units reads:

$$\lambda_J \approx 0.1 \left(\frac{T}{10\,\mathrm{K}}\right)^{1/2} \left(\frac{n}{10^4\,\mathrm{cm}^{-3}}\right)^{-1/2} \mathrm{pc}.. \tag{1.8}$$

Instead of using the physical size, we can also describe the collapse condition in terms of mass. We define the *Jeans mass* $M_J = \frac{4\pi}{3}\rho\lambda_J^3$ as the maximum mass that can be in equilibrium for a given ρ and T. Replacing λ_J, we obtain:

$$M_J \approx 2.6 \left(\frac{T}{10\,\mathrm{K}}\right)^{3/2} \left(\frac{n}{10^4\,\mathrm{cm}^{-3}}\right)^{-1/2} \mathrm{M}_\odot. \tag{1.9}$$

From Eq. 1.8, we see that the higher the density, the smaller the regions that tend to collapse. Replacing typical values for T and n for cores mentioned in Sect. 1.1.2.1, $\lambda_J \lesssim 0.1$ pc, coinciding with the typical sizes of dense cores. Therefore, dense cores are mostly unstable against gravitational collapse, and are thus the units within molecular clouds that will form stars.

1.2.2 Core collapse

Once a core is unstable (given the conditions described above), it will collapse and eventually, due to the increase in density at the center, a protostar or a multiple system is formed. The exact nature of the collapse depends on the initial conditions of the core and how the collapse is triggered.

Two kinds of models have been widely used to picture this collapse, the Larson-Penston model (Larson 1969; Penston 1969) and the Shu model (Shu 1977). These models consist of similarity solutions[2] of the differential equations that follow the evolution of density and velocity of the gas in the core. They describe the collapse of an isothermal, spherically symmetric core with no rotation, magnetic fields, turbulence or influence from the environment. Spherical symmetry implies that the only variables to describe the physical conditions within the core are the radial distance from the sphere's center r and the time t. The main difference between the two models are the initial conditions of the core dynamical conditions of the core at the moment when a protostar forms.

[2]A similarity solution in mathematics is a solution of a partial differential equation found after transforming the independent variables into a set of variables that is smaller than the original set.

1.2.2.1 Larson-Penston (LP) model

We begin by analyzing the collapse model first described by Larson (1969) and Penston (1969), sometimes referred to as "fast core collapse". This model starts at time $t = 0$ with a core of gas with uniform density and follows the formation of a central object in the center in a marginally unstable energy configuration so that collapse ensues. The core is initially at rest, with radial velocity $v = 0$ everywhere, and with a mass slightly higher than the critical mass for collapse.

At $t = 0$, as the density and temperature are constant, there are no pressure gradients, so the core collapses inward with free-fall motion. The collapse starts at the core boundary and collapsing motions travel from the boundary inward, increasing the density toward the center while the outer radius remains constant. The free-fall time within the different layers of the sphere depends on the local density: Equation 1.3 shows that t_{ff} is inversely proportional to the volume, so written in terms of the gas density $\rho \sim M/R^3$:

$$t_{ff} = \sqrt{\frac{3\pi}{32G\rho}}. \tag{1.10}$$

As a consequence, collapse becomes faster in the central regions as density increases. A pressure gradient appears at the outer regions after they collapse, as their density is now lower than toward inner regions of the core, and this slows down the infall in the outer layers. Due to these effects, the density distribution of the core becomes more centrally-pronounced, asymptotically reaching the form $\rho \propto r^{-2}$. The development of this central concentration is shown in Fig. 1.3 left, which corresponds to Fig. 1 of Larson (1969).

When the density is high enough at the center (in Larson 1969, this is $\rho \approx 10^{-19}$ g cm^{-3}), it becomes optically thick and the isothermal assumption in the center breaks. When this happens, the rest of the core, which we now call the envelope, is falling toward the center at *supersonic* speeds (McKee & Ostriker 2007). The protostar is gaining mass as $M_* = \dot{M}_{acc}t$, where $\dot{M}_{acc}$ is the protostellar *accretion rate*. Hunter (1977) extended the LP solution to t after the formation of the central protostar and predicted a constant accretion rate (Larson 2003):

$$\dot{M}_{acc} = 46.9c_s^3/G = 7.4 \times 10^{-5}\left(\frac{T}{10\,\mathrm{K}}\right)\mathrm{M}_\odot\,\mathrm{yr}^{-1}. \tag{1.11}$$

1.2.2.2 Shu model

The Shu model, also known as "inside-out collapse" model, consists of similarity solutions for the density and velocity where the time $t = 0$ is the moment when the protostar is born at the center of the core. To solve the differential equations, Shu (1977) finds that the core must be in marginal hydrostatic equilibrium, which implies a density distribution $\rho \propto r^{-2}$ as an initial condition, known as the *singular isothermal sphere*. Therefore, at $t = 0$, the core with $\rho \propto r^{-2}$ distribution has negligible radial velocities, unlike the LP model that, at this time, has supersonic velocities.

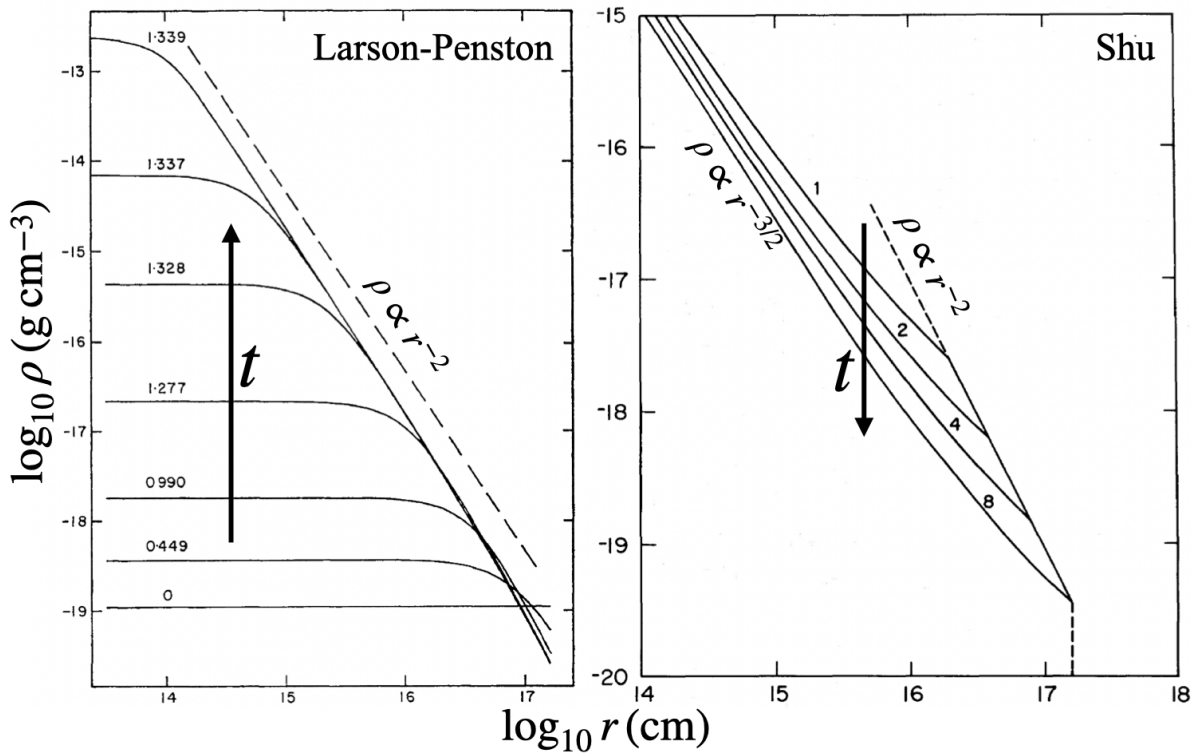

Figure 1.3: Density profiles with respect to radius across different times for the Larson-Penston (left) and Shu (right) core collapse models. Left: density versus radius for the core at different times for the LP model, taken from Larson (1969). The arrow indicates the direction of increasing time: the numbers that label each curve correspond to their time since the start of the collapse in units of 10^{13} s. The dashed line represents the $\rho(r) \propto r^{-2}$ relation. Right: density versus radius for the core at different times for the inside-out collapse model, taken from Shu (1977). The dashed line represents the $\rho(r) \propto r^{-2}$ relation, and the solid lines to its left follow a $\rho(r) \propto r^{-3/2}$ law. The arrow indicates the direction of increasing time: the numbers label each curve with the time after the start of the collapse in units of 10^{12} s.

The collapse in this model starts at the center of the core and produces a rarefaction wave (i.e. a wave where pressure is lower than the ambient), which propagates with the speed of sound (McKee & Ostriker 2007). Within this wave, gas infalls at velocities similar to free-fall. The gas in the outer layers of the core is unmoved, as the initial density distribution is hydrostatic, until the wave reaches these layers. To understand why the motion propagates inside-out, Shu (1977) uses the following analogy: when the core collapses, the gas layer immediately above the core loses the supporting layer that stopped it from falling inwards (i.e. the pressure below it drops), and so it falls. This triggers the layer right above it to also fall, and so this causes a chain reaction.

This infall process produces density profiles that, instead of becoming centrally peaked, becomes centrally *flattened*. At radii within the rarefaction wave, the density $\rho \propto r^{-3/2}$ instead of $\propto r^{-2}$. This is shown in Fig. 1.3 right, originally Fig. 3a from Shu (1977). This solution is valid until the rarefaction wave reaches the outer boundary. When this happens, a shock wave is expected to travel toward the interior of the core (Shu 1977), pushing material inward. The predicted accretion rate in this model is also constant in time but an order of magnitude lower than the LP model accretion rate:

$$\dot{M}_{acc} = 0.975\frac{c_s^3}{G} = 1.54 \times 10^{-6}\left(\frac{T}{10\,\mathrm{K}}\right)\mathrm{M}_\odot\,\mathrm{yr}^{-1}. \tag{1.12}$$

1.2.2.3 Effects of rotation

The previous core collapse models account for the creation of the protostar. However, disks of gas and dust are a common feature around observed protostars (see Dutrey et al. 2014b, and references therein). To account for their existance, it is only necessary to add rotation to our collapse models. It is widely known that star-forming cores rotate (e.g. Goodman et al. 1993; Caselli et al. 2002a). Circumstellar disks are a direct consequence of adding rotation to the original cores, although their specific properties require considering other effects such as magnetism and turbulence (see McKee & Ostriker 2007; Williams & Cieza 2011, for more details).

To explain why the rotation will always produce a disk in a contracting spherical core, lets first assume an isothermal, spherically symmetric core of radius r_0 that is initially following solid body rotation, defined with an angular velocity Ω_0 around an axis $\hat{z}$. All particles within the sphere then have an angular momentum defined by:

$$L = I\Omega_0 = mr_z v_\phi, \tag{1.13}$$

where $I = mr_z^2$ is the moment of inertia of the particle and $v_\phi = r_z\Omega_0$ is the rotational velocity at a distance r_z from $\hat{z}$. It is convenient to introduce the specific angular momentum $j = L/m$ instead, as it is independent of the mass. However, the distance between a particle and the rotation axis is $r_z = r\sin\theta$, where r is the distance from the core's center and θ is the angle with respect to $\hat{z}$. As a consequence, there is a *range* of specific angular momenta in the core (Stahler & Palla 2004):

$$j(r,\theta) = r^2\Omega\sin\theta. \tag{1.14}$$

At $t = 0$, the core starts collapsing inward. The rotation introduces a centrifugal force per unit mass is $F_{cen} = j^2 r_z^{-3}$. When there are no external forces, j is conserved, and so the centrifugal force increases as the particle falls. Therefore, particles within the core will veer away from the center of the sphere, so their trajectories, instead of straight lines as in the case of purely gravitational infall, become *parabolas* (Stahler & Palla 2004). The focus of all parabolas is the center of the sphere, where the protostar is forming. Most importantly, given the spherical symmetry of the core, all trajectories are *mirrored* with respect to the equatorial plane, so particles will collide at the equator ($\theta = \pi/2$). This collision is what forms the equatorial disk, inside which gas can still accrete toward the protostar (Ulrich 1976).

The maximum initial specific angular momentum within the sphere j_c, located at the equator according to Eq. 1.14, defines the edge of the forming disk:

$$R_c = \frac{j_c^2}{GM_{*,d}} = \frac{\Omega_0^2 r_0^4}{GM_{*,d}}, \tag{1.15}$$

where $M_{*,d}$ is the mass of both the protostar and disk together (Ulrich 1976; Stahler & Palla 2004; McKee & Ostriker 2007).

As in the case of core contraction with gravitational forces only, there are two cases that have been extensively studied, which are basically the models described previously but with a small level of initial rotation added (Larson 2003; McKee & Ostriker 2007). In both cases, most of the mass falls first to a disk around the protostar, but rotation will *not* impede the formation of a central density singularity (Narita et al. 1984).

When starting from a uniform density spherical core, numerical calculations show the collapse forms a centrally concentrated disk with a surface density distribution $\Sigma \propto r^{-1}$ (Norman et al. 1980; Narita et al. 1984). The similarity solutions for the uniform sphere case starting from rest were found by Saigo & Hanawa (1998), and found it to be analogous to the LP model but with the addition of rotational flattening (Larson 2003). After a singularity forms in the middle, there is an inner rotating disk and an outer infalling and rotating envelope.

In the case of inside-out collapse, when rotation is added to the model, most of the envelope falls on the disk and not in the central protostar. Similar to the previous model, there is an inner rotating disk with an outer infalling-rotating envelope. Terebey et al. (1984) included the effects of rotation in the inside-out model using perturbation theory and defined three regimes: in the outer parts of the core, matter is unable to infall until the rarefaction wave reaches it to trigger infall. Within the expansion wave, but farther from the centrifugal radius, they found a similarity solution by applying a small perturbation to the spherically symmetric equations without rotation (Shu 1977). This solution departs from a purely radial infall as it comes closer to the disk radius and pressure gradients become negligible. The resulting density profile of the disk is given by the Ulrich (1976) and Cassen & Moosman (1981) model, known as the Ulrich-Cassen-Moosman (UCM) model, which considers the trajectory of the gas as ballistic (i.e. without the effect of pressure gradients).

1.2.3 Protostellar formation and evolution

Independent on the exact functional form of the density profile, once the central density reaches about 10^{13} g cm^{-3}, the isothermal assumption breaks: the opacity of the gas is high enough that now it absorbs the energy that before was just radiated away, and so the contraction becomes adiabatic instead of isothermal. The thermal pressure then increases until it stops gravitational contraction, forming what is known as a First Hydrostatic Core (FSHC). Numerical simulations predict that FHSC have masses of $\approx 10^{-2}$ M$_\odot$, radii between $\sim 3-5$ au and very low luminosities, < 0.1 L$_\odot$ (depending on the conditions of the core, e.g. Masunaga et al. 1998; Commerçon et al. 2012; Bate et al. 2014).

Both in the LP and inside-out collapse models, when this first core forms, the majority of the mass is still in the original isothermal core, which we call the *envelope* (so as to not confuse with the inner FHSC). The mass of the FHSC increases with the mass infalling from the envelope, while its radius decreases due to radiative losses. These processes increase the temperature until it reaches about 2000 K. At this point, H_2 dissociates to atomic H, a process which takes energy away from the pressure support (Stahler & Palla 2004), and so the FHSC becomes unstable and collapses dynamically (Larson 1969, 2003), marking the end of the FHSC stage.

During this second collapse, the density and temperature grow enough to partially ionize the H atoms at the center. The second collapse stops once the H is mostly ionized and the thermal presure again counteracts gravity. This second hydrostatic core is what astronomers call a *protostar*. At its conception, for cores with an initial mass of about 1 M$_\odot$, the mass of the protostar is $10^{-3}-10^{-2}$ M$_\odot$ (Larson 1969; Shu et al. 1987). Material from the FHSC is quickly consumed by the protostar, but around 99% of the final mass of the protostar is inside an envelope that is in free-fall (with supersonic velocities). Accordingly, it it said that the protostar enters its *main accretion phase*. During the formation of the FHSC and the protostar, as dense cores rotate, accretion is not spherical (as explained in Section 1.2.2.3) and so accretion occurs mostly through the disk (Larson 2003).

Assuming all the kinetic energy of the infalling mass is turned into radiation, at this stage we can obtain the accretion luminosity of the protostar:

$$L_{acc} = \frac{GM\dot{M}_*}{R_*}, \tag{1.16}$$

where M_* and R_* are the mass and the radius of the protostar, respectively, and $\dot{M}$ is the accretion rate of the protostar. in the main accretion phase, the radius of the protostar is roughly 4 R$_\odot$ (Stahler et al. 1980; Masunaga & Inutsuka 2000). However, at this stage, the protostar becomes embedded in a dust envelope generated due to the collapse of the core, and therefore the luminosity is mostly reprocessed by the dust. Therefore, we can only observe the object in the near-IR or longer wavelengths.

As the protostar accretes material, it also expels material in the form of winds, which are observed as bipolar outflows and jets perpendicular to the disk rotation (Bally 2016). Jets are highly collimated ejections traveling at high velocities ($\gtrsim$ 100 km s^{-1}) seen in ionized gas (Ray et al. 2007; Tsukamoto et al. 2023). Outflows are the low-velocity ($\sim$ 10

$\mathrm{km\,s^{-1}}$) expanding lobes of molecular gas (Arce et al. 2007). Nevertheless, “outflow" is sometimes used to refer to all out-flowing material from the protostar and disk system. The properties of outflows and jets in general depend on the evolutionary stage of the protostar, but they are an ubiquitous part of the star formation process (Bally 2016). As such, outflows are used to determine if a protostar has been born within a core, as sometimes the outflow or jet can be observed while the protostar is too obscured by its envelope (Fukui et al. 1993). The origin of outflows and jets is magnetohydrodynamic in nature: the magnetic fields that thread the protostar and disk are locked with the gas, and so when material accretes, magnetic flux accumulates toward the center of the system, and the magnetic pressure generated by the increased flux drives the jet, whereas the outflow travels along magnetic field lines (Tsukamoto et al. 2023).

As the envelope is consumed, it becomes more optically thin until it dissapears completely. When this happens, the protostar, in the low-mass star formation scenario, has not yet reached temperature high enough to kickstart nuclear fusion, and so it will slowly contract in until the temperature reaches 10^7 K, where nuclear burning of H starts (Kippenhahn et al. 2013). This contraction is known as the the pre-main sequence phase (PMS, Stahler & Palla 2004). Although the envelope is consumed, the disk remains, which still accretes mass to the protostar. However, part of the disk mass accrete into planetesimals to further form planets, in a process which constitutes an active area of research today (see Drążkowska et al. 2023, and references within).

1.2.4 Observed low-mass protostars

Protostellar evolution models, from its inception to the total consumption of the envelope, are used to explain the observed properties of star forming regions (Dunham et al. 2014). The diagnostic tool to investigate the evolutionary stage of protostars is their Spectral Energy Distribution (SED), which is a plot of the energy λF_λ for each wavelength λ of light emitted by a source. In particular, protostars emit in the infrarred range, due to the reprocessing of the light from the protostar by the surrounding dust (Larson 2003). As the envelope depletes, the spectrum of emitted radiation shifts to shorter wavelengths.

Protostars are classified according to the properties of their observed SED. The idea is that a protostar with more emission in IR wavelengths is embedded in more dust and therefore at a younger evolutionary stage. One quantity used to classify protostars is their spectral IR excess α_{IR}, which quantifies the excess of IR emission due to circumstellar material as the slope of the IR part of the SED:

$$\alpha_{IR} = \frac{d \log \lambda F_\lambda}{d \log \lambda}, \tag{1.17}$$

where λ is the wavelength of the emission and F_λ is the flux. This slope is conventionally taken between 2.2-10 or 2.2-15 μm (Stahler & Palla 2004; McKee & Ostriker 2007). Another quantity which is used to classify protostars is their bolometric temperature T_{bol}, which is the temperature of a blackbody that has the same mean frequency as the observed SED (Myers & Ladd 1993). These quantities, in conjunction with the shape of the SED across

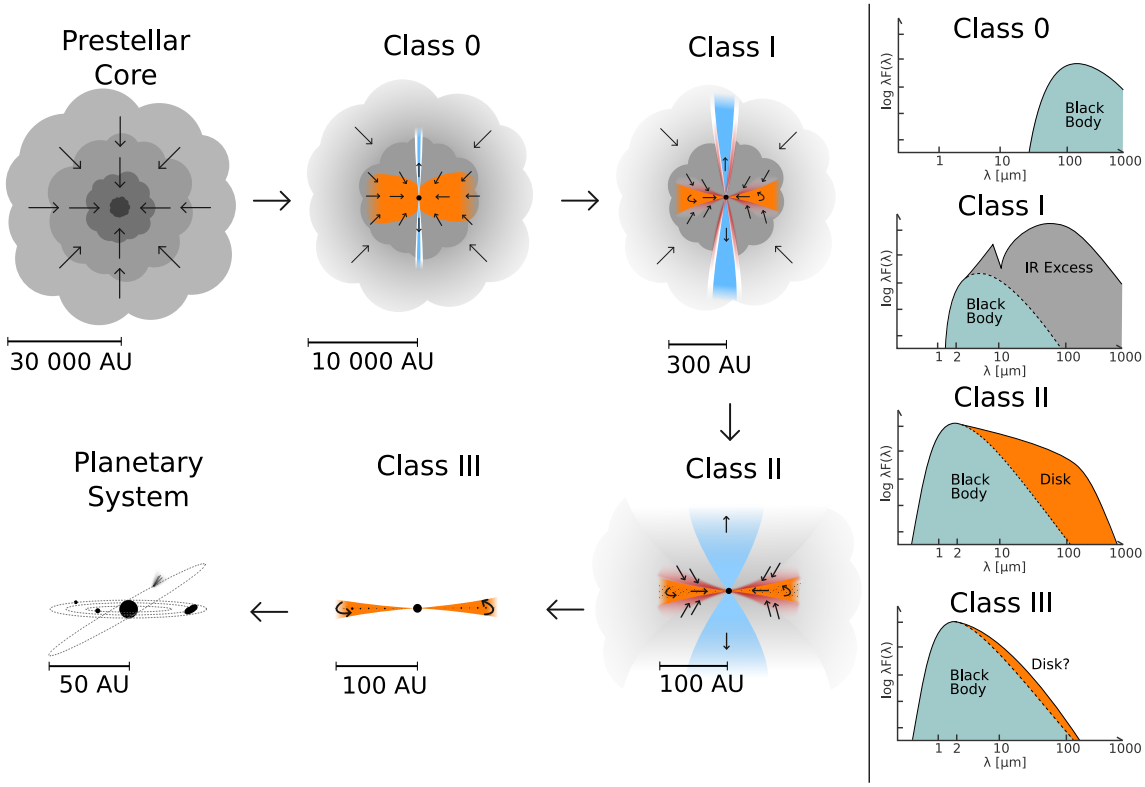

Figure 1.4: Diagram showing the stages of the protostar and disk development with their associated classification according to their SED. Left: Evolution of a protostar and its corresponding observational classification. Gray areas represent envelope material, orange areas show the extent of the protostellar disk, and blue areas show the bipolar outflows. Arrows indicate the direction of the gas flow in each region. Right: expected SED at IR and submillimeter wavelengths for each of the observational classes. IR excess is attributed mostly to the envelope material, whereas in Class II and III it shows the disk component. Figure credit: M. V. Persson.

optical, IR and submillimeter wavelengths, are conventionally used to classify protostars into 4 classes, which are correlated with the different protostellar evolution stages as follows (Lada 1987; Andre et al. 1993; Chen et al. 1995; Andre et al. 2000; Dunham et al. 2014):

- **Class 0**: protostars with $T_{\rm bol} < 70$ K, where their SED is dominated by emission similar to blackbody. These protostars are so deeply embedded in their envelopes that there is practically no IR emission below $\lambda \approx 10$ μm detectable and their emission comes mostly from the dust envelope.

- **Class I**: protostars with $\alpha_{IR} > 0$ or $70 < T_{\rm bol} < 650$ K. Protostars are believed to have a dissipating envelope, so the light from the star and the disk can be seen in the SED, although it is dominated by a strong IR excess.

- **Class II**: protostars with $-1.5 < \alpha_{IR} < 0$ or $650 < T_{\rm bol} < 2800$ K. Almost no envelope is left and the emission in the SED is dominated by the star and the disk.

- **Class III**: protostars with $\alpha_{IR} < -1.5$. Also called Weak T Tauri stars, these are no longer accreting significant amount of matter.

Figure 1.4 summarizes the different stages of the protostellar collapse until the formation of a star with a planetary system and labels each step with its corresponding class. Sources that are Class II and III are believed to already be in the pre-main sequence evolution. Greene et al. (1994) added an intermediate class called Flat SED in between Classes I and II to represent a transition between protostar and pre-main sequence stars.

1.2.5 Limitations of the model

The core collapse models and subsequent protostellar evolution models have successfully accounted for the most general features of star formation and have pushed the field for several years. However, these models have two assumptions that are not true for star forming regions: the axisymmetry of the core collapse and its isolation with respect to their local environment. Within a molecular cloud, hundreds of low-mass stars (and some high-mass stars) form together. For instance, the Perseus molecular cloud, approximately 300 pc away, contains around 100 embedded protostars (Enoch et al. 2009), most of which are concentrated within ~ 10 pc^2 in NGC 1333 (a star forming region within the cloud, Gutermuth et al. 2008). This clumping of stars is a reflection of the clumping of cores: as mentioned previously, most dense cores are harbored within filaments, and therefore do not evolve in isolation. Also, observations of dense cores and protostellar envelopes show that these are anything but axisymmetric (e.g. Pineda et al. 2019; Stephens et al. 2019). The interaction between the natal core and the environment and its subsequent shape must be taken into account to better understand the development of a protostar.

One of the most famous discrepancies between protostellar properties expected from models and those observed is the so-called Luminosity problem. For accretion due to gravitational collapse, the inside-out model shown predicts an accretion rate of about 10^{-6} $M_\odot$ yr^{-1} for a typical temperature of 10 K (Eq. 1.12). The presence of the disk does not greatly affect this estimate, as it only stores a small fraction of the total mass of the system (e.g. Andrews & Williams 2005; McKee & Ostriker 2007). When including the effect of magnetism and rotation, the accretion rate is still on the same order of magnitude (Larson 2003). Other estimates using the average observed timescale of Class I stage (10^5 yr) give that the accretion rate is closer to 10^{-5} $M_\odot$ yr^{-1} (Stahler et al. 1980). As a consequence, Eq. 1.16 gives a luminosity of about $10 - 100$ $L_\odot$. The observed luminiosities of protostars in Class I are $1 - 2$ order of magnitude *lower* than these estimations (Kenyon et al. 1990; Evans et al. 2003). In short, the observed accretion rate of protostars is much lower than what is required to form a protostar in the estimated Class I lifetime of about 10^5 yr. Kenyon et al. (1990) proposed two possible solutions: first, that mass could still be accreted during the T Tauri phase, and second, that accretion during protostellar evolution

can be variable. Accretion toward T Tauri sources is usually on the order of 10^{-8} $M_\odot$ yr^{-1}, but additional infall to the disk in this phase has been recently discovered (as will be discuss in Sect. 1.3). The second solution is supported by observations of FU Orionis (FU Ori) and EX Lupi (EXor) type protostars, which present short periods of extremely high accretion (see Audard et al. 2014, for more details on accretion variability).

There has been significant effort to add more realistic conditions to models and simulations of star forming regions. These works consistently show that the environment around individual cores regulates the growth of protostars (e.g. Padoan et al. 2014; Kuffmeier et al. 2018). As shown in the next section, high-resolution observations of envelopes around protostars are showing new substructures connecting the scales between cloud-scale asymmetries and protostars.

1.3 Streamers: asymmetric infall channels

When the assumptions of axisymmetric and isolated core collapse are dropped, envelopes are now dynamic structures that can have considerable substructure. Numerical simulations repeatedly find accretion toward the circumstellar disk occurs through filamentary or sheet-like structures that transport material from the envelope, or even beyond, when the interaction with the environment (e.g. Kuffmeier et al. 2017) and/or initial levels of turbulence (e.g. Seifried et al. 2015; Hennebelle et al. 2020) are considered. With the advent of powerful interferometers, such as ALMA and NOEMA, we can now peer into the structure of envelopes toward nearby ($\lesssim$ 500 pc away) protostars. These observations reveal that the axisymmetric infall structures from envelope to disk theorized in simulations are real. These structures are now known as *streamers*, first coined in the context of protostellar accretion by Pineda et al. (2020). In this section, I explain the properties of observed streamers toward low-mass protostars and how we confirm their infalling nature.

1.3.1 Definition of streamers

The term “streamer" has sometimes been used to describe asymmetric, arc-shaped structures in gas and/or dust emission that are not associated with outflows. However, we are converging toward a more rigorous definition of what a streamer is after the increase in the discovery of asymmetric structures that deliver mass to circumstellar disks (Pineda et al. 2023). The definition of streamer I use in this work considers the spatial and the dynamical nature of these envelope asymmetries.

A streamer is a velocity-coherent, narrow structure of molecular gas or dust which transports material toward a circumstellar disk. The important part of this definition is the *infalling* nature of these asymmetric structures. Some structures like arcs in the vicinity of protostars might look like streamers, but until their infalling nature is not confirmed, it is not a streamer under this definition. The specific thickness of the streamer is not as vital for the definition, as long as the emission looks asymmetric, given that these infall material could either be observed as a line or a sheet-like structure depending on its

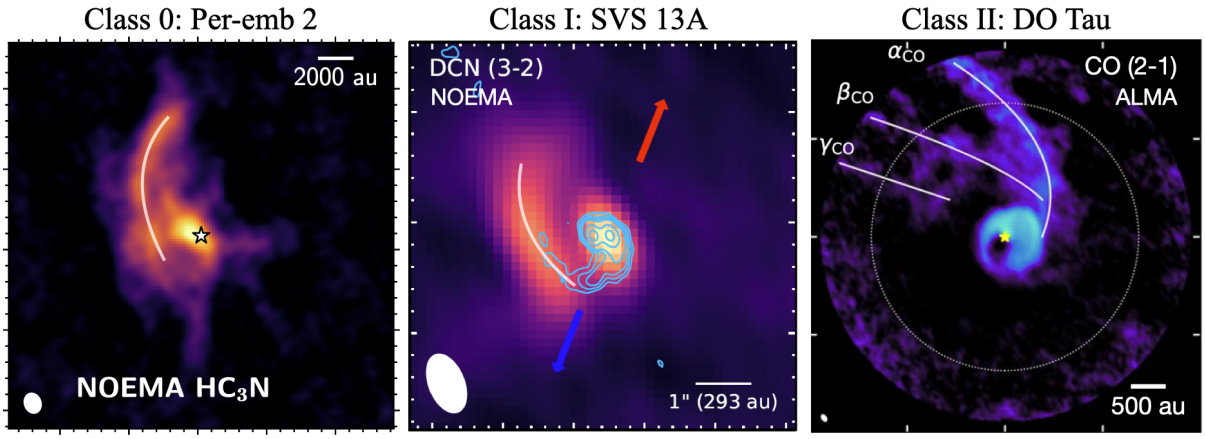

Figure 1.5: Examples of streamers observed toward protostars of different classes (according to the criteria in Sect. 1.2.4).Each image consists of the integrated emission of the molecule indicated. The streamers' directions are indicated with white lines. Each image also includes a white ellipse indicating the spatial resolution of the image and a scalebar for distance reference. Left: streamer toward the Class 0 protostar Per-emb-2 from Pineda et al. (2020), observed in HC_3N emission. Center: streamer toward the Class I protostar SVS 13A from Hsieh et al. (2023b), seen in DCN emission. Right: streamers observed toward the Class II DO Tau by Huang et al. (2022), observed in ^{12}CO emission.

projection in the sky. They differ from the previously defined core collapse models as these can be observed over envelope emission and can bring material from beyond the dense core (e.g., Pineda et al. 2020).

1.3.2 Observations of streamers

While non-axisymmetric infalling envelopes have been observed in the past (Tobin et al. 2012), there has been a steady increase in the discovery of streamers within the last 5 years. Streamers are observed toward protostars in all phases of evolution, from highly embedded Class 0 protostars (e.g. Pineda et al. 2020; Cabedo et al. 2021; Murillo et al. 2022; Thieme et al. 2022) as well as Class I protostars (e.g. Yen et al. 2014; Bianchi et al. 2022; Valdivia-Mena et al. 2022; Hsieh et al. 2023b) and Flat SED disks (e.g. Yen et al. 2019; Harada et al. 2023). Streamers have also been seen feeding T Tauri disks (Huang et al. 2022; Garufi et al. 2022; Gupta et al. 2023). An example of a streamer in integrated intensity emission for each protostellar SED classification is shown in Fig. 1.5. Streamers can occur along the outflow cavity walls (e.g. Thieme et al. 2022) as well as through the envelope almost perpendicular to the outflows (e.g. Valdivia-Mena et al. 2022).

It is important to note that observations of streamers have been mostly serendipitous, i.e. these structures were discovered with data that was designed to investigate other phenomena, such as the physical and chemical structure of gas. For instance, Murillo et al. (2022) discovered toward IRAS 16293 A, which has been extensively studied in the past,

and Thieme et al. (2022) used archival ALMA observations to uncover streamers in Lupus MMS 3. These results highlight the importance of reevaluating previous observations to better understand infall (Pineda et al. 2023).

As more streamers are discovered, some common features have been observed. First, streamers have a range of lengths between a few 100 to several 1000 au. The longest streamer recognized up to date has a length of $\approx$ 10000 au (Pineda et al. 2020), surpassing the radius of its core. Second, almost all streamers have been observed in molecular gas emission (Pineda et al. 2023). This is because observing in dust would require longer integration times. Streamers are usually less bright than other structures such as the disk around the protostar and the outflow. Nevertheless, with longer integration times, it is possible to observe dust emission from streamers, for now only done for one Class I source where the streamer's kinematics were confirmed using gas observations as well (Cacciapuoti et al. 2023). A key quantity for streamers is their infall rate $\dot{M}_{in}$, i.e. the rate of mass transport from the streamer to the protostellar disk. This property is hard to measure, as for this the mass of the streamer must be known as well as its approximate infall speed. On one hand, measuring the mass of a streamer requires assumptions about the abundance of the observed molecular species with respect to H_2 and its optical thickness (see Sect. 1.4). On the other hand, the assumption of free fall from rest at the beginning of the streamer is not always correct and this can affect the estimated infall rate, as we see in Chapter 2 (Valdivia-Mena et al. 2022). When estimated, $\dot{M}_{in}$ is higher or similar to the accretion rate of the protostar $\dot{M}_{acc}$ (i.e. the mass accreted to the protostar from the disk per unit time, e.g. Pineda et al. 2020; Valdivia-Mena et al. 2022; Thieme et al. 2022; Flores et al. 2023). This implies that there is usually more mass entering the disk than exiting, which can generate gravitational instabilities in the disk (e.g. Kuffmeier et al. 2018).

1.3.3 Modelling streamer motion

The infalling nature of streamers is confirmed by comparing their molecular gas emission with the expected velocities from analytical solutions of a gas particle, assuming it is only affected by the gravitational pull of the protostellar system. The most frequently used analytic model is a modification of the UCM pressure-free model (mentioned in Sect. 1.2.2.3) by Mendoza et al. (2009). The original purpose of the UCM and Mendoza models are to predict the disk density structure after core collapse, but the mathematical prescription for individual streamlines can be used to describe individual parcels of gas.

Lets assume a fluid particle has an initial angular velocity Ω_0 with respect to the z axis, at an initial position defined by the spherical coordinates r_0, θ_0 and ϕ_0 with the protostar at the center. Figure 1.6 shows the geometry of the problem. Lets further assume that Ω_0 follows the same direction as the rotation of the disk. As there are no perturbations, the trajectory of the particle is a conical section contained in an orbital plane, which has the shape:

$$r(\varphi) = \frac{r_c}{1 + e\cos(\varphi)}, \tag{1.18}$$

where r and φ are the polar coordinates (distance and angle) within the orbital plane and

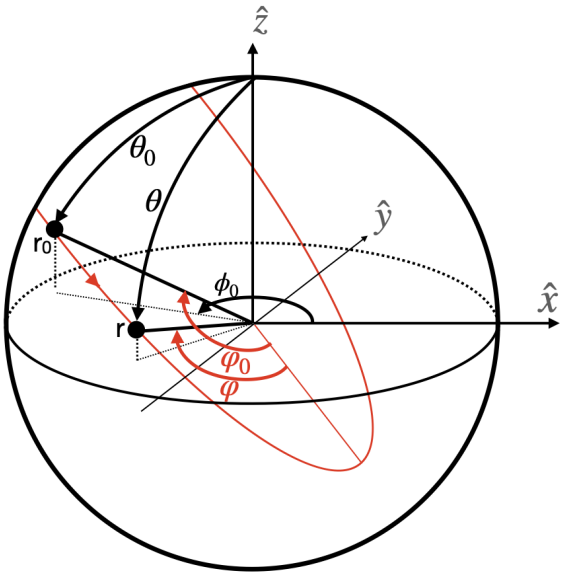

Figure 1.6: Geometry of the streamline model from Mendoza et al. (2009). The black shapes correspond to coordinates in the protostar's reference system while the red curve shows the streamline and the coordinates with respect to its orbital plane.

e is the eccentricity of the conical section. $\varphi = 0$ where r has its minimum value. r_c is the *centrifugal radius* of the streamline:

$$r_c = j^2/GM, \tag{1.19}$$

i.e. the radius at $\varphi = \pi/2$, where the particle reaches the disk (assuming its a thin disk). This trajectory is the red thin curve in Fig. 1.6. The angular momentum j of the particle depends on the angle with respect to its rotation velocity:

$$j = j_0 \sin(\theta_0) = r_0^2 \Omega_0 \sin(\theta_0). \tag{1.20}$$

The UCM model, first mentioned in Section 1.2.2.3, assumes the fluid particle has zero total energy, and so the trajectory has an $e = 1$ and is thus a parabola (Ulrich 1976; Cassen & Moosman 1981). The Mendoza model extends the UCM model and assumes that the specific energy of the particle is a constant of motion that can be different from zero:

$$E = \frac{v_{r,0}}{2} + \frac{j_0^2 \sin^2\theta_0}{r_0^2} - \frac{GM}{r_0}, \tag{1.21}$$

where $v_{r,0}$ is the initial radial velocity of the particle at position r_0. To solve for e, Mendoza et al. (2009) defines two dimensionless parameters that represent a dimensionless radius μ and dimensionless velocity ν:

$$\mu^2 = \frac{j_0^2}{r_0^2 E_0^2},\ \nu^2 = \frac{v_{r,0}^2}{E_0}, \tag{1.22}$$

where $E_0 = GM/R_d$ is the gravitational energy at the disk edge. R_d is the centrifugal radius of the streamline at the equator, given by Eq. 1.15. Defining then the dimensionless energy as $\epsilon = 2E/E_0$, the eccentricity is:

$$e = \sqrt{1 + \epsilon \sin^2 \theta_0}, \tag{1.23}$$

and therefore the trajectory is completely defined within the orbital plane.

The trajectory in the protostar's frame of reference can then be obtained using geometrical considerations. First, the relation between θ_0 and the initial trajectory angle φ_0 is given by considering equation 1.18 at radius r_0:

$$\cos \varphi_0 = \frac{1}{e}(1 - \mu \sin^2 \theta_0). \tag{1.24}$$

Then, the spherical angles θ and ϕ are related to the trajectory φ performing rotations according to the geometry shown in Fig. 1.6:

$$\cos(\varphi - \varphi_0) = \frac{\cos \theta}{\cos \theta_0},\ cos(\phi - \phi_0) = \frac{\tan \theta_0}{\tan \theta}. \tag{1.25}$$

The trajectory r is then only a function of θ instead of φ, as ϕ is also a function of only θ. Replacing then φ in Eq. 1.23 and then using Eq. 1.18 we obtain the trajectory with respect to the protostar (Mendoza et al. 2009):

$$r = \frac{r_0^2 \Omega_0 \sin^2 \theta_0}{GM(1 - \cos \xi)}, \tag{1.26}$$

where we define ξ for convenience:

$$\xi = \cos^{-} 1\Big(\frac{\cos \theta}{\cos \theta_0} + \varphi_0\Big). \tag{1.27}$$

The velocity of the particle along this trajectory is then obtained using the definitions of velocity in spherical coordinates. We note that, as $\frac{d\phi}{dt} = \Omega$:

$$v_\phi = r \sin \theta \frac{d\phi}{dt} = \frac{j \sin \theta_0}{r \sin \theta}. \tag{1.28}$$

The velocity along the trajectory is thus:

$$v_\phi = v_k \frac{\sin^2 \theta_0}{r \sin \theta},\ v_\theta = v_k \frac{\sin^2 \theta_0}{r \sin \theta} \sqrt{\cos^2 \theta_0 - cos^2 \theta},\ v_r = -v_k \frac{e \sin \xi \sin \theta_0 i}{r(1 - e \cos \xi)} \tag{1.29}$$

where $v_k = \sqrt{E_0}$ is the Keplerian rotation velocity at the disk edge, defined for convenience.

To compare these velocities with observations, we need to further transform from spherical to cartesian coordinates (x, y, z). When looking at an edge-on disk, we define the (x, z) plane as the plane of the sky and positive y as the line of sight. The projected trajectory

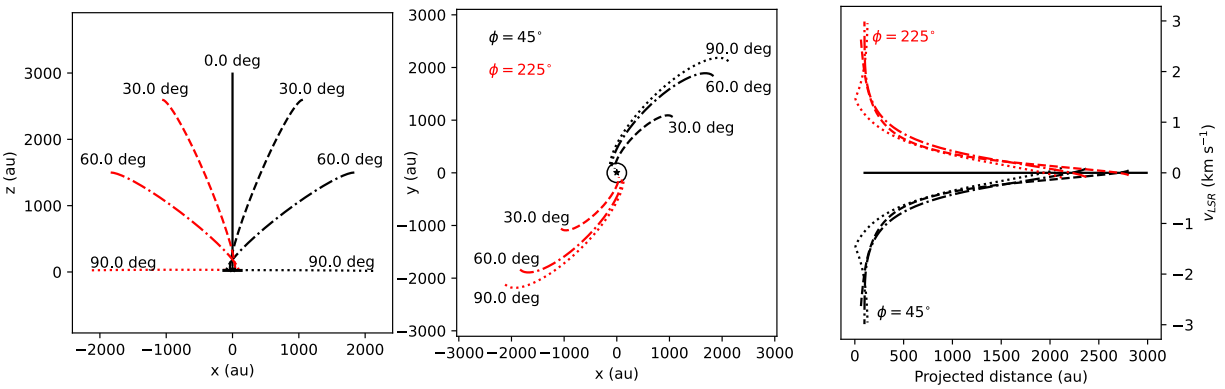

Figure 1.7: Examples of different streamlines using the Mendoza et al. (2009) prescription. The streamlines are calculated for $M = 1$ M$_\odot$, $r_0 = 3000$ au, $\Omega_0 = 3 \times 10^{-13}$ s^{-1} and a fully edge-on configuration ($i = PA = 0$). Each line style (solid to dotted) represents a different θ_0, labeled in the left plot. The black circle represents a disk with centrifugal radius R_d given by Ω_0 and r_0. The black star represents the center of the reference system (i.e. the protostar). Left: Streamlines plotted in the plane of the sky. $\hat{y}$ grows away from the observer. Center: streamlines plotted as observed perpendicular to the plane of the sky. $\hat{z}$ grows toward the observer. For this inclination, this corresponds to the plane of the disk. Right: resulting observed velocity profiles for each streamline. The velocity scale is with respect to the $v_{\rm LSR}$ of the protostar.

in the (x, z) plane is then compared with the observed intensity (either peak brightness temperature $T_{\rm MB}$ or integrated intensity $\int T_{\rm MB} dv$). The observed gas velociy is then comparable with the velocity along the line of sight of the streamline:

$$v_y = v_r \sin\theta \sin\phi + v_\theta \cos\theta \sin\phi + v_\phi \cos\phi \tag{1.30}$$

Different trajectories for this edge-on configuration are shown in Fig. 1.7. When the disk is not observed edge-on, it is necessary to rotate the system in two additional angles to obtain the streamline model: the position angle PA of the disk, which is the angle with respect to the (x, y) plane, and the inclination i of the disk, which is the angle with respect to the (x, z) (i.e. the image) plane. This will affect the observed velocities. Figure 1.8 shows the observed line of sight velocities v_y for some inclined configurations. In general, the streamer can have profiles consistent with monotonically decreasing velocity with radius or regions within the streamline with monotonically *increasing* velocity, depending on the combination of θ_0 and ϕ_0 from the streamline and the i and PA of the system.

1.3.4 Origins of streamers from simulations

Although streamers frequently appear in simulations of protostar and disk formation, their properties have only recently been studied, thanks to the increase in their observations (e.g. Kuffmeier et al. 2023; Tu et al. 2024; Heigl et al. 2024). Simulations usually deal with how different physical conditions in the core and its local environment affect the protostellar

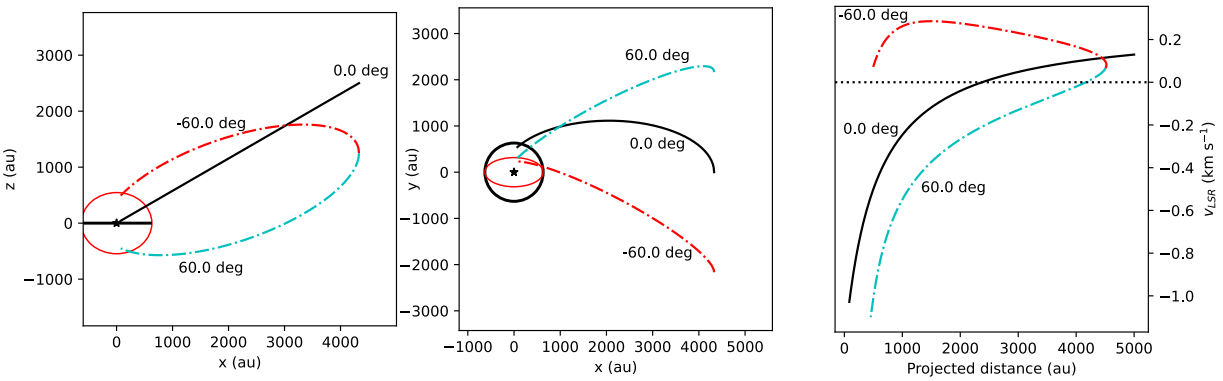

Figure 1.8: Same as Fig. 1.7 but with examples of different streamlines where the protostellar frame of reference is inclined with respect to the observed plane of the sky. The streamlines are calculated for $M = 1$ M$_\odot$, $r_0 = 5000$ au, $\theta_0 = \phi_0 = 60$ deg $\Omega_0 = 2 \times 10^{-13}$ s^{-1} and i takes the values 0 (black line), 60° (cyan dash-dotted line) and −60° (red dash-dotted line). Positive values of i incline the disk away from the observer. The red ellipse represents a disk with centrifugal radius R_d given by Ω_0 and r_0 inclined by i.

disk formation and evolution (see Sect. 5.2 of Pineda et al. 2023, and references within). Nevertheless, based on the disk formation simulations, streamers can originate both within the natal cores of protostars (e.g. Walch et al. 2010; Hennebelle et al. 2020) as well as from outside, bringing material from the larger molecular cloud (Padoan et al. 2014; Kuffmeier et al. 2017; Lebreuilly et al. 2021; Kuffmeier et al. 2023). The suggested mechanisms that drive streamers are turbulence, magnetic fields and late interaction with molecular gas.

Turbulence naturally explains the appearance of asymmetries in protostellar envelopes, as it propitiates non-axisymmetric over-densities in the cores' gas distribution (Smith et al. 2011). Walch et al. (2010) found that converging turbulent flows inside a core generated asymmetric infall channels, and Heigl et al. (2024) found the same for a core collapsing within a filament. When turbulence is added to simulations of a collapsing cloud, where several stars form in a region, natural anisotropies occur at different spatial scales (Bate 2018; Lebreuilly et al. 2021). When turbulence is added to magneto-hydrodynamic (MHD) simulations (i.e. simulations that solve the hydrodynamic equations with added magnetic fields), the resulting anisotropies are similar, both in collapsing cores (Seifried et al. 2013, 2015; Matsumoto et al. 2017; Hennebelle et al. 2020) and in simulations of collapsing clouds (Kuffmeier et al. 2017; Mignon-Risse et al. 2021). Although magnetic fields are not necessary for the formation of streamers (as they appear with or without them, Lebreuilly et al. 2021), their presence aids in the accumulation of material along core asymmetries by driving gas through magnetic field lines, forming "sheetlets" that, depending on the viewing angle, can look as thin infall channels (Tu et al. 2024). Finally, gas capture also causes streamers in later stages of protostellar development. This can happen if a cloud or filament remnant, called "cloudlet", is captured by the gravitational field of the protostar (Kuffmeier et al. 2020; Unno et al. 2022; Hanawa et al. 2024). Infall is then driven by the relative velocity between the two (Dullemond et al. 2019).

1.4 Observing star formation in the Galaxy

In the last sections, we saw how our view of star formation has developed based on our observations of the sky and the physical models we used to explain the observed phenomena. What astronomers analyze is the *light* (photons) coming from star forming regions, as it is impossible to sample interstellar gas directly. There are two types of emission that are used to characterize star forming regions: continuum emission, which varies smoothly with frequency (for instance blackbody emission, described in Sect. 1.4.3), and spectral line emission released by atoms and molecules (explained in Sect. 1.4.2). In this section, I review how light is emitted and how it travels through the Universe.

1.4.1 Relative velocity of moving objects

Emitted photons in the Universe come from sources that are in motion. The velocity of the source changes the perceived wavelength $\lambda = c/\nu$ of the emitted light. For sources moving at non-relativistic speeds, the difference between the observed wavelength λ_{obs} and the wavelength at rest λ_{rest} is given by:

$$\frac{\lambda_{obs} - \lambda_{rest}}{\lambda_{rest}} = \frac{v}{c}. \tag{1.31}$$

This change is known as the *Doppler effect*. If the source is moving with a speed which is a considerable fraction of c, relativistic effects must be taken into account. If we instead describe the light in terms of frequency $\nu = c/\lambda$, the Doppler effect reads:

$$\frac{\nu_{rest} - \nu_{obs}}{\nu_{obs}} = \frac{v}{c}. \tag{1.32}$$

This effect is what allows to determine kinematic properties of gas, for which specific emission lines have known λ_{rest} (ν_{rest}). Usually, a dense core has a range of velocities, where the most dominant one is the central velocity at the local standard of rest $v_{\rm LSR}$. Assuming the distribution of velocities is Gaussian, then the gas velocity is represented by a mean $v_{\rm LSR}$ and a velocity dispersion $\sigma_{\rm v}$, the latter which consists of thermal (given by the temperature of the core) and non-thermal motions (such as those generated by turbulence).

1.4.2 Radiative processes

1.4.2.1 Line emission and the two-level system

Molecules present three kinds of transitions, associated with different methods of excitation (i.e. have energy injection): electronic, where an electron jumps between different energy states; vibrational, corresponding to the vibration of the molecules' nuclei, and rotational, which is the rotation motion of the molecule with respect to its center of mass. In molecular clouds, molecules are excited via collisions due to the thermal motions of the gas and

absorption of radiation from the environment. Then, they emit a photon via de-excitation, which is what we observe on Earth.

Lets first assume a molecular species has two energy states, an upper and lower level, with number densities n_u and n_l respectively. This assumption is known as the "two-level" approximation. A molecule can move between the upper and lower populations via (Rybicki & Lightman 1985; Mangum & Shirley 2015):

1. Spontaneous emission of a photon ($n_u \rightarrow n_l$), characterized by the transition rate (s^{-1}) A_{ul}.

2. Stimulated emission of a photon given an external radiation field $\bar{J}$. The rate of emission per unit time is $B_{ul}\bar{J}$, where B_{ul} is the rate coefficient for stimulated emission.

3. Absorption of a photon ($n_l \rightarrow n_u$) from the external radiation field. The rate of emission per unit time is $B_{lu}\bar{J}$ where B_{lu} is the rate coefficient for photon absorption.

4. Collisions with the surrounding medium, characterized by C_{lu} and C_{ul}, which are the transition rates for collisional excitation and de-excitation, respectively.

The emitted photon in the first two cases has a frequency ν_0 that depends on the energy between the levels as $\Delta E = h\nu_0$, where h is the Planck constant. The energy density per unit time, frequency and solid angle is characterized by the *emission coefficient* j_ν, which assuming an isotropic emitter is given by:

$$j_\nu = \frac{h\nu_0}{4\pi} n_u A_{ul} \phi(\nu). \tag{1.33}$$

$\phi(\nu)$ is the line profile function and describes the probability of emission of a photon with frequency ν. $\phi(\nu)$ is normalized ($\int \phi_\nu d\nu = 1$) and represents that the energy difference between the two levels does not occur *exactly* at an energy $h\nu_0$ but in a range of ν concentrated around ν_0 (Rybicki & Lightman 1985).

If we assume that gas is in thermal equilibrium, which means that the temperature is equal within the medium, then collisions dominate the exchange of molecules between the different energy states, so n_u and n_l are related by the Boltzmann equation:

$$\frac{n_u}{n_l} = \frac{g_u}{g_l} \exp\left(\frac{-h\nu_0}{k_B T_{ex}}\right), \tag{1.34}$$

where g_u and g_l are the statistical weights of each level, k_B is the Boltzmann constant, and T_{ex} is defined as the *excitation temperature* of the transition between both states (Rybicki & Lightman 1985). If the temperature of the medium changes in scales larger than the mean free path of particles, Eq. 1.34 holds. This assumption is known as *local* thermodynamical equilibrium (LTE), and in practice, it means that we can assume a constant temperature for the transitions equal to the temperature of the gas, i.e. $T_{ex} = T$.

1.4.2.2 Rotational transitions

Rotationally excited states are the ones that require the lowest energies to excite, and therefore, the lowest ambient temperatures, so these kind of transitions are observed toward dense cores. These transitions have wavelengths in the millimeter and submillimeter ranges, and are thus observed with radio telescopes.

H_2 is the dominant component of molecular clouds, but it is practically invisible. As mentioned in Section 1.1.2, gas within molecular clouds is at temperatures between $10-80$ K, where H_2 does not emit radiation. To understand why, lets consider the energy between the rotational states of molecules, obtained using quantum mechanics.

The rotational kinetic energy of a diatomic molecule (i.e. consisting of two atoms) is:

$$E = \frac{\hbar}{2I} J(J+1), \tag{1.35}$$

where $\hbar$ is the reduced Planck constant ($\hbar = h/4\pi$), I is the moment of inertia of the molecule (directly proportional to its mass) and J is the rotational quantum number, which describes the energetic state of the molecule using integers ($J = 0, 1, 2...$). As H is the smallest atom of all, H_2 has the smallest mass of all possible molecules, and therefore the smallest I, so ΔE between two rotational energy levels $J \rightarrow J-1$ is large. Moreover, as light it is a vibration of an electromagnetic field, there needs to be a charge difference between the atoms, called a *dipole moment*, for rotation to release light. H_2 is a non-polar molecule (i.e. it has no dipole moment, as both extremes have the exact same charge), so the $J = 1 \rightarrow 0$ transition is not possible. Yet H_2 possesses an electric quadrupole, so the $J = 2 \rightarrow 0$ transition is allowed, which has an associated energy change expressed in temperature of $\Delta E/k_b = 512$ K, requiring an ambient temperature of such. Therefore, H_2 emission lines are virtually non-existent in molecular clouds.

It becomes necessary to use other molecules as tracers of H_2. This requires the assumption that the abundance of a molecule is proportional to the abundance of H_2. The most commonly used tracer of molecular gas in molecular clouds is carbon monoxide (CO), as it is the most abundant in molecular clouds with respect to other found molecules (an estimated abundance of 10^{-4} with respect to H_2, see Bolatto et al. 2013, and references within). CO does have a permanent dipole moment and therefore allows for a $J = 1 \rightarrow 0$ transition, which is easy to populate, requiring $E/k_b = 5.5$ K (using Equation 1.35). The known CO $J = 1 \rightarrow 0$ transition emits a photon with $\lambda = 2.6$ mm. Other molecular tracers used for molecular clouds are CO *isotopologues* such as ^{13}CO and C^{18}O and other molecules like CN, HCO^+ and N_2H^+, all of which have rotational emission lines with millimeter or submillimeter wavelengths.

1.4.3 Radiative transfer

Before light emitted by molecules reaches an observer on Earth, it propagates through different mediums (including itself), and it thus changes depending on the properties of the material it crossed. To describe the changes, lets assume a ray of light crosses a slab

of material of infinitesimal width ds along our line of sight. Crossing this medium changes the specific intensity of light I_ν defined as the energy per unit area, time, frequency and solid angle. The change is given by the *radiative transfer equation*:

$$\frac{dI_\nu}{ds} = j_\nu - \alpha_\nu I_\nu, \tag{1.36}$$

where j_ν is the emission coefficient of the material (Eq. 1.33), and α_ν is the *absorption coefficient*.

α_ν includes the effects of absorption and stimulated emission of the material. Written in terms of the coefficients A and B and under LTE, for emission under a two-level system (as described in Sect. 1.4.2.1, Rybicki & Lightman 1985; Mangum & Shirley 2015):

$$\alpha_\nu = \frac{h\nu_0}{4\pi} n_l B_{lu}\Big(1 - \exp\Big(\frac{h\nu_0}{k_B T_{ex}}\Big)\Big)\phi(\nu) = \frac{h\nu_0}{4\pi} n_u A_{ul}\Big(\exp\Big(\frac{h\nu_0}{k_B T_{ex}}\Big) - 1\Big)\phi(\nu). \tag{1.37}$$

To solve for I_ν, we define the *source function* $S_\nu = j_\nu/\alpha_\nu$ and we solve the equation in terms of the optical depth τ_ν of the medium instead of the path s:

$$\tau_\nu(s) = \int_{s_0}^{s} \alpha_\nu(s')ds'. \tag{1.38}$$

This quantity represents the absorption of light along the path which starts at s_0. A medium is said to be *optically thick* when $\tau_\nu > 1$ and *optically thin* when $\tau_\nu < 1$. Replacing and solving for I_ν gives:

$$I_\nu = I_\nu(0)\exp(-\tau_\nu) + \int S_\nu(\tau')\exp(-\tau_\nu - \tau')d\tau'. \tag{1.39}$$

Under LTE, $S_\nu = B_\nu(T_{ex})$ (Rybicki & Lightman 1985). $B_\nu(T)$ is the Planck function which gives the specific intensity of an object radiating as a *blackbody*:

$$B_\nu(T) = \frac{2h\nu^3}{c^2}\frac{1}{\exp(\frac{h\nu}{k_B T}) - 1}, \tag{1.40}$$

where c is the speed of light in a vacuum. Thus, $B_\nu(T_{ex})$ is constant in optical depth. Therefore the specific intensity *observed* is:

$$I_\nu = I_\nu(0)\exp(-\tau_\nu) + B_\nu(T_{ex})(1 - \exp(-\tau_\nu)). \tag{1.41}$$

When studying molecular clouds, we are interested then in the emission of the material $\Delta I_\nu = I_\nu - I_\nu(0)$. For molecular line emission, $I_\nu(0)$ is therefore the cosmic background radiation, a blackbody radiation at $T = 2.73$ K, $I_\nu(0) = B_\nu(T_{bg})$.

At radio and submillimeter frequencies, where rotational spectra are usually observed, $h\nu \ll k_B T$, and therefore the Planck law can be approximated as the Rayleigh-Jeans law:

$$B_\nu(T) = \frac{2\nu^2}{c^2} k_B T. \tag{1.42}$$

One way to characterize the specific intensity, frequently used in radio astronomy, is through the *brightness temperature* T_B, which is the equivalent temperature of a blackbody emitting at a certain specific intensity assuming emission is within the Rayleigh-Jeans law regime (Rybicki & Lightman 1985):

$$T_B = \frac{c^2}{2\nu^2 k_B}\Delta I_\nu. \tag{1.43}$$

This temperature is sometimes called the *radiation temperature* T_R (Mangum & Shirley 2015), as it a property of the observed radiation. In terms of this observable, the solution to the radiative transfer equation reads:

$$\frac{T_B}{f} = (J_\nu(T_{ex}) - J_\nu(T_{bg}))(1 - \exp(-\tau_\nu)), \tag{1.44}$$

where J_ν is defined for convenience as:

$$J_\nu(T) = \frac{h\nu}{k_B}\frac{1}{\exp(\frac{h\nu}{k_B T}) - 1} = B_\nu(T)\frac{c^2}{2k_B\nu^2}, \tag{1.45}$$

and f called the *filling factor*, which is the fraction of the resolution of our observations that is filled by the observed source, such that $fT_{B,real} = T_B$ (Mangum & Shirley 2015).

1.4.4 Column density from observations

From the radiative transfer process above, it is possible to derive the *column density* of the molecules, which is the number of molecules per unit area along the line of sight. For the two level system, the column density of molecules in the upper level is $N_u = \int n_u ds$. Then, using Eqs. 1.37 and 1.38, and integrating over all ν, we can relate N_u to the optical depth. Rearranging to integrate with respect to the velocity instead of frequency $dv = cd\nu/\nu$ (from Eq. 1.32):

$$N_u = \frac{8\pi\nu_0^2}{A_{ul}c^3}\Big(\exp\Big(\frac{h\nu_0}{k_B T_{ex}}\Big) - 1\Big)^{-1}\int \tau_\nu dv. \tag{1.46}$$

N_u is related to the total column density of the molecules N_{tot} through the rotational partition function Q_{rot}, which represents the relative population of all possible rotational energy states:

$$\frac{N_u}{N_{tot}} = \frac{Q_{rot}}{g_u}\exp\Big(\frac{E_u}{k_B T_{ex}}\Big), \tag{1.47}$$

where E_u is the energy of he upper level with respect to the ground state. Q_{rot} is a property of the molecule (Mangum & Shirley 2015).

When the emission line is optically thin and all excitation states are assumed to have the same T_{ex}, N_{tot} can be related directly to the observed emission I_ν by using T_B. Using Eq. 1.44, and defining the integrated intensity $W = \int T_B dv$, the column density is (Caselli et al. 2002b; Mangum & Shirley 2015):

$$N_{tot} = \frac{8\pi\nu^3 W}{fc^3 A_{ul}}\frac{Q_r ot}{g_u}\exp(\frac{E_u}{k_B T_{ex}})(\exp(\frac{h\nu_0}{k_B T}) - 1)^{-1}(J_\nu(T_{ex}) - J_\nu(T_{bg}))^{-1}. \tag{1.48}$$

The column density is used to determine the observed mass of the medium, after assuming a molecular mass. Usually, the difficulty in obtaining N_{tot} comes from not knowing T_{ex}. If one assumes that a molecular emission has $\tau_\nu \gg 1$, T_{ex} can be derived directly from Eq. 1.44.

1.5 Elements of radioastronomy

How do we capture the emitted light from molecules in space? As mentioned previously, rotational molecular lines are characterized by millimeter and submillimeter wavelengths, so we use *radio telescopes*. The atmosphere is usually a problem to observe celestial objects, as it can absorb photons coming from space, avoiding their detection. Luckily, there are transparent windows in the millimeter and submillimeter wavelength regimes that allow photons to pass through.

Observations within these thesis were taken with two types of telescopes: *single dish telescopes* and *interferometric arrays*. In the following, I describe how we obtain intensity measurements using both types of telescopes.

1.5.1 Single dish telescopes

Single dish telescopes consist of an antenna to collect the light from the sky and an internal hardware to convert it to a digital signal which can then be analyzed. The antenna consists of a primary reflector which collects light and focuses onto a sub-reflector which then directs the captured light to a *feed* or *horn*. An example of a single dish telescope antenna dish and how light concentrated is shown in Fig. 1.9 left.

A single dish antenna measures power coming from the sky per unit frequency P_ν. How much power is captured from different angles depends on the antenna *beam pattern* $P_n(\theta, \phi)$, which shows how emitted power is distributed in solid angle. Thanks to the reciprocity theorem, this beam pattern is the same for *received* power. In single dish antennas, the beam pattern consists of a main lobe or *main beam* where most of the power is concentrated, followed by several side lobes, as shown in Fig. 1.9 right.

The resolution of the observed emission is given by the size of the main lobe. Its full width at half-maximum (FWHM) θ_{FWHM} gives the angular resolution of the observations:

$$\theta_{FWHM} \approx \lambda / D, \tag{1.49}$$

where λ is the wavelength of observed light and D is the diameter of the antenna. The exact relation is dependent on the power pattern of the antenna. The fraction of the power entering through the main lobe with respect to the total is the *main beam efficiency* η_{MB}.

The total power received by the antenna is given in terms of the *system temperature* T_{sys}, which is the equivalent Rayleigh-Jeans temperature of an object emitting that power (Wilson et al. 2008; Thompson et al. 2017):

$$P = k_B T_{sys} G_\nu \Delta\nu, \tag{1.50}$$

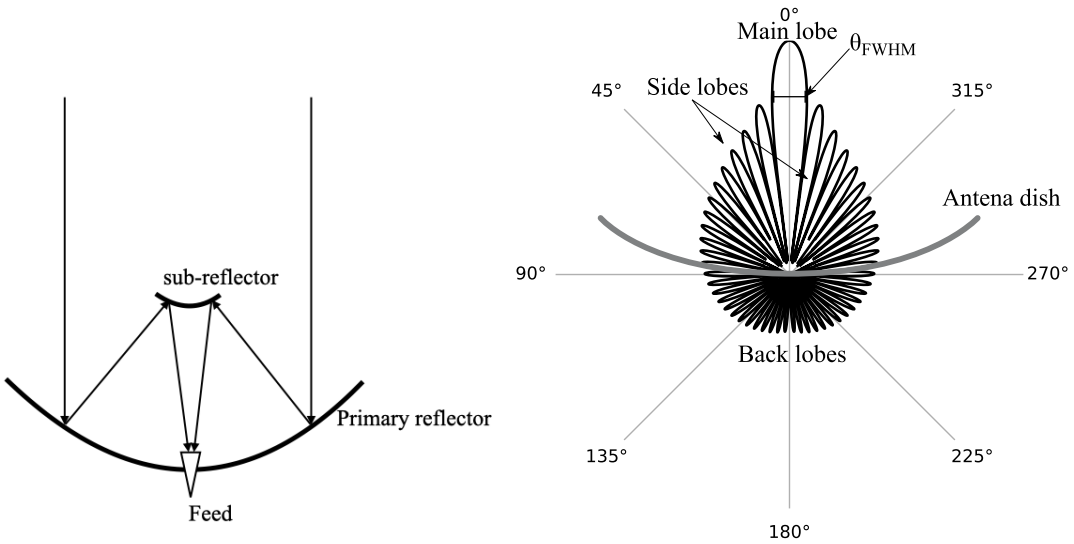

Figure 1.9: Schematics of a radio antenna. Left: Diagram showing the path of light rays toward an antenna and how these arrive to the feed. The two thick curves show the primary and sub-reflectors, respectively. Right: approximated beam pattern for a single dish antenna. The distance from the center to the edge is a measure of the received power. The gray curve represents the primary reflector or dish.

where $\Delta\nu$ is the bandwidth (i.e. the range of sampled frequencies) and G_ν is the *antenna gain*, which is the ratio of output over input power. The system temperature is the sum of all noise contributions to the antenna, including the astronomical source of interest. We separate the contributions of the source in the *antenna temperature* T_A, which is the temperature corresponding to the power received by the source, and the *receiver temperature* T_{Rx}, which groups together the contributions from the receiver, atmosphere and the ground (Wilson et al. 2008):

$$T_{sys} = T_A + T_{Rx}. \tag{1.51}$$

Knowledge about the receiver's properties and the atmosphere at the moment of the observations are needed to obtain T_{Rx} and thus isolate T_A.

The contribution from other sources means that there will always be a noise σ over our observations. This noise is given by the *radiometer equation* (Wilson et al. 2008):

$$\sigma = k\frac{T_{sys}}{\sqrt{\Delta\nu\tau}}, \tag{1.52}$$

where τ is the *integration time* (i.e. the total time the antenna observed the source), and k is a factor that depends on the antenna observing mode. This means that the longer a source is observed, the lower the noise on the system and thus the larger the *signal-to-noise ratio* SNR is.

T_A is related to the source brightness temperature T_B after a series of corrections. First, the antenna temperature corrected for the atmosphere T'_A, ignoring the contribution to T_{sys}

of the atmosphere itself, is (Wilson et al. 2008):

$$T'_A = T_A \exp(-\tau_{atm}), \tag{1.53}$$

where τ_{atm} is the opacity of the atmosphere along the line of sight. Then, the power coming from the source and not from the rest of the sky is defined as the main-beam temperature T_{MB}, when the source is contained within the beam:

$$T_{MB} = \frac{T'_A}{\eta_{MB}}, \tag{1.54}$$

where η_{MB} is the *main-beam efficiency*, the fraction of power concentrated in the main beam with respect to the total power received. Finally, T_{MB} is related to the actual brightness temperature T_B of the source by the source's size in the sky θ_s:

$$T_B = T_{MB} \frac{(\theta_s^2 + \theta_{FWHM}^2)}{\theta_{FWHM}^2}. \tag{1.55}$$

For a point-like source (compared to the beam size), Eq. 1.55 then states that $T_{MB} \approx T_B$.

Usually, instead of using T_{MB}, observations are reported in terms of flux density S_ν coming from a source, which is the sum of all specific intensity that comes from the solid angle covered by the source Ω_s (Rybicki & Lightman 1985):

$$S_\nu = \int_{\Omega_s} I_\nu \cos\theta d\Omega. \tag{1.56}$$

The flux density is usually measured in units of Jansky, where 1 Jy $= 10^{-26}$ W m^{-2} Hz^{-1}. The brightness temperature is related to the flux density *within the beam solid angle* by using Eq. 1.43 (Wilson et al. 2008):

$$T_B = \frac{c^2}{2\nu^2 k_B \Omega_{MB}} S_\nu. \tag{1.57}$$

In this thesis, I employ data from the Institut de Radioastronomie Millimétrique (IRAM) 30-m telescope, a single dish telescope located atop the Pico Veleta mountain in the Spanish Sierra Nevada. Its receivers, the Eight Mixer Receiver (EMIR, Carter et al. 2012) and the New IRAM KID Array 2 (NIKA2, Adam et al. 2018) are designed to observe in the millimeter range. EMIR, the receiver used in this thesis, has bands at 0.9, 1.3, 2 and 3 mm (approximately 330, 230, 150 and 90 GHz), and NIKA2 is designed for continuum observations at 1.1 and 2 mm. As its name states, its dish has a diameter of 30 m, so the beam FWHM is approximately 11″ at 230 GHz (Eq. 1.49).

1.5.2 Interferometry

According to Eq. 1.49, if one wants a higher angular resolution, one must build a larger antenna, but that is sometimes not feasible. For instance, to observe a line at 1 mm with

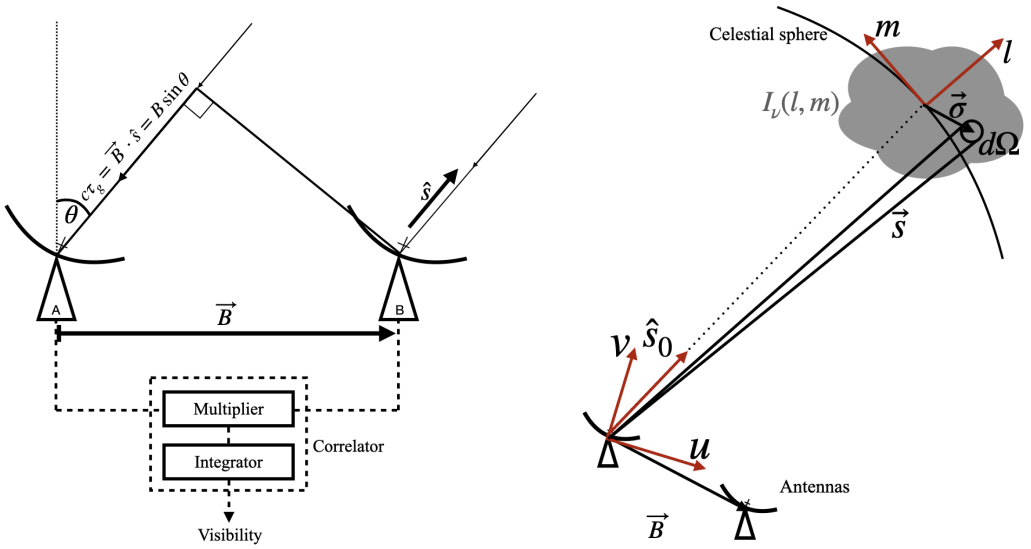

Figure 1.10: Schematics of a two-element interferometer. Left: Geometry of the incident light as it reaches the antennas, showing the geometric delay τ_g due to the angle of the source in the sky. Below the antennas is a diagram of the correlator and the operations it does over incident light. Right: Geometry of each system of reference for $I_\nu(l,m)$ and $\mathcal{V}(u,v)$. Red arrows show the reference systems.

a sub-arcsecond ($\sim 0.1''$) resolution, you would need an antenna with a diameter $D \sim 2$ km! Instead of building a gigantic antenna, an *array* of single dish telescopes, with an extension equal to the maximum diameter needed, can be used to obtain the required resolving power. This technique is called interferometry, and its fundamental idea is that a telecope array measures the Fourier transform of the intensity distribution of a celestial source (Taylor et al. 1999; Thompson et al. 2017).

An interferometric array is basically an ensemble of two-element interferometers, where each pair of antennas measures an interference pattern. Lets consider one of the pairs is separated by a distance $B = |\vec{B}|$, called the *baseline*. The astronomical source is at a direction $\hat{s}$ so far away that we assume that the light wavefront is planar, and reaches the antennas from an angle θ with respect to the zenith . This setup is shown in Fig. 1.10 left. Due to the position of the antennas, the light in antenna A arrives after the light in antenna B, causing a *geometric delay* (Wilson et al. 2008; Thompson et al. 2017):

$$\tau_g = \frac{\vec{B}\cdot\hat{s}}{c} = \frac{B}{c}\sin\theta. \tag{1.58}$$

This time difference causes an interference pattern when the waves are combined. This interference pattern has the shape of a sine wave, with maxima and minima equally spaced for a monochromatic wave. This sinusoidal pattern is known as the *fringe pattern* of an interferometer (Thompson et al. 2017).

Lets suppose the antennas are tracking the source as it moves in the sky, so the center

of the resulting image is $\hat{s}_0$, known as the *phase center*, with an angle θ_0 with respect to the zenith. The antenna looks at a position in the sky defined by a direction vector $\vec{\sigma}$ with respect to $\hat{s}_0$, where the specific intensity is $I_\nu(\vec{\sigma})$. The power received by one antenna from direction $\vec{\sigma}$ within a solid angle $d\Omega$ is $\frac{1}{2}A_n(\vec{\sigma})I_\nu(\vec{\sigma})d\nu d\Omega$, where A_n is the effective collecting area of the antenna (Thompson et al. 2017). The geometric delay with respect to the phase center is now proportional to $\vec{B}\cdot\vec{\sigma}$.

The power received in each antenna is combined in a *correlator*, where the signals of each antenna are multiplied and averaged in time (Fig. 1.10 left, Wilson et al. 2008). The output of the correlator is the *visibility* of the source brightness distribution multiplied by the bandwidth $\Delta\nu$, where the visibility $\mathcal{V}$ is defined by:

$$\mathcal{V} = |\mathcal{V}|e^{i\phi_\mathcal{V}} \int_{4\pi} A_n(\vec{\sigma})I_\nu(\vec{\sigma}) \exp(-2\pi i\vec{D}\cdot\vec{\sigma})d\Omega \tag{1.59}$$

$\mathcal{V}$ has units of flux density and is a complex value, where $|\mathcal{V}|$ is known as the *amplitude* and $\phi_\mathcal{V}$ is the *phase* (Taylor et al. 1999; Thompson et al. 2017).

To obtain the desired intensity distribution I_ν from the correlator's response, we need to define two coordinate systems: one for the baseline and one for the source. The baseline has components (u, v), where u increases eastward and v northward, and u, v define a plane normal to $\hat{s}_0$. The image space is centered at the phase center with coordinates (l, m) which are the direction cosines of (u, v), so (l, m) represent a projection of the celestial sphere into a plane in the sky (Taylor et al. 1999; Thompson et al. 2017). The space (u, v) can be thought of as a *spatial frequency* space with respect to l, m. In terms of these coordinates, and assuming the observed region is small so that $\vec{\sigma}$ is small, then the visibility is written as:

$$\mathcal{V} = \int_{-\infty}^{\infty}\int_{-\infty}^{\infty} A_n(l, m)I_\nu(l, m) \exp(-2\pi i(ul + vm))dldm \tag{1.60}$$

Thus, the visibility is the Fourier transform of the brightness distribution of the source in the sky multiplied by the antenna response. The process of obtaining an image from the complex visibility is called *synthesis imaging.*

In theory, we just need to do an inverse Fourier transform to recover $I_\nu(l, m)$ given that we know $A_n(l, m)$. In reality, $\mathcal{V}$ is sampled at specific positions within the u, v plane, which is described through the *sampling function* $S(u, v)$, which equals 1 where the u, v plane is sampled and 0 elsewhere (Thompson et al. 2017). The Fourier transform of the sampled visibility is called the *dirty image* (Taylor et al. 1999):

$$I_\nu^D(l, m) = \int_{-\infty}^{\infty}\int_{-\infty}^{\infty} \mathcal{V}(u, v)S(u, v) \exp(2\pi i(ul + vm))dudv. \tag{1.61}$$

Given the properties of the Fourier transform, a multiplication in frequency space (u, v in this case) transforms into a convolution. Therefore, the true brightness distribution is convolved with a function $B(l, m)$ known as the *synthesized or dirty beam*, given by the inverse Fourier transform of $S(u, v)$. Methods to recover the "clean" image $I_\nu(l, m)$ are known as *deconvolution* algorithms (Taylor et al. 1999). The most famous of these, called the CLEAN algorithm, assumes the source consists of a collection of point sources and

the brightness distribution is the sum of the brightness of these sources convolved by a Gaussian beam (Högbom 1974).

This thesis employs data from two inteferometric arrays. The first is the IRAM Northern Extended Millimetre Array (NOEMA), located at the Plateau de Bure in the French Alps. The array consists of 12 antennas, each with a diameter of 15 m, that can be placed in three different configurations. The most extended configuration has a maximum baseline of 1.7 km, corresponding to a resolution of approximately 0.4″ at 230 GHz. NOEMA has receivers in the 1.3, 2 and 3 mm atmospheric windows.

The second array used in this thesis is the Atacama Large Millimeter/Submillimeter Array (ALMA), established in the Chajnantor Plateau in the Chilean Atacama desert[3]. It consists of 50 12-m antennas with baselines up to 16 km, allowing a minimum beam of 0.02″ at 230 GHz. It is complemented by the Atacama Compact Array (ACA), also known as the Morita array, 12 antennas with a diameter of 7 m, and four additional 12-m antennas to operate as single-dish telescopes. There are 10 frequency bands in ALMA, which observe from a range of 35-50 GHz (8.5-6 mm) in Band 1, to 787-950 GHz (0.38-0.32 mm) in Band 10, although Band 2 is currently under development[4].

1.6 Contents of this thesis

After introducing the main theoretical and practical concepts necessary for this thesis, the following chapters present the results and analysis of three observational projects regarding streamers. I summarize here each chapter:

- In Chapter 2, I analyze the gas kinematics around a Class I (embedded) protostar in the crowded star-forming region NGC 1333. I discover a streamer using molecular gas observations from the NOEMA large program PRODIGE. For this source, I am able to determine its mass infall rate and observe its landing site through shock tracing molecules. I further discuss the possible effects of the asymmetric mass infall in this protostar's evolution.

- Chapter 3 presents a study of gas flow from the larger filamentary scales to protostellar disk scales in the quiescent Barnard 5 dense core. I use NOEMA and 30-m telescope observations that cover the filamentary structure for the larger scales, and ALMA data to observe the envelope around B5-IRS1, the lonely Class I protostar in this core. I find that the filaments are fed chemically fresh gas from the ambient cloud, as well as a streamer toward the protostellar disk. I discuss the possible connection between the two gas flows.

- Chapter 4 presents the first systematic search for streamers in a clustered star forming region. For this purpose, I use new observations from the ProPStar project, which combines NOEMA and 30-m observations toward a filament in the southeast of NGC

[3]https://www.almaobservatory.org/en/about-alma/
[4]https://almascience.eso.org/about-alma/alma-basics

1333. Based on the common properties of previously found streamers, I found candidates toward 7 out of 16 protostars in the region. I evaluate the possibility that the gas feeding these streamer candidates comes from cloud material and not necessarily from the filament.

- In Chapter 5, I give a summary of the presented work and describe future projects based on the results of this thesis.

Chapter 2

PRODIGE – envelope to disk with NOEMA I. A 3000 au streamer feeding a Class I protostar

The contents of this chapter were published in Astronomy & Astrophysics.

Abstract

Context. In the past few years, there has been a rise in the detection of streamers, asymmetric flows of material directed toward the protostellar disk with material from outside a star's natal core. It is unclear how they affect the process of mass accretion, in particular beyond the Class 0 phase.
Aims. We investigate the gas kinematics around Per-emb-50, a Class I source in the crowded star-forming region NGC 1333. Our goal is to study how the mass infall proceeds from envelope to disk scales in this source.
Methods. We use new NOEMA 1.3 mm observations, including $C^{18}O$, H_2CO, and SO, in the context of the PRODIGE MPG - IRAM program, to probe the core and envelope structures toward Per-emb-50.
Results. We discover a streamer delivering material toward Per-emb-50 in H_2CO and $C^{18}O$ emission. The streamer's emission can be well described by the analytic solutions for an infalling parcel of gas along a streamline with conserved angular momentum, both in the image plane and along the line-of-sight velocities. The streamer has a mean infall rate of 1.3×10^{-6} $M_\odot$ yr^{-1}, five to ten times higher than the current accretion rate of the protostar. SO and SO_2 emission reveal asymmetric infall motions in the inner envelope, additional to the streamer around Per-emb-50. Furthermore, the presence of SO_2 could mark the impact zone of the infalling material.
Conclusions. The streamer delivers sufficient mass to sustain the protostellar accretion rate and might produce an accretion burst, which would explain the protostar's high luminosity

with respect to other Class I sources. Our results highlight the importance of late infall for protostellar evolution: streamers might provide a significant amount of mass for stellar accretion after the Class 0 phase.

Keywords: ISM: kinematics and dynamics – ISM: individual objects: Per-emb-50 – ISM: structure – stars: protostars – stars: formation

2.1 Introduction

The classical picture of star formation allows us to understand the collapse of a dense, individual core through simple physical assumptions, but does not fully explain the current observations of protostars and protoplanetary disks. In general, the classical models consist of a dense, mostly isolated core inside a molecular cloud that undergoes axisymmetric collapse and, due to the conservation of angular momentum, flattens and creates a disk around the central protostar (e.g., Shu 1977; Terebey et al. 1984). The first limitation of the classical models is that they depend on two assumptions: the spherical symmetry of the core collapse and its lack of interaction with material outside the protostar's natal core. In reality, molecular clouds are asymmetric at all scales (André et al. 2014; Pineda et al. 2023), from the parsec-sized filaments (e.g., Hacar & Tafalla 2011; André et al. 2010), to asymmetric envelopes around protostars (Tobin et al. 2010). Numerical simulations of molecular clouds that follow the collapse of several cores, including turbulence and magnetic fields, can reproduce these observed filaments and asymmetric structures (e.g., Lebreuilly et al. 2021; Kuznetsova et al. 2019; Kuffmeier et al. 2017; Padoan et al. 2014).

A second problem with the standard model of inside-out, axisymmetric collapse of an isolated core is that it predicts a constant mass accretion rate $\sim 10^{-5}$ $M_\odot$ yr^{-1} (Stahler et al. 1980), but observed bolometric luminosities in embedded protostars imply accretion rates that are ten to 100 times lower than this value (Kenyon et al. 1990; Evans et al. 2009). This is known as the "luminosity problem". Proposed solutions to this problem include an initial strong accretion phase followed by an accretion rate decay (Padoan et al. 2014), and strong bursts of accretion during the protostellar phase (Kuffmeier et al. 2018; Zhao et al. 2018; Vorobyov & Basu 2015). These solutions show that the accretion process is asymmetric both in space and time, which is incompatible with fully axisymmetric collapse. Therefore, even if the simple symmetric model allows for a comprehension of isolated sources, it does not capture all the phenomena that affect the star formation process.

Recently, numerical simulations have shown that the local environment surrounding the protostar has a deep impact on its evolution (Hennebelle et al. 2020; Kuffmeier et al. 2018, 2017; Padoan et al. 2014). In particular, simulations focusing on star and disk formation repeatedly find asymmetric flows toward the disk (e.g., Wurster et al. 2019; Kuznetsova et al. 2019; Kuffmeier et al. 2019, 2017). These long, thin inflows, called streamers, can deliver mass from outside the natal core to increase the available mass for the protostar (Pelkonen et al. 2021) and might have effects on the structure of protoplanetary disks (Kuffmeier et al. 2017). All these simulations show that the collapse from core to protostar

is more complex than axisymmetric inside-out collapse.

In the last few years, observations have begun to find streamers from envelope to disk scales (see Pineda et al. 2023, and references within). Streamers are found from the highly embedded Class 0 phase (Pineda et al. 2020; Le Gouellec et al. 2019) through the less embedded Class I (Segura-Cox et al. in prep., Chou et al. 2016), all the way to Class II sources (e.g., Ginski et al. 2021; Garufi et al. 2022; Alves et al. 2020; Akiyama et al. 2019; Yen et al. 2019; Tang et al. 2012). They have also been found feeding not only single protostars, but also protostellar binaries, both funneling material toward the inner circumstellar disks (Phuong et al. 2020; Alves et al. 2019; Dutrey et al. 2014a) and to the binary system as a whole (Pineda et al. 2020). These structures are observed in a diversity of molecules, such as ^{12}CO (Alves et al. 2020) and HC_3N (Pineda et al. 2020), and also in scattered light (Ginski et al. 2021; Akiyama et al. 2019). The first streamer to be characterized using only free-fall motion, and thus confirming it is infalling toward the protostar, is located toward the Class 0 source Per-emb-2 (Pineda et al. 2020). This streamer transports material from outside the dense core ($>$ 10 000 au) into the protoplanetary disk and protostar system. The infall rate of this streamer, which describes how much mass is deposited into disk-forming scales, is comparable to the accretion rate toward the protostar, implying that the streamer could change the future protostellar accretion rate by funneling extra material. This streamer was discovered with a carbon-chain species, HC_3N, which traces the chemically evolved material better than it traces the more evolved protostellar core seen in N_2H^+ (Bergin & Tafalla 2007). These objects prove that the environment influences the star's development and support the results from simulations that state the mass available to the protostar could be coming from further away than the natal core (Pelkonen et al. 2021).

Even though asymmetric infall is a ubiquitous feature in numerical simulations, to the best of our knowledge, only a few streamers have been found, and their infall properties quantified, using either average estimates of infalling material and/or free-fall motion models toward the disk and protostar system (e.g., Ginski et al. 2021; Pineda et al. 2020; Alves et al. 2019). This is where the MPG - IRAM observing program "PROtostars & DIsks: Global Evolution" (PRODIGE, CO-PIs: P. Caselli, Th. Henning) comes in; this program is designed as a coherent study of the physical and chemical properties of young protostellar systems, targeting 32 Class 0 and I sources, and eight Class II protoplanetary disks. One of its goals is to search for material flowing into Class 0 and I sources, and to investigate the mass budget during these phases. PRODIGE observations are done with the IRAM NOrthern Extended Millimeter Array (NOEMA), located at the Plateau de Bure in the French Alps. This program takes advantage of the PolyFix correlator to make an unbiased survey of molecular lines, thus allowing for the search of streamers in multiple chemical tracers.

In this paper, we present new NOEMA 1.3 mm ($\approx$ 220 GHz) observations from the PRODIGE survey of five molecules (H_2CO, $C^{18}O$, ^{12}CO, SO, and SO_2) toward the Class I protostar Per-emb-50. Our aim is to characterize the core kinematics around this embedded protostar from approximately 300 au scales out to 3000 au from the source, to investigate how the mass infall proceeds from envelope to disk scales. The paper is divided as follows.

Section 2.2 describes the NOEMA observations, data reduction, and imaging procedures. Section 2.3 shows the observed structures in each molecular tracer and how we separate the different kinematic components. We discuss how the structures found might affect the protostar and protostellar disk evolution in Per-emb-50, and how they fit in the general star formation paradigm in Sect. 2.4. We summarize our results in Sect. 2.5.

2.2 Observations and data reduction

2.2.1 Per-emb-50

Per-emb-50 is an embedded Class I protostar, according to its spectral energy distrubution (SED) in the near- and mid-infrared (Evans et al. 2009; Enoch et al. 2009). It is located in the active star-forming region NGC 1333, at a distance of 293 pc (Ortiz-León et al. 2018; Zucker et al. 2018), in the Perseus giant molecular cloud. This protostar is approximately ten times brighter than other Class I sources in the vicinity (Dunham et al. 2015; Enoch et al. 2009) and its protostellar accretion rate is estimated between $(1.3 - 2.8) \times 10^{-7}$ $M_\odot$ yr^{-1}, also around ten times larger than other Class I sources (Fiorellino et al. 2021). It has a clear outflow observed in ^{12}CO (2–1) emission with an east-west orientation (Stephens et al. 2019).

VLA 8 mm continuum analysis shows a large dust disk in Per-emb-50, with a characteristic radius between $27 - 32$ au (where there is a significant drop in the dust flux profile), and dust mass around $0.28 - 0.58$ $M_\odot$ (Segura-Cox et al. 2016). Radiative transfer models applied to millimeter observations suggest that grain growth has proceeded within the envelope, producing grains with sizes ~ 100 μm (Agurto-Gangas et al. 2019).

Properties of the protostar and its disk taken from the literature are summarized in Table 2.1.

Property	Value	Reference
RA (J2000, deg)	03:29:07.76	1
Dec (J2000, deg)	+31:21:57.2	1
M_* ($M_\odot$)	$1.5 - 1.9$	2
M_{disk} ($M_\odot$)	$0.28 - 0.58$	3
R_c (au) *	$27 - 32$	3
i_{disk} (deg)	67	3
PA_{disk} (deg)	170	3
d (pc) **	293 ± 22	4

Table 2.1: Properties of Per-emb-50 from the literature. *This is a characteristic radius at which there is a significant drop in the dust flux exponential profile, a proxy for the radius. **This distance corresponds to the distance to NGC 1333. References: [1]Enoch et al. (2009), [2]Fiorellino et al. (2021), [3]Segura-Cox et al. (2016), [4]Ortiz-León et al. (2018); Zucker et al. (2018).

2.2.2 NOEMA observations

The observations were obtained with NOEMA and are part of the MPG-IRAM Observing Program PRODIGE (Project ID L19MB). In this program, we used the Band 3 receiver and the new PolyFix correlator, tuned with a local-oscillator (LO) frequency of 226.5 GHz. PolyFix provides a full 16 GHz of bandwidth at coarse spectral resolution (2 MHz channel width) and is divided into four units (LSB Outer, LSB Inner, USB Inner and USB Outer). Simultaneously, we placed 39 high spectral resolution windows of 62.5 kHz channel resolution within the coarse resolution 16 GHz bandwidth.

Observations of Per-emb-50 were conducted in two separate periods for each antenna configuration. The C configuration data were observed on 29 December 2019 and 5 January 2021. The D configuration observations were taken on 6 August 2020, and on 7 and 8 September 2020. The maximum recoverable scale (MRS) for our data is 16.9″ at 220 GHz, approximately 5000 au at the distance of Per-emb-50.

We calibrated the data using the standard observatory pipeline in the Grenoble Image and Line Data Analysis Software (GILDAS) package Continuum and Line Interferometer Calibration (CLIC). We used 3C84 and 3C454.3 as bandpass calibrators. Phase and amplitude calibration sources were 0333+321 and 0322+222, and observations for these calibrators were taken every 20 min. LKHA101 and MWC349 were used as flux calibrators. The uncertainty in flux density was 10%. The continuum was bright enough to allow for self calibration. Only for the continuum image used in this work, self-calibration was performed iteratively with solution intervals of 300 s, 135 s, and 45 s. The line observations were not done with self-calibrated data. The resulting continuum image, shown in Appendix A.1, was done with the lower inner (LI) continuum window and has a noise of 0.2 mJy beam^{-1}.

Continuum subtraction and data imaging were done with the GILDAS package `mapping` using the `uv_baseline` and `clean` tasks. All line cubes were imaged using natural weight to minimize the rms, while the continuum maps were imaged with robust = 1, to improve the angular resolution. We imaged the continuum-subtracted cubes using the standard CLEAN algorithm and a manual mask for each channel. Once we converged to a final mask, we performed a final CLEAN down to the rms level using multiscale CLEAN algorithm implemented in `mapping`. This had an effect of reducing imaging artifacts (mainly negative emission bowls), thus improving the general image quality around bright sources.

Toward Per-emb-50, we detected ^{12}CO (2−1), C^{18}O (2−1), H_2CO ($3_{0,3}-2_{0,2}$), SO (5_5-4_4) and SO_2 ($11_{1,11}-10_{0,10}$) line emission. The ^{12}CO (2–1) line is located in the coarse resolution bandwidth, whereas the rest of the lines are inside the high-resolution windows. The final line cubes have a beam full width half maximum (FWHM) θ of approximately 1.2″, a primary beam FWHM of 22″ at 220 GHz, a field of view (FoV) of 45.8″ diameter, and a channel spacing of 0.08 km s^{-1}. The effective spectral resolution is approximately 1.7 times the channel spacing. The average rms is around 13 mJy beam^{-1} or around 400 mK. The resulting properties of each line cube are reported in Table 2.2.

Molecule	Transition	E_{up} (K)	Frequency[1] (GHz)	$\theta_{maj} \times \theta_{min}$ (PA) ($''\times''$, $^\circ$)	rms (mJy beam^{-1})	$\Delta V_{\rm chan}$ (km s^{-1})
SO	5_5 – 4_4	44.1	215.2206530	1.25×0.73 (21.48)	13.01	0.08
H_2CO	$3_{0,3}$ – $2_{0,2}$	21.0	218.2221920	1.24×0.72 (21.43)	11.97	0.08
SO_2	$11_{1,11}$ – $10_{0,10}$	60.4	221.9652196	1.24×0.72 (20.89)	11.54	0.08
$C^{18}O$	2 – 1	15.8	219.5603541	1.24×0.71 (20.87)	13.94	0.08
^{12}CO	2 – 1	5.5	230.5380000	1.15×0.67 (21.20)	7.43	2.60

Table 2.2: Properties of the molecular line observations from NOEMA.

2.3 Results

2.3.1 Streamer in Per-emb-50

The integrated intensity images for H_2CO $(3_{0,3} - 2_{0,2})$ and SO $(5_5 - 4_4)$ are shown in Figure 2.1. The former unveils a large streamer in the southwest of the central star, whereas the latter shows extended emission surrounding the protostar. We refer to $H_2CO(3_{0,3} - 2_{0,2})$ as H_2CO and $SO(5_5 - 4_4)$ as SO in the rest of this paper. The integrated intensity maps were calculated between 5.5 and 9.5 km s^{-1} in the case of H_2CO, and between -1 and 14 km s^{-1} in SO, which are the velocity ranges where all emissions over 3σ in each channel (see Table 2.2 for σ values) are present for each molecule.

The streamer stretches from the location of the protostar toward the southwest to the edge of the primary beam, with a total length of approximately 3000 au ($22''$) and a width of approximately 300 au ($1''$). As the width of the streamer is barely resolved, this width is considered an upper limit. Also, as the streamer reaches up to the primary beam FWHM, it is possible that it extends further, so the length is a lower limit as well. The peak integrated intensity in H_2CO presents a signal-to-noise ratio (S/N) of 11. The streamer is detected with an S/N ≥ 6 along its 3000 au length.

This streamer is spatially unrelated to the outflow of Per-emb-50, since the emission does not spatially overlap with the outflow. The left panel of Fig. 2.1 shows the outflow observed in ^{12}CO(2–1) emission, from the wide-band setup of our NOEMA observations. ^{12}CO is integrated from $V_{LSR} = -4$ to 4 km s^{-1} for the blueshifted emission and from 11 to 20 km s^{-1} for the redshifted emission. The outflow, previously observed by Stephens et al. (2019), is in the east-west direction, whereas the H_2CO streamer extends in the northeast-southwest direction.

Outside the primary beam and to the southwest of Per-emb-50, there is also enhanced H_2CO and SO emission. It is difficult to characterize the nature of this structure because it is outside the primary beam, even after primary beam correction; emission in this region might be contaminated by emission from outside our FoV, leaking through the side-lobes of the antenna response pattern. In Section 2.4.1, we discuss the possibility that this emission consists of an extension of molecular emission further away from the protostar.

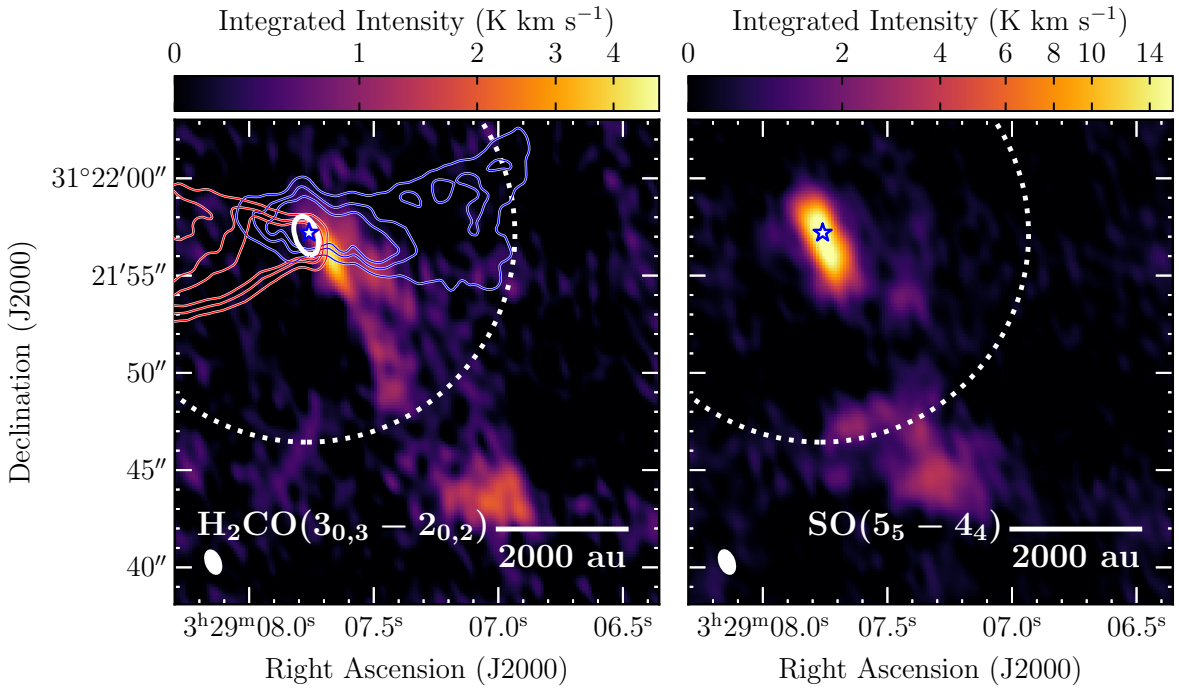

Figure 2.1: Integrated intensity images of $H_2CO\,(3_{0,3} - 2_{0,2})$ and $SO\,(5_5 - 4_4)$, before primary beam correction, are shown on the left and right, respectively. Primary beam FWHM sizes are represented with filled dashed white circles in each image. The blue star represents the location of Per-emb-50. Beam sizes are represented by white ellipses in the bottom left corner of each image. **Left:** $H_2CO\,(3_{0,3} - 2_{0,2})$ integrated intensity between 5.5 and 9.5 km s^{-1}. Red and blue contours correspond to the redshifted and blueshifted emisions coming from the outflow, respectively, traced in our wideband $^{12}CO\,(2-1)$ emission. Contour levels are shown at 8, 16, and 24 K km s^{-1}. The white contour represents the continuum emission at a 7 mJy beam^{-1} level (see Fig. A.1). **Right:** $SO\,(5_5 - 4_4)$ integrated intensity between -1 and 14 km s^{-1}.

2.3.2 Streamer kinematics

We fit a Gaussian to the H_2CO line emission without primary beam correction using `pyspeckit` (see Appendix A.2 for details). The central velocity $V_{\rm LSR}$ and velocity dispersion $\sigma_{\rm v}$ of the Gaussians that best fit the spectrum at each pixel with S/N > 4 are shown in Fig. 2.2.

H_2CO line emission is characterized by mostly blueshifted emission with respect to Per-emb-50's $V_{\rm LSR}$ (7.5 km s^{-1}, see Section 2.3.3). The velocity of the streamer further away from the protostar consists of mostly constant blueshifted velocities (with $V_{\rm LSR} \approx 7.2$ km s^{-1}) and low velocity dispersion of $\sigma_{\rm v} = 0.1 - 0.2$ km s^{-1}. Closer to the protostar, between positions 2 and 3 marked in Fig. 2.2, and shifted to the west with respect to the general direction of the streamer, there is a sudden increase in velocities, from 7.2 to 7.5 km s^{-1}. We refer to this region as the "kink" in the rest of this paper, as it is a kink or bend in the overall shape of the emission and an abrupt break in the velocity distribution. It is improbable that the sudden redshift in velocities is caused by the outflow, as its west side consists of blueshifted emission, whereas the kink in the streamer is redshifted with respect to the rest of the streamer's velocities. The kink is followed by a reversal back to blueshifted velocities approaching the protostar, in the inner 1000 au. There is a steep velocity ($V_{\rm LSR}$) gradient, a change of 7.1 to 6.5 km s^{-1} in $\sim$ 750 au, and the velocity dispersion ($\sigma_{\rm v}$) increases from 0.4 to 0.7 km s^{-1} in the same region. This gradient suggests that the gas follows infall motions dominated by the central gravitational force of the protostar, disk, and inner envelope.

2.3.3 Protostellar mass and velocity

The integrated intensity image of $C^{18}O\,(2-1)$ is shown in the left panel of Fig. 2.3. We refer to $C^{18}O\,(2-1)$ as $C^{18}O$ in the rest of this paper, unless otherwise stated. The $C^{18}O$ observations show the most extended emission of our NOEMA observations and have a similar velocity range as SO, between -1 and 14 km s^{-1}. This molecule's emission closest to the protostar allowed us to determine the protostar's velocity and mass.

We produced a position-velocity (PV) diagram for $C^{18}O$ along the major axis of the disk in Per-emb-50 found by Segura-Cox et al. (2016) (170° counter-clockwise from north, see Fig. 2.3). We used the astropy package `pvextractor` (Ginsburg et al. 2016) to obtain the PV diagram along a path centered on the protostar, spanning a total length of 2400 au and a total width of 1″. The resulting PV diagram in the right panel of Fig. 2.3 is consistent with rotation, with increasing velocity toward the protostar. The $C^{18}O$ emission might be tracing Keplerian rotation.

Our observations of $C^{18}O$ allowed us to constrain the mass of the protostar. We obtained a central protostellar velocity $V_{\rm LSR}$ of 7.5 km s^{-1}, and a central protostellar mass $M_* = 1.7 \pm 0.2$ M$_\odot$ from the $C^{18}O$ PV diagram. For this, we first manually determined the velocity that minimizes the asymmetries in the PV diagram. This resulted in a $V_{\rm LSR} = 7.5$ km s^{-1}, marked with a horizontal dotted line in Fig. 2.3. Afterward, we compared the PV diagram with the Keplerian rotation curves produced by the masses previously estimated

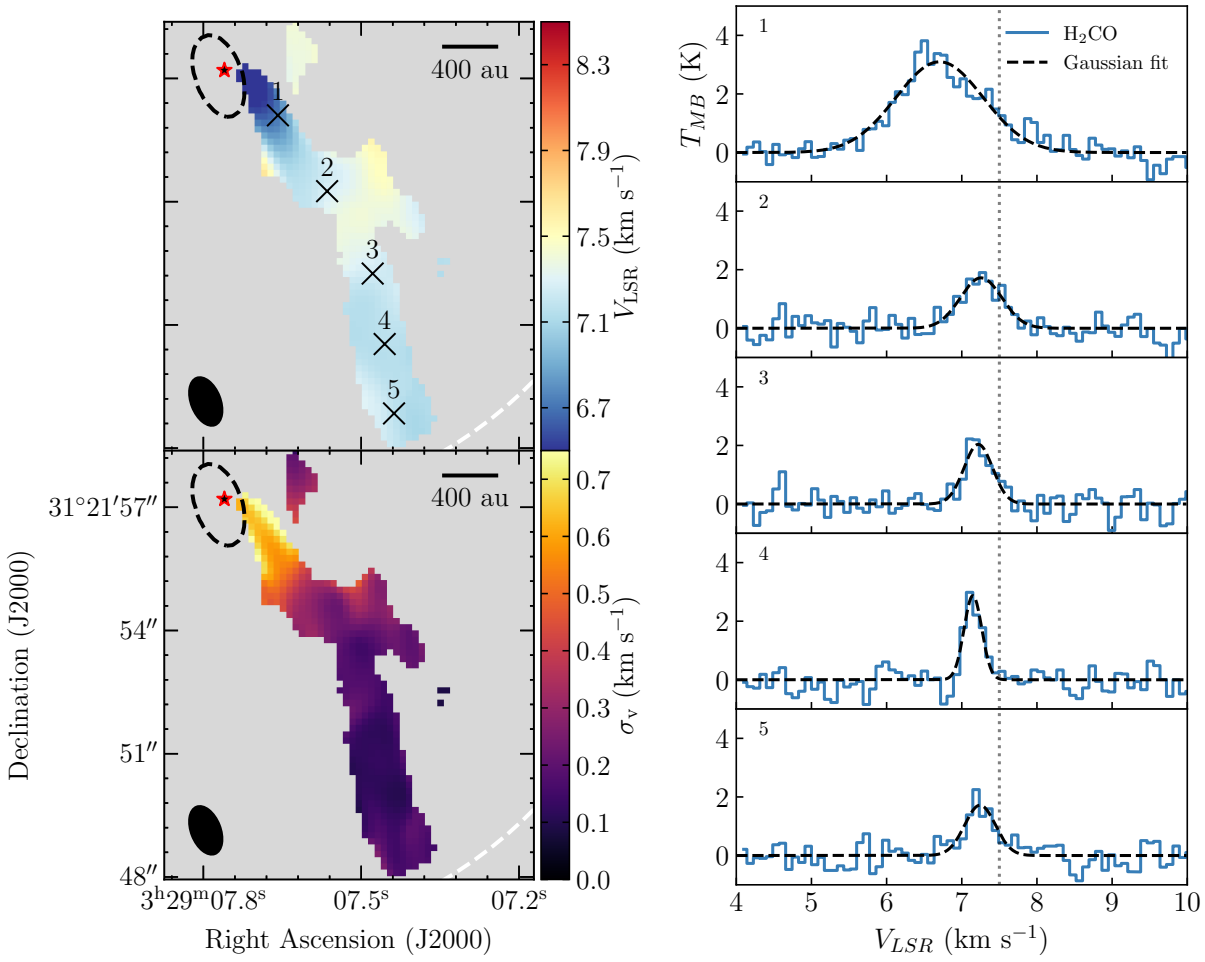

Figure 2.2: Results of the Gaussian fit to the H_2CO line emission toward Per-emb-50. **Left:** Central velocity $V_{\rm LSR}$ and velocity dispersion $\sigma_{\rm v}$ of the H_2CO streamer are shown in the top and bottom panels, respectively. These are obtained from the Gaussian model for H_2CO emission of each spectra with S/N > 4. The red star represents the central position of Per-emb-50. Black labeled crosses mark the positions where we extract spectra, shown to the right. Dashed black contours correspond to the continuum emission at a brightness level of 7 mJy beam^{-1} (see Fig. A.1). Dashed white lines represent the primary beam FWHM, centered at the location of Per-emb-50. The beam is drawn in the lower left corners of each image. **Right:** H_2CO spectra at selected positions along the streamer, together with the Gaussian that best fits each spectrum. Blue lines indicate the H_2CO spectra and the dashed black lines represent the best fit Gaussian function. The uncertainty in T_{MB} is 0.3 K. The dotted gray line represents the protostar's $V_{LSR} = 7.5$ km s^{-1}.

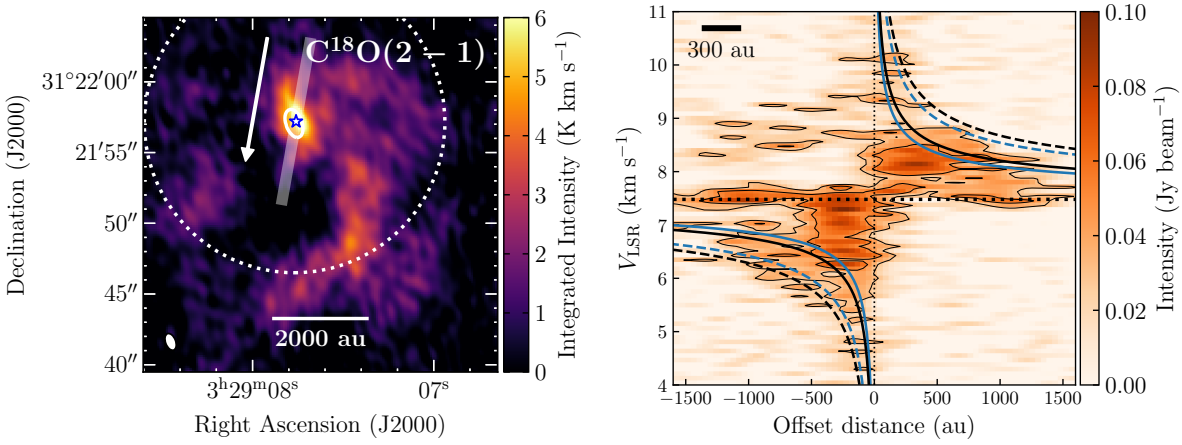

Figure 2.3: $C^{18}O$ integrated emission before primary beam correction alongside its PV diagram. **Left:** Integrated intensity image of $C^{18}O$ between -1 and 14 km s^{-1}. The semi-transparent white line represents the position and width of the PV cut, built with the position angle of the disk from Segura-Cox et al. (2016). The white arrow represents the direction of positive offset of the PV cut. The primary beam FWHM size is represented with a dashed white circle. The beam size is represented by a white ellipse in the bottom left corner. **Right:** PV diagram of the $C^{18}O$ line emission along the indicated PV cut. The horizontal dotted line represents Per-emb-50's $V_{LSR} = 7.5$ km s^{-1}. The vertical dotted line marks the central position of Per-emb-50. The PV diagram has an rms of 0.01 Jy beam^{-1}. Intensity contours are placed at 5, 15, and 25 times the rms. The blue and black curves represent the Keplerian rotation curve for the minimum and maximum stellar mass, respectively, from Fiorellino et al. (2021): The solid lines represent masses calculated assuming the star is located at the birthline of the Palla & Stahler (1993b) model (0.53 –0.70 $M_\odot$), whereas dashed lines represent the masses calculated for a 1 Myr protostar (1.52 – 1.90 $M_\odot$). Velocities are weighted according to the inclination angle as $V = V_{kep} \sin(i)$. The preferred Keplerian curve is the average between the dashed curves, with a mass of 1.7 $M_\odot$. The scalebar in the top left represents a distance of 300 au, equivalent to the resolution of the NOEMA data.

for Per-emb-50 by Fiorellino et al. (2021) using IR spectroscopy; they obtain a range between $0.5 - 0.7$ $M_\odot$ for a star located at the birthline at the HR diagram (using the Palla & Stahler (1993b) model) and $1.5 - 1.9$ $M_\odot$ for a 1 Myr old protostar. The Keplerian rotation curves were weighted according to the inclination angle as $v = v_{kep} \sin(i)$, where $i = 67°$ (see Table 2.1, Segura-Cox et al. 2016), with $i = 0°$ corresponding to a face-on disk. The Keplerian rotation curves for a central protostar of 1 Myr present a good correlation with the 3σ contours ($\sigma = 14$ mJy beam^{-1}, see Table 2.2) of the $C^{18}O$ PV diagram. We use the average between the 1 Myr mass upper and lower limits, 1.7 $M_\odot$, and their difference as uncertainty (± 0.2 $M_\odot$), for the rest of this work.

2.3.4 Streamline model

We modeled the kinematics of the streamer observed with H_2CO emission to confirm that the velocity gradient observed in H_2CO emission is consistent with infall motion, using the analytic solution for material falling from a rotating, finite-sized cloud toward a central object, dominated by the gravitational force of the latter. We used the analytic solutions of Mendoza et al. (2009), previously used by Pineda et al. (2020) on the Per-emb-2 streamer. The model returns the position $\vec{x_i} = (x, y, z)_i$ in au and velocity $\vec{V_i} = (v_x, v_y, v_z)_i$ in km s^{-1} (in Cartesian coordinates) of a parcel of mass along a streamline, where the z axis is defined along the angular momentum vector of the disk and the x-y plane is the disk plane. The model's input was the initial position and radial velocity of the parcel of mass within the cloud in spherical coordinates (initial radial distance r_0, position angle ϑ_0 with respect to the z axis, inclination angle φ_0 which marks the initial angle within the disk plane and radial velocity $v_{r,0}$), and the initial angular velocity of the cloud Ω_0. We also applied two rotations due to the inclination angle i and position angle PA of the disk, to obtain the position and velocity with respect to the observer's point of view from the disk's reference system.

The streamline model required as input the central mass that dominates the gravitation of the system. We used the sum of the masses of the protostar, disk, and envelope, $M_{tot} = M_* + M_{env} + M_{disk}$. We used $M_* = 1.7 \pm 0.2$ $M_\odot$ (see Sect. 2.3.3) and $M_{disk} = 0.58$ $M_\odot$, the upper limit calculated in Segura-Cox et al. (2016). For the envelope mass, we used an upper limit of 0.39 $M_\odot$ and a lower limit of 0.18 $M_\odot$, obtained using the Bolocam 1.1 mm image from Enoch et al. (2006), taking the emission of Per-emb-50 with the disk component removed (see Appendix A.3 for details).

We manually input the initial position (r_0, ϑ_0 and φ_0), velocity $v_{r,0}$, and inclinations i and PA to find the best parameters. We first assumed that the streamer's rotation direction, given by i and PA, were the same as the dust disk i and PA from Segura-Cox et al. (2016) (see Table 2.1). The inclination angle i obtained from the dust disk was degenerate in three-dimensional space (it could be inclined in 67° or −67°). We used the rotation direction given by the $C^{18}O$ PV diagram in Sect. 2.3.3 and the outflow direction (see the left panel of Fig. 2.1) to determine that the angular velocity vector of the disk $\vec{\omega}$ points toward the west (in the direction of the blueshifted outflow component) and is inclined toward the observer, thus $i = -67°$. Then, we attempted to find analytic

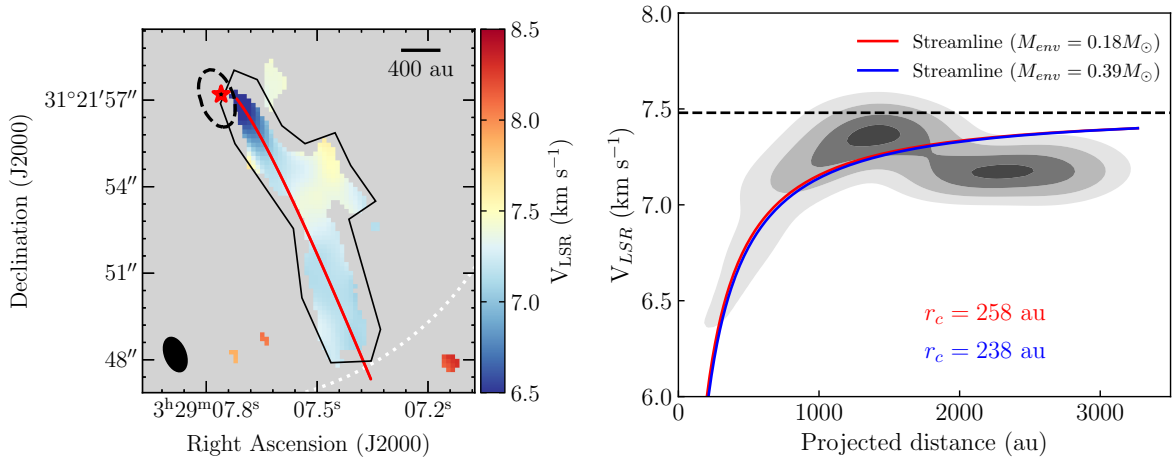

Figure 2.4: Central velocity of the best fit for each spectra in the H_2CO line emission, together with the streamline model for H_2CO. The red and blue lines represent the best streamline model for an envelope mass of 0.18 $M_\odot$ (total central mass of 2.47 $M_\odot$) and 0.39 $M_\odot$ (total mass of 2.68 $M_\odot$), respectively. **Left:** Central velocities with respect to position in the sky. The black polygon represents the region where velocities are sampled to build the kernel density estimation (KDE). The primary beam FWHM size is represented with a dashed white circle. The beam size is represented by a black ellipse in the bottom left corner. **Right:** Central velocity KDE as a function of projected distance to Per-emb-50 is plotted in grayscale. The KDE levels are drawn from 0.5σ in steps of 0.5σ, where the σ level is equivalent to the standard deviation of a normalized bivariate normal distribution. The horizontal dashed line represents the central velocity of Per-emb-50 $V_{\rm LSR} = 7.5$ km s^{-1}. The centrifugal radius resulting from each envelope mass are located below the curve.

solutions with other i and PA values. The i and PA from Segura-Cox et al. (2016), and our disambiguation gave the only rotation direction where we could find a solution for the velocity profile of the streamer.

Table 2.3 lists the parameters that resulted in the analytic solutions for an infalling mass that best reproduce the H_2CO line profiles in the image plane and the structure of the velocity along the line of sight. Figure 2.4 shows the projected trajectory of the streamline model with the best parameters over the central velocity of the Gaussian fit to the H_2CO emission, both in the image plane (left panel), and over the kernel density estimate (KDE) of the velocity and projected distance in the data (right panel). We used the KDE implementation in the python package `SciPy` (Virtanen et al. 2020) over the resulting central velocities obtained in Sect. 2.3.2. The streamline model is able to reproduce the general shape of the KDE and the acceleration toward the protostar in the inner 1000 au. The model is not able to reproduce the slight discontinuity seen in the KDE at $\sim$ 1700 au, which is related to the kink feature (see Sec. 2.3.2). The difference between using the upper and lower limits of the envelope mass was negligible in both the image and velocity planes (red and blue curves in Fig.2.4).

Parameter	Unit	Value
ϑ_0	deg	61.5
φ_0	deg	28.0
r_0	au	3330
$v_{r,0}$	$\mathrm{km\,s^{-1}}$	1.25
Ω_0	$\mathrm{s^{-1}}$	4.53×10^{-13}
i	deg	-67
P.A.	deg	170

Table 2.3: Parameters of the streamline model that reproduce best the H_2CO observations.

The centrifugal radius r_c (called r_u in Mendoza et al. 2009) given by the parameters in Table 2.3 is between $r_c = 238 - 258$ au, using the upper or lower limit for the envelope mass, respectively, both of which are within the beam size. This radius is the limit where the streamer can be modeled as free-falling matter with constant angular momentum, so we interpret this radius as approximately where the streamer deposits its material. This implies that the streamer deposits its mass at a distance about 150 au from the gas disk's edge, which we estimate has a radius of approximately 90 au using the SO line emission obtained in this work (see Sect. 2.3.8). We do not use the streamline model solutions for distances smaller than r_c, as the model does not include motions within the gas and dust disk.

2.3.5 Streamer mass

We calculated the streamer's mass and infall rate using the primary beam corrected $C^{18}O$ emission in the area where the streamer was detected in H_2CO emission, as we could convert $C^{18}O$ emission to gas emission with simple assumptions. We used the primary beam corrected emission because we used the intensity of the $C^{18}O$ line, which we obtained by multiplying the map by the primary beam response, whereas in Sect. 2.3.2 we only needed the central velocity and velocity dispersion of each spectrum to characterize the streamer's kinematics.

The $C^{18}O$ emission is the most extended of all the molecular transitions used in this work, as it traces not only the gas in the streamer, but also the extended gas in the inner envelope and the filament in which the protostar is embedded, which has a larger extension than the FoV. Nevertheless, the streamer is easily detected in $C^{18}O$, with a S/N ≈ 10 at the streamer's tail. The $C^{18}O$ emission shows a similar structure as in the H_2CO map. We could not characterize the $C^{18}O$ extended emission and kinematics outside of the streamer as we lacked zero-spacing data, and we see some negative bowls in the image (see the black areas in the right panel of Fig. 2.3), indicating missing flux from larger scales. Therefore, for this work we use $C^{18}O$ emission to describe the protostar's and the streamer's masses only.

[1]Taken from the Cologne Database for Molecular Spectroscopy (Endres et al. 2016)

The $C^{18}O$ emission shows a similar central velocity as H_2CO at the streamer's tail but a different velocity distribution at the position of the protostar, as shown in Fig. 2.5. We used the same procedure for H_2CO to obtain the best Gaussian that fits the spectrum of each pixel with S/N > 4, described in Appendix A.2. Where the emission is coincident with H_2CO, $C^{18}O$ is well described with one Gaussian component that shares the same $V_{\rm LSR}$ and $\sigma_{\rm v}$ as the H_2CO emission (a comparison can be made between Fig. 2.2 and Fig. 2.5). The kink in velocities observed in the middle of the streamer is also observed in $C^{18}O$. Surrounding the protostar, outside of the area traced by the continuum, there is blueshifted emission toward the northwest and redshifted emission toward the east. These emissions probably trace a mixture of part of the inner envelope and disk rotation, and the inner section of the outflow, as it follows the same east-west direction as the ^{12}CO outflow detected by Stephens et al. (2019). Therefore, it is safe to use $C^{18}O$ emission within the region used to characterize the streamer's kinematics (black polygons in Fig. 2.2 and Fig. 2.5) to determine the streamer's mass.

We obtained a mass lower limit for the streamer within the region drawn in Figures 2.2 and 2.5. We detail the reasons why this is a lower limit in Sect. 2.4.1. We calculated the mass within the streamer assuming that $C^{18}O$ is optically thin, under local thermodynamic equilibrium (LTE), and that the streamer has a constant temperature T_{ex}. We used the values in the vicinity of Per-emb-50 in Friesen et al. (2017) and Dhabal et al. (2019), which are between 10 and 20 K, and thus we assumed $T_{ex} = 15 \pm 5$ K. First, we obtained the column density of the $C^{18}O$ molecule, $N(C^{18}O)$, using the primary beam corrected $C^{18}O$ image. We explain the details of this procedure in Appendix A.4. The $C^{18}O$ column density is around 2.8×10^{15} cm^{-2} within 1000 au of the protostar, then it falls to $\approx 8.0 \times 10^{14}$ cm^{-2} and in the outer 1500 au it reaches up to 3.6×10^{15} cm^{-2}. Afterward, we transformed $N(C^{18}O)$ to molecular Hydrogen column density $N(H_2)$ using $N(H_2) = X_{C^{18}O} N(C^{18}O)$. We used the canonical ratio $X_{C^{18}O} = 5.9 \times 10^6$ (Frerking et al. 1982). Finally, we obtained the gas mass in the streamer using:

$$M_{\rm streamer} = M_{gas} = \mu m_H d^2 \, \delta x \, \delta y \sum N_{H_2}, \tag{2.1}$$

where $\sum N_{H_2}$ is the sum of N_{H_2} in the streamer in cm^{-2}, d is the distance to the protostar in cm, $\delta x \, \delta y$ is the size of the pixels in radians, $\mu = 2.7$ is the molecular weight of the gas, considering the contribution from H_2, He and heavy elements, and m_H is the H atom mass. We used $d = 293 \pm 22$ pc, the distance to NGC 1333 (Ortiz-León et al. 2018, see Table 2.1).

We obtained a lower limit for the total mass of the streamer $M_{\rm streamer} = 1.2 \times 10^{-2}$ M$_\odot$, with an uncertainty of 15% due to uncertainties in flux calibration and in the distance to NGC 1333 (see Table 2.1).

2.3.6 Streamer infall rate

We calculated the mean infall rate and the infall rate along the streamer using the mass obtained in Sect. 2.3.5, and compared it to the protostellar accretion rate. In this work,

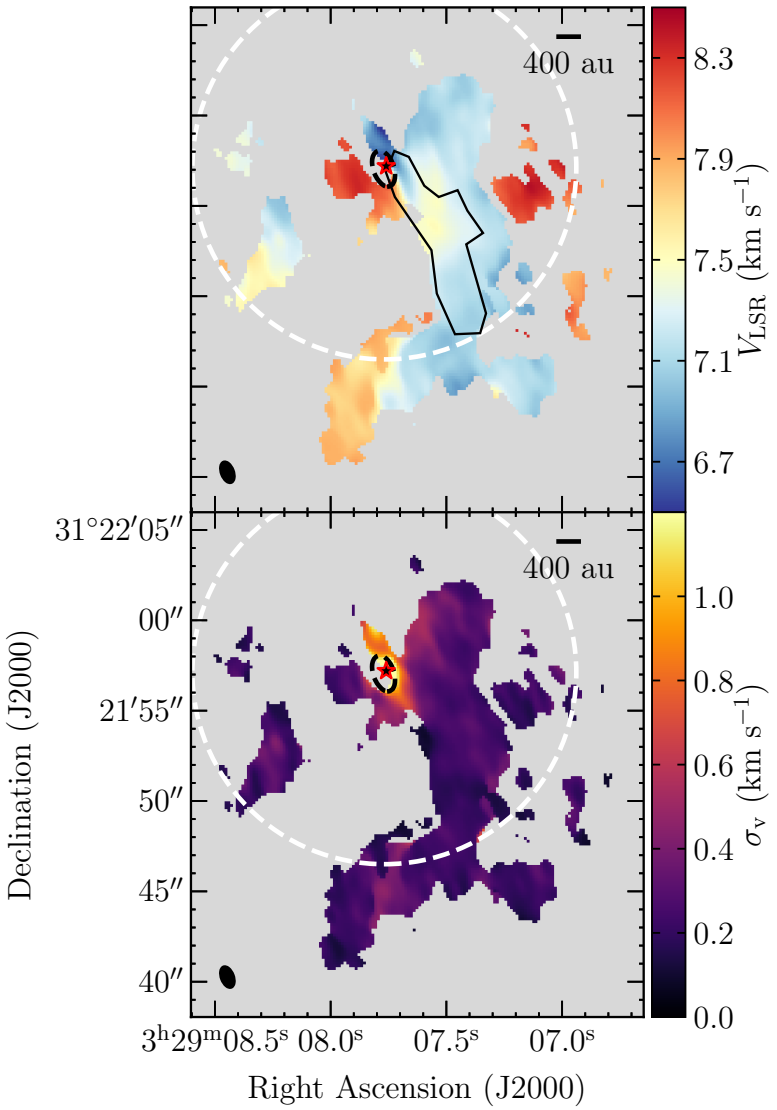

Figure 2.5: Velocity $V_{\rm LSR}$ and velocity dispersion $\sigma_{\rm v}$ of the best Gaussian fit for $C^{18}O$ emission. Gaussian fits are only done for spectra with S/N > 4. The primary beam FWHM size is represented with a white dashed circle. The beam size is represented in a white ellipse in the bottom left corner. **Top:** Central velocity of the best fit Gaussian profile for each spectrum. The black contour shows the same region plotted in the right panel of Fig. 2.2, from where the mass is calculated. **Bottom:** Velocity dispersion of the best fit Gaussian profile for each spectrum.

Property	Unit	Value
$M_{\rm streamer}$	$M_\odot$	$(1.2 \pm 0.2) \times 10^{-2}$
$t_{\rm ff}$	kyr	20.5 – 21.3
$t_{\rm ff,model}$	kyr	8.6 – 8.7
$\langle \dot{M}_{in} \rangle$	$M_\odot$ yr^{-1}	$(5.4 - 5.6) \times 10^{-7}$
$\langle \dot{M}_{in,\rm model} \rangle$	$M_\odot$ yr^{-1}	1.3×10^{-6}

Table 2.4: Global properties of the streamer found in Sect. 2.3.5 and Sect. 2.3.6.

there are two different rates: the infall rate $\dot{M}_{in}$, which is the rate at which mass is deposited from the envelope to the disk scales; and accretion rate $\dot{M}_{acc}$, which is the rate at which the protostar is accreting mass.

The free-fall timescale of the streamer, assuming the classic free-fall time equation,

$$t_{\rm ff} = \sqrt{\frac{R^3}{GM_{tot}}}, \tag{2.2}$$

is 21.3 ± 0.8 kyr for an envelope mass of 0.18 $M_\odot$ ($M_{tot} = 2.47$ $M_\odot$), and 20.5 ± 0.7 kyr for $M_{env} = 0.39$ $M_\odot$ ($M_{tot} = 2.68$ $M_\odot$). In Equation 2.2, M_{tot} is the total mass within a distance $R = r_0 = 3300$ au from the protostar (obtained from the streamline model in Sect. 2.3.4), and G is the gravitational constant. We divided the total mass with the free-fall timescale to obtain an average $\langle \dot{M}_{in} \rangle$ between $(5.4 - 5.6) \times 10^{-7}$ $M_\odot$ yr^{-1}. The upper limit is plotted as a dotted line in Fig. 2.6.

Since we constrained the streamer's kinematics (see Sect. 2.3.4) and its column density at each position, we then derived the infall rate at every position of the streamer. We first calculated the free-fall timescale $t_{\rm ff,model}$ and average infall rate $\langle \dot{M}_{in,\rm model} \rangle$ using the analytic solutions from Sect. 2.3.4 to compare it to the classical free-fall timescale $\langle \dot{M}_{in} \rangle$. For this, we calculated the travel time along the streamer by using the streamer's trajectory and velocities from the streamline model, from $r_0 = 3300$ au to the centrifugal radius, which we assumed is the landing point (we used $r_c = 238$ au). We obtained a total free-fall time of 8.7 kyr for $M_{env} = 0.18$ $M_\odot$ and 8.6 kyr for $M_{env} = 0.39$ $M_\odot$, around two times lower than the times calculated previously, because the classic free-fall timescale (Equation 2.2) does not consider that the streamline already has an initial velocity toward the protostar at R. The resulting infall rate is $\langle \dot{M}_{in,\rm model} \rangle = 1.3 \times 10^{-6}$ $M_\odot$ yr^{-1} for both envelope masses. The average $\langle \dot{M}_{in,\rm model} \rangle$ using the streamline model is plotted as a dashed line in Fig. 2.6. The mass and average infall rates found for the streamer are summarized in Table 2.4.

We also studied how the infall rate changes along the streamer, to determine if there are significant differences in the infall rate within the streamer. The left panel of Fig. 2.5 shows that molecular emission is clumpy on scales of the beam size, which suggests that there might be small-scale variations along the streamer. We separated the streamer into radial bins and obtained the mean three-dimensional distance to the protostar r_{bin}, the total mass M_{bin}, the time taken to traverse the bin Δt_{bin}, and the infall rate $\dot{M}_{bin}$ in each bin. The bins were 360 au wide (which is the major axis FWHM of the beam) and

consisted of all pixels that were within a certain range of projected distances $[r, r+360]$ au from Per-emb-50. We sampled every 120 au (one-third of the major axis of the beam) from 200 au to 3300 au from the protostar, in projected distance. The resulting mass, crossing time, and infall rates for each bin are shown in Fig. 2.6.

We calculated r_{bin} as the distance of the streamline model point that is closest to the center of mass of the bin in the image plane. We used $N(\mathrm{C^{18}O})$ to find the center of mass within each bin and then find the point in the streamline model closest to it. Then, the distance r_{bin} is the three-dimensional distance between that point and the protostar. We express this distance as the free-fall timescale from r_{bin} using:

$$t_{bin} = -\int_{r_{bin}}^{0} \frac{dr'}{\sqrt{\mathrm{v}_{r,0}^2 + 2GM_{tot}\left(\frac{1}{r'} - \frac{1}{r_0}\right)}}, \tag{2.3}$$

where $\mathrm{v}_{r,0}$ is the initial velocity (1.25 $\mathrm{km\,s^{-1}}$) at r_0 (3300 au) from the streamline model toward the direction of the protostar. The integral is done numerically using the python package `SciPy` function `integrate`. The difference between the solution of Equation 2.3 and the free-fall timescale given by the streamline model is less than 20 yr, which is negligible for the timescales we are working with.

We computed the infall rate of the streamer using the mass within each bin M_{bin} and the bin's crossing time Δt_{in}. M_{bin} is calculated using Equation 2.1, adding $N_{\mathrm{H_2}}$ in all pixels that belonged to the bin. We then calculated Δt_{bin} the same way as the total free-fall timescale, but adding up the time obtained from the trajectory and velocities within the bin only. The infall rate for each bin is therefore $\dot{M}_{bin} = M_{bin}/\Delta t_{bin}$.

The infall rate along the streamer is consistently larger or equal to the accretion rate estimated for Per-emb-50, independent of the variations along the streamer. Figure 2.6 shows the resulting M_{bin}, Δt_{bin}, and $\dot{M}_{bin}$ with respect to the distance to the protostar r_{bin}, and compares the infall rates $\dot{M}_{bin}$ with the accretion rates $\dot{M}_{acc}$ for Per-emb-50 estimated in Fiorellino et al. (2021). The average $\dot{M}_{bin}$, $\langle\dot{M}_{in}\rangle$, estimated using the streamline model is between five to ten times larger than the $\dot{M}_{acc}$ estimated for a 1 Myr protostar ($(1.3 - 2.8) \times 10^{-7}$ $\mathrm{M_\odot\ yr^{-1}}$), and just above the upper limit for the $\dot{M}_{acc}$ of Per-emb-50, assuming it is located at the birthline of the Palla & Stahler (1993b) model (1.2×10^{-6} $\mathrm{M_\odot\ yr^{-1}}$). The protostellar mass calculated in Sect. 2.3.3 is consistent with a 1 Myr protostar, so likely the accretion rate is the former, resulting in $\langle\dot{M}_{in}\rangle/\dot{M}_{acc} = 5 - 10$. Therefore, the streamer is feeding more than enough mass to sustain the accretion rate of the protostar, and according to our total free-fall time, we can expect a similar infall rate for at least the next 8.7 kyr.

The mass per bin varies from 6×10^{-4} to 2×10^{-3} $\mathrm{M_\odot}$ from bin to bin. This variation drives the fluctuations observed in the infall rates, which are within a factor of three, with minima located at ∼1000 and ∼2000 au. Nevertheless, these variations are small and the streamer shows a consistently high infall rate along its full length, reflected in $\langle\dot{M}_{in}\rangle$. The fluctuations are present in spatial scales larger than 300 au, so these are not affected by the resolution limit. The mass variations might be because the streamer is clumpy, with

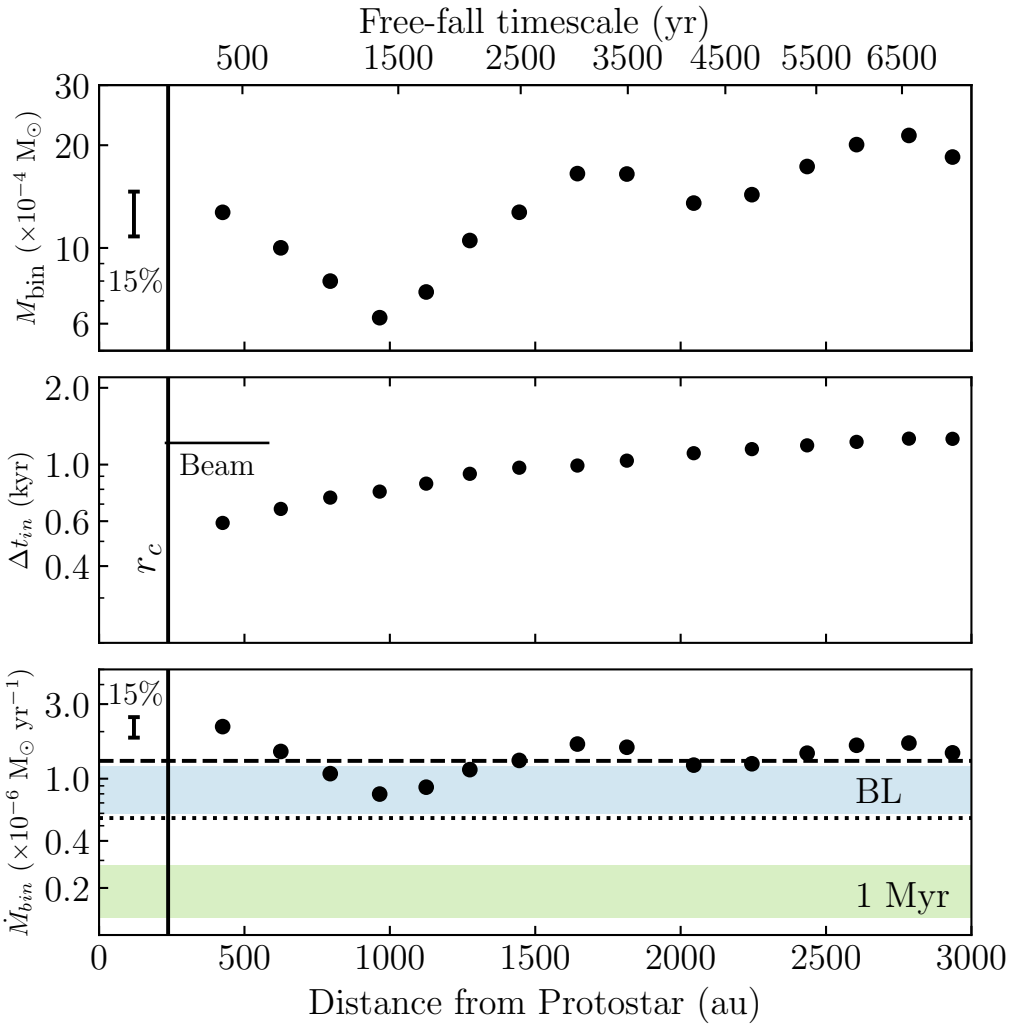

Figure 2.6: Mass, timescale, and infall rate with respect to the distance to the protostar along the streamline. Δt_{in} is obtained from the model with $M_{env} = 0.39$ M$_\odot$. The dotted line represents the mean infall rate obtained with the free-fall timescale from rest, $\langle \dot{M}_{in} \rangle = 5.6 \times 10^{-7}$ M$_\odot$ yr^{-1}, whereas the dashed line marks the mean infall rate obtained from the streamline model, $\langle \dot{M}_{in,\rm model} \rangle = 1.3 \times 10^{-6}$ M$_\odot$ yr^{-1} (see Table 2.4). The blue and green areas correspond to the estimated accretion rates at the birthline (BL) and after 1 Myr of birth (Fiorellino et al. 2021). Systematic errors are plotted as vertical bars and are 15% of the nominal values. Random errors represent around 5%.

changes in scales smaller than our 300 au resolution. On the other hand, the MRS of the data is around 22″, but the data are already less sensitive to extended emission before reaching that distance, at around 4″. Thus, the apparent minima in the infall curve of Fig. 2.6 might be explained by a decreased sensitivity to extended sources.

2.3.7 Asymmetries in SO and SO_2 emission

The right panel of Fig. 2.1 shows the SO integrated emission obtained with NOEMA. Unlike H_2CO and $C^{18}O$, SO emission in Per-emb-50 is brightest at about 150 au south of the protostar, and extended out to around 1000 au from it (see also Fig. A.2). The southern part of the SO emission overlaps with the brightest H_2CO emission. It also presents emission at $\gtrapprox$ 3000 au from the protostar, but since this emission lies outside the primary beam, we will not describe it further in this work. SO is known to be a tracer of cold, dense gas (e.g., Swade 1989; Hacar & Tafalla 2011) and it is sublimated from dust grains by sufficient heating, for example, by accretion shocks around the centrifugal barrier (e.g., Sakai et al. 2014; van Gelder et al. 2021). SO is found in young, embedded sources, but not in T Tauri disks (Guilloteau et al. 2016; Dutrey et al. 2011), suggesting an increasing S depletion with disk age. This hints that SO traces the dense inner envelope and gas disk around the protostar.

We used SO_2 ($11_{1,11} - 10_{0,10}$) emission to aid in the interpretation of the SO emission. The SO_2 integrated intensity image is shown in Fig. A.3, together with selected spectra. SO_2 emission is compact and peaks at the south of Per-emb-50, close to where H_2CO emission ends. Its peak is at the same location as the SO peak, but its emission is approximately five times weaker than SO. The SO_2 molecule is a known shock tracer as it can trace warm areas in accretion shocks (van Gelder et al. 2021), in particular at the disk-envelope surface (e.g., Artur de la Villarmois et al. 2019). This suggests that the SO_2 emission in the south of Per-emb-50 might trace shocked material, probably due to either the streamer impacting zone or another phenomena.

We generated the PV diagrams of SO and SO_2 line emission along the same cut done for $C^{18}O$ in Sect. 2.3.3 to investigate the kinematics that these molecular lines trace. The resulting PV diagrams are shown in Fig. 2.7. The shapes of both PV diagrams differ from the $C^{18}O$ PV diagram (see Fig. 2.5), indicating that these molecules trace different kinematic components. SO has a skewed diamond-shaped emission, with both blueshifted and redshifted components at the north and south parts of the cut, which suggests a mixture of infall and rotation motions, whereas $C^{18}O$ has a bowtie shape consistent with motion dominated almost entirely by Keplerian rotation. Additionally, the brightest SO emission comes from redshifted velocities both toward the north and south of Per-emb-50, whereas blueshifted emission comes almost fully from the northern side of the inner envelope. Unlike SO, SO_2 emission is only present around the peak, with no recognizable characteristic shape and it barely presents emission over 3σ at blueshifted velocities. Both diagrams peak at the same position, within the inner 300 au from the protostar toward the southeast, and in velocity, at approximately 9.5 $\mathrm{km\,s^{-1}}$. The shape of these two molecules' emissions suggests that they follow motions that are asymmetric in the north-south direction.

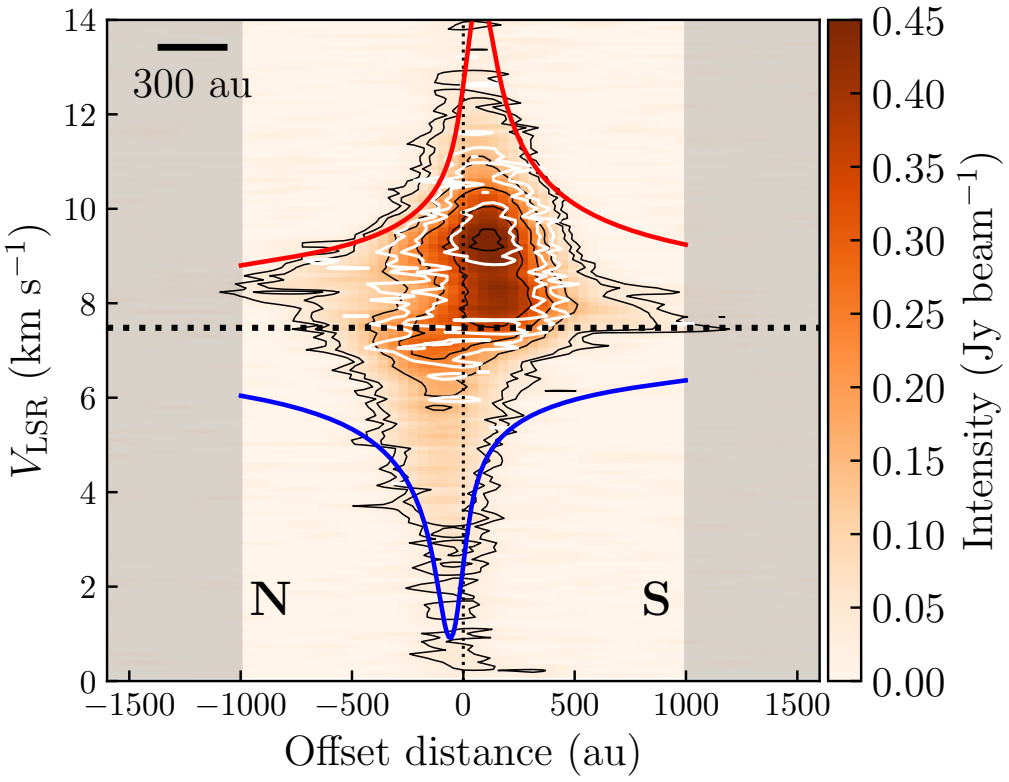

Figure 2.7: Position-Velocity diagram of SO(5_5 – 4_4) (colored and black contours) and $SO_2(11_{1,11} - 10_{0,10})$ (white contours) line emission along the position angle of the disk from Segura-Cox et al. (2016), plotted along the same offset scale as the right panel of Fig. 2.3. Negative offsets represent distances toward the north and positive offsets toward the south. The horizontal dotted line represents Per-emb-50's V_{LSR} = 7.48 km s^{-1}. The vertical dotted line marks the central position of Per-emb-50. Both PV diagrams have an rms of 0.01 Jy beam^{-1}. Intensity contours for SO are placed at 3, 5, 15, 25, 35, and 45 times the rms, whereas SO_2 intensity contours are placed at 3, 5, and 10 times the rms. The red and blue solid curves show the model of rotation and infall that best match the SO for the redshifted and blueshifted velocities with respect to the protostar, respectively. The scalebar in the top left represents a distance of 300 au, equivalent to the resolution of the NOEMA data.

We fit the "toy model" for infall and rotation motion from Sakai et al. (2014) to the SO PV diagram to investigate if the diamond shape is consistent with the rotation and infall kinematics of a flattened inner envelope. The free parameters in this model were the centrifugal radius of the material in the envelope $r_{c,\mathrm{env}}$ (not to be confused with the centrifugal radius of the streamer, r_c) and the mass of the central object M_{tot}. The best fit curves from this toy model are plotted in red and blue for the redshifted and blueshifted sides, respectively, overlaid on top of the SO PV diagram in Fig. 2.7. The model had to be divided in two parts to be able to reproduce the shape of the diagram: the redshifted and blueshifted side were best fitted with a different set of parameters. The redshifted side was best fitted with a toy model with $M_{tot,\mathrm{r}} = 4$ M$_\odot$ and $r_{c,\mathrm{env,r}} = 130$ au, whereas for the blueshifted side, $M_{tot,\mathrm{b}} = 2.9$ M$_\odot$ and $r_{c,\mathrm{env,b}} = 100$ au. Therefore, SO molecular emission traces asymmetric kinematics in the inner envelope consistent with infall and rotation, where the redshifted emission (which is brighter) possesses a different motion than the blueshifted side. The fact that the masses $M_{tot,\mathrm{r}}$ and $M_{tot,\mathrm{b}}$ are higher than the protostellar mass we determined kinematically (1.7 M$_\odot$, see Sect. 2.3.3), plus the fact that they are different, suggests that the model does not capture all the kinematic phenomena in the envelope. These results lead us to investigate the SO emission in more detail.

2.3.8 Gaussian components of SO emission

The complex shape of the SO PV diagram, the strong peak at redshifted velocities, and the fact that it can be fitted with the Sakai et al. (2014) toy model with two different sets of parameters for the redshifted and blueshifted parts, suggest that there are at least three components being traced: rotation, infall, and a bright redshifted component. We separated the different kinematic components through Gaussian spectral fitting of SO to study them separately.

We fit one, two, and three Gaussians to the SO spectrum of each pixel with S/N > 4 using the same method for H_2CO and $C^{18}O$ emission, described in Appendix A.2. Figure A.2 shows four spectra in different regions with their respective best fit curves. Most of the SO spectra required two Gaussians, or in some cases, three Gaussians to be reproduced. For each pixel, we evaluated how much improvement we obtained by adding a second and third Gaussian using the Akaike information criterion (AIC, see Appendix A.2 for details). With the decomposed spectra, we investigated the separate physical components of SO emission that can be described using each Gaussian.

We find four signature components in SO emission: one consistent with inner envelope rotation, a compact feature around the protostar with a large velocity dispersion ($\sigma_\mathrm{v} > 2$ km s^{-1}), a third component consistent with the streamer's kinematics from Sect. 2.3.1, and a fourth component completely redshifted with respect to Per-emb-50. We separated each of the components using the following steps. First, all Gaussian curves that had a velocity dispersion $\sigma_\mathrm{v} > 2$ km s^{-1} correspond to the broad feature, which is consistent with marginally resolved disk rotation. Then, all Gaussians with $\sigma_\mathrm{v} < 2$ km s^{-1} that had a central velocity $V_{LSR} > 8.1$ km s^{-1} correspond to the bright, redshifted component. Third, the Gaussians left that had $V_{LSR} < 7.2$ km s^{-1} and were located at a lower declination

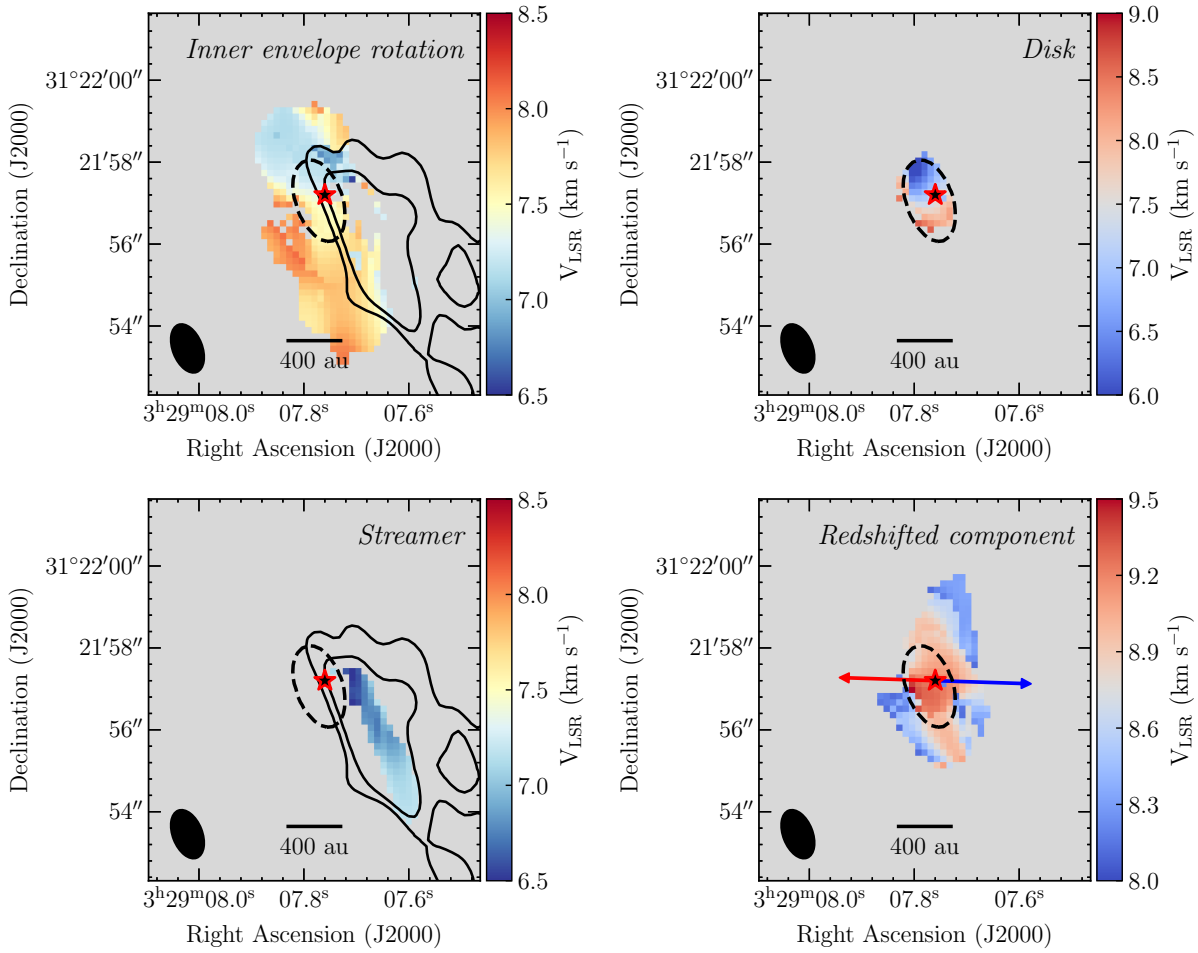

Figure 2.8: Best fit central velocity maps for the four signature components found in SO (5_5-4_4) emission in the inner 1000 au of Per-emb-50's envelope. Examples of the individual spectra decomposition for each of these components are shown in Fig. A.2. Solid black contours represent the integrated intensity of H_2CO emission at three and five times the rms of the integrated intensity map (0.25 K km s^{-1}). Dashed black contours mark the continuum emission at a 7 mJy beam^{-1} level (see Fig. A.1). The red and blue arrows indicate the outflow direction determined by the redshifted and blueshifted CO (2 – 1) emissions, respectively, from Stephens et al. (2019). The clean beam is represented as a black ellipse in the bottom left corner of all of the images. It should be noted that the velocity ranges plotted in each figure are different, which is why the figures on the right have a different color scheme. **Top left:** Inner envelope rotation.**Top right:** Broad feature ($\sigma_v > 2$ km s^{-1}). **Bottom left**: Streamer. **Bottom right**: Redshifted component.

than +31°21′57.6” are consistent with the streamer. Finally, all pixels left contain only one Gaussian curve, which had a central velocity map consistent with inner envelope rotation.

The central velocity $V_{\rm LSR}$ of the four separated components are shown in Fig. 2.8. We show the best fit parameters (central velocity and dispersion) for each component in Appendix A.6. Figure A.2 shows the components in selected SO spectra.

The inner envelope rotation component contributes to the diamond shape shown in the PV diagram in Fig. 2.7, with the blueshifted emission on the northern side and the redshifted emission on the southern side. This rotation component is resolved in our observations, extending by a factor of approximately two farther in radius than the continuum emission (see the top left panel in Fig. 2.8), so it does not correspond to disk rotation, and has the same rotation direction shown in our $C^{18}O$ data (see Fig. 2.3).

Within the continuum emission contour, the SO spectra present emission fitted with Gaussians with blueshifted and redshifted velocities with respect to Per-emb-50, and with $\sigma_{\rm v} > 2$ km s^{-1} (see the top right panels in Fig. 2.8 and in Fig. A.4). The observed gradient in its central velocities is consistent with rotation kinematics, with the same rotation direction suggested by the $C^{18}O$ PV diagram (see Fig. 2.3) and the inner envelope rotation. However, as this component only emits within the continuum emission, we assume this gas belongs to the gas disk only, unlike $C^{18}O$ which also traces the flattened inner envelope rotation. Using the stellar mass obtained in Sect. 2.3.3 and the velocity dispersion from this SO component, we estimate the radius of this compact component assuming it traces Keplerian rotation and that at the disk edge the Keplerian velocity is $v_k \sim \sigma_{\rm v} \approx 4$ km s^{-1}. This estimate returns a disk radius of approximately 90 au. Therefore, this component is consistent with a gas disk around the protostar.

Toward the south of Per-emb-50, one of the fitted Gaussian components is consistent with the streamer structure found in H_2CO, both in position in the sky and velocity (a comparison can be made between Fig. 2.2 and the bottom left panel in Fig. 2.8). This component is clearly separated from all other components in the south as it is blueshifted with respect to the protostar's $V_{\rm LSR}$, whereas the other component close-by (inner envelope rotation) is redshifted (see Fig. 2.8 and the left panel in Fig. A.2). This component's SO spectra shows the same central velocity as H_2CO (see Spectra d in Fig. A.3) and acceleration toward blueshifted velocities found in the H_2CO Gaussian fitting (see the bottom left panel in Fig. 2.8). SO traces only the inner 1000 au of the streamer, likely tracing its denser regions.

The fourth component found through Gaussian decomposition is strongly redshifted with respect to the protostar (see the bottom right panel in Fig. 2.8). This component has a larger velocity close to the center of the continuum emission (around 9.5 km s^{-1}) and decreases radially (to approximately 8.0 km s^{-1}). Its radial velocity gradient is not consistent with the direction of the outflow or the streamer. We propose that this component might trace another asymmetric infall, located along the line of sight. This infall is asymmetric as we do not see a strongly blueshifted counterpart ($V_{LSR} < 7$ km s^{-1}) covering a similar area, expected for an axisymmetric infall. The only strongly blueshifted component is very thin and located in the same area as the streamer. With the present observations, we do not have enough spatial resolution to characterize this infall further.

2.4 Discussion

2.4.1 Understanding why mass and infall rate are lower limits

The estimated mass of the streamer (see Sect. 2.3.5) is a lower limit because of observational limits in our data and the assumptions made in the mass calculation. We estimated the length of the streamer as 3300 au, using H_2CO emission and the streamline model. This is possibly not the full length of the streamer for three reasons. First, the H_2CO emission is cut off by the primary beam of the NOEMA observations (22″), and our observations are not sensitive to strong emission beyond this radius. Second, there is a strong offset emission toward the southwest of Per-emb-50, located just outside the primary beam at ~ 3000 au, seen in all of the molecular tracers used in this work (see Figs. 2.1 and 2.5). Moreover, there is significant $C^{18}O$ emission observed in the SMA MASSES program (Stephens et al. 2019) in the same location as the H_2CO streamer, which extends to a bright emission located beyond the streamer's observed extent in this work. Third, the streamline model requires an initial velocity $v_{r,0} = 1.25$ km s^{-1} in the direction of the protostar to fit the outer 1500 au of the streamer (see Table 2.3). The initial velocity might indicate that the streamer starts farther away and was already infalling by the time it reached r_0.

Another observational limitation is the lack of zero-spacing data. $C^{18}O$ emission is extended and the observations have no sensitivity to scales larger than the MRS (22″), but our observations start losing sensitivity to scales larger than 4″ due to the coverage in u-v space. Therefore, we are not certain if the clumpiness observed in $C^{18}O$ is real or if it is influenced by missing flux due to lack of zero-spacings.

The main assumptions that we used in the streamer's mass calculation were, first, a fixed ratio between column densities, which is suitable for an undepleted gas, $X_{C^{18}O} = 5.9 \times 10^6$ (Frerking et al. 1982), and second, a constant excitation temperature T_{ex}. Most likely, $X_{C^{18}O}$ is not constant along the streamer. Within the dense core, it is more probable that there is a larger $C^{18}O$ depletion into grains due to an increase in density (see Bergin & Tafalla 2007, and references within). Where $C^{18}O$ is depleted, $X_{C^{18}O}$ should be higher to estimate the mass correctly. Also, this conversion factor was calibrated using Taurus molecular clouds, and might differ in Perseus. Pineda et al. (2008) show that there is variation in the conversion factors of the $C^{18}O$(1–0) line in different regions in Perseus. Furthermore, a constant T_{ex} along the streamline is unlikely; the temperature might be higher closer to the protostar due to thermal heating. This is also suggested by the presence of SO_2 emission toward the south of Per-emb-50. Unfortunately, we do not have a good estimation of the gas temperature in the vicinity of Per-emb-50. NH_3 is a commonly used chemical thermometer, combining the (1,1) and (2,2) inversion transitions, both observed in NGC 1333 with Green Bank Telescope (GBT, Friesen et al. 2017). Although the NH_3(1,1) line is present in Per-emb-50, the NH_3(2,2) line is too faint to be detected around the protostar and provide a gas temperature estimation. Higher spatial resolution observations of both NH_3 lines do not detect emission in this region (Dhabal et al. 2019). Instead, we used the values in the vicinity of Per-emb-50 in Friesen et al. (2017) and Dhabal et al. (2019), which are between 10 and 20 K. The variance in T_{ex} adds less than 5% of the total

uncertainty, and therefore it does not dominate the uncertainties.

Given that the mass and mass infall rates we report are lower limits, the general results of this paper are strengthened: the streamer delivers more than enough mass toward the protostellar disk to sustain its high accretion rate in comparison with its neighbors (see Sect. 2.3.5 and Sect. 2.4.4). If the streamer masses or infall rates are actually higher, this streamer can deliver even more mass than what we report here.

2.4.2 Classical free-fall time versus the streamline model

For the first time, we calculated the infall timescales along a streamer using the streamline model based on the analytical solution from Mendoza et al. (2009). We show that in Per-emb-50, where the streamline model requires an initial radial velocity, the infall rate is underestimated by at least a factor of two when calculated with the classic – and initially static – free-fall timescale. The factor by which the timescale is underestimated depends on the initial velocity of the streamer: if the streamer presents an initial impulse at the starting radius r_0, it will take less time to reach the protostellar disk than if the streamer started from rest. The streamline model allows us to estimate the initial radial velocity. This highlights the importance of the use of a streamline model to calculate the timescales involved in infall.

The calculation of the initial radial velocity (and consequently, the infall rate) relies on a streamer model that has good constraints both spatially in the image plane and kinematically in the velocity along the line of sight. If the streamer is fully contained along the line of sight, the velocity is correctly characterized, but we do not have information about the length of the streamer. On the other hand, if the streamer moves completely within the plane of the sky, there is information about the length and path of the streamer, but the velocity cannot be characterized. Fortunately, in the case of Per-emb-50, the streamer is mostly contained in the plane of the sky, with a small inclination at the start of the streamline (approximately 10° according to the streamline model in Sect. 2.3.4), and it becomes more inclined with respect to the line of sight where we see the acceleration closer to the disk. This allows us to sample both the distance (up to the primary beam edge) and the velocity, and therefore constrain the initial radial velocity.

2.4.3 Streamer is landing within disk scales

Our results indicate mass is infalling to disk scales (which corresponds to distances of $\sim 100 - 200$ au), both in the case of the streamer and the asymmetric infall seen in the redshifted component of SO emission (see Sect. 2.3.8). We can model the streamer down to ≈ 250 au from the edge of the gas disk (see Sect. 2.3.4) and the toy model in Sect. 2.3.7 has a centrifugal radius between 100 and 130 au, similar to the 90 au of the gas disk. It is possible that SO_2 traces the impact zone where gas is infalling, either that of the streamer or the redshifted SO component. H_2CO and SO emission that trace the streamer end within a beam size of the location of the SO_2 peak emission (located at ~ 150 au, see Fig. A.3). This is compatible with the centrifugal radius of ≈ 250 au (see Sect. 2.3.4)

obtained for the streamline model, as the emission is seen in projected distance and r_c is a three-dimensional distance. According to the streamline model, the impact velocity component along the line of sight at the assumed impact location (r_c) is 1.7 $\mathrm{km\,s^{-1}}$. The FWHM of the SO_2 emission spectra at the location of the streamer's end is similar to the estimated impact velocity, suggesting that the impact of the streamer is responsible for the SO_2 velocity dispersion. However, SO_2 peaks at the same velocity as the strong, redshifted component, which could be attributed to another asymmetric infall, and at the peak location, both have the same shape (see the top right panel of Fig. A.3). Therefore, it is unclear which infalling feature most influences the SO_2 emission.

One interesting result is that the centrifugal radius of the streamer r_c ($\sim$ 250 au, see Sect. 2.3.4) is about twice the centrifugal radii obtained for the rotating-infalling envelope, $r_{c,\mathrm{env,r}} = 130$ au and $r_{c,\mathrm{env,b}} = 100$ au (see Sect. 2.3.7). This suggests that the streamer and envelope have different origins and that the streamer might come from outside the dense core. The streamer component seen in the SO emission might indicate the entrance of the streamer to the inner envelope, where the latter is flattened and has a rotating and infalling motion of its own (represented by the redshifted component in Sect. 2.3.8). For the streamer material to reach the centrifugal radius of the inner envelope, which is slightly larger than the gas disk radius (90 au, see Sect. 2.3.8), and for its material to reach the gas disk, it must lose angular momentum, for example, through magnetic braking (Mestel & Spitzer 1956; Mouschovias & Paleologou 1980; Basu & Mouschovias 1994). Loss of angular momentum of material coming from $> 10\,000$ au has been observed for Class 0 sources by Pineda et al. (2019) down to $\sim$ 1000 au, becoming low enough to generate a rotationally supported disk in scales $<$ 100 au. Future high-resolution observations can clarify the interaction between the streamer and the inner envelope for Class I sources.

2.4.4 Relation between streamers and accretion outbursts

The presence of streamers with a high infall rate, such as the one found toward Per-emb-50, are linked to accretion variability and luminosity outbursts. Simulations of turbulent molecular clouds suggest that infall from larger scales regulates the accretion toward the protostar, even in phases later than Class 0 (Padoan et al. 2014; Kuffmeier et al. 2018). In the case presented in this work, the relation between the streamer and an accretion burst (current or future), is supported by the high accretion rate and luminosity of Per-emb-50 in comparison with other Class I protostars, as well as other asymmetric structures found toward current (and past) outbursting sources.

The streamer feeding Per-emb-50 might explain the high accretion rate of this protostar in comparison to other Class I sources in NGC 1333. Its $\dot{M}_{acc}$ is $\sim$10$\times$ higher than for other Class I sources in NGC 1333 (Fiorellino et al. 2021), and the infall rate provided by the streamer five to ten times larger than $\dot{M}_{acc}$ (see Sect. 2.3.6), more than enough to replenish the mass consumed by accretion. The luminosity (between 10 and 25 $L_\odot$, Enoch et al. 2009; Dunham et al. 2015) and accretion rate are consistent with those of Class Is undergoing an accretion burst (Hsieh et al. 2019). However, Per-emb-50's envelope mass is similar to those around other Class I objects (at 2.2 $M_\odot$, Enoch et al. 2009; Agurto-Gangas

et al. 2019), and the streamer might be the key ingredient to sustaining Per-emb-50's high accretion rate.

It is also possible that we are seeing the protostar in the onset of an accretion burst, as it is significantly brighter than other Class I protostars, or the streamer might produce one in the future. Since the streamer's infall rate is five to ten times larger than the current accretion rate, it is possible that in the future 9000 yr the accretion rate could grow by one order of magnitude. This shows that streamers might provide a significant amount of mass for stellar accretion, and suggests that intense accretion events can take place during the Class I phase. Moreover, if more streamers in Class I protostars are found and their masses characterized (e.g., in this work and Yen et al. 2014), this also suggests that the main accretion phase of the protostar might extend beyond the Class 0 phase.

Recent observations toward young stellar objects find a correlation between accretion bursts and infall from larger scales. Asymmetric structures with a length of 1000 au have been associated with some FU Ori protostars (Liu et al. 2016). Other protostars with a known accretion burst in the past, such as Per-emb-2 (Pineda et al. 2020) and V883 Ori (White et al. 2019), also have streamers with an infall rate higher than their accretion rate. For these sources, it is suggested that the large-scale infall regulates the episodic accretion. This might be the case for Per-emb-50 as well, and we propose that the mass is delivered to the protostellar disk, which triggers a disk instability (similar to a gravitational instability, as suggested by Kuffmeier et al. 2018; Hennebelle et al. 2017), the mass is transported through the disk, and afterward is accreted by the protostar in a burst. This idea is supported by the disk's mass in comparison to other disks: Per-emb-50's dust disk has between $0.28 - 0.58$ $M_\odot$, around twice the mass seen in other Class I disks (Segura-Cox et al. 2016, 2018), which suggests that this disk might be accumulating mass coming from the streamer. Additionally, even if we are currently unable to resolve this disk, it has been suggested that gravitational instabilities produced by infalling material account for the spiral structures found in the disks of other protostars, for instance, in IRAS16293–2422 B (a Class 0 source, Zamponi et al. 2021), HH 111 VLA 1 (a Class I source, Lee et al. 2020), and Elias 2-27 (a Class II protostar, Paneque-Carreño et al. 2021). Higher-resolution observations of the gas disk around Per-emb-50 are required in order to study these possible instabilities.

2.4.5 Understanding where the streamer comes from

The streamer possibly connects to larger scale structures such as filaments and fibers. Within molecular clouds, simulations suggest that that up to 50% of the final protostellar mass comes from beyond their natal core (Pelkonen et al. 2021), and observations of other protostars show that gas can flow from beyond the protostar's natal core, connecting the protostar with other structures (e.g., Chou et al. 2016). Our data, together with the observed environment where Per-emb-50 lives, suggest that this might be the case for this protostar as well.

First, as discussed previously (see Sect. 2.4.1), the H_2CO and $C^{18}O$ emission are truncated by the NOEMA primary beam and there is significant $C^{18}O$ $(2-1)$ emission

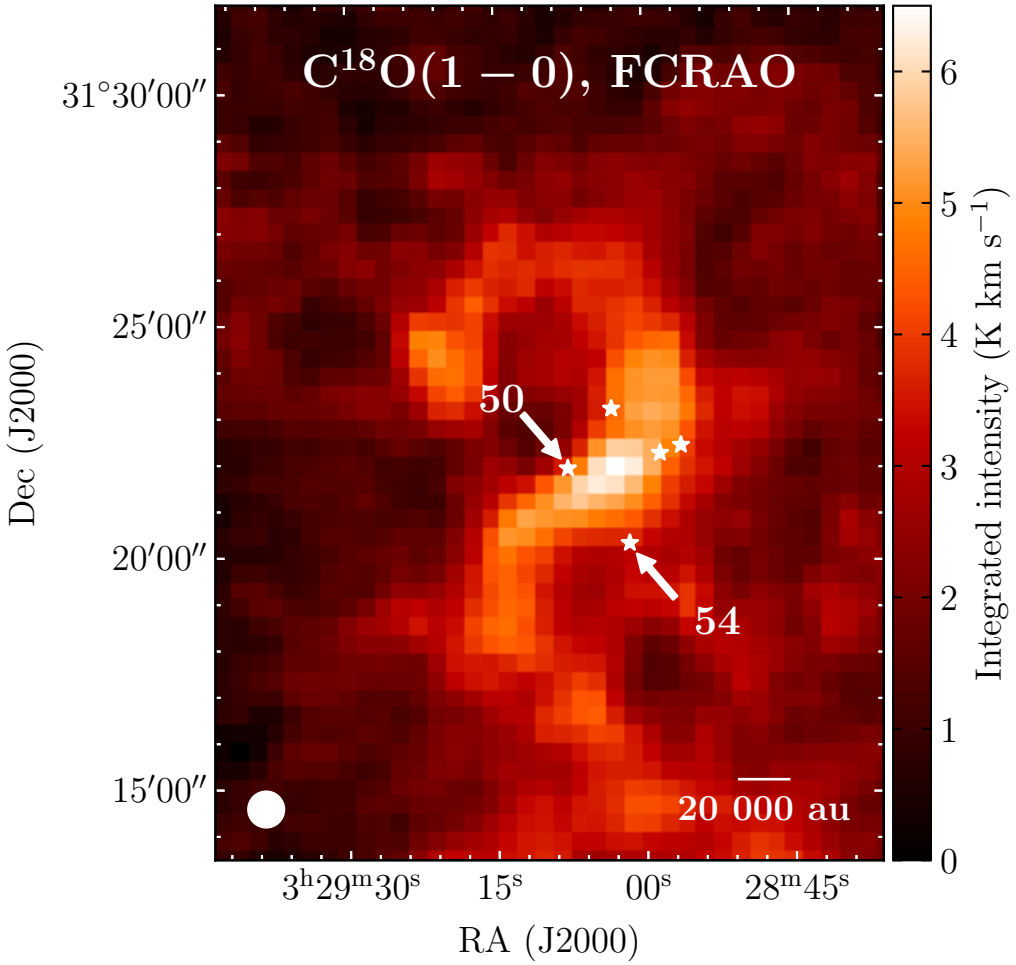

Figure 2.9: Integrated intensity map of $C^{18}O(1–0)$ emission of NGC 1333 from Hatchell et al. (2005), between 5 and 10 km s^{-1}, centered at the location of Per-emb-50. White stars represent the location of close-by Class I protostars. Per-emb-50 and Per-emb-54 are indicated and labeled with white arrows. The white circle in the lower left corner represents the beam of the $C^{18}O(1-0)$ observations (46″).

observed in the SMA MASSES program (Stephens et al. 2019), located at the position of the offset emission outside the primary beam, directly in line with the streamer. Moreover, the MASSES emission is also cut short at its primary beam (48″, Stephens et al. 2019). The gas reservoir seen in MASSES $C^{18}O$ observations might be funneled by the streamer or might be part of it, implying that streamers might connect with larger structures in their natal molecular clump.

Zooming out, NGC 1333 consists of a complex association of filaments, revealed in dense gas observations (Chen et al. 2020b; Dhabal et al. 2019; Friesen et al. 2017). At larger scales, the streamer points directly toward the crossing of two dense gas filaments observed in NH_3 observations (filament b in Chen et al. 2020b) and toward a bright extended emission source observed in $C^{18}O$ (see Fig. 2.9), located between Per-emb-50 and Per-emb-54. If the streamer continues outside the primary beam, it may connect both protostars, as observed with the protostar L1544-IRS1 and the starless core HRF40 by Chou et al. (2016). There are currently no observations at intermediate resolution ($6-10''$) with an appropriate tracer in NGC 1333 that connects the large-scale clumps and filaments surrounding Per-emb-50 to the core. Studies of filaments and fibers, such as those of Chen et al. (2020b) and Dhabal et al. (2019), show an intricate connection between filaments and cores, but they are not sensitive enough to detect emission close to Per-emb-50, and the $C^{18}O(1-0)$ has too coarse a resolution (46″ beam, Hatchell et al. 2005). Nevertheless, the general direction of the streamer suggests that this streamer is connected to the larger-scale filaments.

2.4.6 Asymmetries in SO and SO_2 emission

The SO and SO_2 emission (see Fig. 2.7) are asymmetrical: they are both brighter toward the south and in redshifted velocities. SO shows that the kinematic properties of gas toward Per-emb-50 are complex and include both asymmetric infall and rotation. This is more evident in the Gaussian decomposition (see Sect. 2.3.8). These asymmetries show that the inner envelope of Per-emb-50 is not infalling monolithically, and thus does not follow the classical picture of core collapse (Terebey et al. 1984; Shu 1977).

Through Gaussian decomposition, we find that the redshifted component that dominates the SO emission is centered around the protostar and has a central velocity of approximately 9.5 $\mathrm{km\,s^{-1}}$ (2 $\mathrm{km\,s^{-1}}$ redshifted with respect to Per-emb-50, see Sect. 2.3.8). We interpret this emission as another asymmetric infall completely contained within the line of sight. Given the velocity gradients seen in the bottom right panel of Fig. 2.8, this component might not be a streamer but rather a wider asymmetric infall, comprising one side of the envelope located between the observer and the protostar. Finding a possible second infall feature in Per-emb-50 shows that the envelope infall kinematics are complex and reaffirms the idea that mass accretion does not follow an inside-out, axisymetric fashion. The asymmetries might be related to the environment where Per-emb-50 is located, close to the intersection of two filaments in NGC 1333 (Chen et al. 2020b) and close to several other protostars (Enoch et al. 2009; Dunham et al. 2015).

2.4.7 Comparison with other streamers

Streamers, defined as long ($\gtrsim$ 1000 au) and asymmetric accretion flows toward disk-forming scales ($\lesssim$ 300 au, as in Pineda et al. 2020), are a relatively new phenomenon that are proving to be relevant in star formation, with new discoveries both in gas tracers (Alves et al. 2020, Segura-Cox et al. in prep) and dust (Ginski et al. 2021). Per-emb-50's streamer is the first Class I protostellar streamer to be characterized using a free-falling model. We illustrate the streamer and its relation with the various components found surrounding Per-emb-50 in Fig. 2.10.

Per-emb-50's structure and kinematics are similar to other asymmetric features found in protostars in Perseus and other molecular clouds. The observed streamer size in this work is within the range of other observed streamers (between 1000 and 10 000 au), such as toward [BHB2007]11 (Alves et al. 2020), Per-emb-2 (Pineda et al. 2020), and SU Aur (Ginski et al. 2021; Akiyama et al. 2019). Similar infalling structures have been found at smaller scales (between roughly 200 to 1000 au), within inner envelopes of single systems (e.g., Garufi et al. 2022; Tang et al. 2012) and within the circumbinary disk and inner envelope of binary systems (e.g., Phuong et al. 2020; Takakuwa et al. 2017; Dutrey et al. 2014a; Takakuwa et al. 2014). The streamer in this work also shows a velocity gradient and a curved appearance in the image plane, similar to many of the streamers mentioned above (e.g., Pineda et al. 2020; Akiyama et al. 2019). We note that the infalling structures in smaller scales (200 – 1000 au) might be of a different nature, possibly driven by the tidal forces of the binary systems instead of pure free fall. However, these structures also play a role in feeding the circumstellar disks.

Our work uses the same analytical solution as in Pineda et al. (2020) for Per-emb-2, a Class 0 protostellar close binary ($<$ 20 au), the first streamer where mass and infall rate were obtained, but extends the method to include the analysis of infall rates along the streamer. In Per-emb-2, the streamer's kinematics are consistent with a model with $v_{r,0} = 0$, so using the free-fall timescale does not severely underestimate the infall rate. Per-emb-50's mean streamer infall rate $\langle \dot{M}_{in} \rangle_{\rm Per50} = 1.3 \times 10^{-6}$ M$_\odot$ yr^{-1} is similar to the infall rate in Per-emb-2, $\dot{M}_{in,\rm Per2} \approx 10^{-6}$ M$_\odot$ yr^{-1} (Pineda et al. 2020). While the infall rate is similar in both sources, the mean ratio $\dot{M}_{in}/\dot{M}_{acc}$ is higher for Per-emb-50 (5-10, in contrast with 1.4 for Per-emb-2). Nevertheless, both are > 1, even assuming the highest accretion rate possible for Per-emb-50, $(0.6 - 1.2) \times 10^{-6}$ M$_\odot$ yr^{-1} (blue area in Fig. 2.6). Per-emb-50 is unique in that it is the first streamer to definitively show, through the use of a free-fall model, that the infall rate can sustain the accretion rate. This implies that streamers can contribute important amounts of mass in later phases than Class 0, therefore suggesting that important accretion events can happen in the Class I phase, and in some cases, can occur in Class II sources (as suggested by Garufi et al. 2022; Alves et al. 2020; Tang et al. 2012).

It is still uncertain if the lack of streamers found in observations is due to an observational bias, or if streamers are uncommon in the majority of star-forming systems. If streamers live as much as the estimated free-fall timescale of Per-emb-50 ($t_{ff} \sim 9000$ yr) and the protostar has only one streamer in their life, there is between a 2% and a 30%

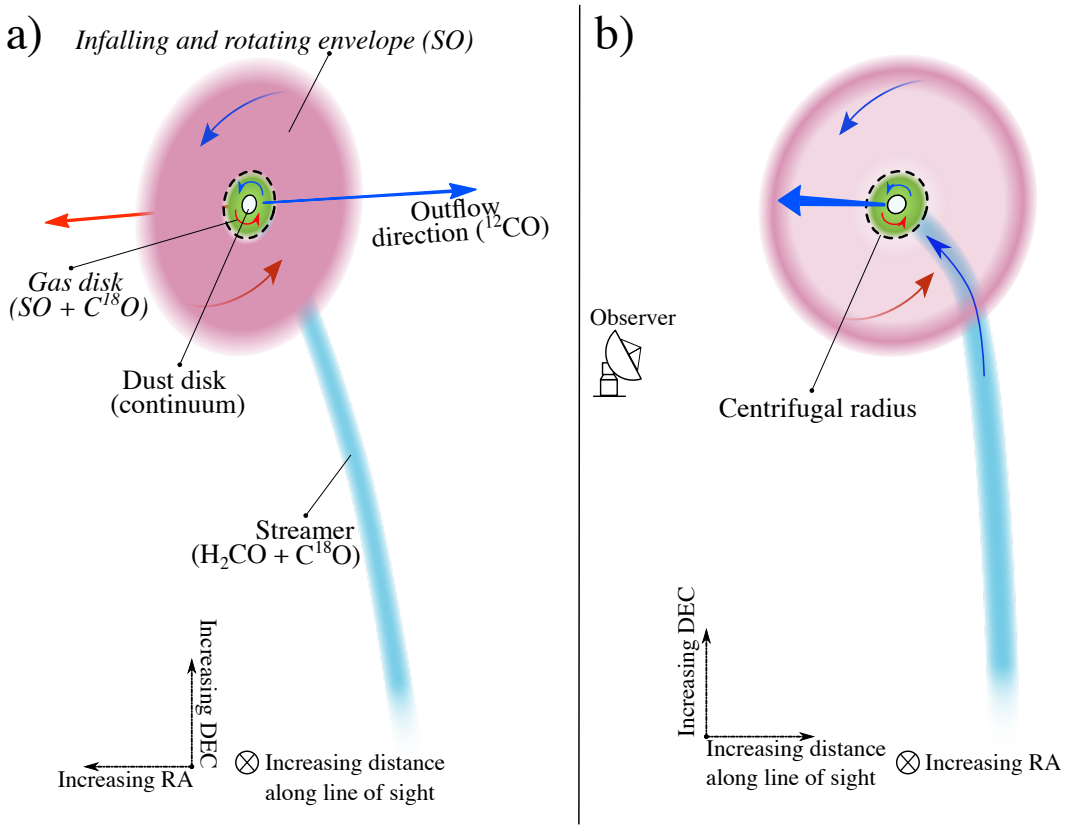

Figure 2.10: Schematic illustration of the different elements present around Per-emb-50. The streamer is represented as a thick light-blue line. The inner envelope is represented in light pink and the rotating gas disk is represented with a green ellipse. The inner envelope has a transparent gap inside to see the streamer behind it. The blue and red straight arrows show the outflow direction in the blueshifted and redshifted directions, respectively. The white circle shows the dust disk and the solid black ellipse marks its edge. The dashed circle represents the centrifugal radius. Curved arrows show the general direction of motion of each component: red and blue arrows show if the motions are seen as redshifted or blueshifted line emission, respectively. **a:** Image plane view, where the right ascension increases toward the left and declination increases upward. **b:** Line-of-sight view, where the observer is on the left and distance increases toward the right.

chance of observing one during the Class I phase, with the lower limit obtained by dividing t_{ff} by the estimated Class I phase duration (0.44. Myr, Evans et al. 2009) and the upper limit by dividing t_{ff} by itself plus the time between accretion bursts, estimated to occur once every few 10 000 yrs(Frimann et al. 2017; Jørgensen et al. 2015). This is just an order of magnitude estimate, as the time between bursts is uncertain and has a wide range of values in different protostars (from a few thousand to a few tens of thousands of years, e.g., Hsieh et al. 2018; Frimann et al. 2017; Jørgensen et al. 2015), and previous works show this time might increase from Class 0 to Class I protostars (Hsieh et al. 2019; Audard et al. 2014). Nevertheless, asymmetric infall features are seen along the complete simulations of star formation within a molecular cloud (Kuznetsova et al. 2019; Kuffmeier et al. 2018).

As streamers are a new emerging phenomenon in observations, it is unclear which are the best molecules to trace them. Per-emb-50 shows the first streamer characterized with H_2CO emission, whereas other streamers are observed in ^{12}CO (e.g., Alves et al. 2020), HC_3N (e.g., Pineda et al. 2020), and HCO^+ (e.g., Yen et al. 2019). Upcoming NOEMA observations from the PRODIGE project can uncover more asymmetric infalls and streamers around Class 0 and Class I sources and, in the future, we might be able to make a statistical study of streamers in protostars and investigate which molecules are the best tracers of this phenomenon.

2.5 Conclusions

In this work, we present new NOEMA observations of H_2CO, $C^{18}O$, ^{12}CO, SO, and SO_2 molecular lines toward Per-emb-50, a Class I source in NGC 1333. We use these observations to characterize the kinematics from envelope to disk scales around the protostar. An illustration of our main findings is shown in Fig. 2.10. The main results are summarized as follows:

1. We find a streamer depositing material close to the edge of the gas disk around Per-emb-50. It presents an almost constant velocity in H_2CO emission in the line of sight from roughly 1500 to 3000 au from the protostar. There is acceleration toward more blueshifted velocities closer to the protostar, up to around 1000 au.

2. The analytical solutions for infalling gas along a streamline can reproduce the observed kinematics of the H_2CO emission. An initial velocity of 1.25 $\mathrm{km\,s^{-1}}$ at the initial position 3330 au away from the protostar is required to replicate the observed velocity along the line of sight. Taking the initial velocity into account, the free-fall timescale of the streamer is $\sim$ 9000 yr.

3. The streamer delivers more than enough mass to sustain its protostellar accretion rate. We estimate a lower limit to the streamer's mass at 1.2×10^{-2} $M_\odot$, from which we obtain a mean infall rate of 1.3×10^{-6} $M_\odot$ yr^{-1}, with variations of up to a factor of three along the streamer. The infall rate is consistently about five to ten times larger than the estimated accretion rate of the protostar. This means that the streamer can

deliver enough mass to sustain the high accretion rate of this protostar for at least the next 9000 yrs.

4. We find signatures of asymmetry in SO and SO_2 emission. The PV diagram of SO shows a diamond shape consistent with rotation and infall motions, but there is an asymmetry between the redshifted and blueshifted velocities. Through Gaussian decomposition, we find that SO traces mostly the inner envelope rotation and a redshifted asymmetric infall located along the line of sight. SO also traces the inner 1000 au of the streamer. SO_2 emission hints at an impact zone toward the south of Per-emb-50, which is consistent with both the estimated landing site of the streamer and the peak of the redshifted asymmetric infall.

The description of the envelope around Per-emb-50 and each of its distinct kinematic components are limited by the resolution and primary beam of our observations, together with the lack of zero-spacing data. We emphasize that the streamer might extend further than the 3000 au we characterize in this work, as it is traced in $C^{18}O$, which is observed outside of the primary beam of our observations, and points toward the crossing of two dense gas filaments. We also point out that the mass is a lower limit. Further observations with single dish antennas will allow the total flux (and therefore, mass) along the streamer to be obtained and its mass fluctuations to be confirmed. Intermediate resolution observations ($\approx 6''$) that cover an area larger than the NOEMA primary beam will allow us to investigate the connection of this streamer to the larger filament. Higher spatial resolution data of more than one SO and SO_2 molecular transition will help determine the precise landing site of the streamer and allow us to characterize the redshifted infall better. Observations of other transitions of the same molecules observed in this work will allow the physical parameters (volume density and temperature) of the streamer and its landing site to be derived.

The presence of the streamer and the redshifted SO component highlight the importance of asymmetric infall for the growth and development of protostars at all evolutionary stages. The high infall rate of this source and the presence of streamers in Class I and II sources suggest that important accretion events of protostars can occur after the Class 0 phase.

Chapter 3

Flow of gas detected from beyond the filaments to protostellar scales in Barnard 5

This chapter is based off the paper Valdivia-Mena, M. T. et al. A&A, 677, A92, 2023.

Abstract

Context. The infall of gas from outside natal cores has proven to feed protostars after the main accretion phase (Class 0). This changes our view of star formation to a picture that includes asymmetric accretion (streamers), and a larger role of the environment. However, the connection between streamers and the filaments that prevail in star-forming regions is unknown.
Aims. We investigate the flow of material toward the filaments within Barnard 5 (B5) and the infall from the envelope to the protostellar disk of the embedded protostar B5-IRS1. Our goal is to follow the flow of material from the larger, dense core scale, to the protostellar disk scale.
Methods. We present new HC_3N line data from the NOEMA and 30m telescopes covering the coherence zone of B5, together with ALMA H_2CO and $C^{18}O$ maps toward the protostellar envelope. We fit multiple Gaussian components to the lines so as to decompose their individual physical components. We investigated the HC_3N velocity gradients to determine the direction of chemically fresh gas flow. At envelope scales, we used a clustering algorithm to disentangle the different kinematic components within H_2CO emission.
Results. At dense core scales, HC_3N traces the infall from the B5 region toward the filaments. HC_3N velocity gradients are consistent with accretion toward the filament spines plus flow along them. We found a $\sim$ 2800 au streamer in H_2CO emission, which is blueshifted with respect to the protostar and deposits gas at outer disk scales. The strongest velocity gradients at large scales curve toward the position of the streamer at

small scales, suggesting a connection between both flows.
Conclusions. Our analysis suggests that the gas can flow from the dense core to the protostar. This implies that the mass available for a protostar is not limited to its envelope, and it can receive chemically unprocessed gas after the main accretion phase.
Keywords: ISM: kinematics and dynamics – ISM: individual objects: Barnard 5 – stars: formation – ISM: structure

3.1 Introduction

Stars form in dense cores, which are defined as local overdensities at a sub-parsec scale with respect to their background. These contain cold ($\sim$ 10 K) and dense ($n \geq 10^5$ cm^{-3}) gas from which an individual star or a bound stellar system could form (Bergin & Tafalla 2007; Pineda et al. 2023). The classical picture of low-mass star formation ($\lesssim$ 1 M$_\odot$) considers a core as an isolated unit with initial angular momentum that collapses to form a protostar and a protostellar disk (Shu 1977; Terebey et al. 1984). However, cores do not live in isolation: observations of star-forming regions show that they are mostly harbored within filaments, which continuously accrete gas from the larger molecular cloud and evolve (André et al. 2010; Könyves et al. 2015). Filaments themselves are highly structured and present preferential velocity-coherent flows of gas within them, called fibers (e.g., Hacar et al. 2013, 2017). Observations show that material tends to collapse to the densest parts of filaments on $\sim$ 0.1 pc scales ($\sim$ 20 000 au) and toward cores while star formation is underway (André et al. 2010; Arzoumanian et al. 2011). Therefore, the assumption of isolation and symmetry breaks when looking at cores harbored within filaments, and understanding the kinematics of dense cores allows us to trace the origin of gas that forms a protostar. In particular, infall phenomena are vital to understand the growth and final masses of protostars and their planetary systems.

Recently, it has been found that at smaller scales ($\sim$ 1000 au) within the core, infall also proceeds in an asymmetric manner, through channels called streamers (Pineda et al. 2020; Garufi et al. 2022; Valdivia-Mena et al. 2022). Streamers are found from the highly embedded Class 0 phase (Le Gouellec et al. 2019; Pineda et al. 2020) to Class II sources (e.g., Yen et al. 2019; Akiyama et al. 2019; Alves et al. 2020; Garufi et al. 2022; Ginski et al. 2021). They have also been found feeding not only single protostars, but also protostellar binaries, both funneling material toward the inner circumstellar disks (Phuong et al. 2020; Alves et al. 2019; Dutrey et al. 2014a) and to the binary system as a whole (Pineda et al. 2020). It has been suggested that streamers can deliver material from beyond the dense core (Kuffmeier et al. 2023), bringing even more material toward protostars than that supplied from their own envelopes (Pineda et al. 2020; Valdivia-Mena et al. 2022). These results show that star formation is an asymmetric and chaotic process driven by the motions of gas within a molecular cloud. A new picture of low-mass star formation is thus emerging, where the relationship of the protostar and the local environment, together with asymmetries, is much more relevant (Pineda et al. 2023).

While our understanding of both streamers and infall toward filaments is growing, if

and how these infall mechanisms connect at large and small scales is still an open question. For this work, we probed two scales of infall, first the infall of fresh gas toward the filaments and condensations, and then the infall of gas from a protostellar envelope to a protostar. For this, we studied the dense core region of Barnard 5 (B5), regarded as a quiescent core at a distance of 302 pc from our Solar System (Zucker et al. 2018), located at the eastern edge of the Perseus molecular cloud. Barnard 5 has been the subject of several studies, most of them tracing the dense gas structure using NH_3, but also through other tracers such as CO, $C^{18}O$, N_2H^+, and HCN (Fuller et al. 1991; Pineda et al. 2010, 2015; Schmiedeke et al. 2021). We refer to Pineda et al. (2015) as P15 and Schmiedeke et al. (2021) as S21. Within this core, there is a clear coherence region, defined as the area where the nonthermal velocity dispersion of dense gas is subsonic (Pineda et al. 2010). Inside this coherent zone, there are two filaments seen in NH_3, each about 0.3 pc ($\sim 60\,000$ au) long (Fig. 3.1). These filaments have supercritical masses per unit length, indicating that they are not supported against gravitational collapse and that they are currently fragmenting (S21). Within these filaments, there are three condensations likely to form stars and a Class I protostar, B5-IRS1, which together will form a wide-separation (more than 1000 au) quadruple system (P15).

B5-IRS1, also known as Per-emb-53, is identified as a Class I protostar from its spectral energy distribution (SED, Enoch et al. 2009). It is located at the northern edge of Fil-2, between Cond-2 and 3 (using the nomenclature from P15; S21) and it has a central velocity $v_{\rm LSR} = 10.2$ km s^{-1} (P15). It has a disk, which remains spatially unresolved, with an estimated mass of 0.03 $M_\odot$ at most, using the mass found by Zapata et al. (2014) and correcting for a distance of 302 pc to B5 (Zucker et al. 2018). Its outflow cone is almost perpendicular to the orientation of the filament it is embedded in (Fig. 3.1, Zapata et al. 2014).

This paper is organized as follows. In Sect. 3.2, we describe the data from several different telescopes we used for this work and how they were processed. In Sect. 3.3 we describe the new data cubes and how we discovered individual velocity components in the spectra. Section 3.4 explains how we analyzed the discovered velocity components and determined the kinematic properties of B5 and the envelope surrounding IRS1. In Sect. 3.5 we discuss our results and connect the (large-scale) kinematic properties of the filaments within B5 to the (small-scale) infalling gas in the protostellar envelope. Section 3.6 summarizes the main results and conclusions of our work.

3.2 Observations and data reduction

We used observations from different telescopes to investigate the kinematics of the two B5 filaments within the coherent core, and the envelope around B5-IRS1 ($3^{\rm h}47^{\rm m}41.591^{\rm s}$, $+32^\circ\ 51'\ 43.672''$ (J2000), Tobin et al. 2016). We used $HC_3N\,(10-9)$ and $(8-7)$ line observations taken on the Northern Extended Millimeter Array (NOEMA) at Plateau the Bure (France) and the 30m telescope at Pico Veleta (Spain), from Institut de Radioastronomie Milimétrique (IRAM). We also used $H_2CO\,(3_{0,3}-2_{0,2})$ and $C^{18}O\,(2-1)$ line

Molecule	Transition	Frequency[1] (GHz)	Telescope	Spatial resolution ($''$)	Spectral resolution (km s^{-1})	rms (K)
HC_3N	8 – 7	72.783822	NOEMA + 30m	5.13×4.70	0.257	0.17
HC_3N	10 – 9	90.979023	NOEMA + 30m	4.07×3.79	0.206	0.15
H_2CO	$3_{0,3}$ – $2_{0,2}$	218.222195	ALMA	0.41×0.27	0.084	0.98
$C^{18}O$	2 – 1	219.560354	ALMA	0.40×0.27	0.042	1.47

Table 3.1: Properties of the molecular line observations and telescopes used in this work. The rms is a mean value. [1]Frequencies taken from the Cologne Database for Molecular Spectroscopy (CDMS, Endres et al. 2016).

cubes observed with the Atacama Large Millimeter/Submillimeter Array (ALMA) at the Chajnantor Plateau (Chile). We refer to $H_2CO\,(3_{0,3} - 2_{0,2})$ and $C^{18}O\,(2-1)$ as H_2CO and $C^{18}O$ for the rest of this work, respectively. A summary of the molecular transitions used in this work and the data properties are in Table 3.1. Additionally, we used NH_3 (1,1) line observations and spectral fit from P15, taken with the Karl G. Jansky Very Large Array (VLA) in New Mexico and with the Green Bank Telescope (GBT) in West Virginia (USA). Details about these observations and fits can be found in Appendix B.1.

3.2.1 NOEMA

NOEMA observations were carried out under project S18AL (PI: J. E. Pineda) using the Band 1 receiver. B5 was observed on 2018 August 24 and between 2018 September 15 and September 23 in D configuration, using a mosaic with 53 pointings. We used the PolyFix correlator tuned with a LO frequency of 82.499 GHz. The $HC_3N\,(8-7)$ and $(10-9)$ line frequencies (Table 3.1) are located at high resolution chunks, with a channel width of 62.5 kHz. For the observing period between August 24 and September 16, the source was observed with eight antennas, while the rest of the period there were ten antennas available. The data were calibrated using the standard observatory pipeline in the Continuum and Line Interferometer Calibration (CLIC) program, which is part of the Grenoble Image and Line Data Analysis Software (GILDAS) package.

3.2.2 30m Telescope

Observations of Barnard 5 with the IRAM 30 telescope were obtained with the EMIR 090 receiver. The observations were made under project 034-19 (PIs: J. E. Pineda and A. Schmiedeke), between 2019 August 24 and 26, using on-the-fly mapping and connected to the FTS50 backend. The 30m data were reduced using CLASS. We used J0319+4130 for pointing and the data are calibrated using the two-load method (Carter et al. 2012).

3.2.3 Combination of NOEMA and 30m

We used the GILDAS software `mapping` to combine and image the NOEMA and 30m data of both HC_3N molecular transitions used in this work. The command `uv_short` is used to

combine the 30-m and NOEMA data into a combined uv-table. We used natural weight and the multiscale CLEAN algorithm implemented in `mapping` to obtain a CLEANed datacube. We manually did the mask using the `support` command in `mapping`. The final properties of the HC_3N data cubes are in Table 3.1. Finally, we integrated the obtained cubes to make velocity integrated images from 9.2 to 11.2 $\mathrm{km\,s^{-1}}$, so as to cover the full range of velocities where emission has a signal-to-noise ratio $(S/N) > 3$.

3.2.4 ALMA

We observed the envelope surrounding B5-IRS1 at high resolution with ALMA Band 6 under project 2017.1.01078.S (PI: D. Segura-Cox). Observations were done during 2018 September 22 with the 12m array using 49 antennas. The total integration time was 20.16 minutes. The phasecenter of our observations is $3^{\mathrm{h}}47^{\mathrm{m}}41.588^{\mathrm{s}}$, $+32^\circ\ 51'\ 43.643''$ (J2000). The minimum baseline length was 15.07 m, resulting in a maximum recoverable scale (MRS) of $4''$, and maximum baseline of 1398 m. The primary beam for our observations is approximately $15.4''$ for both molecules.

We used the Common Astronomy Software Applications (CASA, McMullin et al. 2007) version 5.4.0-68 for data calibration. We used the calibration results from the pipeline ran by the ALMA OSF. We used J0237+2848 and J0510+1800 as bandpass calibrators. J0336+3218 was used by the pipeline for gain calibration. The data presented here are self-calibrated in an iterative process, with phase-only self-calibration having a shortest solution interval of the integration time (6.05s) and a final round including amplitude self-calibration with an infinite solution interval.

We imaged the data using CASA version 6.4.0. The H_2CO and $C^{18}O$ spectral cubes are produced using robust (Briggs) weight with a parameter $r = 0.5$ to balance flux sensitivity and resolution. We used the `tclean` procedure through a manually selected mask on the visible signal. We first use the classic Hogbom CLEAN algorithm to create the masks. For the final cubes, we used multiscale CLEAN with scales [0, 5, 25, 50] pixels (which correspond to scales of [0, 0.27, 1.35, 2.7]$''$ in angular units, approximately [0, 0.7, 3 and 7] times the beam) for the H_2CO emission, and the same for $C^{18}O$ plus 100 pixels, which corresponds to $5.2''$. This significantly reduces the presence of artifacts (or regions of negative emission) due to the presence of extended emission that we cannot fully recover. The final properties of the H_2CO and $C^{18}O$ emission cubes are in Table 3.1.

After imaging, we found that the calibration process over-subtracted continuum emission around the position of the protostar. This effect is small and reduces the baseline of line emission only by 0.5 K on average. To correct for this, we took the median value of each spectrum in channels that do not have emission and subtract this median value to each spectrum. As the median value around the protostar's position is negative, this subtraction raises the values of the spectra.

3.3 Results[1]

3.3.1 Morphology of HC_3N emission

Figure 3.1 shows the integrated intensity of $HC_3N\,(10-9)$ emission. We overplot the contours from the NH_3 condensations and filaments from P15 and S21, data which we further describe in Appendix B.1. $HC_3N\,(8-7)$ emission shows the same morphology, so this description applies to the $(8-7)$ transition as well. The $HC_3N\,(8-7)$ integrated intensity map is shown in Appendix B.5.1. In general, $HC_3N\,(10-9)$ follows the shape of the NH_3 (1,1) filaments, but its emission is more extended than the filaments, with a width of $\sim 40''$. Toward the northeast, the $HC_3N\,(10-9)$ emission continues beyond the edge of Fil-1 with a bright peak ($S/N > 10$) near the edge of the NOEMA map, possibly connecting to the region defined as Clump 1 in S21. We note that, with the exception of the extended emission toward the north, HC_3N emission is not detected in the extended coherent core defined in Pineda et al. (2010). The peak of $HC_3N\,(10-9)$ emission is located toward B5-IRS1, with two dimmer peaks in integrated emission, one centered on Cond-1 and the other at the southern edge of Cond-2.

Figure 3.2 shows the $HC_3N\,(10-9)$ channel maps in approximately 0.2 $\mathrm{km\,s^{-1}}$ steps. These channel maps show that $HC_3N\,(10-9)$ emission consists of two lanes of extended emission, one lane for each filament seen in NH_3 (1,1), and peaks of emission located at the condensations, the protostar and toward the north of Fil-1 in the direction of Clump-1. Emission along the filaments is usually detected within 3 to 4 channels, except at locations such as Cond-1 and the protostar, where emission is present in more than 5 channels.

3.3.2 Morphology of H_2CO line emission

Figure 3.3 shows the H_2CO integrated image from 8 to 12 $\mathrm{km\,s^{-1}}$, and Fig. 3.4 shows channel maps of H_2CO emission in approximately 0.2 $\mathrm{km\,s^{-1}}$ steps. The details of the observed $C^{18}O$ emission morphology are described in Appendix B.3. The integrated image peaks toward the position of B5-IRS1 and shows stronger emission toward the east of the protostar than to the west, immediately hinting at asymmetries in the envelope. In the channel maps it is shown that the asymmetry is due to strong emission surrounding the protostar (within a ~ 500 au diameter) only toward the northeast, showing a curved shaped emission between 9.20 and 9.54 $\mathrm{km\,s^{-1}}$, which then decreases in intensity but expands toward the east in consecutive channels as it reaches the central velocity of the protostar $v_{\mathrm{LSR}} = 10.2$ $\mathrm{km\,s^{-1}}$ (P15). Channels from 9.7 to 10.3 $\mathrm{km\,s^{-1}}$ are affected by negative emission bowls adjacent to the extended emission, due to missing short-spacing data in the uv-plane. In the rest of the channels emission is more compact, and it is well recovered with the ALMA only observations. In higher velocity channels, from 10.45 to 10.95 $\mathrm{km\,s^{-1}}$ in fig. 3.4, there is asymmetric envelope emission toward the west of the protostar that is not evident in the integrated image. These features are evident in the image moments 1

[1]All codes used to obtain the following results can be accessed through Github.

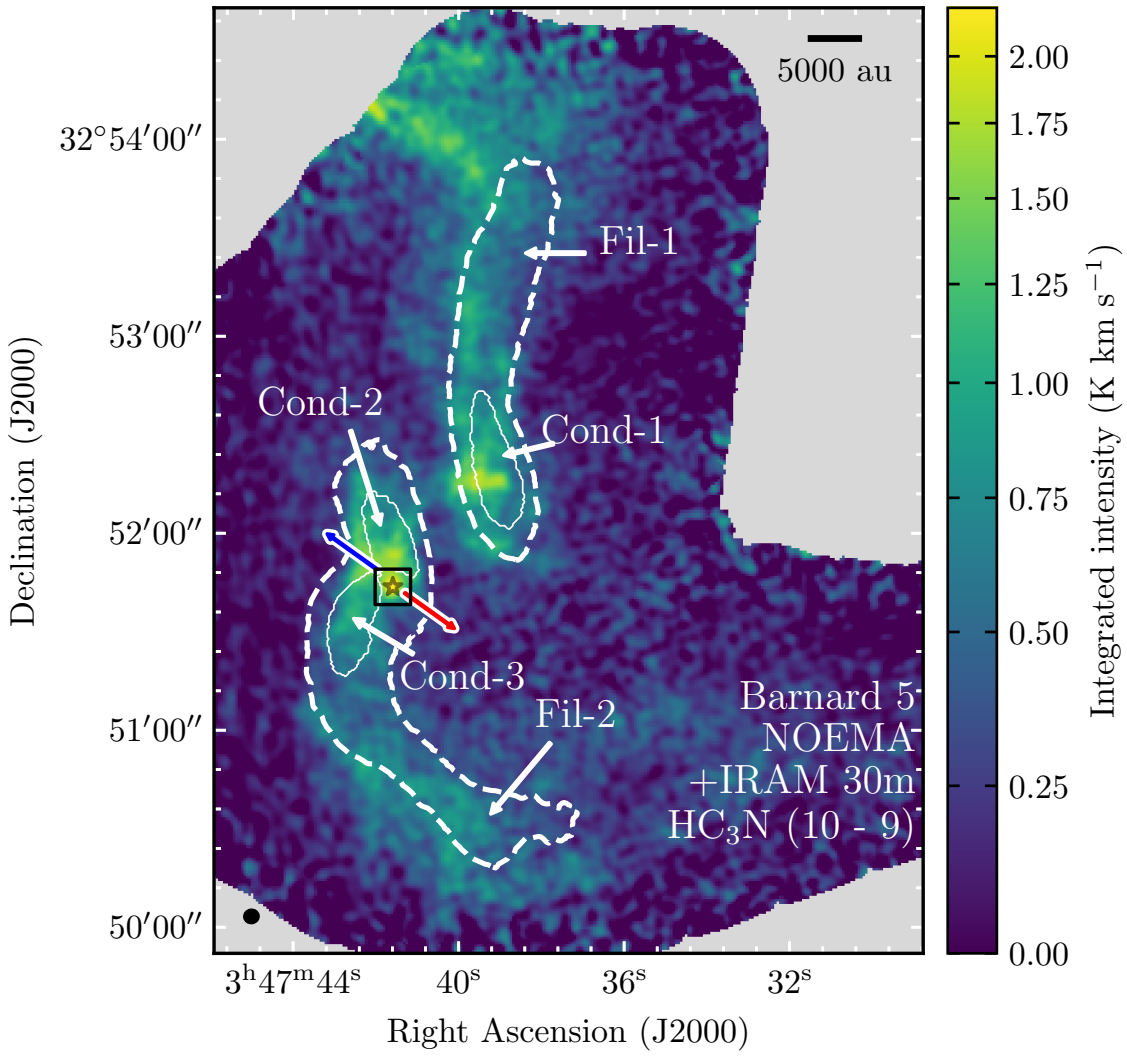

Figure 3.1: Velocity integrated HC_3N $(10-9)$ emission. HC_3N is integrated from 9.2 to 11.2 km s^{-1}. White dashed contours correspond to the filaments identified in NH_3 emission by P15 and S21. White solid contours outline the edges of the condensations labeled as in P15. The gray star marks the position of the protostar B5-IRS1. The black square represents the area observed with ALMA. The blue and red arrows indicate the direction of the blueshifted and redshifted lobes of the outflow in B5-IRS1 (Zapata et al. 2014).

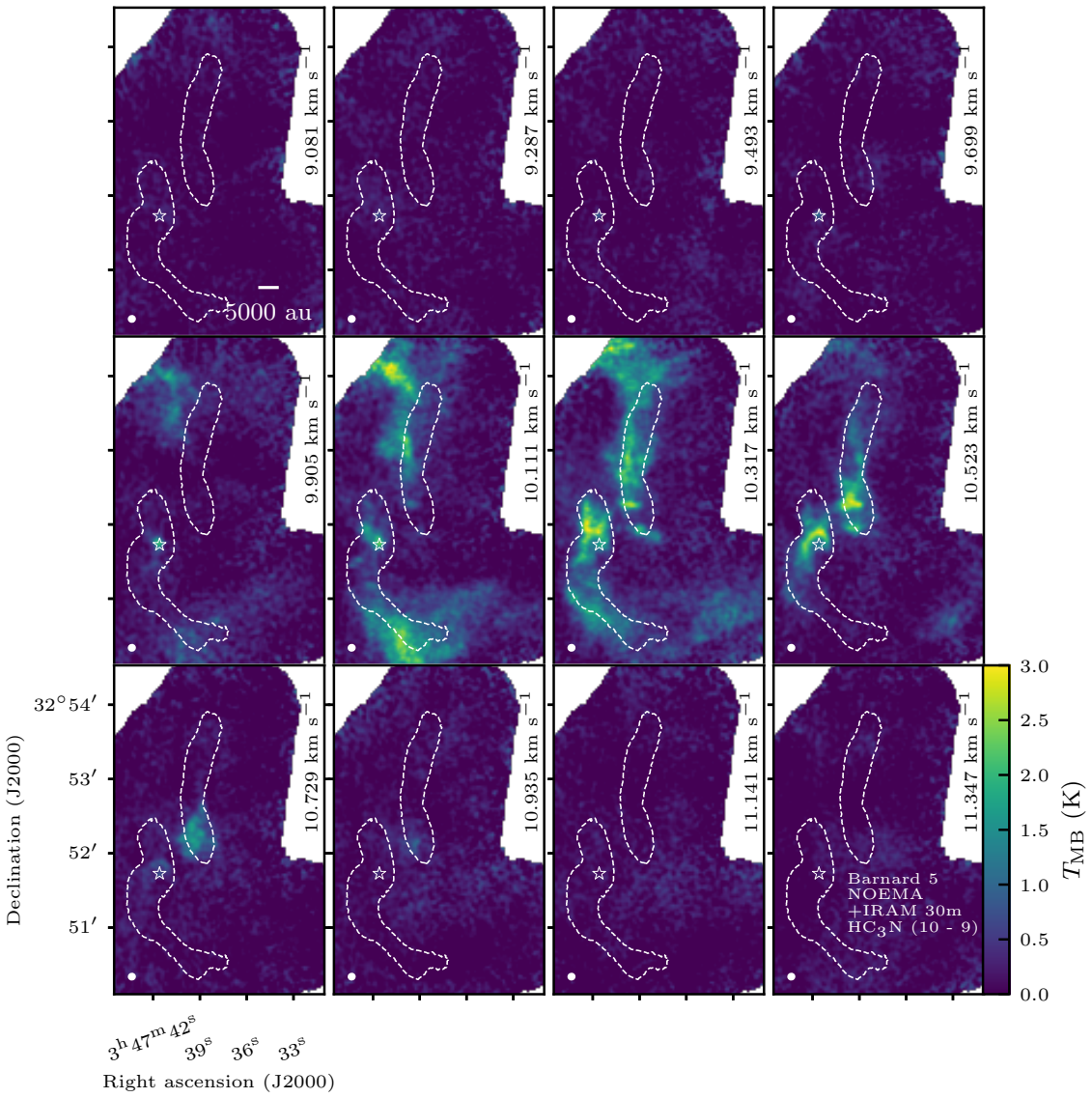

Figure 3.2: Channel maps between 9.081 and 11.347 km s^{-1} for the NOEMA and 30m HC_3N (10 – 9) spectral cube, in 0.206 km s^{-1} steps. The white dashed contours outline the NH_3 filaments defined in P15. The white star represents the location of the protostar, which has a systemic velocity $v_{LSR} = 10.2$ km s^{-1} (P15). The white ellipse at the bottom left corner represents the size of the beam. The white line in the top left channel map is a scalebar representing a length of 5000 au.

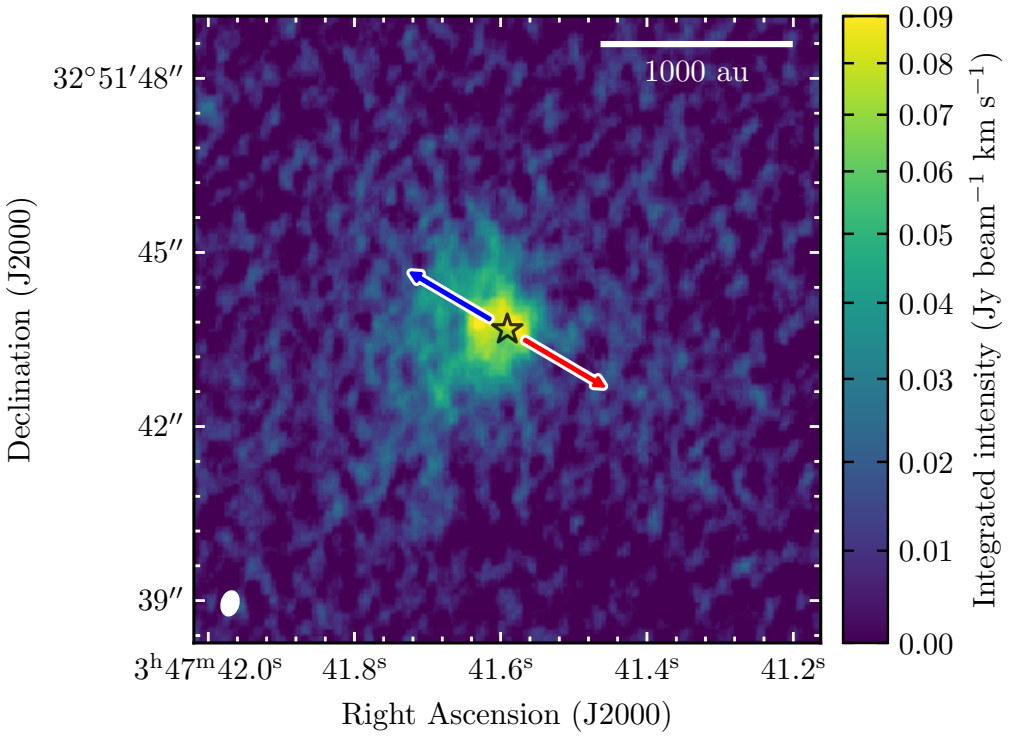

Figure 3.3: Velocity integrated image of H_2CO from 8 to 12 $\mathrm{km\,s^{-1}}$. The black star represents the position of the protostar. The blue and red arrows indicate the directions of the blue and redshifted outflow lobes from Zapata et al. (2014). The scalebar indicates a length of 1000 au. The white ellipse in the bottom left corner represents the beam size. The primary beam of the image is out of the map.

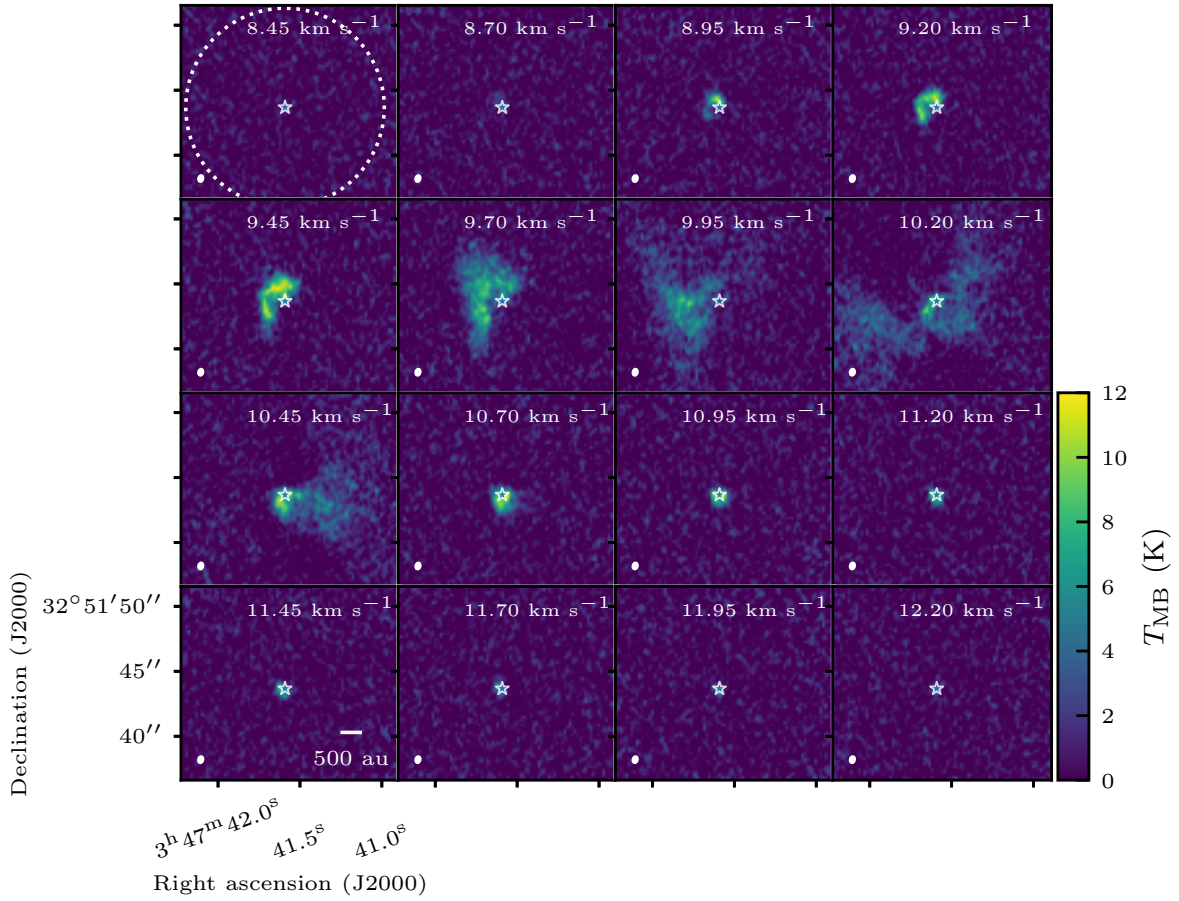

Figure 3.4: Channel maps between 8.45 and 12.2 km s^{-1} for the ALMA H_2CO ($3_{0,3}$ – $2_{0,2}$) spectral cube, in steps of 0.25 km s^{-1}. The white star represents the location of the protostar, which has a systemic velocity v_{LSR} = 10.2 km s^{-1} (P15). The white dotted circle marks the extent of the primary beam. The white ellipse at the bottom left corners represents the beam size. The scalebar in the bottom left panel shows a 500 au length in the map.

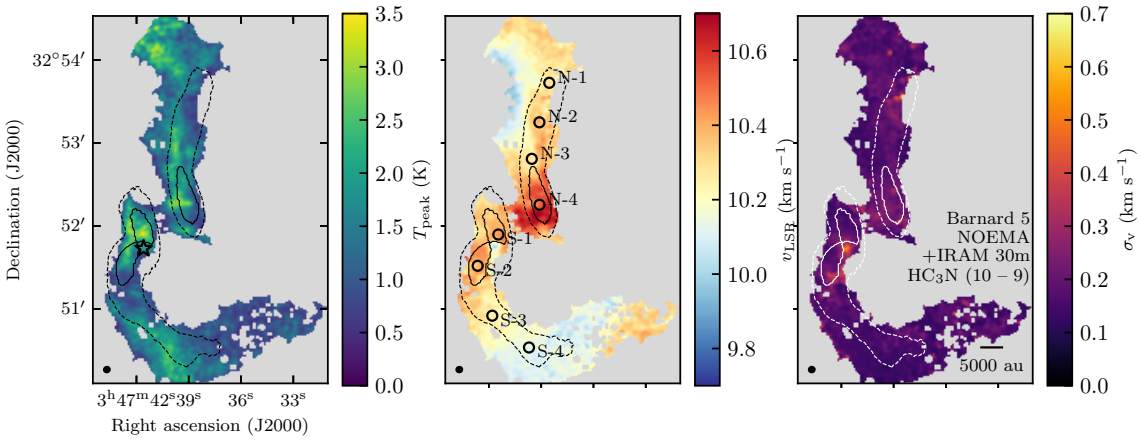

Figure 3.5: Peak intensity, central velocity, and velocity dispersion resulting from the Gaussian fit to the $HC_3N\,(10-9)$ spectra. Black and white dashed contours represent the edges of the filaments as defined in P15 and S21. The black and white solid contours mark the condensations as defined in P15. The black star marks the position of B5-IRS1. Black labeled circles indicate the position of the sampled spectra in Fig. 3.6. The black ellipse represents the beam size.

and 2, which are shown in Appendix B.2. The peak of velocity dispersion is offset from the protostar to the east, where two sections with different velocities are joined. Also, there is an increase in velocity dispersion toward the southeast of the protostar, where emission is primarilly blueshifted. The moment maps and channel maps reveal that H_2CO emission shows complex structure both spatially and spectrally.

3.3.3 HC_3N (10 – 9) line fitting

We fit one Gaussian profile to the $HC_3N\,(10-9)$ line emission using the Python package `pyspeckit` (Ginsburg & Mirocha 2011; Ginsburg et al. 2022). We describe our procedure in detail in Appendix B.4. In summary, we fit one Gaussian to all spectra with $S/N > 5$ using moment maps to estimate the initial parameters, and then attempt the fit again using the results as initial guesses. The best fit parameters of each spectrum are shown in Fig. 3.5. We select four locations within each filament, labeled N-1 to N-4 and S-1 to S-4 for Fil-1 and Fil-2, respectively, to show their spectra in Fig. 3.6. The spectra are taken from a single pixel, which has a size of $(0.6'')^2$. Almost all spectra with $S/N > 5$ are well fit using only one Gaussian, as seen in Fig. 3.6, with the exception of spectra located within a beam of the protostar's position, which we explore further.

At the position of B5-IRS1, there are several spectra within a radius of $\sim 4''$ where it is possible to fit a second component to the $HC_3N\,(10-9)$ emission that has a lower velocity than its surroundings. We describe this second fit in more detail in Appendix B.4.1. Previous works have been able to detect two and even three Gaussian components in NH_3 emission (Choudhury et al. submitted, Chen et al. 2022), so it is expected that

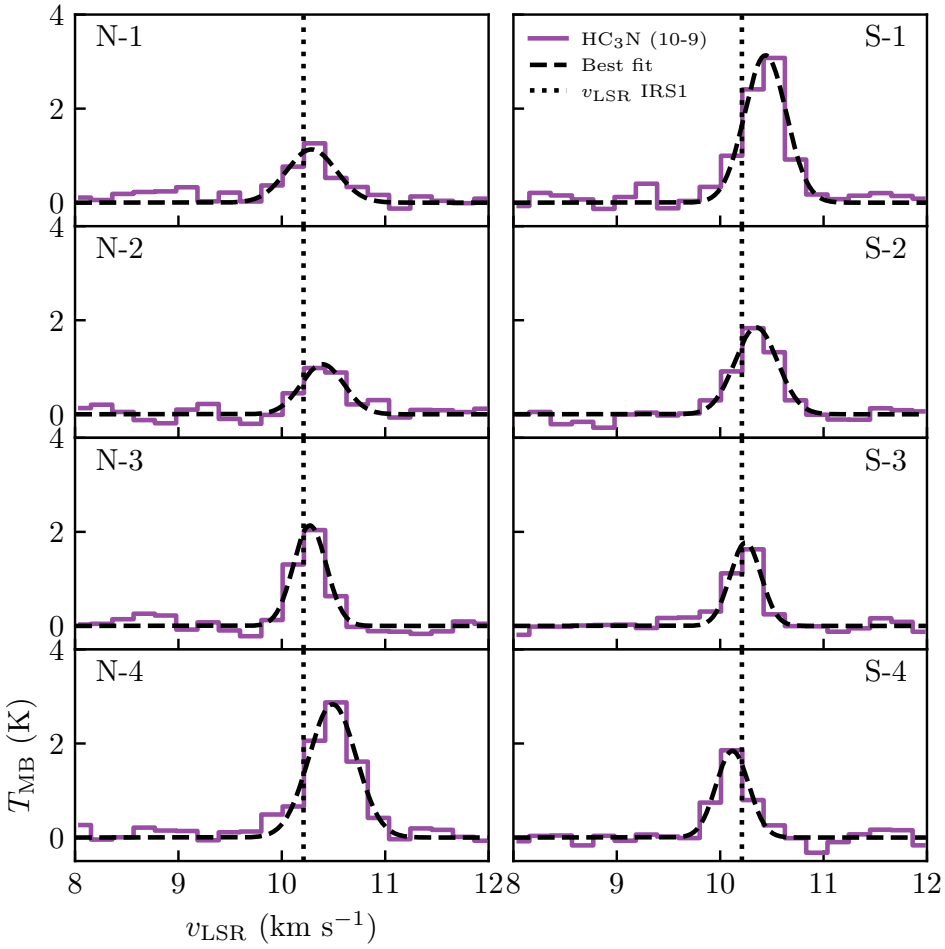

Figure 3.6: $HC_3N\,(10-9)$ spectra at selected locations within both filaments, ordered in position from north to south. Fil-1 spectra, labeled N-X, are on the left column and Fil-2 spectra, labeled S-X, are on the right. Purple lines show the spectra, whereas black curves show the best fit Gaussian curve for each.

$HC_3N\,(10-9)$ can trace more than one component as well. We describe how we evaluated this second fit in Appendix B.4. According to our criteria, there are not enough spectra with a good enough two Gaussian fit to justify keeping it in our analysis. To separate the gas emission into more components in this region, we require observations with higher spectral resolution, as the Gaussians are covered by 3 or 4 channels only in most cases (Fig. 3.6), which is not enough to fit two Gaussians with certainty. Therefore, we stay with the one Gaussian fit for all regions for further analysis.

The central velocities $v_{\rm LSR}$ of each spectrum, shown in Fig. 3.5 center, range from 9.8 to 10.7 $\mathrm{km\,s^{-1}}$. The uncertainties in $v_{\rm LSR}$ are 0.025 $\mathrm{km\,s^{-1}}$ on average, ranging from 0.01 $\mathrm{km\,s^{-1}}$ at the center of the filaments and condensations, and increasing to approximately 0.05 $\mathrm{km\,s^{-1}}$ toward the edges of the filaments, where the $S/N \approx 5$. The $v_{\rm LSR}$ map shows filament-scale gradients both parallel to the direction of the filaments and perpendicular to them. The central velocity within Fil-1 shows a velocity gradient parallel to the filament length of approximately 0.4 $\mathrm{km\,s^{-1}}$, starting from 10.3 $\mathrm{km\,s^{-1}}$ at the northern tip of Fil-1 and ending toward Cond-1 with 10.7 $\mathrm{km\,s^{-1}}$. Perpendicular to this filament, there is a gradient from lower to higher $v_{\rm LSR}$ from east to west, starting from 10.0 $\mathrm{km\,s^{-1}}$ outside of the filament defined in NH_3 and reaching 10.4 $\mathrm{km\,s^{-1}}$ on the opposite side. The gas within Fil-2 contour also shows a parallel velocity gradient, from 10.1 $\mathrm{km\,s^{-1}}$ in the south tip to 10.4 $\mathrm{km\,s^{-1}}$ in the north, reaching its maximum velocity within Cond-2 and 3. There is also a perpendicular gradient that is not apparent at first sight because it is smaller than the one present in its northern counterpart. The largest observed difference between the edges of Fil-2 is at the southern edge of Cond-3, where the $v_{\rm LSR}$ goes from 10.4 $\mathrm{km\,s^{-1}}$ in the east to 10.2 $\mathrm{km\,s^{-1}}$ in the west. The $HC_3N\,(10-9)$ velocity gradients are produced by two continuous bodies of extended emission, one spatially correlated to Fil-1 and another to Fil-2, as seen in the channel maps (Fig. 3.2), and not from two or more spatially separated components in each filament.

Within a beam of the protostar there is a decrease in velocities with respect to its surroundings. At Cond-2 and 3, the velocity is around 10.4 $\mathrm{km\,s^{-1}}$, whereas around B5-IRS1, the velocity drops down to 10.0 $\mathrm{km\,s^{-1}}$. This sudden blueshift is partially due to the second component suggested at that location. However, the main peak at the location of the protostar is still blueshifted with respect to B5-IRS1 $v_{\rm LSR}$ (Fig. B.5).

The $HC_3N\,(10-9)$ velocity dispersion stays rather constant along both filaments, varying within beam areas randomly between 0.12 and 0.2 $\mathrm{km\,s^{-1}}$, except at the position of the protostar, where it increases suddenly to 0.5 $\mathrm{km\,s^{-1}}$, and toward the south of Cond-3, where the dispersion increases to ~ 0.33 $\mathrm{km\,s^{-1}}$. This is the reason why the peak of integrated emission (Fig. 3.1) is at the protostar's location but the peak in the $T_{\rm peak}$ map (Fig. 3.5 left) is located inside of Cond-2. The protostar might produce the higher velocity dispersion around it, including toward Cond-3. Assuming the gas temperature in this region is 9.7 K (obtained from Pineda et al. 2021), the sound speed is $c_{\rm s} = 0.18$ $\mathrm{km\,s^{-1}}$, so for the most part, the obtained velocity dispersion indicates the gas speed is mostly subsonic.

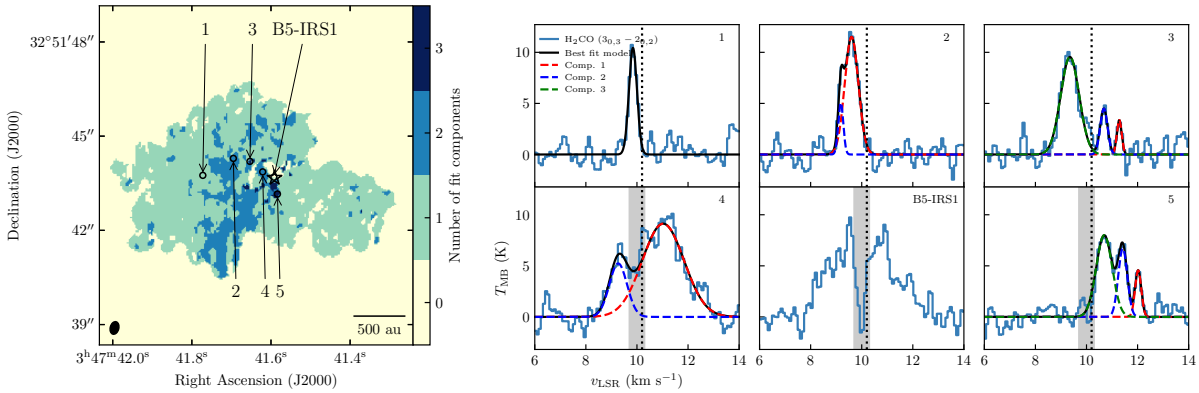

Figure 3.7: Results of the Gaussian fit to the ALMA H_2CO spectra. **Left:** Number of components that best fit each H_2CO spectrum according to the criteria described in Appendix B.4. The black ellipse in the bottom left corner represents the beam size. The black star marks the position of the protostar. Locations of sampled spectra are marked with empty black circles and labeled. **Right:** Selected H_2CO spectra with the best fit Gaussian components. The spectra are taken from one single pixel. The data are plotted with a solid blue line. The dashed lines represent the best fit Gaussians, with red for the first component, blue for the second and green for the third. The black solid line represents the sum of all components. The gray vertical area marks the channels that were masked for the fit for spectra located within 0.8″ from the protostar. The dotted black vertical line marks the protostar's $v_{\rm LSR}$.

3.3.4 H_2CO multicomponent line fitting

Figure 3.7 shows a sample of spectra from the ALMA H_2CO emission cube, with increasing numbers representing decreasing distance to the protostar. The spectra are taken from a single pixel, which has an area of $(0.003'')^2$. The spectra show that close to and at the location of B5-IRS1, H_2CO emission has more than one velocity component along the line-of-sight. This component multiplicity explains the sudden increase of velocity dispersion shown in the moment 2 map (Fig. B.2 right).

We fit one, two, and three Gaussians to the H_2CO line emission for each spectrum inside a mask created using all pixels with $S/N > 5$. The details of the procedure, including the mask creation and the criteria to determine the number of components along each line of sight, are detailed in Appendix B.4. The general procedure is similar to the Gaussian fit in Sect. 3.3.3, but takes into account the possible effects of missing short- and zero-spacings in our interferometric data by masking the spectra between 9.7 and 10.3 $\mathrm{km\,s^{-1}}$ for pixels within a radius of 0.8″ from the protostar. An observation of these central spectra determines that these are the most affected by missing short-spacing data.

The number of Gaussian components that best fit the spectra are shown in Fig. 3.7 left and we show spectra with their corresponding best fits in Fig. 3.7 right. Most of the spectra are best fit using only one Gaussian, but closer to the protostar and toward the

south, there are spectra that are better fit with 2 and 3 Gaussians. There are very few spectra that are best fit with 3 Gaussians, and most of these are located in the region where we mask the central velocity channels (between 9.7 and 10.3 $\mathrm{km\,s^{-1}}$) for the fit. Our criteria determined that in 0.1% of the spectra, located at a distance < 500 au from the protostar, the best model has a probability lower than 95% of representing a considerable improvement in comparison to the other models. In paritcular, at the position of the protostar, the spectrum shows two peaks with a dip at the $v_{\rm LSR}$ of the protostar. This dip is most probably caused by the missing short-spacing information, as it is located right on the channels that are masked. At this location, the Gaussian fits showed very large uncertainties for its parameters (more than 50%), and therefore the spectra within one beam of the protostar are left unfit.

3.4 Analysis

3.4.1 Gas flow from Barnard 5 dense core to the filaments

3.4.1.1 Comparison between core HC_3N and NH_3 velocities

We compared the $HC_3N\,(10-9)$ central velocities $v_{\rm LSR}$ with the $NH_3\,(1,1)$ $v_{\rm LSR}$ found in P15 (shown in Fig. B.1) to observe the relative motions of the chemically fresh gas with respect to the filaments. According to chemical models of cold, dark molecular clouds, NH_3 and other nitrogen-bearing molecules are regarded as a "late-type" molecule, tracing advanced stages of gravitational core collapse, whereas HC_3N and the cyanopolyyne ($HC_{2n+1}N$) molecule family trace chemically fresh gas (i.e., unprocessed by core collapse processes, Herbst & Leung 1989; Bergin & Tafalla 2007; Aikawa et al. 2001). We subtracted the NH_3 $v_{\rm LSR}$ from the $HC_3N\,(10-9)$ $v_{\rm LSR}$, obtaining $\delta v_{\rm LSR} = v_{\rm LSR,HC_3N} - v_{\rm LSR,NH_3}$. For this, we first convolved the $HC_3N\,(10-9)$ $v_{\rm LSR}$ (Fig. 3.5 Center) to the spatial resolution of the $NH_3\,(1,1)$ data (Table 3.1), using the `photutils` routine `create_matching_kernel` to obtain the matching kernel between the image beams and the `astropy.convolution` function `convolve` to smooth the map. Afterwards, we reprojected the spatial grid of the $NH_3\,(1,1)$ central velocities image to the $HC_3N\,(10-9)$ spatial grid, using the `reproject_exact` routine from the `reproject` python package. We regridded the NH_3 map to the $HC_3N\,(10-9)$ map grid because the pixel size of the NH_3 map is about 1.5 times smaller than the $HC_3N\,(10-9)$ image pixel size. Finally, we subtracted the $v_{\rm LSR}$ of NH_3 from the $HC_3N\,(10-9)$ $v_{\rm LSR}$.

Figure 3.8 left shows the resulting $\delta v_{\rm LSR}$ in the image plane. The map shows that $HC_3N\,(10-9)$ is consistently redshifted with respect to NH_3 except for a few locations, mostly without systematic variations within the NH_3 filament regions. The median value of $\delta v_{\rm LSR}$ is $0.08^{+0.06}_{-0.05}$ $\mathrm{km\,s^{-1}}$. This difference is more than 3 times larger than the average uncertainty for $\delta v_{\rm LSR}$, which is dominated by the uncertainty of the $HC_3N\,(10-9)$ $v_{\rm LSR}$ (Sect. 3.3.3). Toward the southern tip of Cond-1, $HC_3N\,(10-9)$ $v_{\rm LSR}$ is larger than $NH_3\,(1,1)$ $v_{\rm LSR}$ by ≈ 0.28 $\mathrm{km\,s^{-1}}$, but the rest of the spectra are consistent with the median value. Figure 3.8 Right shows the $HC_3N\,(10-9)$ central velocities versus the respective

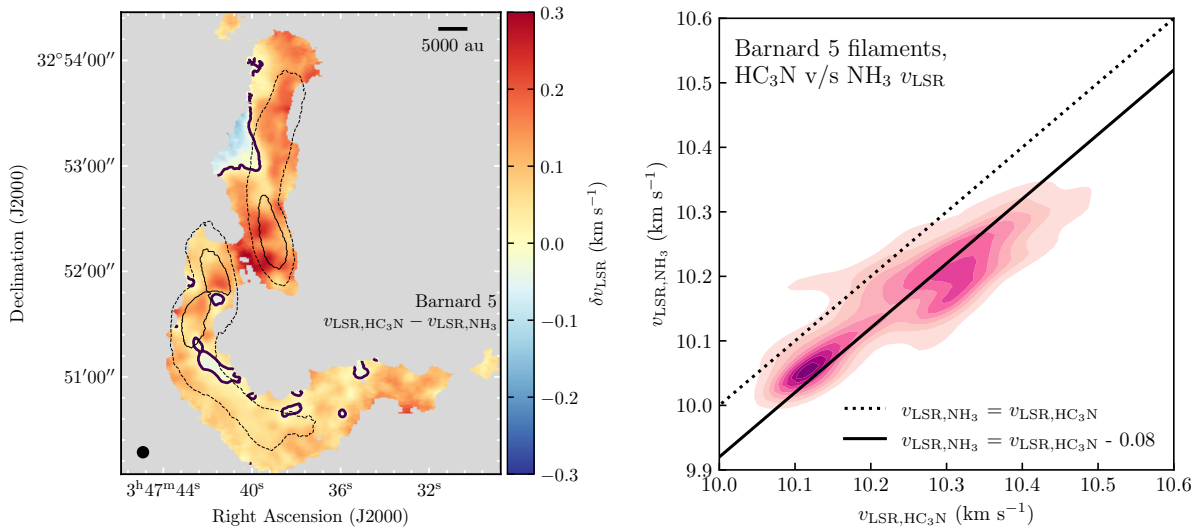

Figure 3.8: Difference between $HC_3N\,(10-9)$ line emission and NH_3 (1,1) line emission central velocities in both filaments of Barnard 5. Left: Spatial map showing the difference of $HC_3N\,(10-9)$ central velocities with respect to NH_3 (1,1) velocities. Black thick contours mark the positions where the difference is 0. The resolution of the $HC_3N\,(10-9)$ data is on the lower left corner. The dotted contours show the filaments and the black solid contours outline the condensations as defined in P15 and S21. Right: v_{LSR,HC_3N} versus v_{LSR,NH_3} Distribution of the velocity difference shown using its KDE. The dashed vertical line represents the 1:1 line, and the solid line is shifted by -0.08, which is the median value of the difference between both velocities.

NH_3 v_{LSR} at the same location, estimated using a two-dimensional Gaussian Kernel Density Estimate (KDE) obtained with the `scipy.stats` python package `gaussian_kde` function (Virtanen et al. 2020) assuming all pixels have the same weight. The KDE shows there is an approximately linear relation between both v_{LSR} with a shift of -0.08 km s^{-1}. This comparison shows that $HC_3N\,(10-9)$ follows a different kinematic component of the gas in Barnard 5 than NH_3.

There are a few locations where $HC_3N\,(10-9)$ emission is blueshifted with respect to $NH_3\,(1,1)$ emission. At the right of Fil-1, δv_{LSR} drops down to ≈ -0.1 km s^{-1}. Also, just below Cond-3 in Fil-2, there is a region where δv_{LSR} also reaches ≈ -0.1. The blueshifted emission at these positions, which are elongated along the filaments, suggest there is a perpendicular velocity gradient of HC_3N with respect to NH_3. In particular, there is a sudden shift from positive to negative δv_{LSR} at the location of the protostar, reaching down to $\delta v_{LSR} \approx -0.06$km s^{-1}. The area of the reversal is approximately the $NH_3\,(1,1)$ beam size. Comparing the $HC_3N\,(10-9)$ fit with the $NH_3\,(1,1)$ fit (Fig. B.1) shows that both molecules present a sudden decrease in v_{LSR} at that location, but the difference between v_{LSR} in this position and its surroundings is larger for $HC_3N\,(10-9)$ than for NH_3.

3.4.1.2 HC_3N velocity gradients

In Fig. 3.5 center, there is a velocity gradient perpendicular to Fil-1 observed in $HC_3N\,(10-9)$ central velocities. The perpendicular gradient in Fil-2 is overshadowed by a strong gradient running parallel to the filament length. We calculated the velocity gradients ∇v_{LSR} present in the map to determine the direction of gas flow at the positions where the condensations and the protostar are and to determine if there are gradients perpendicular to Fil-2 that are hidden by an analysis by eye. We employed the same procedure used to calculate velocity gradients in Barnard 5 $NH_3\,(1,1)$ emission by Chen et al. (2022), which is described in detail in Chen et al. (2020c). In summary, we calculated the gradient pixel-by-pixel by fitting a plane centered around the pixel, using a square aperture with a width of 2 beams ($\approx 8''$ width), to ensure the capture of velocity gradients across non-correlated regions. We only fit pixels which have a number of neighboring pixels equivalent to one third of the aperture area available to ensure the quality of the fit.

Figure 3.9 shows the resulting $HC_3N\,(10-9)$ ∇v_{LSR} visualized using line integral convolution (LIC, Cabral & Leedom 1993) textures over the absolute magnitude of the gradient $|\nabla v_{LSR}|$. We used the `LicPy` package[2] (Rufat 2017) to generate a texture that represents the directions of the gradients, and then overlaid the resulting texture. The uncertainty in $|\nabla v_{LSR}|$ is between 0.3 and 1 km s^{-1} pc^{-1} and increases toward the edges of the $HC_3N\,(10-9)$ emitting region. We focus our discussion on a qualitative description of the resulting ∇v_{LSR} map.

The vector field is well ordered within the brightest HC_3N emissions, in particular, in and around the condensations and filaments defined by NH_3 contours and toward the bright emission toward the north of the map (which connects with Clump-1 from S21). Figure

[2]https://github.com/drufat/licpy

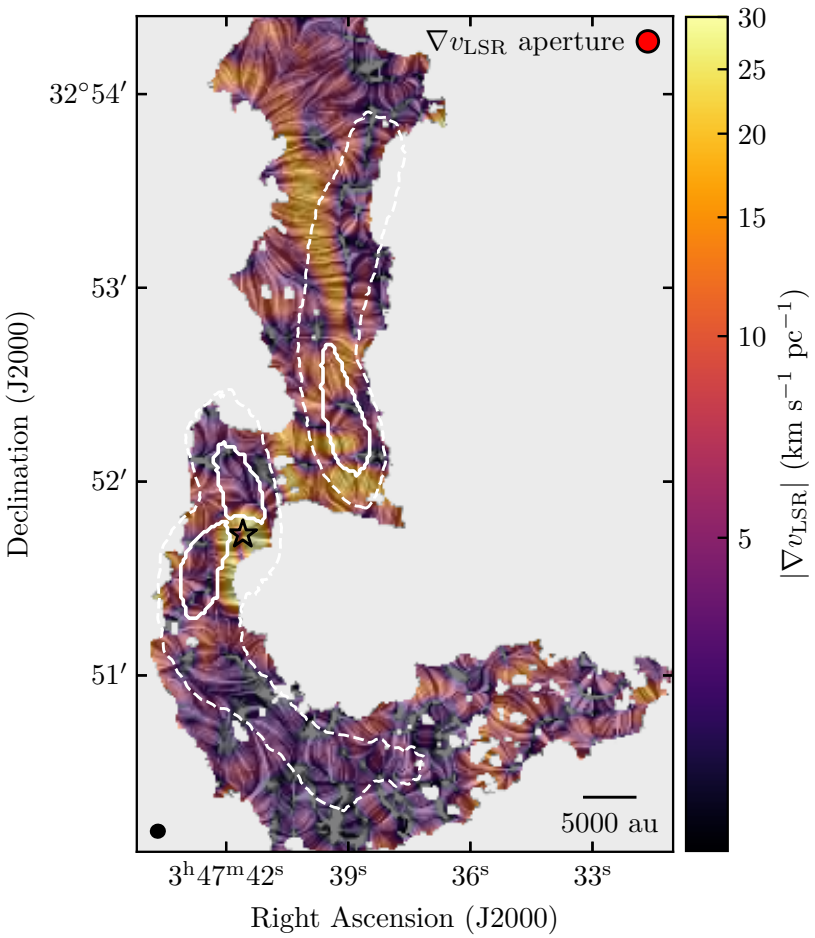

Figure 3.9: Velocity gradient intensities $|\nabla v_{\rm LSR}|$ calculated from the Gaussian fit to HC_3N $(10-9)$ emission, with the gradient directions visualized as an overplotted texture using line integral convolution (LIC, Cabral & Leedom 1993). The black star indicates the position of B5-IRS1. The black ellipse in the bottom left corner represents the beam size. The red circle at the top right corner represents the area used to calculate the gradients. White dashed contours outline the NH_3 filaments (P15; S21). White solid contours outline the edges of the condensations (P15). The scalebar at the bottom right corner represents a physical distance of 5000 au.

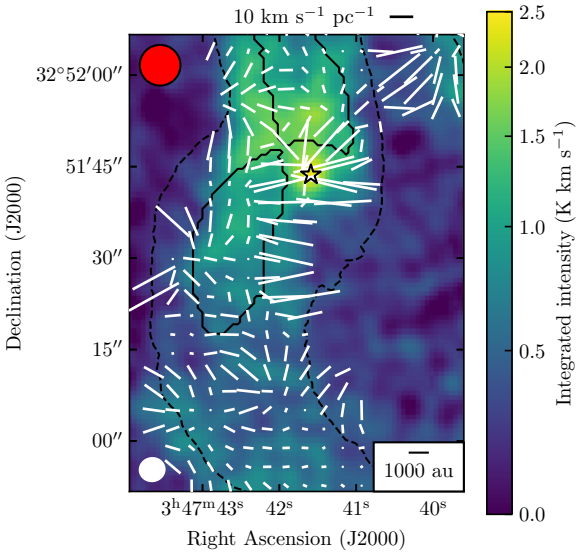

Figure 3.10: Zoom of the integrated intensity map toward Cond-2, -3 and the protostar, with the $\nabla v_{\rm LSR}$ vector orientations from Fig. 3.9 shown with white lines. The black line at the top represents a gradient magnitude of 10 km s^{-1} pc^{-1}. The black star indicates the position of B5-IRS1. The white ellipse in the bottom left corner represents the beam size. Black dashed contours outline the NH_3 filaments (P15; S21). Black solid contours outline the edges of the condensations (P15). The red circle at the top left corner represents the area used to calculate the gradients. The scale bar at the bottom right marks a length of 1000 au.

3.9 reveals that gas in and around both filaments have both parallel and perpendicular gradients.

The $\nabla v_{\rm LSR}$ field reveals the flow of gas toward the condensations. Within the contours of Fil-1, the perpendicular gradients are toward the edges of HC_3N emission with $|\nabla v_{\rm LSR}| \approx 12 - 15$ km s^{-1} pc^{-1}). The vector field reveals a strong ($|\nabla v_{\rm LSR}| \approx 20$ km s^{-1} pc^{-1}) parallel gradient of ~ 8000 au in length above Cond-1. The vector field is particularly well ordered at the north of Fil-1, where there is HC_3N emission which could possibly connect to Clump-1 toward the north. Cond-1 is surrounded by flows with magnitudes between 25 and 30 km s^{-1} pc^{-1}. that point toward its center, but at the center of the condensation the flow stagnates (i.e., drops to 0 km s^{-1} pc^{-1}). This indicates HC_3N moves inward to Cond-1 from all directions.

The $\nabla v_{\rm LSR}$ calculation also reveals the parallel flow of gas in Fil-2 that was not evident by eye. Toward the south of Cond-3, most of Fil-2 shows perpendicular gradients with $|\nabla v_{\rm LSR}|$ between 3 and 10 km s^{-1} pc^{-1}, much lower than the perpendicular gradients at Fil-1. The western edge of Cond-3 presents the strongest velocity gradient of the map ($\nabla v_{\rm LSR} \approx 40$ km s^{-1} pc^{-1}) and its direction is parallel to the filament. Both condensations (Cond-2 and -3) show stagnating flows within them. This indicates that gas flows from the outside in, as in the case of Cond-1. Most notably, a zoom into the condensations within

Fil-2, shown in Fig. 3.10, reveals that the gradient direction curves toward the protostar and the parallel gradient ends there as well. This plot suggests that fresh gas, traced by HC_3N, flows toward the protostar, and the large-scale flow along the filament is hence shared by the protostar, Cond-2 and Cond-3.

3.4.1.3 Mass inflow from Barnard 5 dense core to the filaments

We estimated the mass transport and the infall rate from the flows traced by HC_3N emission. In Choudhury et al. (submitted), they estimate an infall rate $\dot{m}$ for Fil-1 of 1.1×10^{-4} $M_\odot$ yr^{-1} and for Fil-2 of 1.8×10^{-4} $M_\odot$ yr^{-1}. We used the same geometry for both filaments and their Eq. 8 to estimate $\dot{m}$:

$$\dot{m} = S\rho v_{\rm inf}, \tag{3.1}$$

where S is the surface area where infall occurs, ρ is the total mass volume density within the surface area and $v_{\rm inf}$ is the estimated infall velocity.

We obtained $\rho = n(H_2)\mu m_{\rm H}$ by using the line ratio between HC_3N $(10-9)$ and $(8-7)$ molecular transitions. This procedure is described in detail in Appendix B.5. In summary, we obtained a number density $n(H_2) \approx 10^5$ cm^{-3} based on the non-LTE radiative transfer code RADEX (van der Tak et al. 2007). The mean difference in velocity, which is defined as half the difference in $v_{\rm LSR}$ across a filament, is $v_{\rm inf} = 0.2$ km s^{-1} for Fil-1 (the same as the one observed in Choudhury et al. submitted) and 0.1 km s^{-1} for Fil-2 (Sect. 3.3.3). The resulting mass infall rate is $\dot{m} = 4.3\times10^{-5}$ $M_\odot$ yr^{-1} in Fil-1 and $\dot{m} = 3.5\times10^{-5}$ $M_\odot$ yr^{-1} for Fil-2, about 3 times lower than the Fil-1 infall rate found in Choudhury et al. (submitted). The difference is due to the obtained $n(H_2)$ in both works. We estimated $n(H_2)$ using our observed HC_3N transitions (Appendix B.5). On the other hand, Choudhury et al. (submitted) used the filament masses from S21, which in turn were calculated by comparing Barnard 5's NH_3 emission and the JCMT 0.45 mm emission.

3.4.2 Infall from envelope to disk scales

3.4.2.1 Clustering of physically related structures in H_2CO

We separated the different Gaussian components found in H_2CO in Sect. 3.3.4 into clusters, which helps to interpret the kinematic properties of the B5-IRS1 envelope. It is challenging to do this separation by eye, especially where there are two components in the same line of sight that can belong to two different components indistinguishably. For example, in the boundary between blueshifted and redshifted sides of the H_2CO emission, toward the south and east of the protostar, there are two Gaussian components with velocities blueshifted with respect to the protostar's $v_{\rm LSR}$ (see Fig. 3.7 Left). Also, the locations where there are three Gaussian components are small and sparse, as well as spectra at the east and west edges of the H_2CO emission. It is possible that the additional fitted components are either noise or extended emission that is not fully sampled due to missing short- and zero-spacing observations. We describe our procedure in Appendix B.6, where we also show the resulting clusters in Fig. B.9. In summary, we employed the density-based

spatial clustering of applications with noise (DBSCAN) algorithm to separate the different physical components in position-position-velocity space.

The two largest clusters returned by DBSCAN (Groups 0 and 1 from Fig. B.9) contain about 90% of the points not categorized as noise. The largest cluster is a group of points that are all blueshifted with respect to the protostar's $v_{\rm LSR}$ (10.2 km s^{-1}), and the second largest, a fully redshifted group. We refer to these two groups as blueshifted and redshifted clusters throughout the rest of this work. More details about these two clusters are in Appendix B.6. The central velocities of the Gaussian fits belonging to each of these clusters are shown in Fig. 3.11. The blueshifted cluster has a velocity gradient toward lower (more blueshifted) velocities as it gets closer to the protostar. This gradient is stronger for higher declinations. The redshifted cluster has an increase in velocity when it gets closer to the protostar.

The remaining three clusters represent $\approx 10\%$ of the points not considered noise. The clustering algorithm is able to assign one of the two blueshifted Gaussian components toward the south of the protostar (Fig. 3.7) to the blueshifted cluster and leave the other as another group (Group 3 from Fig. B.9). This allows us to observe the velocity gradient more clearly. The main difference between the largest clusters and groups 4 and 5 is these two last groups show highly blueshifted and redshifted $v_{\rm LSR}$ very close to the protostar, representing a jump in the velocity gradient of groups 0 and 1. Group 3 has a central velocity of 10.8 km s^{-1} and group 4, of 9.2 km s^{-1}. Groups 3, 4, and 5, as well as possibly part of the points categorized as noise, could be emission coming from other mechanisms observed in H_2CO, such as inner gas disk rotation or a more extended envelope, that due to the resolution or the missing short-spacing data cannot be fully observed. Group 3, for example, shows a central velocity redshifted with respect to the protostar at the same position as the redshifted high-velocity $C^{18}O$ emission, described in Appendix B.4. We suggest the high-velocity $C^{18}O$ and H_2CO emission components trace the protostellar disk kinematics. Another possibility is that within 500 au from the protostar H_2CO gas is optically thick, which would cause self-absorbed emission that is being fitted as separate velocity components and then categorized as the purple and orange groups (labeled as 3 and 4, respectively) by the algorithm.

3.4.2.2 Streamline model of the H_2CO clusters

The two main clusters found by DBSCAN each have a gradient where velocity (with respect to the protostar) increases as distance decreases, similar to streamers confirmed kinematically toward other protostars, for example Per-emb-2 (Pineda et al. 2020) and Per-emb-50 (Valdivia-Mena et al. 2022). We determined if the kinematics of the blueshifted and redshifted components are consistent with streamers infalling toward the protostellar disk of B5-IRS1.

First, we checked if H_2CO emission is tracing or is affected by the outflow. In some protostellar sources, H_2CO traces the outflow or the extremely high-velocity jet (Tychoniec et al. 2021). The position of the blueshifted component is at the east of the protostar, in the same side as the blueshifted outflow cone, and the redshifted component and outflow

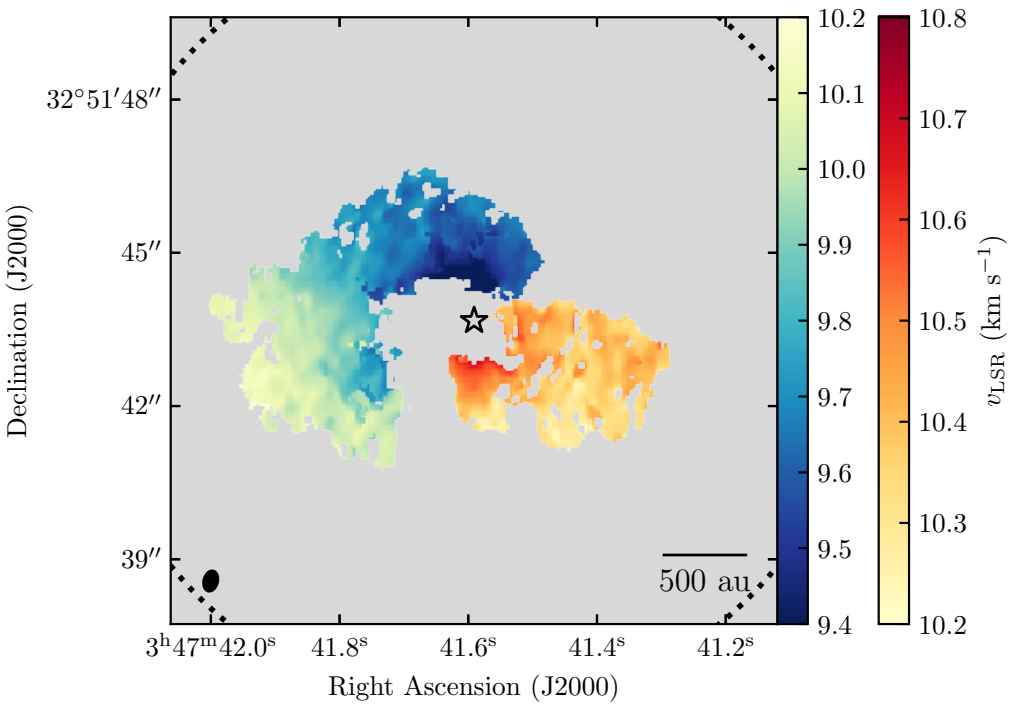

Figure 3.11: Central velocities for the blueshifted and redshifted clusters found using the methods described in Appendix B.6. The colorbar from yellow to blue corresponds to the velocities for blueshifted cluster, whereas from yellow to red corresponds to the redshifted cluster. The black ellipse in the bottom left corner represents the beam size. The black star represents the position of the protostar. The black dashed circle (only seen at the corners) represents the size of the primary beam. We note that the velocity ranges for both envelope components are not symmetric.

cone are both toward the west (Fig. 3.3). However, the velocity gradients of the blueshifted and redshifted components are opposite to the gradient expected for an outflow. For the blueshifted component, $v_{\rm LSR}$ goes from 10.1 km s^{-1} at a distance of about 1000 au to 9.2 km s^{-1} at approximately 200 au from the protostar. This means that it is accelerating toward more blueshifted velocities with respect to the protostar's $v_{\rm LSR}$ (10.2 km s^{-1}) as distance decreases. For the redshifted component, $v_{\rm LSR}$ is approximately 10.3 km s^{-1} at about 1000 au and accelerates to 10.6 km s^{-1} at a distance of 300 au, which also represents an acceleration with respect to the protostar' $v_{\rm LSR}$ with decreasing distance. For an outflow, the velocity with respect to the protostar increases with distance, opposite to the behavior of $v_{\rm LSR}$ shown by both components. Therefore, the motion observed in these H_2CO components is not consistent with outflow motion.

Second, we checked the velocity dispersion $\sigma_{\rm v,fit}$ of the Gaussians in the blueshifted and redshifted clusters and compare them to the thermal sound speed. Nonthermal velocity dispersion larger than the sound speed can indicate that the motion traced by H_2CO is not simple envelope infall, but can be affected by turbulence and shocks produced by the outflow in the same line of sight. We describe the procedure and the resulting nonthermal velocity dispersion of the blueshifted and redshifted clusters in Appendix B.6.1. The velocity dispersion is subsonic for the majority of the emission in both components, but it becomes trans-sonic for emission within $r < 600$ au from the protostar. This suggests that within this radius, H_2CO gas is possibly affected by the outflow. Additionally, there is a larger density of trans-sonic emission for the redshifted component. This is due to the smaller area covered by this component and the fact that it is mostly contained in the observed direction of the outflow cone. The H_2CO gas contained in this cluster is therefore contaminated by outflow emission. For this reason, we leave the redshifted component as a streamer candidate and do not do further analysis on it in this work.

We modeled the kinematics of the blueshifted cluster observed with H_2CO emission to confirm that the velocity gradient observed in Fig. 3.11 is consistent with streamer motion, using the analytic solution for material falling from a rotating, finite-sized cloud toward a central object, dominated by the gravitational force of the latter. We used the analytic solutions of Mendoza et al. (2009), previously used by Pineda et al. (2020) and Yen et al. (2014). The model's input and output are described in detail in Valdivia-Mena et al. (2022), here we describe briefly the input parameters used for this source.

The streamline model requires the central mass that is causing the gravitational pull as input, which is the sum of the masses of the protostar, disk, and envelope, $M_{\rm tot} = M_* + M_{\rm disk} + M_{\rm env}$. We estimate the protostellar mass by fitting a two-dimensional Gaussian to individual $C^{18}O$ (2 – 1) channels and comparing the resulting distance and velocity (with respect to B5-IRS1) with the Keplerian curves predicted for different protostellar masses. We describe the process in detail in Appendix B.7. Through this analysis, we obtain a central protostellar mass $M_* \approx 0.2$ M$_\odot$. For the disk mass, we use an upper limit of $M_{\rm disk} = 0.03$ M$_\odot$ found by Zapata et al. (2014). As this value is small, it does not have a significant effect on the resulting parameters of the model. We use an envelope mass of $M_{\rm env} = 0.27$ M$_\odot$ from Andersen et al. (2019), obtained through the comparison of continuum observations from the Submillimeter Array (SMA) and single-dish observations.

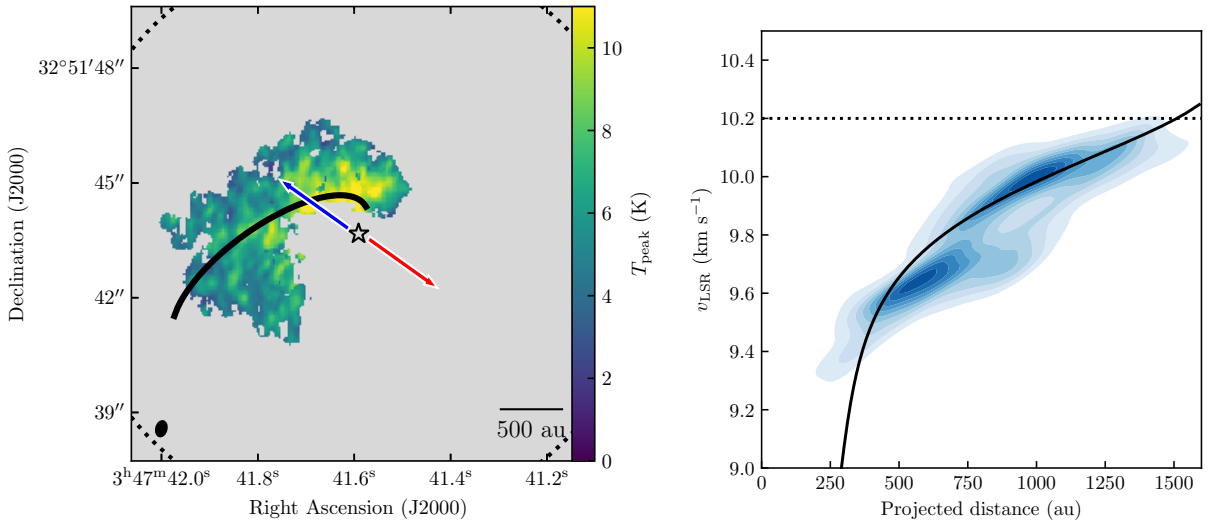

Figure 3.12: Streamline model that best fits the observed blueshifted envelope component in H_2CO line emission. In both image and velocity space, the black curve represents the streamline model solution that best describes the bulk motion of the streamer. **Left:** Peak main beam temperature $T_{\rm peak}$ for each pixel in the blue component found with DBSCAN. The blue and red arrows show the direction of the blue and red outflow lobes from Zapata et al. (2014), respectively. The black ellipse in the bottom left corner represents the beam size. The black star represents the position of the protostar. The black dashed circle represents the size of the primary beam. **Right:** central velocity KDE for the blueshifted envelope plotted against the projected distance from the protostar.

The disk and envelope mass are corrected for a distance to B5 of 302 pc (Zucker et al. 2018), as the original masses reported in those works are calculated with a distance of 240 pc.

To decrease the number of free parameters to explore, we fixed the inclination angle i and position angle PA of the rotating cloud using previous information from the outflow and disk in B5-IRS1. The outflow inclination angle is -13° (where 0° is on the plane of the sky and positive is away from the observer, Yu et al. 1999) and its position angle is 67.1° (where 0° is north, Zapata et al. 2014). Assuming the disk belongs in a plane perpendicular to the outflow, then $PA = 157.1°$ (from north, if 0° is a disk aligned in the north to south direction) and $i = 13°$ (from the plane of the sky). In this setup, the angular velocity vector of the disk $\vec{\omega}$, and therefore of the streamer, points toward the southwest, away from the observer.

We explored the initial position (r_0, ϑ_0 and φ_0) and velocity $v_{r,0}$ to find the set that best fits the observed positions and velocities. We manually changed the parameters to obtain streamline model curves that resemble the shapes of both the peak emission and the line-of-sight velocities of each component (Fig. 3.12). As the infall motion covers a large area in the image plane and does not look like a thin, collimated streamer (as in the

Parameter	Unit	Value
ϑ_0	deg	101
φ_0	deg	65
r_0	au	2810
$v_{r,0}$	$\mathrm{km\,s^{-1}}$	0
Ω_0	$\mathrm{s^{-1}}$	2.8×10^{-13}
i	deg	13
P.A.	deg	157.1
r_c	au	245

Table 3.2: Parameters of the streamline model that reproduce best the H_2CO blueshifted cluster and resulting centrifugal radius.

cases of Pineda et al. 2020; Valdivia-Mena et al. 2022), there must be a family of solutions that describe the whole streamer. We find the streamline model that best describes the bulk motion of the blue cluster, that is, the one that best fits the observed velocities and is contained within the emission region of the blue cluster in the image plane. Its parameters are in Table 3.2. We explored other combinations of r_0, ϑ_0 and φ_0 to find other possible solutions. The parameters presented in Table 3.2 are the ones that replicate best the approximate shape of the streamer in the image plane and the velocities at the same time.

Figure 3.12 shows the projected trajectory of the streamline model over the blue cluster peak temperature (left panel) and over the KDE of the velocities and projected distance in the streamer (right panel). We used the KDE implementation in the python package `SciPy` (Virtanen et al. 2020) over the resulting central velocities obtained for the cluster. The streamline model reproduces the velocity gradient shown in the KDE. The resulting centrifugal radius r_c (as defined in Mendoza et al. 2009), which is the distance down to which the movement can be modeled with constant angular momentum, is 249 au. This radius is an upper limit to the location where the mass flow ends, as any process that can affect the streamer motion, such as interaction with the outflow (as mentioned in Appendix B.6.1), will decelerate the gas flow and therefore, reduce its angular momentum. This radius is consistent with the infall material being deposited at gas disk-scale distances from the protostar: the dust disk has an estimated radius ~ 50 au using mm-continuum emission (Yang et al. 2021), and although we cannot define a gas disk radius with our $C^{18}O$ data (Appendix B.7), the gas disk extension tends to be much larger than what can be seen in dust emission, up to several 100 au (Miotello et al. 2023, and references within).

3.5 Discussion

3.5.1 Chemically fresh gas feeds the filaments

In this work, we present new $HC_3N\,(10-9)$ and $(8-7)$ emission data within the coherent core of B5. Our results and analysis of $HC_3N\,(10-9)$ velocities and its comparison to

previous results with NH_3 (1,1) emission indicate that HC_3N traces chemically fresh gas infalling toward the filaments and condensations, following the curvature of the filaments. We explain our reasoning below.

Figure 3.8 shows that HC_3N emission is consistently redshifted with respect to NH_3. The systematic difference in centroid velocities shows these molecules do not trace the same material within B5. As mentioned in Sect. 3.4.1.1, HC_3N traces material unprocessed by core collapse, whereas NH_3 is expected to be more abundant in regions where core collapse is underway. Previous results in other star formation regions also show kinematic differences between carbon-chain molecules and nitrogen bearing molecules (e.g., Friesen et al. 2013). Therefore, HC_3N traces the kinematics of chemically fresh material with respect to the main filamentary structure.

That being said, the velocities shown by HC_3N emission are consistent with infall from the B5 dense core to the filaments and condensations. The Gaussian fit to the HC_3N spectra (Fig. 3.5) and the further velocity gradient analysis (Sect. 3.4.1.2) reveal that both filaments show a velocity gradient running parallel to the filaments' full length. The velocity gradients of the filaments run in opposite directions: in Fil-1, the global gradient runs from lower $v_{\rm LSR}$ toward the north to higher $v_{\rm LSR}$ in the south, with the highest $v_{\rm LSR}$ in Cond-1, whereas in Fil-2 the global gradient starts from lower $v_{\rm LSR}$ at the south and increases toward the north, following the curvature of the filament. We interpret this as a flow of gas running along the direction of the filaments toward the condensations. NH_3 (1,1) emission also shows parallel velocity gradients with the same orientations (Fig. B.1, S21). These large-scale parallel velocity gradients are similar in to those found in other filament, such as NGC 1333 (Hacar et al. 2017; Chen et al. 2020c) and L1517 (Hacar & Tafalla 2011). Assuming filament lengths of 0.24 pc for Fil-1 and 0.31 for Fil-2 from S21, the average gradients along each filament are approximately 1.7 $\rm km\,s^{-1}\ pc^{-1}$ and 1.0 $\rm km\,s^{-1}\ pc^{-1}$, respectively. These values resemble the magnitude of the parallel velocity gradients found in other filaments and fibers ($\sim 1\ \rm km\,s^{-1}\ pc^{-1}$, e.g., Kirk et al. 2013; Fernández-López et al. 2014; Chen et al. 2020c).

The velocity gradients running perpendicular to the filament orientations are suggestive of infall from the B5 dense core to the filaments themselves. Fil-1 and the HC_3N emission just outside of it to the north and to the east show an east-west velocity gradient that crosses the full width of the filament (Fig. 3.5 center) whereas small-scale perpendicular gradients in Fil-2 are revealed when calculating $\nabla v_{\rm LSR}$ at scales of 2.5 times the beam (Fig. 3.9). This type of velocity gradient is consistent with the contraction of a sheet-like cloud, as argued in filament simulations (Chen et al. 2020a), as well as rotation around the filaments's main axis. This type of gradient has been observed in other filaments, for example, within Perseus and Serpens molecular clouds (Fernández-López et al. 2014; Dhabal et al. 2018). We interpret the velocity gradient as infall dominated gas because these filaments are not supported against gravitational collapse given the turbulence in the B5 core, unless a magnetic field is present, and show signs of contraction (S21). Infall of material toward the center of the filaments has been suggested for B5 in previous works which analyze the kinematics of NH_3 (1,1) (Schmiedeke et al. 2021; Chen et al. 2022, Choudhury et al. submitted). Our results support the interpretation that the additional

components found by Choudhury et al. (submitted) are, as suggested, signs of infall from the coherent core. We suggest that HC_3N is more sensitive to the flow of mass from the Barnard 5 core to the filaments, whereas NH_3, as it is a later type molecule, only traces the flow of gas within the filaments toward the condensations and differentiates regions of subsonic and supersonic turbulent motions (Pineda et al. 2010).

3.5.2 A streamer toward B5-IRS1

The two main H_2CO emission clusters in position-position-velocity space found in Sect. 3.4.2.1 have velocity gradients consistent with infall motion. We confirmed that most of the emission on these structures is not affected by the outflow, at least beyond ~ 600 au from the protostar. The nonthermal dispersion decreases as the distance to the protostar increases for both clusters (Fig. B.10). Most of the spectra located at distances > 600 au have subsonic $\sigma_{\rm v,nt}$. There are, however, some spectra with trans-sonic velocity dispersion ($\mathcal{M}_s \gtrsim 1$) within 600 au of the protostar. This result suggests that H_2CO gas located closer to the protostar is becoming affected by the outflow, which increases $\sigma_{\rm nt}$.

We were able to confirm the infall nature of the blueshifted streamer using the streamline model. The best fit solution starts from the outer edge of the blue cluster's emission with null initial radial velocity. We note that the blue streamer is not a thin, long structure such as other streamers in the literature, but more similar to a bulk of gas infalling due to gravity. Moreover, as the channels that trace the streamer at a distance of about 2800 au from the protostar are affected by missing short-spacing data (as seen in Fig. 3.4, between 9.6 and 10.4 $\rm km\,s^{-1}$), it is possible we miss some of the extent of this bulk. The spatial width of the emission we do trace suggests that the component could be fitted by a family of streamlines. We only took the one that best matches the general velocity KDE that passes through the emission seeen in the plane of the sky, because this allowed us to confirm its infalling nature. Nevertheless, this streamer has a similar length (≈ 2800 au) to other streamers found toward Class I protostars (Yen et al. 2014; Valdivia-Mena et al. 2022).

Understanding the kinematic nature of envelope emission helps disentangle the chemical history of the protostar. A previous work by van't Hoff et al. (2022) shows $H^{13}CO^+$ (2 – 1) emission with a ridge-like structure toward the east of B5-IRS1, similar to the arc shaped blueshifted envelope cluster. They suggest that emission is either associated with an extended water snowline due to a previous accretion burst in this source, or the larger protostellar envelope. We compare the H_2CO blueshifted envelope component with the $H^{13}CO^+$ emission from van't Hoff et al. (2022) in Appendix B.8. Both emissions overlap in the image plane, although $H^{13}CO^+$ is more extended than H_2CO. The velocity gradients are the same and there are no significant differences between the central velocities of both molecular emissions. Therefore, we confirm that $H^{13}CO^+$ traces the envelope's infalling motion and not an extended snowline due to an accretion burst in this source. This suggest that using the $H^{13}CO^+$ emission without further kinematic information about the source can overestimate the water snowline distance. This example highlights the importance of the kinematic information toward a source to interpret its chemical history.

Confirming the streamer nature of the redshifted cluster is not as clear as for the blueshifted cluster. The red cluster could be described using the same initial distance and angular velocity as the blue cluster streamline model. However, this model assumes that the blue and red clusters are part of the same envelope (i.e. have the same Ω_0, i and PA), which cannot be confirmed with the available data. Also, it is possible that the red streamer is more affected by missing short-spacings of our interferometric data than the blue streamer. In projected distance (i.e. in the RA-DEC plane), the streamline model of the blue streamer measures approximately $12''$, so if the red streamer emission extends as suggested by the streamline model, the MRS of our data ($\approx 6''$, Sect. 3.2.4) does not allow us to detect its emission and we are only detecting the brightest part. Therefore, the classification of "streamer" is left as tentative for the red component of the envelope, and ALMA ACA observations of this region are required to confirm its streamer nature. If confirmed, B5-IRS1 would have twin streamers instead of only one as in other protostellar sources. This is similar to the case of L1489 IRS (Yen et al. 2014), a Class I source with two streamers observed in $C^{18}O$ (2 – 1), and of [BHB2007] 11 (Alves et al. 2020), a Class I/II source with two streamers detected with ^{12}CO (2 – 1). Simulations show that when a protostar is still embedded in its natal core, there are several asymmetric channels from which matter is funneled (e.g., Padoan et al. 2014; Kuffmeier et al. 2017, 2023), but in most cases, only one streamer is observed (e.g., Pineda et al. 2020; Garufi et al. 2022; Valdivia-Mena et al. 2022). The fact that we do not see multiple streamers in other sources does not mean that they are not present, it is possible that their column density is too low to be detected. Further discoveries of streamers will help determine if dual streamers are a common occurrence or an exceptional phenomenon.

3.5.3 Connection between large scale and small scale infall

In this work, we observed infall motions both at large scales, from the core to the filaments, and at small scales, from the protostellar envelope to the disk. Even if the difference in resolution for these datasets is approximately tenfold, our results suggest that the confirmed streamer's origin lies within the fresh gas flowing from the B5 dense core. We discuss the connection between these infall mechanisms.

Figure 3.8 shows that the relative velocity of HC_3N with respect to NH_3 reverses at the position of the protostar, showing a blueshifted zone about the size of the NH_3 beam. Interestingly, zooming into this region (Fig. 3.13 Left) reveals that this blueshifted area is located approximately at the position of the blue streamer found using H_2CO with ALMA data, which has a 10 times smaller beam. To prove that the difference between HC_3N and NH_3 bluehsifted emission is significant, we show horizontal and vertical cuts of HC_3N (10 − 9) and NH_3 (1,1) $v_{\rm LSR}$, centered at the position of the minimum $\delta v_{\rm LSR}$, in Fig. 3.13. The difference between both molecules' velocities is larger than the uncertainties of each fit: HC_3N decreases within a beam-sized area at the location of the protostar by approximately 0.4 $\mathrm{km\,s^{-1}}$ with respect to its surroundings, whereas NH_3 has a decrease in $v_{\rm LSR}$ of about 0.1 $\mathrm{km\,s^{-1}}$ in the same region, only evident in the horizontal cut. Therefore, HC_3N (10 − 9) emission has larger variations around the protostar than NH_3 (1,1). Moreover, this region

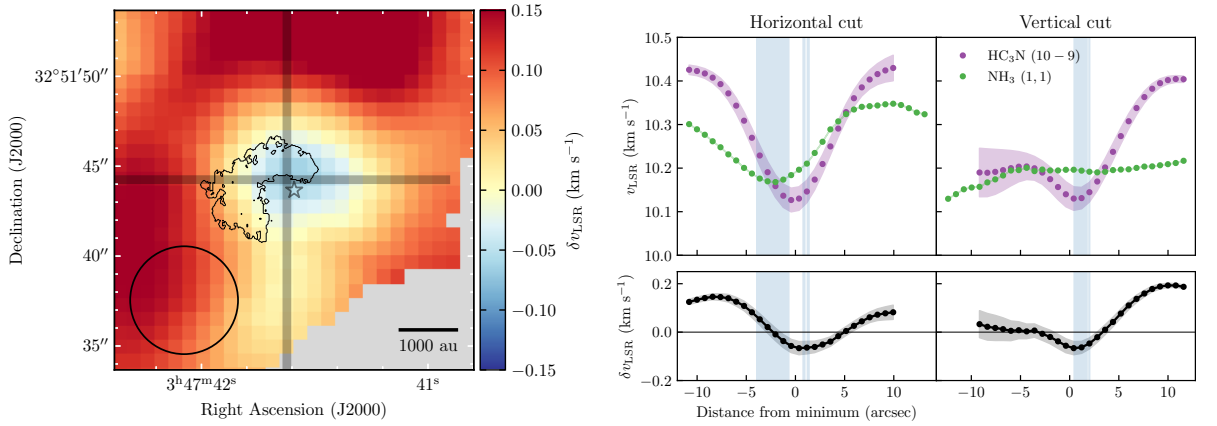

Figure 3.13: **Left:** Zoom into δv_{LSR} from Fig. 3.8 toward the position of the protostar. The black contours mark the region of the blue streamer found in Sect. 3.4.2.1. The horizontal and vertical black lines show the positions of the horizontal and vertical cuts for the plots on the right. The black circle at the lower left corner represents the beam size of the NH_3 (1,1) observations. **Right:** Horizontal and vertical cuts of HC_3N v_{LSR} and NH_3 v_{LSR}. The purple points with the purple area represent the HC_3N $(10-9)$ v_{LSR} and its associated uncertainty after smoothing to reach the same resolution as the NH_3 (1,1) v_{LSR}. The green points represent the NH_3 (1,1) v_{LSR} (the uncertainties are roughly the size of the points). The black curves and black areas represent the difference between HC_3N $(10-9)$ NH_3 (1,1) v_{LSR}. The blue areas represent the location covered by the blue streamer.

coincides with where the AIC suggests two Gaussians fit HC_3N better than one Gaussian, but with not enough certainty (Fig. B.6). The low certainty from the AIC criterion is caused by insufficient spectral resolution to separate both components, but it suggests that, with better spectral resolution, we might be able to disentangle two velocity components, one related to the kinematics of the core gas infalling toward the filaments, and another, more blueshifted gas component which could trace the streamer. Overlaying the region where the streamer is present (blue vertical bands in Fig. 3.13 Right), the streamer is close to the location of the minimum $v_{\rm LSR}$ for HC_3N. This coincidence suggests that HC_3N is sensitive to the infall motions close to the protostar in the dense core.

The velocity gradients seen in HC_3N also suggest the streamer is connected to chemically fresh gas. The strongest HC_3N velocity gradients are present toward Cond-1 and the protostar. A zoom into the north of Fil-2, shown in Fig. 3.10, shows that gas flows along the filaments and reaches the condensations and the protostar, where they distribute between the three, as seen from the change in direction in the $\nabla v_{\rm LSR}$ vectors. The gradient orientation at the east of the protostar is similar to the orientation of the velocity gradient of the blue cluster as seen in Fig. 3.11, which in Sect. 3.4.2.2 we determine is consistent with an accretion streamer. Consequently, HC_3N could trace the streamer's motion.

These results suggest that the large scale flow traced by HC_3N connects to the tail of the streamer and, therefore, fresh gas coming from the B5 dense core reaches the protostellar disk through the streamer. Previously discovered streamers have large extensions ($\sim 10\,000$ au, e.g., Pineda et al. 2020) and for others, their full extension has not been imaged (Valdivia-Mena et al. 2022), showing that streamers can originate from great distances from the protostar. Due to the limited MRS of our data, this can be the case for B5-IRS1 as well. However, our current dataset's difference in resolution is too large to connect the two structures seamlessly. Higher spectral resolution observations ($\lesssim 0.1$ km s^{-1}) are required disentangle the second velocity component where the decrease in $v_{\rm LSR}$ occurs. Intermediate resolution ($\approx 1''$) observations of HC_3N, together with and a spectral resolution comparable to our H_2CO data, could connect the flow from filament to streamer directly.

3.6 Summary

We studied the kinematic properties of gas at $4''$ (~ 1200 au) scales toward the B5 coherent core filaments using HC_3N $(10-9)$ and $(8-7)$ transition line maps, and $0.4''$ (~ 120 au) scales toward the protostellar envelope surrounding B5-IRS1 using H_2CO ($3_{0,3}$ – $2_{0,2}$) and $C^{18}O$ $(2-1)$ line emission maps. We compared our results with previous NH_3 emission observed toward this region. The main structures seen in HC_3N and H_2CO are summarized in Fig. 3.14. Our main results are summarized below.

1. **HC_3N emission traces the gas flow from the coherent core to the filaments.** It is consistently redshifted with respect to the dense gas, observed in NH_3, which indicates that it follows different kinematic properties than the dense core tracer. HC_3N $(10-9)$ shows velocity gradients perpendicular to the filament length, which

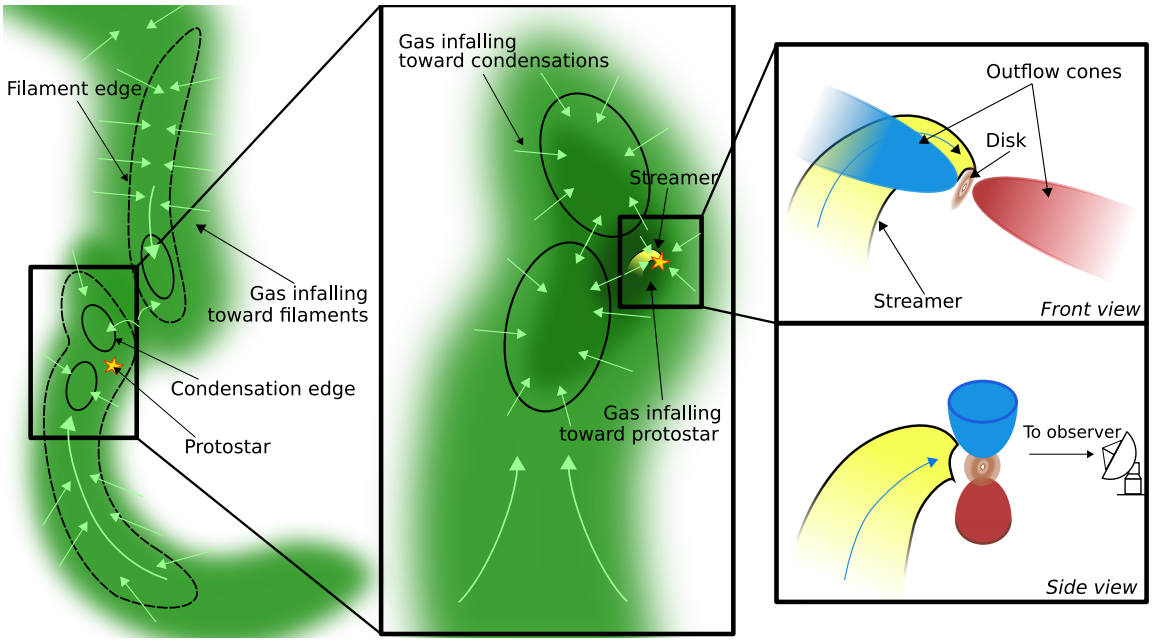

Figure 3.14: Diagram showing the flows of gas at the different scales investigated in this work. The yellow star indicates the position of the protostar. **Left:** Infall of fresh gas (green clouds) from B5 dense core toward the filaments (black dashed contours), with the flow direction indicated by the light green arrows. Black solid contours outline the condensations. **Center:** Infall of fresh gas from the filament toward the condensations (black solid contours) and the protostar, showing the change in direction from the filament to the condensations. The yellow curve shows the streamer transporting material toward the protostellar disk. **Top Right:** Infall of gas into the protostellar disk (brown disk) through the streamer (yellow flow), which is behind the blue outflow cone (blue cone). The blue arrow indicates the flow direction of the blueshifted streamer. **Bottom right:** Same as in the top right, but rotated by 90° to observe the streamer unobstructed by the outflow cone.

is consistent with the velocity profile expected from the contraction of a sheet-like cloud forming a filament (Chen et al. 2020a).

2. Using $HC_3N\,(10-9)$ and $(8-7)$ transitions, we obtain a mean H_2 volume density $n(H_2) \approx 10^5$ cm^{-3}. With this value, we estimate that HC_3N traces accretion rates of $\dot{m} = 4.3 \times 10^{-5}$ M$_\odot$ yr^{-1} in Fil-1 and $\dot{m} = 3.5 \times 10^{-5}$ M$_\odot$ yr^{-1} in Fil-2, similar to the accretion rates obtained in previous works which used NH_3 emission.

3. **We find one streamer and one streamer candidate toward B5-IRS1, using a clustering algorithm on the velocity components found in H_2CO emission.** We confirm that H_2CO emission is mostly unaffected by the outflow cone in this region. We confirm the infalling nature of the clustered component which is blueshifted with respect to the protostar using a streamline model. The categorization of the component that is redshifted with respect to IRS1 is left as tentative as we only traced a small part of this infall. We estimate that the streamer has a total length of around 2800 au through the resulting parameters of the applied streamline model.

4. **We sugest that the infall of chemically fresh gas toward the condensations and filaments is connected to the protostar via the streamer.** At the location of the protostar, $HC_3N\,(10-9)$ central velocities decrease with respect to its surroundings. The location of the blueshift coincides with the location of the streamer and the velocity gradients seen in HC_3N coincide in orientation with the velocity gradient shown by the streamer. We suggest HC_3N is also sensitive to the infall at small scales, which we know are present because of the high-resolution observations.

Our results highlight the importance of the environment in the comprehension of the physical and chemical processes around protostars. The properties of both the core and the protostellar disk can be affected by the infall mechanisms we observe: there is both chemically fresh gas being deposited toward the filaments, as well as a preferential channel to deposit gas from the envelope to the disk. Intermediate spatial resolution observations are required to confirm the large-scale infall traced using $HC_3N\,(10-9)$ with the small-scale infall seen in H_2CO emission.

Chapter 4

Probing the Physics of Star-Formation (ProPStar) II. The first systematic search for streamers toward protostars

The contents of this chapter are submitted for publication on A&A (the first referee report was received and contained minor comments). The submitted article is integrally copied (Valdivia-Mena, M. T. et al. 2024, to be published with ©CC-BY 4.0.).

Abstract

Context. The detection of streamers, narrow channels of accretion toward protostellar disks, has increased in number in the last few years. However, it is unclear if streamers are a common feature around protostars that we have missed, or if they are a rare phenomenon.
Aims. Our goal is to obtain the incidence of streamers toward a region of clustered star formation and to trace the origins of their gas, so as to determine if they originate from filamentary structure within molecular clouds.
Methods. We use combined observations of the nearby NGC 1333 star-forming region, carried out with the NOEMA interferometer and the IRAM 30m single dish. Our observations cover the area between the IRAS 4 and SVS 13 systems. We trace the chemically fresh gas within NGC 1333 with HC_3N molecular gas emission and the structure of the fibers in this region with N_2H^+ emission. We fit multiple velocity components in both maps and use clustering algorithms to recover velocity-coherent structures.
*Results.*We find streamer candidates toward 7 out of 16 young stellar objects within our field of view. This represents an incidence of approximately 40% of young stellar objects with streamer candidates when looking at a clustered star forming region. All streamers are found in HC_3N emission.
Conclusions. Given the different velocities between HC_3N and N_2H^+ emission, and the

fact that, by construction, N_2H^+ traces the fiber structure, we suggest that the gas that forms the streamers comes from outside the fibers. This implies that streamers can connect cloud material that infalls to the filaments with protostellar disk scales.
Keywords: stars: circumstellar matter – stars: formation – stars: protostars – ISM: kinematics and dynamics

4.1 Introduction

Molecular clouds are composed of filaments (André et al. 2014; Hacar et al. 2023), which contain the cores where protostars and binary systems are born (e.g. André et al. 2010; Offner et al. 2023). These filaments are highly dynamic structures: gas has been observed to flow along them and they also accrete more gas from their surroundings (see Hacar et al. 2023, for more details). Within filaments, molecular gas tends to be organized in velocity-coherent structures called fibers (e.g. Hacar et al. 2017). Observations of filaments and fibers highlight their relevance in directing molecular gas toward the sites of star formation.

Although astronomers have observed and modeled how mass flows within filaments and fibers in general, how that mass reaches the protostellar disk (on scales of $\lesssim 0.1$ pc) is not well understood. The way that mass reaches a protostellar system plays an important role in the star and planet formation process. For instance, infall from the envelope to the disk that is variable in time influences the accretion rate of the protostar, affecting its luminosity (Padoan et al. 2014; Kuffmeier et al. 2018) and the chemical composition of the disk, represented, for instance, by the location of its snowline (Hsieh et al. 2019) Numerical simulations also show that when infall from the envelope to the disk is heterogeneous in space, this can produce changes in disk structure, such as rings and gaps (Kuznetsova et al. 2022) and second-generation disks misaligned with inner disks (Kuffmeier et al. 2021). Therefore, observing the mass flow from fiber scales ($\gtrsim 0.1$ pc or $\sim 20\,000$ au) to disk scales (few ~ 100 au) is crucial to understand the influence of filaments and fibers in protostellar and disk properties.

In the last few years there has been a rise in the observations of streamers, which are defined as velocity-coherent, narrow structures that deposit their material to protostellar and protoplanetary disks (Pineda et al. 2023), unlike fibers, which are velocity-coherent structures within the filaments. They are observed as asymmetries in the protostellar envelopes with total lengths between 500 au (Garufi et al. 2022) to even 10 000 au away from the protostar, beyond the natal protostellar core (Pineda et al. 2020). Streamers have been mostly detected and characterized toward embedded protostars (which are known as Class 0 and I sources, e.g. Chou et al. 2016; Valdivia-Mena et al. 2022, 2023; Kido et al. 2023; Aso et al. 2023), but some streamers have been detected toward T Tauri sources (also known as Class II protostars) as well (e.g. Ginski et al. 2021; Garufi et al. 2022; Harada et al. 2023). Although mostly characterized toward low-mass young stellar objects (YSOs), recently accretion streamers have been discovered toward high-mass YSOs as well (Fernández-López et al. 2023).

Although streamers appear increasingly common, their role in the larger puzzle of star formation is unclear. One open questions is where do streamers come from? Numerical simulations show asymmetric accretion channels both within the core itself generated by turbulence (e.g. Walch et al. 2010; Seifried et al. 2013; Hennebelle et al. 2020), as well as coming from outside the natal core (Kuffmeier et al. 2017, 2023). Valdivia-Mena et al. (2023) suggested that the observed gas falling toward fibers at scales of $\sim$ 20 000 au is connected to a streamer feeding disk scales in Barnard 5, but they cannot directly confirm this suggestion due to the different tracers and spatial resolutions of the observations.

Another point of debate is how frequent streamers actually are. The previously mentioned discoveries of streamers were mostly serendipitous. It is possible that accretion streamers are a common feature within protostellar envelopes of all ages, but they have not been characterized because the data targeted other features, such as the disk or outflows (e.g. Thieme et al. 2022). For instance, the the primary goal of the ALMA Large Program eDisk is to find substructures in young, embedded disks, yet their observations reveal streamers as well (Kido et al. 2023; Aso et al. 2023). To this date, there has not been a systematic search for streamers toward YSOs. To better understand the role of streamers in our new picture of star formation, it is necessary to actively search for streamers in data that can also trace the larger fiber kinematics.

We present the first systematic study of gas flow from filament scales to individual protostellar envelopes with the explicit goal to search for streamers. This is part of the "Probing the Physics of Star-formation" (ProPStar) survey, where we explore the connection between the molecular gas within filaments and the circumstellar disk scales. We trace the flow of gas from a filament to YSOs, using a set of observations that allows us to characterize the flow of gas at fiber scales as well as toward the individual protostars. The goal of this work is to search for streamers in a systematic fashion within a region where the kinematic properties of the fibers are known, to investigate the connection between fibers and streamers. For this purpose, we select NGC 1333, one of the closest young embedded clusters, containing close to 150 YSOs (Gutermuth et al. 2008). It is the most active star forming region within the Perseus molecular cloud, located at 293 pc from Earth (Ortiz-León et al. 2018; Zucker et al. 2018). Its high protostellar activity is reflected in the dozens of outflows stirring the local gas (Plunkett et al. 2013). For this work, we select a region that covers two fibers with known kinematic properties which include the SVS 13 and the IRAS 4 protostellar systems. The observed area includes a total of 16 YSOs between Class 0 and Class II. We refer to this whole area as the southeast (SE) filament.

This article is divided as follows: In Section 4.2, we describe the observations with the NOEMA and 30-m telescopes and their combination. In Section 4.3, we describe the mathematical approach to interpret the data. Section 4.4 shows the resulting structure of the fibers seen in the chosen gas tracers, the steps followed to find streamers in the data, and the description of the streamers in this area. We discuss our results and their physical interpretation in Section 4.5. Finally, in Section 4.6, we summarize the main results of our work.

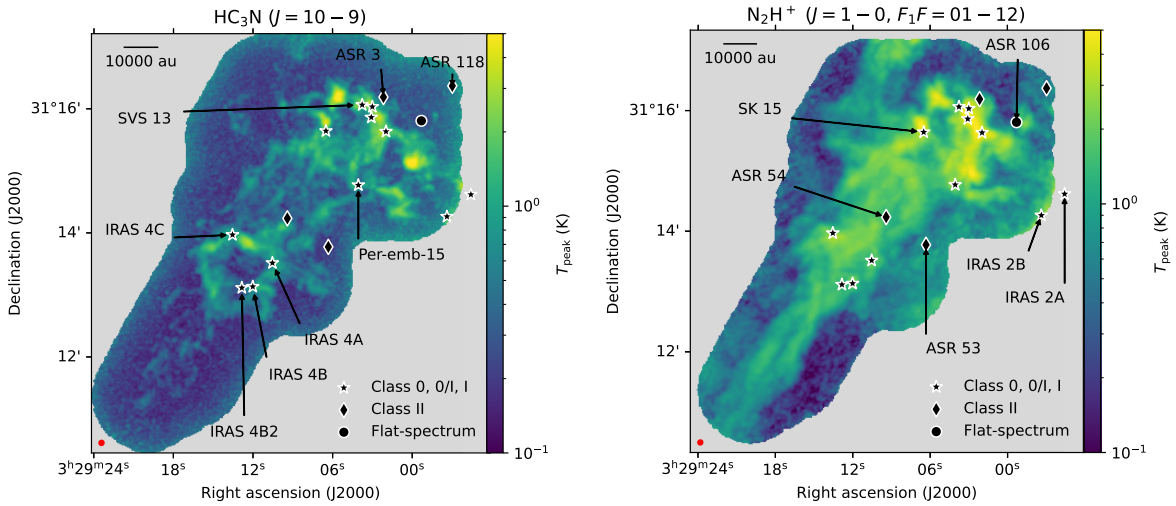

Figure 4.1: Peak temperature $T_{\rm peak}$ maps of the NOEMA and 30-m telescope observations. The black symbols represent YSOs in the region, summarised in Table 4.2: stars mark the positions of Class 0, I and 0/I protostars, circles represent Flat-spectra objects, and diamonds mark Class II sources. The protostars are labeled following Table 4.2. Left: HC_3N $(10-9)$ $T_{\rm peak}$. Right: N_2H^+ $(1-0)$ $F_1F = 01-12$ $T_{\rm peak}$.

4.2 Observations and Data reduction

We summarize the single dish and interferometric observations of NGC 1333 SE that we use from the ProPStar survey. The same observational setup is described in the ProPStar I paper (Pineda et al. submitted).

4.2.1 IRAM 30-m telescope

The single-dish observations were carried out using the 30-m telescope from IRAM, located in the Pico Veleta mountain in Spain. The observations are part of project 091-21 and were done during 2021 November 9, 10, and 11; and 2022 February 19, 20. We tuned the EMIR 090 receiver to cover the ranges between 72.3 – 78.8 GHz and 87.8 – 94.3 GHz. The FTS50 backend was employed, yielding a spectral resolution of 52.5 kHz. The complete map is $\approx 150'' \times ''150$ and was mapped using an on-the-fly technique with position switching.

Data reduction was performed using the CLASS program of the GILDAS package[1]. The beam efficiency, B_{eff}, was obtained using the Ruze formula (available in CLASS), and was used to convert the observations into main beam temperatures, $T_{\rm mb}$.

[1] `http://www.iram.fr/IRAMFR/GILDAS`

4.2.2 NOEMA

The observations were carried out with the IRAM NOrthern Extended Millimeter Array (NOEMA) interferometer as part of the the S21AD program using the Band 1 receiver, with the array in D configuration. The observations were taken on 2021 July 18, 19, and 21; August 10, 14, 15, 19, 22, and 29; and September 1. The mosaic consists on 96 pointings, centered at α_{J2000}=03$^{\rm h}$29$^{\rm m}$10.2$^{\rm s}$, δ_{J2000}=31°13′49.4″, which were separated on four different scheduling blocks. We used the PolyFix correlator with a LO frequency of 82.505 GHz, an instantaneous bandwidth of 31 GHz spread over two sidebands (upper and lower) and two polarisations. The centers of the two 7.744 GHz wide sidebands are separated by 15.488 GHz. Each sideband is composed of two adjacent basebands of ∼3.9 GHz width (inner and outer basebands). In total, there are eight basebands which are fed into the correlator. The spectral resolution is 2 MHz throughout the 15.488 GHz effective bandwidth per polarization. Additionally, a total of 112 high-resolution chunks are placed, each with a width of 64 MHz and a fixed spectral resolution of 62.5 kHz. Both polarizations (H and P) are covered with the same spectral setup, and therefore the high-resolution chunks provide 66 dual polarisation spectral windows. In this work, we used the spectral windows containing the N_2H^+ $J = 1 - 0$ line and its hyperfine components (F_1F) at approximately 93 GHz, and the HC_3N $J = 10 - 9$ line at approximately 91 GHz (Table 4.1).

Data reduction was done using the CLIC program from the GILDAS package. We used the NOEMA pipeline to obtain the calibrated uv-tables, which we then combined with the single-dish data as explained in the next section.

4.2.3 Combination of single-dish and interferometric data

Molecule	Transition	ν (MHz)	E_{up} (K)	n_{crit} (cm^{-3})	beam size	rms (mK)
N_2H^+	$J = 1 - 0$, $F_1F = 01 - 12$	93176.2522	4.47	6.1×10^4	5.76×5.48	70
HC_3N	$J = 10 - 9$	90979.0230	24.01	1.6×10^5	4.89×4.69	80

Table 4.1: Spectral lines observed in the high-resolution chunks used in this work. Frequencies taken from the CDMS catalog. Critical densities taken from Shirley (2015). The rms is taken from the combined NOEMA and 30-m data cubes.

The original 30-m data is resampled to match the spectral setup of the NOEMA observations. We use the task `uvshort` to generate the pseudo-visibilities from the 30-m data for each NOEMA pointing. The imaging is done with natural weighting, a support mask, and using the SDI deconvolution algorithm.

The final cubes are in K and have a channel resolution of approximately 0.2 km s^{-1}. The properties of the final data cubes are described in Table 4.1. The channel maps for each of the molecules are presented in Appendix C.1. The HC_3N (10−9) peak temperature map is shown in Fig. 4.1. The observations cover an area of approximately 150″ × 150″. The clean beam at this frequency is approximately 4.9″ (1400 au). The mean rms of the HC_3N $J = 10 - 9$ emission cube is approximately 12 mJy beam^{-1} (80 mK) and increases

at the edges of the map due to the primary beam response. We refer to HC_3N $(10-9)$ line emission as HC_3N in the rest of this work, as is the only HC_3N emission line presented.

As we are interested in the kinematic structure of the filaments, we isolate one of the hyperfine structure emission lines of N_2H^+ $J = 1-0$, the $F_1F = 01-12$ component at 93176.2522 MHz. We chose this hyperfine component because it is the one that is the most separated from the other hyperfine structure lines, and therefore each individual peak can be interpreted as an individual velocity structure along the line of sight (Fig. 1 in Caselli et al. 1995). The N_2H^+ $J = 1-0$, $F_1F = 01-12$ peak temperature map is in Fig. 4.1. The clean beam size for this molecule is approximately $5.8''$ (1750 au). The mean rms of N_2H^+ $J = 1-0$, $F_1F = 01-12$ cube is approximately 15.7 mJy beam^{-1} (70 mK). For the rest of the article, we refer to the N_2H^+ $J = 1-0$, $F_1F = 01-12$ as N_2H^+ unless otherwise stated.

Source	RA (J2000)	DEC (J2000)	Other Names	Class[a]	Multiple? [b]	v_{LSR}[c] (km s^{-1})	Outflow P.A.[d] (°)	Disk i[e] (°)
IRAS4A	03:29:10.54	+31:13:30.93	Per-emb 12	0	Y	6.9 ± 0.005[1]	19[6]	35
IRAS4B	03:29:12.02	+31:13:08.03	Per-emb 13	0	Y	7.1 ± 0.009[1]	176[6]	49
Per-emb-14	03:29:13.55	+31:13:58.15	NGC 1333 IRAS4C	0	N	7.9 ± 0.03[1]	96[7]	64
Per-emb-15	03:29:04.06	+31:14:46.24	RNO15-FIR, SK 14	0	N	6.8 ± 0.01[1]	-35[5]	
Per-emb-27	03:28:55.57	+31:14:37.03	NGC 1333 IRAS2A	0/I	Y	8.1 ± 0.02[1]	105[5,f]	
Per-emb-36	03:28:57.37	+31:14:15.77	NGC 1333 IRAS2B	I	Y	6.9 ± 0.02[1]	24[5]	
Per-emb-44	03:29:03.76	+31:16:03.81	SVS13A	0/I	Y	8.7 ± 0.02[1]	140[8]	
SVS13C	03:29:01.97	+31:15:38.05		0	Y	8.9 ± 0.02[1]	8[8]	75
SVS13B	03:29:03.08	+31:15:51.74		0	Y	8.5 ± 0.01[1]	170[6]	61
IRAS4B2	03:29:12.84	+31:13:06.89	NGC 1333 IRAS4B'	0	Y		-99[9]	
EDJ2009-183	03:28:59.30	+31:15:48.41	ASR 106	Flat	Y	8.69[2]		
EDJ2009-173	03:28:56.96	+31:16:22.20	ASR 118, SVS15	II	N	9.08[2]		
VLA 3	03:29:03.00	+31:16:02.00		0				
SK 15	03:29:06.50	+31:15:38.60	ASR 6, HRF 50	I		7.95[3]		
ASR 3	03:29:02.16	+31:16:11.40	[GMM2008] 76	II				
ASR 53	03:29:02.16	+31:16:11.40	[GMM2008] 89	II		13.5 ± 3.4[4]		
ASR 54	03:29:09.41	+31:14:14.10	[GMM2008] 135	II				

Table 4.2: Properties of the protostellar objects found within the HC_3N and N_2H^+ maps. We only describe the properties of protostars that are on regions where there is HC_3N emission or the outflow lobe is within the HC_3N emission map. [a]SED classification from the literature (Enoch et al. 2009; Evans et al. 2009). We indicate also when a source is a Class 0/I according to the classification in the VANDAM sample (Tobin et al. 2018). [b]Y if the source contains more than one protostar, N if it is single (Tobin et al. 2018). [c]Obtained from available molecular tracer observations of cores or from spectroscopic surveys. References: (1) Stephens et al. (2019), (2) Foster et al. (2015), (3) Imai et al. (2018), (4) Kounkel et al. (2019). [d]Angle of the red lobe from North to East. References: (5) Stephens et al. (2017), (6) Lee et al. (2016), (7) Zhang et al. (2018b), (8) Plunkett et al. (2013), (9) Podio et al. (2021). [e]Disk inclination with respect to the plane of the sky from Segura-Cox et al. (2018). [f]In IRAS 2A, there are two outflows perpendicular to each other. Here we list the most collimated one, where the red lobe is included in the footprint of our HC_3N data.

The protostars that are found within the observed area and their general characteristics are summarised in Table 4.2. We plot these protostars in Fig. 4.1 and label each one so

that the reader has a quick reference of where each one is in for the following analyses. We include IRAS 2A even though our map does not cover the protostar as it has a strong outflow that needs to be taken into account to understand the gas kinematics of the region.

4.3 Line decomposition methods

The peak temperature maps shown in Fig. 4.1 do not fully reflect the complexity of the obtained data. Both molecular lines show several emission peaks, some located at or within a beam of protostars, others apparently unrelated to protostellar sources. However, an initial inspection of the data cube shows that there are several locations in the map where the spectra have two or three velocity components along the line of sight. Previous molecular gas observations done both with similar resolution (Dhabal et al. 2019) as well as with single-dish telescopes (Hacar et al. 2017; Dhabal et al. 2018; Chen et al. 2020b) show that there are multiple velocity components in this region. Hacar et al. (2017) and Chen et al. (2020b) found that these velocity components are due to three velocity-coherent fibers of gas in the region, two of which run in the northwest to southeast direction that overlap in line of sight. For the kinematic analysis of the gas surrounding the protostars, it is necessary to separate these velocity components.

In this section, we describe the procedure used to separate the velocity components of NGC 1333 SE. In summary, we first separate the individual velocity components of each spectrum within the HC_3N and N_2H^+ maps by fitting multiple Gaussians. Next, we cluster the velocity components to recover individual, velocity-coherent fibers in the region. This process allowed us to analyse the velocity structure around the protostars more easily.

4.3.1 Identification of velocity components

Fitting a model using a simple minimization algorithm, such as least squares, has issues in identifying the best parameters for faint signals. Moreover, quantifying how much better a more complex model (i.e. with more parameters) is compared to a simpler one is a delicate task (e.g. Protassov et al. 2002). A quick look at the data cubes indicates that there are lines of sight where the possible second component has a signal-to-noise ratio (SNR) ~ 5. Therefore, a simple least squares fit followed by a statistic evaluation might not be enough to effectively separate the kinematic components within the filaments.

Bayesian model selection using nested sampling can solve these problems. Nested sampling is a parameter exploration algorithm that evaluates how probable the combination of parameters is, therefore allowing parameter estimation and model comparison, even in low SNR data. We refer the reader to Skilling (2004, 2006) and Sokolov et al. (2020) for more details. In summary, for the model selection, the algorithm returns the Bayesian Evidence $\mathcal{Z}$ of a model, which is a likelihood integral of the parameter values:

$$\mathcal{Z} = \int p(\theta)\mathcal{L}(\theta)d\theta, \tag{4.1}$$

where θ are the probable parameter values, $p(\theta)$ is the probability density function, and $\mathcal{L}(\theta)$ is the likelihood function. From $\mathcal{Z}$, we can then calculate the relative probability K^n_{n-1} that a number of components n returns a better fit than $n-1$ components:

$$K^n_{n-1} = \frac{P(\mathcal{M}_n)\mathcal{Z}_n}{P(\mathcal{M}_{n-1})\mathcal{Z}_{n-1}} = \frac{\mathcal{Z}_n}{\mathcal{Z}_{n-1}}, \tag{4.2}$$

where $P(\mathcal{M}_n)$ is the probability *a priori* of a model with n Gaussian components (for our case). We assume that all competing models are equally likely *a priori*, so $P(\mathcal{M}_n) = P(\mathcal{M}_{n-1})$.

We used the `gaussian` model in the Python package `pyspeckit` to fit the spectra with 1 and 2 Gaussian components for N_2H^+ and up to 3 Gaussian components for HC_3N. The third component in the case of HC_3N is to account for outflow emission. To run the nested sampling, we use `pymultinest` (Buchner et al. 2014), a package designed to connect Python to the Fortran-based package `MultiNest` (Feroz et al. 2009; Feroz & Hobson 2008). We use the python package `pyspecnest`[2] (Sokolov et al. 2020), a package designed to wrap the `pyspeckit` fitting classes to use them in `pymultinest`. We follow the steps and code used in Sokolov et al. (2020)[3].

From this process, we obtain the best fit parameters and their uncertainties for every spectra in the cubes with SNR>2. We adopted a conventional cut for K of $\ln K^n_{n-1} > 5$, so if $\ln K^n_{n-1} \leq 5$, we select $n-1$ components. We use this criterion to obtain a map with the number of components n in each pixel. There are small regions (consisting of less than 100 pixels) of emission in this map that are surrounded by noisy data, so we ran two additional steps to reduce the variation of n due to noise.

First, we eliminate small regions of consisting of n components surrounded by $n-1$ components or emission surrounded by noise, which we call islands, using the following thresholds:

- for islands where $n = 1$ in less than 100 pixels, we replace with $n = 0$
- for islands where $n = 2$ in less than 7 pixels, we replace with $n = 1$
- for islands where $n = 3$ in less than 2 pixels, we replace with $n = 2$

These thresholds are based on a visual inspection of the resulting fits, where islands with a size smaller than the threshold tend to fit noise peaks outside the observed emission range (5 to 10 $\mathrm{km\,s^{-1}}$). Nevertheless, the exact size of the islands does not influence the final results.

The second step is to filter the fit results using the parameter uncertainties. For our analysis we only use the fit results that have an uncertainty in central velocity smaller than the channel size. We evaluate each individual fit component to determine its quality. If the central velocity of one component has a larger uncertainty than the channel width, that

[2]https://github.com/vlas-sokolov/pyspecnest
[3]https://github.com/vlas-sokolov/bayesian-ngc1333

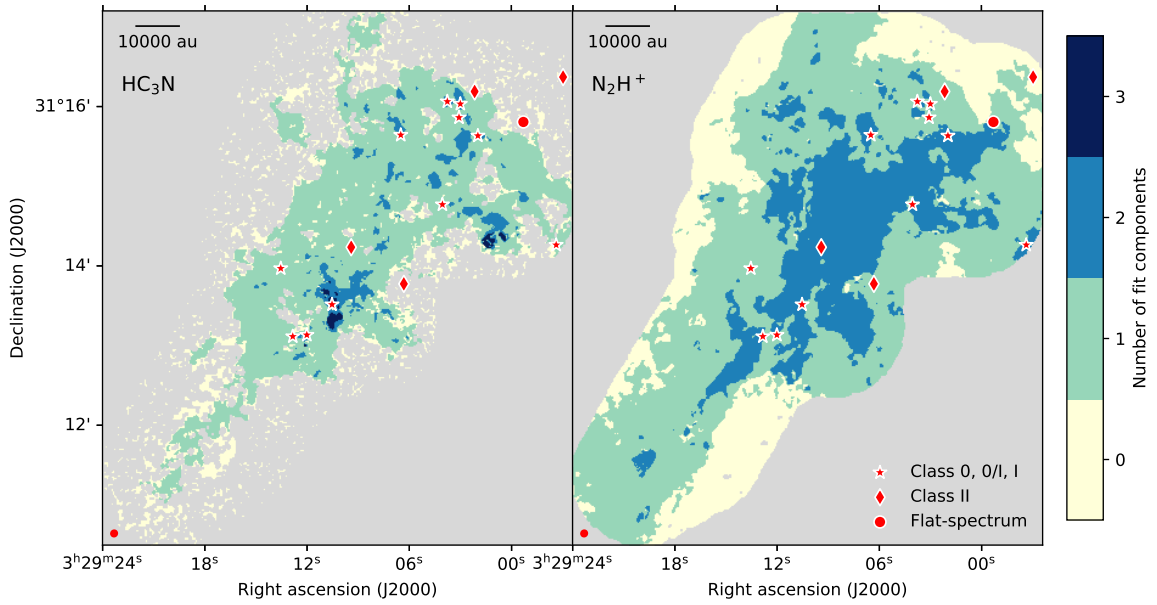

Figure 4.2: Resulting number of individual velocity components fitted along each line of sight for HC_3N (left) and N_2H^+ (right). The red symbols represent protostellar objects in the region as in Fig. 4.1. The gray regions correspond to pixels with SNR$\leq$ 2 or areas without data. The red ellipse at the bottom left corner of each plot represents the beam size.

component is eliminated, without affecting the other components that might be present in the same spectrum. The n map is updated accordingly, i.e. if there are 3 components in a pixel and one of them is eliminated, now $n = 2$ in that position. After this filtering, we obtain central velocities that have uncertainties between 0.03 and 0.05 km s^{-1} in for HC_3N and between 0.02 and 0.03 km s^{-1} for N_2H^+ .

Figure 4.2 shows the final number of Gaussian components per spectrum in the HC_3N and N_2H^+ emission cubes. We require up to 2 components for N_2H^+ and up to 3 in HC_3N to adequately fit the spectra, where the third Gaussian component in all cases was used to fit extended wings of emission in the HC_3N spectra. Section 4.4.1.1 describes these outflows in more detail.

4.3.2 Clustering of velocity structures

We cluster the individual velocity components of each of the molecular gas emissions to compare HC_3N emission with N_2H^+ emission. This comparison is not straightforward due to the presence of multiple velocity components distributed differently in both molecules. Figure 4.2 shows that N_2H^+ has mostly two velocity components at the center of the map, consistent with the observed overlapping fibers observed at lower resolution (approximately 30″) by Hacar et al. (2017) (in N_2H^+) and Chen et al. (2020b) (in in NH_3). However, HC_3N does not show this overlap, with regions of two and three velocity components

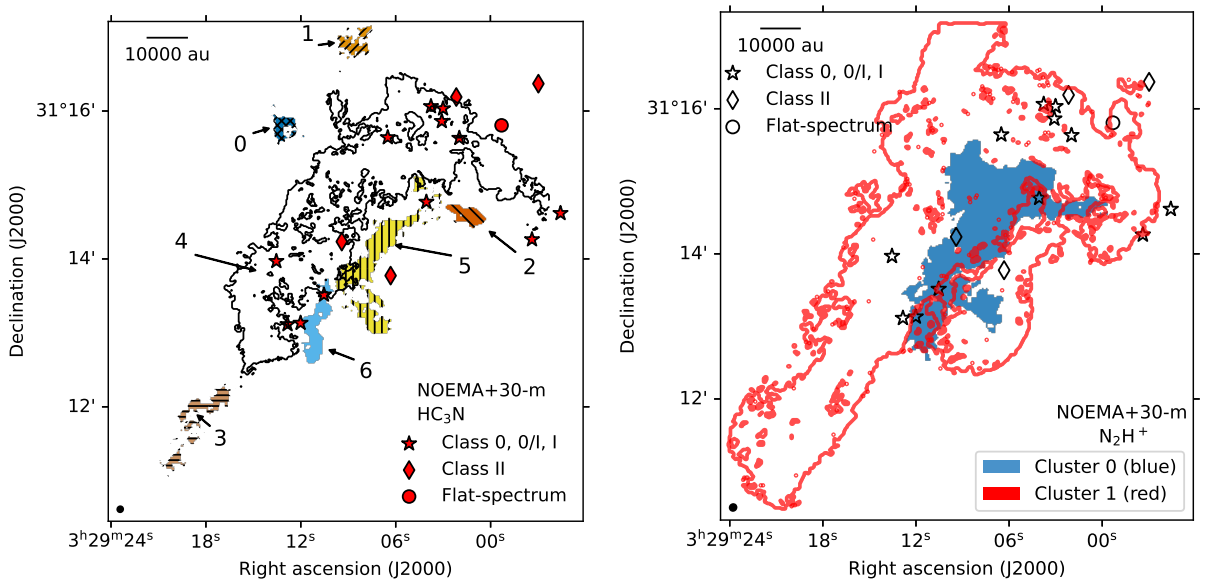

Figure 4.3: Results of the clustering algorithms for the Gaussian components of HC_3N and N_2H^+. The black circles at the bottom left corners represent the beam size of the respective data. The scalebar at the top left corner represents a length of 10 000 au. Left: cluster groups for HC_3N, labeled 0 to 6. Right: cluster groups for N_2H^+, labeled as red and blue representing the more redshifted and blueshifted groups, respectively.

scattered throughout the map. Therefore, it is not clear which Gaussian component in HC_3N should be compared with what N_2H^+ component. By clustering the Gaussian peaks, the comparison between both molecules is now possible.

We cluster the components using a density-based clustering algorithm because it is not possible to separate them manually using a simple velocity threshold. If we group all velocity components larger than a certain $v_{\rm LSR}$ together, it is possible we separate emission that is connected with the grouped emission but that has a large velocity gradient and so has components with a lower $v_{\rm LSR}$ than the threshold. A look at the velocities obtained after the nested sampling (Fig. C.3) shows that both molecules present complex velocity structures.

We describe all the details of the clustering process for each molecule in Appendix B.6. In summary, we use Hierarchical Density-Based Spatial Clustering of Applications with Noise (HDBSCAN) to find clusters of emission in position-position-velocity space. This algorithm is able to find clusters with varying density in space. We exclude from the clustering the Gaussian components with $\sigma_{\rm v} > 1$ km s^{-1}, as these trace outflow cones (Sect. 4.4.1.1). Figure 4.3 shows the resulting clusters and their labels. The complete set of properties (peak temperature, velocity and velocity dispersion) are in Fig. C.3 for HC_3N clusters and in Fig. C.4 for N_2H^+ clusters.

We recover the fiber structure observed in previous works with HDBSACAN in N_2H^+ emission. HDBSCAN recovers two clusters: we name cluster 0 the blueshifted (blue) fiber

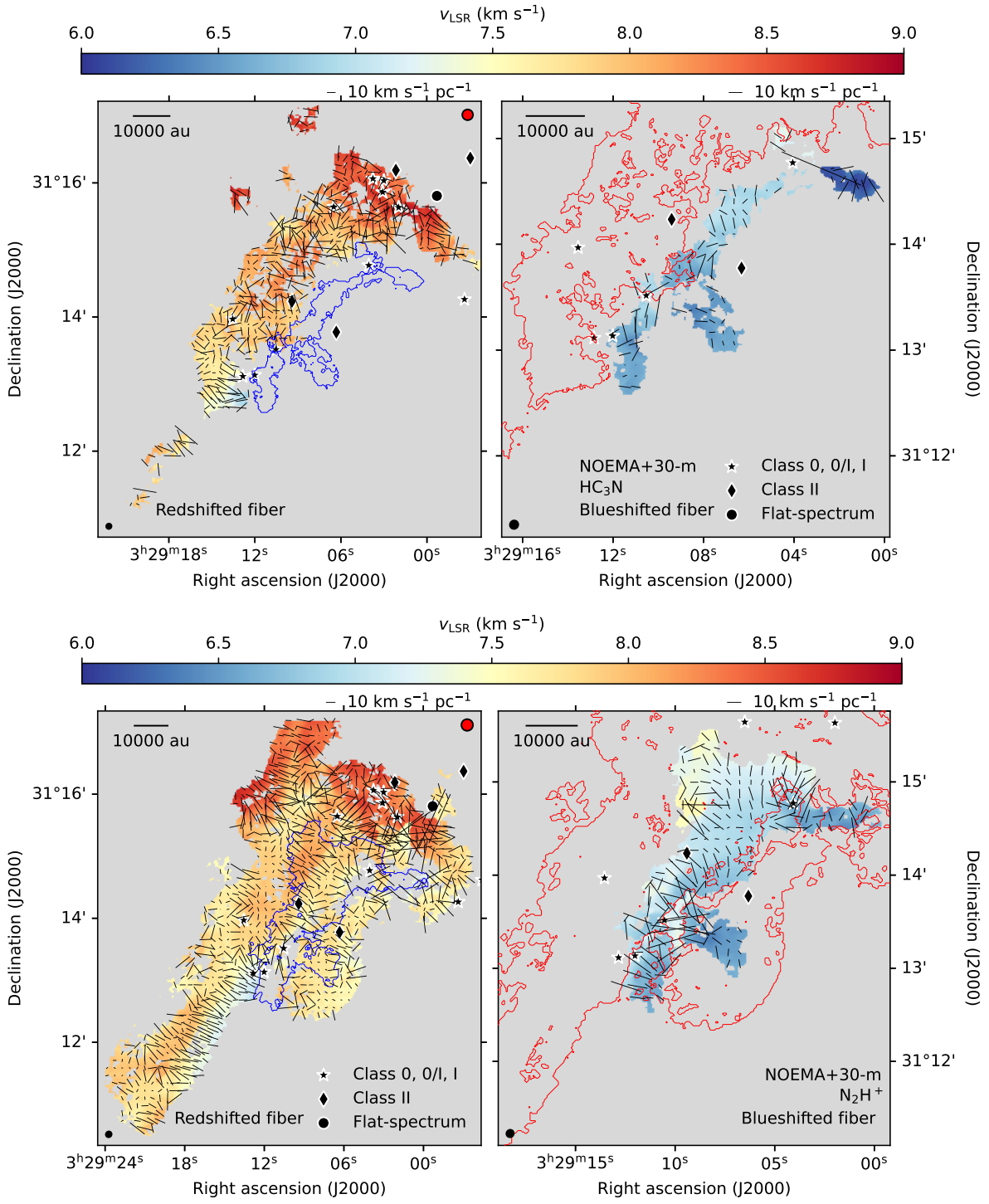

Figure 4.4: Resulting velocity groups for HC_3N and N_2H^+ emission after the clustering process. The left plots show the v_{LSR} of the redshifted fiber, whereas the right plots show the same for the blueshifted fiber. The blue contour marks the area occupied by the blueshifted fiber and the red contour, the redshifted fiber. The black symbols represent protostellar objects in the region as in Fig. 4.1. The black ellipse at the bottom-left corner of both plots represents the beam size. The black lines represent the velocity gradient directions measured at each position, with their size representing the gradient magnitude. The red circle at the top right corner of the left plot shows the size of the sampled area to calculate the gradients. The panels do not have the same spatial scales. Top: HC_3N emission v_{LSR} after grouping the clusters according to their velocities with respect to the N_2H^+ clusters.

and cluster 1, the redshifted (red) fiber as these resemble the fibers found in Hacar et al. (2017) and Chen et al. (2020b) where one has a larger $v_{\rm LSR}$ than the other. The clustering does not recognize a third separate fiber toward the SVS 13 region as in the case of Hacar et al. (2017). Figure 4.4 shows the $v_{\rm LSR}$ of each of the fibers. The redshifted fiber has an average $< v_{\rm LSR} >= 7.87$ km s^{-1} and the blueshifted fiber, $< v_{\rm LSR} >= 6.95$ km s^{-1}. The red cluster captures additional emission toward the northeast of the map, part of the Northeast (NE) filament (as named by Dhabal et al. 2019), and toward the west, which is part of the extended emission not covered by our observations but observed in N_2H^+ emission (Hacar et al. 2017).

The clustering in HC_3N, however, separates the emission into 7 clusters. There are no HDBSCAN parameters that give a similar clustering to N_2H^+. We group the HC_3N clusters into redshifted and blueshifted groups according to their velocity with respect to the average velocity of the N_2H^+ clusters, so as to compare their velocities (Sect. 4.4.1.2). Clusters in HC_3N which have an average velocity closest to the redshifted N_2H^+ fiber are altogether called redshifted fiber, and clusters closer in velocity to the blue N_2H^+ are grouped under the blueshifted fiber. The $v_{\rm LSR}$ of the resulting groups are shown in Fig. 4.4.

4.4 Results and analysis

4.4.1 Properties of the NGC 1333 SE gas

4.4.1.1 Correlation of HC_3N emission with outflows

Figure 4.5 left shows the integrated intensity of HC_3N together with the ^{12}CO $J = 2{-}1$ integrated emission maps toward the protostars, available from the MASSES survey (Stephens et al. 2019). We show the spectra at the locations where there are three Gaussians in the HC_3N cube (toward the north and south of IRAS 4A and toward the east of Per-emb 36) in Fig. 4.5 right. The spectra at these locations present extended wings: at the south of IRAS 4A, the wing is blueshifted with respect to the emission peak, and toward the north of IRAS 4A and the east of IRAS 2B, the wing is redshifted. All of these wings are fitted with one or two broad ($\sigma_{\rm v} > 2$ km s^{-1}) Gaussian components. The presence of these wings and their velocity (blueshifted or redshifted) coincide with the outflows shown in ^{12}CO $J = 2 - 1$.

The wings in the spectra close to IRAS 4A are caused by the outflow driven by IRAS 4A, but the bright HC_3N redshifted wing to the east of IRAS 2B coincides with the tip of the outflow lobe of IRAS 2A (also known as Per-emb 27). IRAS 2A is a binary system that has two outflows, one collimated in the east-west direction and a wider one in the north-south orientation (Plunkett et al. 2013). The redshifted lobe of the collimated outflow is toward the east and shows intense ^{12}CO emission at the same location of the brightest peak of the HC_3N integrated intensity map. Part of this redshifted ^{12}CO emission is at the eastern edge of the IRAS 2B MASSES image and the other part is at the western edge of the Per-emb 15 MASSES map. As this emission does not coincide with other protostars or

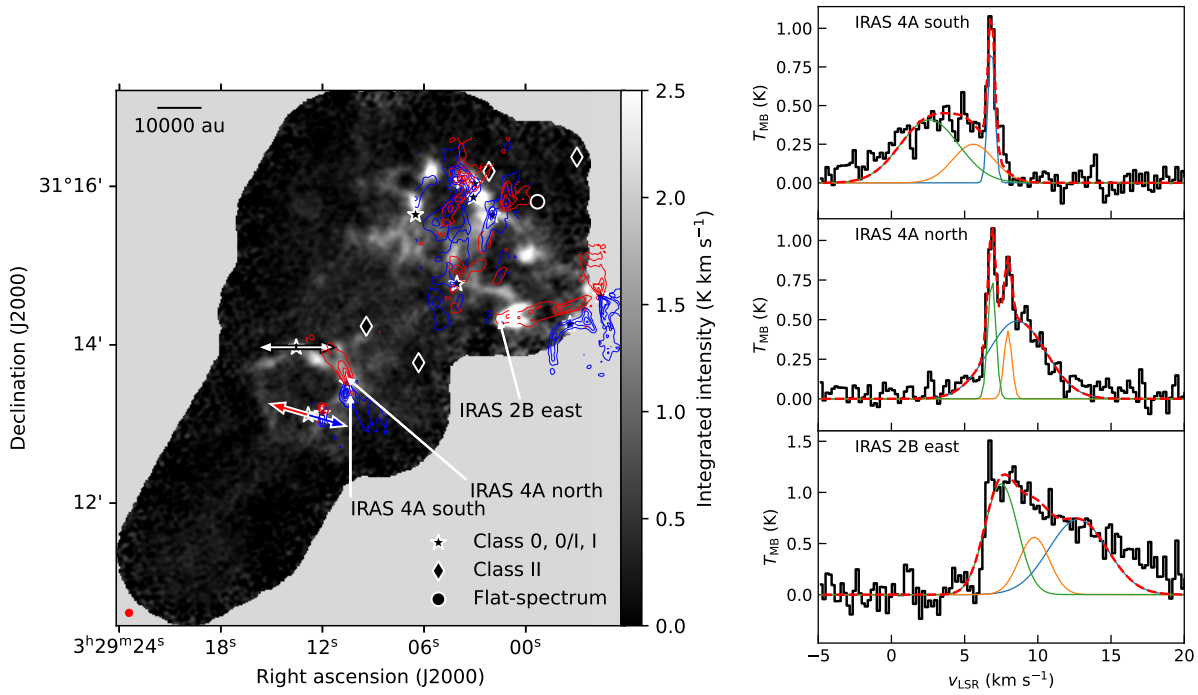

Figure 4.5: Correlation between the HC_3N emission and outflows. Left: Integrated intensity map of HC_3N (10−9) between 5 and 10 km s^{-1}. The red symbols represent protostellar objects in the region as in Fig. 4.1. The red and blue contours correspond to the ^{12}CO red and blue outflow lobes, respectively, obtained from the MASSES survey (Stephens et al. 2019). The labels indicate where each of the spectra is taken from. Right: HC_3N (10 − 9) spectra at the locations of the IRAS 4A outflow and at the bright emission to the east of IRAS 2B. For each location, we take the spectrum at an individual pixel. The blue, green and red curves represent the individual three Gaussians fitted at each position, and the red dashed curve represents the sum of all the Gaussians.

peaks in N_2H^+ emission, we conclude this HC_3N enhancement is a bow shock due to the outflow from IRAS 2A impacting the cloud material. In the HC_3N channel maps, between 6.5 and 6.9 km s^{-1} (Fig. 3.2), the images show a v shape at the position of the bright feature. We suggest this is due to the collision of the outflow lobe with cloud material, which produces a bow shock in the gas and enhances the presence of HC_3N.

Not all of the outflows cause wings in HC_3N emission. HC_3N is enhanced approximately along the IRAS 4C and IRAS 4B2 outflows (Fig. 4.5), but the directions of the enhancements are not over the position angles of the corresponding outflows. In the SVS 13 system, HC_3N emission is brighter at the locations of the protostars and extends all along the ridge that joins the protostars together, but does not present extended wings in the spectra. Moreover, comparing the ^{12}CO outflows from MASSES with the integrated HC_3N emission (without the outflow wings) in Fig. 4.5, HC_3N seems to be brighter *outside* of the regions covered by ^{12}CO, with the exception of the IRAS 2A and IRAS 4A outflows.

Therefore, the outflows influence HC_3N emission differently depending on the location, but in general, HC_3N seems to be enhanced at the outflow cavities, while tracing extended material in general.

4.4.1.2 Comparison between HC_3N and N_2H^+ velocities

We compare the extent and $v_{\rm LSR}$ of both molecules independently for each fiber. N_2H^+ is used as a proxy for the dense gas, as in Perseus N_2H^+ correlates well with locations of dense cores, where CO is depleted (Johnstone et al. 2010). Previous works in this region show that N_2H^+ follows the same structures as dust and NH_3, which means that N_2H^+ traces of the physical structure of each fiber (Hacar et al. 2017; Dhabal et al. 2019). HC_3N is a known "early type" molecule together with other carbon-chain molecules (such as CCS and cyclic-C_3H_2), meaning that in chemical models of molecular cloud collapse, these molecules appear at early times in comparison to, for example, nitrogen-bearing molecules (Suzuki et al. 1992; Bergin & Tafalla 2007). We used the channel maps together with the spectral decomposition made in Sect. 4.3 to describe the gas structure.

In general, HC_3N structure consists of several small peaks in emission connected via less bright, extended emission. The positions with the brightest HC_3N emission are correlated with the presence of outflows. However, there are three bright spots in the HC_3N integrated intensity map, located around the SVS 13 system, and one to the west of IRAS 4C, that have narrow ($\sigma_{\rm v,LSR}$) line profiles. HC_3N does not cover the full extent of the NGC 1333 SE filament nor each of the N_2H^+ fibers: the area covered by HC_3N emission is smaller than the one covered by N_2H^+ emission, as seen in Fig. 4.2, and is particularly scattered toward the filament tail in the south. HC_3N is detected inside the area defined for both fibers with N_2H^+ emission: in the redshifted fiber, HC_3N is roughly detected along the center, whereas in the blueshifted fiber HC_3N is detected only toward the west side of the fiber.

We compare the velocities traced by both molecules in each fiber. Figure 4.6 left shows the velocity difference between HC_3N and N_2H^+ $\delta v_{\rm LSR} = {\rm v}_{\rm LSR,HC_3N} - {\rm v}_{\rm LSR,N_2H^+}$. We reproject the HC_3N images of each velocity component to the pixel grid of the N_2H^+ cube, because the pixel size and beam is larger. Most of the redshifted fiber has HC_3N velocities that are larger than the velocity of N_2H^+ gas. The exception to this is a band that runs east to west below the SVS 13 area. The blueshifted fiber shows considerable differences between the molecules' velocities close to IRAS 4A and 4B, but in the rest of the gas, there is no apparent difference.

We evaluated if the values of $\delta v_{\rm LSR}$ are significant using the Kernel Density Estimate (KDE) of the differences between the $v_{\rm LSR}$ of both molecules. This KDE is in Fig. 4.6 right. The median difference is 0.11 km s^{-1} for the redshifted fiber and 0.01 km s^{-1} for the blueshifted fiber. $\delta v_{\rm LSR}$ for the red fiber is larger than the sum of the uncertainties in both ${\rm v}_{\rm LSR,HC_3N}$ and ${\rm v}_{\rm LSR,N_2H^+}$ obtained from the Gaussian fitting (0.08 km s^{-1}), and therefore show that the gas in both molecules presents different velocities. This is not the case for the blue fiber.

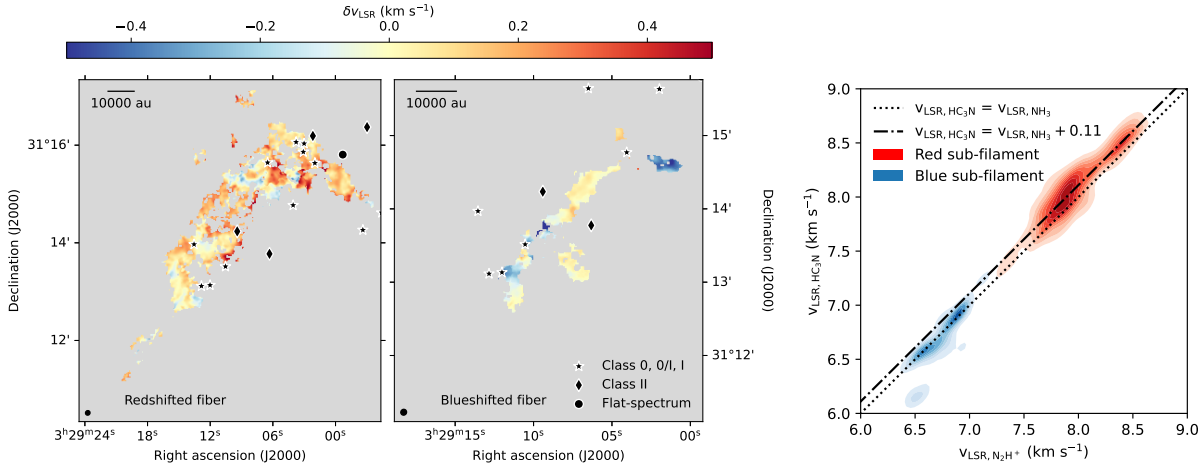

Figure 4.6: Difference between the velocity components of each fiber in NGC 1333 SE, as recognized after the clustering. Left: Resulting difference after subtracting the N_2H^+ v_{LSR} from the HC_3N v_{LSR} of the clusters belonging to the redshifted fiber. Middle: Resulting difference after subtracting the N_2H^+ v_{LSR} from the HC_3N v_{LSR} of the clusters belonging to the blueshifted fiber. Note that the blueshifted fiber map is zoomed into the region covered by the emission. Right: two-dimensional KDE of the HC_3N v_{LSR} versus N_2H^+ v_{LSR}. The dotted line represents the location where the velocities are equal, and the dash-dotted line, where the HC_3N v_{LSR} is larger by 0.11 km s^{-1} (the median difference for the redshifted fiber).

4.4.1.3 Velocity gradients within the fibers

We calculated the gradients present in the HC_3N and N_2H^+ velocity fields. The local velocity gradients describe the fluctuations of gas motion within the fibers, and will be of assistance to identify infall toward individual YSOs or binaries. We use a similar approach as used in Chen et al. (2022) and Valdivia-Mena et al. (2023). We calculated the local velocity gradient by fitting a plane centered at one pixel, with a width of 2 beams, so that we capture gradients in uncorrelated pixels. The plane is defined as:

$$v_{\rm LSR} = {\rm Ax} + {\rm By} + {\rm v_c}, \tag{4.3}$$

where A is the slope in the x (right ascension) direction and B in the y (declination) direction. We use the velocity gradient implementation within the `velocity_tools` package[4].

The resulting gradient orientations and magnitudes are plotted over the $v_{\rm LSR}$ of each fiber in Fig. 4.4 for HC_3N and N_2H^+. In both fibers, the velocity gradient field for HC_3N is more randomly aligned than for N_2H^+. This indicates that the gas traced by HC_3N presents larger changes at local scales, in part due to the effect of outflows in the region.

Both HC_3N and N_2H^+ show large (about 20 $\rm km\,s^{-1}\ pc^{-1}$) gradients within the fibers, almost completely perpendicular to the filament, in regions where there are no protostars. The gradient at the south of the blueshifted fiber in both molecules can be explained in part due to the fork that joins both fibers, but the continuation of this perpendicular gradients toward the southern tail of the redshifted fiber shows that this velocity gradient is intrinsic to the fiber.

Between IRAS 4 and SVS 13, the velocity gradients between both molecules are different. The N_2H^+ gradient vectors are more or less perpendicular to the length of the filament in the blueshifted fiber, but with a lower magnitude ($\lesssim 10\ \rm km\,s^{-1}\ pc^{-1}$). In the redshifted fiber, there is a region with a sudden change in velocity that produces local, perpendicular gradients of about 20 $\rm km\,s^{-1}\ pc^{-1}$, but in the rest of the region the local gradients are smaller than 5 $\rm km\,s^{-1}\ pc^{-1}$ and do not show clear patterns. On the other hand, HC_3N emission presents strong variations in the redshifted fiber, up to 30 $\rm km\,s^{-1}\ pc^{-1}$, but apparently randomly oriented, and roughly perpendicular with magnitudes between 10 and 20 $\rm km\,s^{-1}\ pc^{-1}$ in the blueshifted fiber.

4.4.2 Streamer candidates

We analyze the molecular tracers surrounding the YSOs in search for signatures of streamers. The observations in this work are designed to follow the flow from the larger scales of the filaments to the smaller, protostellar scales. We list the general properties of the YSOs within our field of view in Table 4.2.

The search for streamers in the region is done using the following signatures: we first looked for velocity gradients in our HC_3N and N_2H^+ maps where the difference between the $v_{\rm LSR}$ of our observations and the protostar increases as the distance between the gas and

[4]https://github.com/jpinedaf/velocity_tools

the protostar decreases. This is a common characteristic of streamers observed towards protostars and pre-main sequence stars (e.g. Thieme et al. 2022; Valdivia-Mena et al. 2022, 2023; Hsieh et al. 2023b). We analysed both the maps of the velocity gradients within clusters (Fig. 4.4) as well as the central velocities fitted to regions that were not clustered in Sect. 4.3.2. For embedded protostars (Class 0, 0/I and I), we used the $v_{\rm LSR}$ reported in the MASSES survey (Stephens et al. 2019) as protostellar velocity, obtained using a Gaussian fit to SMA $C^{18}O$ (2-1) emission observations within an area of 1.2″. If the velocity is not available in MASSES, we use the $v_{\rm LSR}$ reported in single-dish observations of DCN (Imai et al. 2018). For Class II sources, we used reported $v_{\rm LSR}$ values from APOGEE spectra (Foster et al. 2015; Kounkel et al. 2019). When the velocity of the protostar is not available from the previous observations, we adopt the velocity of N_2H^+ at the source location. Then, we determine if the velocity gradient comes from a preferential direction and is not a radial velocity gradient centered at the protostar. Finally, we observe if there is any elongated structure, such as bright lanes or peaks not centered at the protostar's location, in $T_{\rm MB}$. We define the region that makes up the potential streamer manually, while including emission within the SNR = 10 contours.

We construct sub-cubes of HC_3N and N_2H^+ emission and images of the Gaussian component properties (Sect. 4.3.1) and clusters (Sect. 4.3.2), centered at each protostar and including all pixels within a 10, 000 au radius. We choose 10, 000 au based on the longest confirmed streamer found to date (Pineda et al. 2020), which was characterized using HC_3N emission. We exclude from our analysis the broad components correlated with outflow activity seen in Sect.4.4.1.1. We expect HC_3N to reveal streamer motion, as streamers have been mostly observed in carbon-bearing molecules (Pineda et al. 2020), and N_2H^+ can give information about the surrounding envelope, but we also check the N_2H^+ velocity gradients. The beam of our HC_3N data is 4.9″, which corresponds to a length of almost 1500 au. Based on this, we are able to determine the presence of streamers (or asymmetric infall) using HC_3N that are at least $\sim$ 1500 au in projected length. We note that streamers can be longer in reality, but we are limited by their projected length in the plane of the sky unless we are able to model their infall kinematics, which is evaluated in each individual case. Therefore, our HC_3N data has the potential to reveal asymmetric infall of sizes typical of previously discovered streamers toward Class 0 and I protostars (Thieme et al. 2022; Valdivia-Mena et al. 2022, 2023). There is no detected HC_3N emission around ASR 53, EDJ2009-183 (ASR 106) and EDJ2009-173 (ASR 118), and Per-emb 27 (IRAS 2A) is out of the imaged area, so these sources are not analysed.

We find streamer candidates toward 7 out of the 16 YSOs from Table 4.2. In the following, we present the analysis of each individual protostar that has a streamer candidate. We present IRAS 4A first as it is the only one where there is enough resolution and information about its stellar properties to confirm its infall motion using a free-fall model. Figure 4.7 shows the peak brightness, velocities and streamer trajectory solution zoomed at the selected 10, 000 au scale. Figure 4.8 shows the same (except for the free-fall model) for the rest of the streamer candidates. We find no evident streamer candidates in IRAS 4B2, IRAS 4C (Per-emb 14), SVS 13B, SVS 13C and ASR 3.

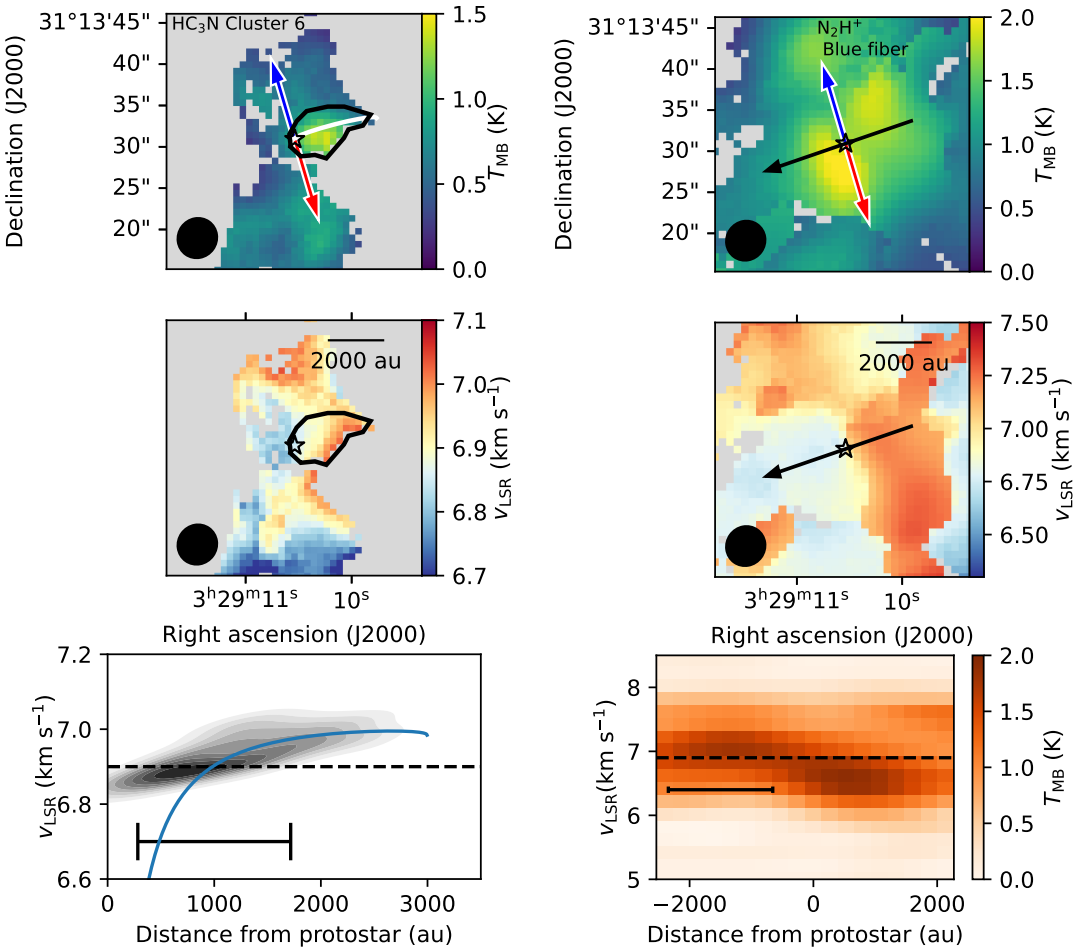

Figure 4.7: Zoom-in plots of HC_3N (left) and N_2H^+ (right) emission for IRAS 4A, together with the best free-fall trajectory found for the T_{MB} and v_{LSR} maps. Top: Amplitude T_{MB} of the Gaussian components corresponding to HC_3N cluster no. 6 and to N_2H^+ blue cluster. The black polygon marks the region selected as a potential streamer. The white curve marks the potential streamer's trajectory. The blue and red arrows indicate the direction of the outflow lobes for IRAS 4A and 4B, and the black arrow over the N_2H^+ map shows the orientation of the position-velocity diagram at the bottom. Middle: central velocities v_{LSR} of the Gaussian component. A scalebar representing 2000 au is at the top right of the image. Bottom left: KDE of the v_{LSR} within the selected region. The black line at the bottom of the plot represents a length of one beam. The blue curve marks the velocity versus the distance for the found free-fall solution. The black dashed line represents the protostar's v_{LSR}. Bottom right: N_2H^+ position-velocity diagram along the path indicated in the top panel. The dashed horizontal line marks the v_{LSR} of the source (6.9 $km\,s^{-1}$, Stephens et al. 2019). The black scalebar represents a length equivalent to one beam.

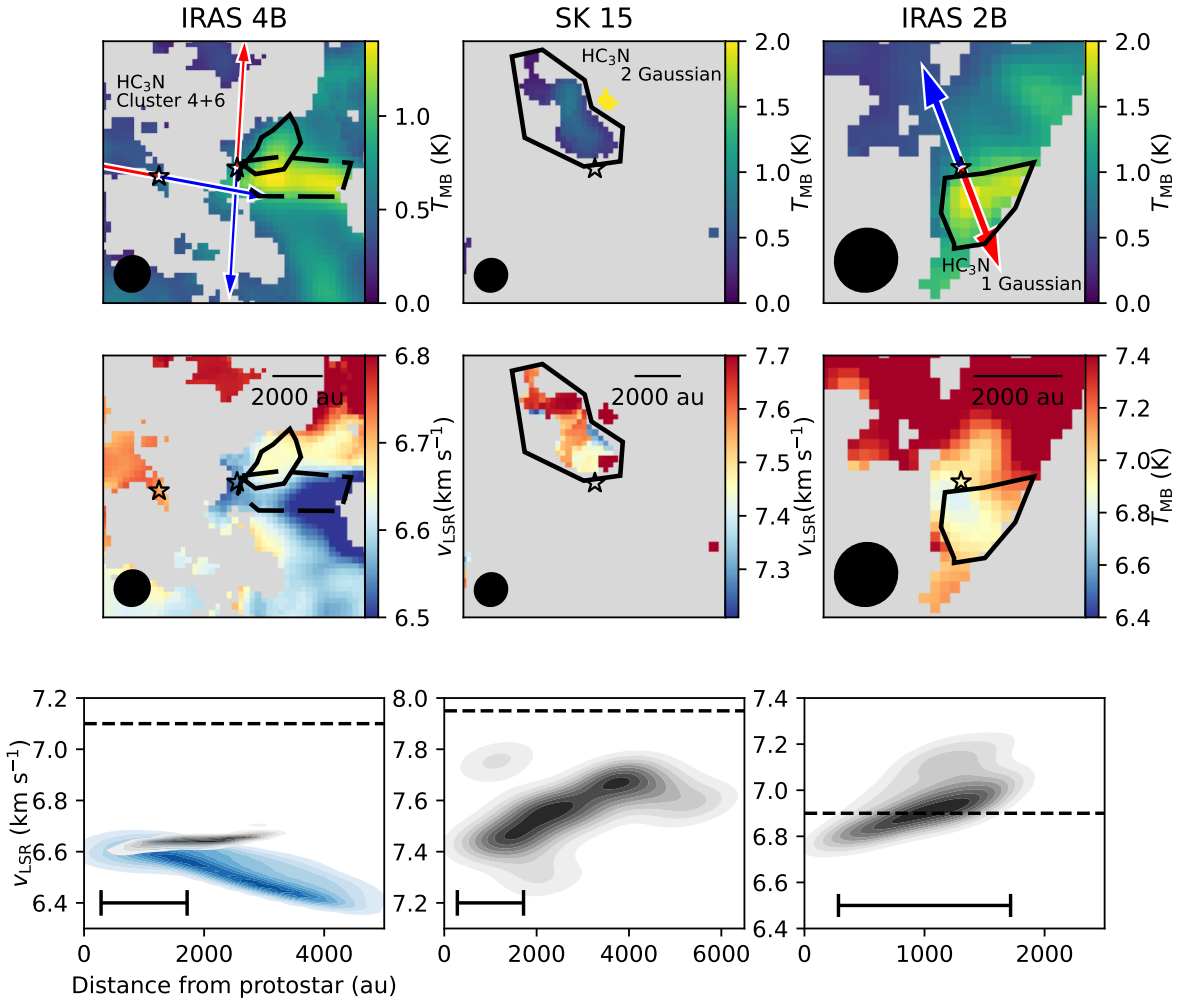

Figure 4.8: Zoom-in plots of HC_3N emission for IRAS 4B (left), SK 15 (center) and IRAS 2B (right), with the same panels as shown in Fig. 4.7 left. The Gaussian component for each protostar is labeled accordingly. The black polygon marks the region selected as a potential streamer. The black ellipse at the bottom left corner represents the beam. For IRAS 4B, the dashed black polygon represents the region analyzed in relation to IRAS 4B2. Top: Amplitude T_{MB} of the Gaussian component plotted. The blue and red arrows indicate the direction of the blueshifted and redshifted outflow lobes, respectively, for known outflows in the plotted area. Middle: Central velocity v_{LSR} of the Gaussian component selected. The scalebar represents a length of 2000 au. Bottom: KDE of the v_{LSR} within the selected region. The black density histograms represent the KDE of the velocities within the black polygons. The dashed lines mark the v_{LSR} of each protostar. The black scalebar represents a length equivalent to one beam. For IRAS 4B, the blue KDE represents the velocities within the dashed polygon.

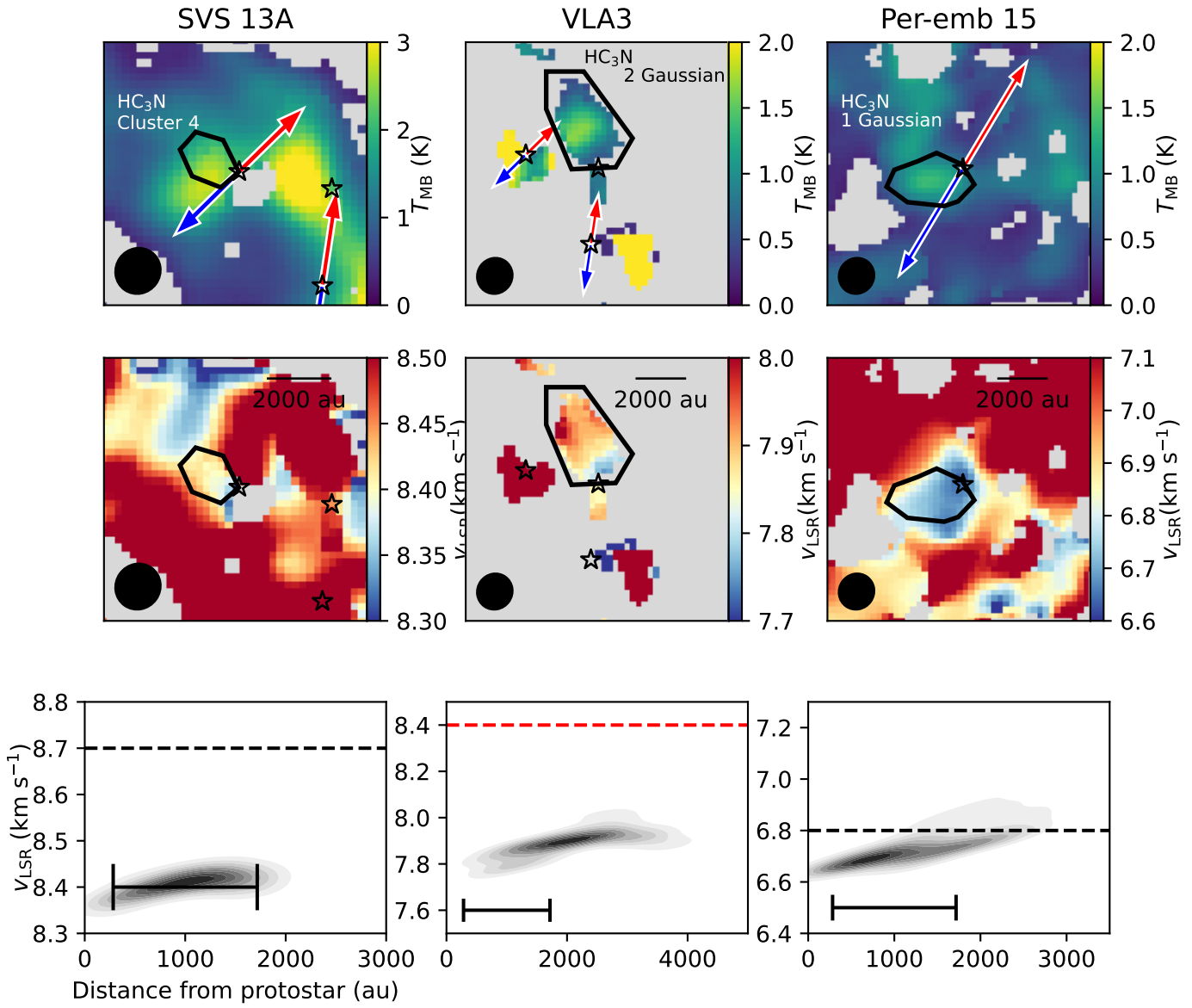

Figure 4.8 (cont.): Zoom-in plots of HC_3N emission for SVS 13A (left), VLA 3 (center) and Per-emb 15 (right), with the same panels as shown in Fig. 4.7 left. For VLA 3, the red dashed line marks the v_{LSR} of the fiber component toward the position of the protostar.

4.4.2.1 IRAS 4A

IRAS 4A is a Class 0 protostar that drives a strong outflow, described in several previous works (e.g., Plunkett et al. 2013). We also observe the effect of this outflow in the HC_3N emission (Sect. 4.4.1.1). We examined the different cutout images for the surroundings of IRAS 4A and found a region with a velocity gradient consistent with infall motion. There is an increase in T_{MB} toward the west of the protostar in the HC_3N cluster no. 6, part of the blueshifted fiber. We show the T_{MB} of this cluster in Fig. 4.7 top left. This region has a velocity gradient from west to east, which we show in Fig. 4.7 bottom left: at approximately 2500 au from IRAS 4A, HC_3N gas has a $v_{LSR} = 7.0$ km s^{-1}, whereas closer to the protostar it reaches $v_{LSR} = 6.85$ km s^{-1}. The uncertainty in the fitted velocity is 0.03 km s^{-1} on average for this region, so the difference between both extremes is significant. Therefore, we define this region as a streamer candidate in HC_3N emission.

We were able to confirm that this velocity profile is consistent with free-fall infalling gas toward the protostar. Using the methods detailed in Pineda et al. (2020) and Valdivia-Mena et al. (2022), we modeled the velocity gradient in the image plane and the velocity plane, assuming a free-fall, ballistic trajectory from Mendoza et al. (2009). We retrieve the disk inclination from the VANDAM survey results (Segura-Cox et al. 2018) and the position angle from the MASSES survey (Lee et al. 2016). We only used the mass of the envelope determined in Jørgensen et al. (2007), $M_{env} = 2.3$ M$_\odot$ for the total mass of the system, which is a good enough approximation to model the free-fall for a Class 0 protostar, as most of the mass is in the envelope. Table 4.3 shows the set of parameters that can approximately reproduce the KDE of the observed HC_3N velocities within a region that surrounds the T_{MB} peak area. The resulting trajectory from these parameters is plotted in Fig. 4.7 left. We note that this is a rudimentary adjustment of these velocities, and that the region we believe the streamer to cover has an equivalent size of two beams. At scales smaller than ~ 1000 au from the protostar, the best free-fall solution diverges from the observed v_{LSR} distribution as there are possibly other gas components within the beam (for instance, protostellar envelope and disk rotation). Our current resolution limits our interpretation to scales larger than about 1500 au. Higher resolution observations of HC_3N line emission will allow for a better trajectory modelling.

The N_2H^+ velocity profile is significantly different than what HC_3N shows in this region. IRAS 4A is located at $\approx 4''$ from a local N_2H^+ peak, as seen in Fig. 4.7 top right. There is a velocity gradient from redshifted to blueshifted velocity with respect to the protostar's v_{LSR} (6.9 km s^{-1}) going from west to east (Fig. 4.7 middle right). The eastern side of this gradient is blueshifted with respect to the protostar's v_{LSR} and is brighter than its redshifted counterpart. We made a position-velocity (PV) cut perpendicular to the outflow direction, shown in Fig. 4.7 bottom right. The shape of the N_2H^+ PV diagram is suggestive of rotation within the envelope surrounding the protostar. IRAS 4A is expected to be within an envelope as it is classified as a Class 0 source. In previous works, gas surrounding IRAS 4A was found to be infalling (Belloche et al. 2006). This profile then could be associated with a rotating-infalling envelope.

Parameter	Unit	Value
ϑ_0	deg	92
φ_0	deg	-5
r_0	au	3000
$v_{r,0}$	$km\,s^{-1}$	0
Ω_0	s^{-1}	2.3×10^{-13}
i^*	deg	-35
P.A.**	deg	19

Table 4.3: Parameters of the trajectory that best reproduce the HC_3N observations around IRAS 4A. *Angle obtained from the disk inclination (Segura-Cox et al. 2018). **Angle obtained from the outflow direction (Lee et al. 2016).

4.4.2.2 IRAS 4B

IRAS 4B is a Class 0 protostar that is to the southeast of IRAS 4A. Together with IRAS 4B2 they form a binary system. There is a bright HC_3N emission perpendicular to the outflow that dominates the emission around IRAS 4B, marked with a dashed black polygon in Fig. 4.8 left. The direction of the lane coincides with the direction of the IRAS 4B2 outflow (Fig. 4.8 left) and the velocity of this lane increases with increasing distance, so this bright lane is probably not asymmetric infall. However, at a 45 deg angle from this lane, there is another signature of extended HC_3N emission, fitted with one Gaussian and belonging to cluster no. 6, and therefore part of the blueshifted fiber seen in Sect. 4.3.2. This smaller region is marked with a black polygon in Fig. 4.8 top left. This bright emission has a velocity gradient that is consistent with infall toward IRAS 4B, based on the KDE of the observed velocities in Fig. 4.8 bottom left (black KDE). The difference between the $v_{\rm LSR}$ of the protostar and the $v_{\rm LSR}$ of the candidate at the beginning of the streamer (at about 3000 au, Fig. 4.8) is about 0.4 $km\,s^{-1}$, which indicates that, to model this with a streamline model, we may require an initial radial velocity $v_{r,0} \neq 0$. Nevertheless, the central velocity of this protostar has been reported between 6.8 and 7.1 (Imai et al. 2018; Stephens et al. 2019). We choose the value from (Stephens et al. 2019) as it is the one obtained with the best resolution.

At the position of IRAS 4B, there is a local N_2H^+ brightness peak. By doing a PV cut on the direction perpendicular to the outflow direction (Fig. C.5 left), we observe that this peak is slightly blueshfted with respect to the protostellar $v_{\rm LSR}$. There is no sign of a rotating or infalling envelope in the N_2H^+ surrounding either IRAS 4B or 4B2: both regions are dominated by emission at fiber scales.

4.4.2.3 SK 15

SK 15 (from the nomenclature of Sandell & Knee 2001) is a Class I protostar toward the southeast of SVS13A. Its $v_{\rm LSR}$ is estimated between 8 $km\,s^{-1}$ (Imai et al. 2018) and 8.1 $km\,s^{-1}$ (Higuchi et al. 2018). To the best of our knowledge, it does not have an observed

outflow of its own, but lies close to the outflow driven by SVS 13A (northern part of the map in Fig. 4.5). We found a streamer candidate in HC_3N emission in the two-Gaussian fit around this protostar (Fig. 4.8 center). One of the HC_3N Gaussian components is part of cluster no. 4, within the redshifted fiber (Fig. 4.3), whereas the other is recognized as noise by HDBSCAN. This extra component is the weakest of the two in $T_{\rm MB}$ (0.5 K versus 2.2 K). Looking at the component that is not part of the larger filament, the tail-shaped extension has a velocity gradient that gets more blueshifted with respect to SK 15's $v_{\rm LSR}$ as gas gets closer to SK 15 (Fig. 4.8 center).

SK 15 is located within 7″ of a N_2H^+ $T_{\rm MB}$ peak. This peak is located at the position of the streamer candidate (Fig. C.5 middle). In this peak, there are two Gaussian components in the N_2H^+ spectral decomposition (Sect. 4.3.1). The component responsible for the $T_{\rm MB}$ peak has a $v_{\rm LSR}$ of approximately 8.1 $\rm km\,s^{-1}$ and belongs to the redshifted fiber. The other component, not clustered by HDBSCAN, has similar $v_{\rm LSR}$ to the HC_3N emission that we consider as streamer candidate, but it does not show a velocity gradient.

4.4.2.4 IRAS 2B

IRAS 2B (also known as Per-emb-36, Enoch et al. 2009) is a Class I protostar located at the western edge of the ProPStar map. There is denser gas beyond the edge of the map, as shown in previous works covering this region in, for instance, NH_3 (Friesen et al. 2017; Dhabal et al. 2019). Towards this edge, we find a bright extension of HC_3N gas that has a gradient from redshifted to blueshifted $v_{\rm LSR}$ with respect to IRAS 2B's $v_{\rm LSR} = 6.9$ $\rm km\,s^{-1}$ (Fig. 4.8 right). This region is about the size of the HC_3N beam. We consider this as a streamer candidate as it shows a velocity gradient almost perpendicular to the outflow direction, although the complete gradient is contained within a beam. The brightness distribution suggests the streamer candidate could continue beyond the extend of the HC_3N map.

The N_2H^+ map also shows that the dense gas emission continues to the right of IRAS 2B. Previous N_2H^+ observations from Dhabal et al. (2019) show that there is considerable emission outside our coverage, toward the west of IRAS 2B, so we only get a glimpse of the kinematics toward the east of IRAS 2B. Figure 4.2 shows that toward the northwest and southeast of the protostar, N_2H^+ emission can be fit with two Gaussians. We take a PV cut perpendicular to the outflow direction, shown in Fig. C.5 right. Within 4000 au from the protostar at each side, we see no clear indication of a rotating envelope, so we conclude that the N_2H^+ emission is dominated by the fiber kinematics.

4.4.2.5 SVS 13A

SVS 13A, also known as Per-emb-44 (using the nomenclature of Enoch et al. 2009), is a Class 0/I close binary system (separated by approximately 70 au, Anglada et al. 2000). It drives powerful outflows and jets that dominate the CO emission of this region (Plunkett et al. 2013; Stephens et al. 2019). There is a detected streamer toward this source seen in DCN emission by Hsieh et al. (2023b). The cut HC_3N images toward SVS 13A show a

beam-sized region consistent with the velocity gradient shown by Hsieh et al. (2023b). The HC_3N cluster no. 4 shows a sudden drop in v_{LSR} at the position of SVS 13A (Fig. 4.8 (cont.) left). The fiber's v_{LSR} around SVS 13A is between 8.4 and 8.5 km s^{-1}, and in the region where the streamer was found using DCN the velocity drops down to approximately 8.3 km s^{-1}. This change is similar to the velocity gradient observed in the SVS 13A streamer (Hsieh et al. 2023b, in their Fig. 6). However, the HC_3N brightness distribution is difficult to interpret as this particular streamer. As seen in Fig. 4.8 (cont.) top left, there is a local peak in T_{MB} located at 4.5″ east from the SVS 13A. This peak might blend with the less bright emission from the streamer. It is also possible that the streamer is small, about the size of our beam ($\sim$ 1500 au), and at this resolution, any HC_3N emission coming from the streamer is blended with the larger, fiber-dominated emission. Nevertheless, we are able to detect the small velocity gradient even in the blended image, which means that it is possible that HC_3N emission traces the streamer toward SVS 13A. A higher spatial resolution image should be able to separate the emission corresponding to the fiber and the streamer.

SVS 13A lacks an N_2H^+ peak. The brightest peak near SVS 13A is located on SVS 13B to the southwest. We plot a PV diagram centered on SVS 13A and in the direction perpendicular to the outflow in Fig. C.5 (cont.) left. Chen et al. (2009) show that SVS 13B and VLA 3 are embedded in the same core, which shows signs of rotation. Therefore, to the west, the N_2H^+ velocity field is dominated by the SVS 13B and VLA 3 joint core. To the east, the velocity field is dominated by the extended N_2H^+ component tracing the redshifted fiber.

4.4.2.6 VLA 3

VLA 3 is a protostellar source located 10″ toward the west of SVS 13A. It does not have an outflow direction on record, nor information about a potential disk. However, it lies on the path of the SVS 13B outflow. As mentioned in Sect. 4.4.2.5, VLA 3 and SVS 13B are embedded in a common core, suggesting these two sources are forming a bound binary system (Chen et al. 2009). As with the case of SK 15, one of the HC_3N Gaussian components located near VLA 3 is part of the redshifted fiber, within the HDBSCAN cluster no. 4. The other HC_3N Gaussian component was categorized as noise by the clustering algorithm. Looking at this remaining component, there is a velocity gradient that points toward VLA 3. We show the T_{MB} map and the observed velocities in the region of the streamer candidate in Fig. 4.8 (cont.) center. As there is no recorded velocity for this protostar, we use the N_2H^+ fiber velocity at the location of VLA 3 (v_{LSR} = 8.4 km s^{-1}) as reference. The difference between the v_{LSR} of the HC_3N gas and the N_2H^+ v_{LSR} decreases with increasing distance from VLA 3. We also plot the outflow directions of SVS 13A and 13B to see if they interfere with the HC_3N gas that could potentially trace a streamer. The selected HC_3N component is not affected by the outflow: the redshifted cones of SVS 13A and 13B have $v_{LSR} > 10$ km s^{-1}, whereas the HC_3N emission from this Gaussian component is lower than 8 km s^{-1}; the HC_3N velocity dispersion is average for its surrounding cloud (0.2 km s^{-1}); and finally, there is no discernible velocity gradient in

the direction of the outflows (northwest).

Also similar to SK 15, there is a local N_2H^+ peak at the position of the streamer candidate to the north of VLA 3, with two Gaussian components (Fig. C.5 middle). Unlike the case of SK 15, the region where there are two Gaussian components is smaller than the area covered by the HC_3N streamer candidate, barely the size of the N_2H^+ beam. The Gaussian component responsible for the peak is within the cluster that makes up the redshifted fiber and has a velocity of about 8.51 $km\,s^{-1}$. The second, weakest component shows an almost constant velocity between 7.88 and 7.91 $km\,s^{-1}$, similar to the velocity of the streamer but without a clear gradient.

4.4.2.7 Per-emb 15

Per-emb-15 (also known as SK 14, Sandell & Knee 2001; Enoch et al. 2009) is a Class I protostar located toward the south of the SVS 13 system. Within the HC_3N single Gaussian fit, there is a velocity gradient within a local T_{MB} peak (Fig. 4.8 (cont.) right). This structure was not recognized in the HDBSCAN as part of any cluster, possibly because it is located where the fibers overlap. Inspection of the HC_3N spectra confirms that there is a well-fitted single Gaussian component along the defined region, and not two Gaussian components fitted as one. The HC_3N velocity gradient follows the expected direction for asymmetric infall toward the protostellar disk (Fig. 4.8 (cont.) bottom right).

Per-emb 15 has no N_2H^+ peak within a beam of its location. the closest N_2H^+ brightness peak is at about 18″ to the northwest, where the outflow traced by MASSES seems to end. The N_2H^+ emission of cluster no. 2 shows a blueshift in velocity toward the protostar. This is more clear in Fig. C.5 (cont.) right. We made a PV diagram perpendicular to the outflow direction, shown in Fig. C.5 (cont.) right bottom. This diagram is dominated by the emission from the fibers, as this source is located where the two fibers overlap in our line of sight. The blueshifted emission might be produced by the protostar or might be part of the velocity gradient seen in the fiber and caused by gas infall toward the fiber spine.

4.5 Discussion

4.5.1 Infall of gas onto the fibers

Our results suggest that HC_3N and N_2H^+ trace different structures toward NGC 1333 SE. First, both molecules follow the filament direction, but their distributions are different. N_2H^+ recovers more area within the fibers located in this region (Sect. 4.3.1), whereas HC_3N is more patchy and is affected by the presence of outflows (Sect. 4.4.1.1). Part of the difference in their structure can be due to the different densities traced, where HC_3N $(10-9)$ molecular line has a critical density about an order of magnitude higher than the N_2H^+ $(1-0)$ line, as well as a higher E_{up} (Table 4.1). HC_3N has a higher T_{peak} closer to the protostars. However, we also detect a systematic redshift of HC_3N with respect to N_2H^+ in the case of the redshifted fiber, as shown in Sect. 4.4.1.2. This result shows that

the kinematics of the HC_3N gas are different from N_2H^+ gas in the redshifted fiber, and thus, the HC_3N is not part of the dense fiber structure but traces dense gas that is less chemically evolved than the gas in the fibers.

For the blueshifted fiber, the difference along the line of sight is not significant when compared to the velocity uncertainties (Sect. 4.4.1.2). However, it is possible that this is a projection effect and that the motion of HC_3N with respect to N_2H^+ is mostly perpendicular to our line of sight. Previous works have suggested that gas is being pushed by an expanding bubble, responsible for the formation of the filament, from the southwest of IRAS 4A (Dhabal et al. 2019; De Simone et al. 2022). HC_3N emission traces the blueshifted fiber only toward the west side, which fits into this picture if this newly deposited gas is moved by this expanding shell. We note that close to IRAS 4A and 4B, HC_3N gas is considerably blueshifted with respect to N_2H^+ gas. This is due to the effect of the outflows of these two protostars that stir the fresh gas more than the dense core structure (traced by N_2H^+).

Given the different kinematics and structures traced, we propose that the HC_3N emission represents a layer of chemically fresh material feeding the fibers. In chemical models of low-mass star forming regions, HC_3N appears at earlier times (a few 100 kyr from $t = 0$) than nitrogen-bearing molecules like N_2H^+ (Bergin & Tafalla 2007; Sakai & Yamamoto 2013), as nitrogen chemistry starts from neutral-neutral reactions, which are much slower than the ion-neutral reactions that dominate the carbon chemistry. HC_3N has also been suggested as a product of outflow shock fronts (Shimajiri et al. 2015), and in our work we observe that outflows help to stir the gas traced in HC_3N, but we do not include the velocity components of HC_3N with outflow wings in our clustering (Sect. 4.3.2) and subsequent structures' analysis. This ensures that the HC_3N gas that we compare with N_2H^+ is not affected by possible shock chemical enhancement. This indicates that there is chemical replenishment, delivered from the patchy structure seen in HC_3N. The fact that HC_3N is detected in a smaller extension and is patchy with respect to N_2H^+ suggests that the region could be more chemically evolved than other regions in Perseus, e.g. in Barnard 5, where HC_3N is more extended than the filaments' structures traced by NH_3 (Valdivia-Mena et al. 2023). Nevertheless, there is still some fresh material for star formation, in the shape of sparsely distributed gas.

The presence of N_2H^+ perpendicular gradients in both fibers suggests that gas falls toward the fiber spines. These are most prominent toward the south of the filament, where there are no protostars. These kind of gradients are also described for this region in Dhabal et al. (2018) and Chen et al. (2020b). Dhabal et al. (2018) suggested the presence of a global velocity gradient for what they call subfilament A, which corresponds in velocity to our redshifted fiber, but it was unclear for their subfilament B, corresponding approximately in $v_{\rm LSR}$ with our blueshifted fiber. We confirm that there is also a perpendicular velocity gradient for the blueshifted fiber in N_2H^+. As suggested in these previous works, the velocity gradients observed in the fibers can be related to accretion flow toward the fibers, seen as contraction of a sheet-like cloud (Chen et al. 2020a). The velocity gradients could also be consistent with fiber rotation, but in simulations of filament formation, these motions do not seem favorable in fibers (Smith et al. 2016). HC_3N also shows prominent perpendicular velocity gradients where there are no protostars, but the regions which follow

this motion are smaller. In general, the gradients in HC_3N tend to change more drastically near protostars (Fig. 4.4 top). This suggests that the presence of the protostars stirs the surrounding gas, which is reflected in more complex gas motions at smaller scales.

4.5.2 Discovery of streamer candidates in NGC 1333 SE

We found streamer candidates toward 7 out of 16 YSOs within our field of view. Moreover, we confirmed the infalling motion toward one of them (IRAS 4A). For the rest of the candidates, we do not have enough spatial resolution or information about the protostar and disk masses to efficiently model the free-falling gas. What we can say about their three-dimensional structure is that these streamers come from behind the protostars, as they all become more blueshifted with respect to the protostellar $v_{\rm LSR}$ with decreasing distance. The streamer candidates in our work were found towards Class 0, 0/I and I protostars. This represents a streamer frequency of approximately 40% if we consider all the YSOs within the maps' field of view. If we consider only the early stage protostars (Class 0 to I, for which we have 12 within the map), the frequency of streamers is higher, about 60%. Although these are small number statistics, it is a first approach to quantify the prevalence of streamers toward YSOs (if we are able to confirm the infall nature of the emission in the future).

This is a first coarse estimate to the real frequency of streamers in the area, as these are candidates still not confirmed dynamically, and it is possible we have missed streamers. First, we miss any streamer that is smaller than approximately 1500 au in projected length, as that is our resolution limit. This decreases our chances to find small streamers and also those almost fully contained along our line of sight. In particular, this limits our chances to find Class II streamers (of which we do not find any), as they are usually on the order of 300 to 500 au (Garufi et al. 2022; Ginski et al. 2021), although longer arms of up to $\sim$ 2000 au surrounding T Tauri disks have been suggested to be streamers (Alves et al. 2020; Huang et al. 2021, 2022). Most Class II sources in the field have no detected HC_3N emission: only one Class II source (ASR 54) has HC_3N emission detected around it, and its velocity structure is not suggestive of streamer motion, but appears dominated by the infall of fresh gas into the fiber. This does not mean that there are no streamers toward these sources, but the tracer (HC_3N) and/or the resolution are not adequate to find streamers toward these sources. Secondly, the assumption of monotonically decreasing velocity with distance along the line of sight can miss streamers. This assumption helps to recognize infalling motion and to differentiate it from outflowing gas, but there are instances where a streamer will not show this kind of gradient along the line of sight. If the acceleration is completely contained in the plane of the sky, the observed $v_{\rm LSR}$ of the gas is constant. It is also possible that, due to projection effects, the velocity appears to be monotonically *increasing*, such as in the case of Per-emb 2 (Pineda et al. 2020). This streamer was confirmed using the free-fall analytic solution from Mendoza et al. (2009). As an acceleration proportional to distance is usually attributed to outflowing gas, it is necessary to take other factors into account (like the shape of the emission and the position of the known outflow) to disentangle outflowing emission from inflowing gas. Considering the spatial and spectral

resolution of our HC_3N data and the median velocity gradient found in our streamers (~ 15 km s^{-1} pc^{-1}), the probability to miss a streamer is about 50%, either because it is contained along our line of sight or close enough to the plane of the sky that its gradient is not observable.

We define the structures found in this work, including toward IRAS 4A, as streamer candidates. The limiting factors at the time of describing the structure of the streamers is the lack of angular resolution and the lack of information about the protostar and disk masses. We show that HC_3N traces infall given the velocity of the gas that surrounds a protostar and the location of the local velocity gradient, but we do not have enough information about the protostars themselves to confirm that the velocity profiles correspond to free-fall. To confirm the streamer nature of these candidates, it is necessary to replicate their structure (a thin and long structure in $T_{\rm MB}$ and a velocity gradient) with a free-fall model. In the case of IRAS 4A, even if we could model the infall, the resolution is not high enough to describe the structure in the image plane. Therefore, we require follow-up observations with a resolution higher than 4.9″ to fully describe the structure of these streamers.

4.5.3 Relation of streamers to the larger gas infall

Our results indicate that the gas that builds up the streamers comes from beyond the fibers. There are three main reasons for this conclusion. First, we do not see signs of infall using N_2H^+. The N_2H^+ $v_{\rm LSR}$ close to each protostar is different than the HC_3N $v_{\rm LSR}$, and we do not observe stream-like structures in N_2H^+, although this could be due to projection effects. Second, by construction, the structure of the fibers is traced using N_2H^+, and we observe significant differences in the central velocities of the redshifted fiber with respect to the HC_3N flows within. In the case of the blueshifted fiber, we do not see a significant difference (Sect. 4.4.1.2). However, this might be a projection effect, where we do not see signs of any kinematic difference because the movement is along the plane of the sky. Third, the apparent direction of the streamer candidates does not coincide with the orientation of the filament.

Our results suggest that the mass that composes the streamers does not come from the fiber structure, but from the fresh gas that is infalling toward the fibers. Although HC_3N can be enhanced by the presence of outflows, we took out the velocity components affected by outflows for this analysis, so the streamer gas being chemically fresh is the most probable origin. A similar relation between gas outside the filament and streamers is suggested for Barnard 5, another region in Perseus, but with different tracer for each scale (Valdivia-Mena et al. 2023). This result is consistent with research that indicates that cores must be replenished with fresh gas to form protostars, as the amount of envelope mass dispersed through the outflow is substantial (Hsieh et al. 2023a). Streamers, therefore, can be the mechanism that can feed the protostellar system with mass that is not from the original core, connecting the material coming from outside the fibers and delivering it toward the protoplanetary disks.

4.6 Conclusions

In this work, we analysed the distribution and velocity structure of the NGC 1333 SE fibers in search for accretion signatures toward YSOs. Our results are summarised below.

- The distribution of HC_3N gas in this region is patchy and does not cover the full extent of the fibers seen in N_2H^+. The HC_3N velocity along the line of sight is redshifted with respect to N_2H^+ in the redshifted fiber. Together, these results indicate that HC_3N is following different kinematics than N_2H^+. We suggest HC_3N traces gas that is infalling later to the filament, after star formation has started in the region.

- N_2H^+ shows velocity gradients perpendicular to the fibers' orientations. We suggests, as previous works have done as well (Chen et al. 2020b; Dhabal et al. 2018), that this indicates infall toward the fibers's spines.

- The outflows of IRAS 4A and IRAS 2A generate wings and strong brightness peaks in the HC_3N spectra. In these regions, HC_3N is enhanced at the bow shocks of the protostellar outflows.

- We find streamer candidates toward 7 out of 16 YSOs in the field of view of our mosaic. **This represents an incidence of about 40% of YSOs with streamers when looking within a region.** The 7 candidates are all found toward early stage protostars (Class 0 to I), which represent a total of 11 sources within our field of view, so for early stages in particular, the incidence of streamers is about 64% for this given filament.

- The gas that composes the streamers is coming from outside the fiber structure, as there is a difference between the velocity structure of HC_3N with N_2H^+ and no streamers are detected in N_2H^+ emission. Only 2 protostars show N_2H^+ emission with similar velocities in the same position as the HC_3N streamers, but do not show the same velocity profiles.

We define these structures as candidate streamers because the resolution of our data is not enough to resolve the width of the flow and does not allow for an accurate modelling of the infall. Further information on the mass and orientation of the protostars and disks in the region are required to model the infall and determine the true length of the streamers. If we take NGC 1333 as a "typical" star-forming region, then we expect streamers to be a frequent feature toward protostellar envelopes. This work highlights the relevance of streamers in our new picture of low-mass star formation.

Chapter 5

Summary and Future Perspectives

In this thesis, I presented the results from three observational projects about streamers, in particular regarding their structure and incidence. These make use of molecular gas observations in different regions of the Perseus molecular cloud to analyze the dynamic properties of matter that feeds protostellar systems. This chapter summarizes the main results of each project and offers an overview of future work to be done in the area.

5.1 Chapter summary

In Chapter 2, I studied how mass is delivered toward a low-mass protostar through a textbook example of a streamer, aligned almost perpendicular to the outflow. Using data from the NOEMA large program PRODIGE, I studied the dynamics of gas found within a few 1000 au surrounding the embedded protostar Per-emb-50, located in an active star-forming region in Perseus. I found a streamer in H_2CO emission using a single-component fit to the data, which shows velocities consistent with infall motion. By combining the column density obtained from $C^{18}O$ within the streamer, and the analytic model that best describes the infall (Mendoza et al. 2009), I determined that it deposits $\geq 10^{-6}$ $M_\odot$ yr^{-1} directly into the protostellar disk, with small variations in this value throughout the length of the streamer. This infall rate is at least 5 times larger than the disk-to-protostar mass accretion rate (Fiorellino et al. 2021), so the streamer easily replenishes the material consumed from the disk for at least 9000 yr, and might produce gravitational instabilities in the disk or trigger future luminosity bursts. Through the clustering of multiple Gaussian components of SO emission along the line of sight, I separated the different components of the gas surrounding the protostar (including the rotating-infalling envelope and disk), and found an additional infall component, indicating even more mass is falling to the disk on top of the already considerable amount delivered by the streamer. This work suggests that asymmetric infall has the potential to change the physical conditions of a disk during the early stages of star formation, and highlights the need for high spectral resolution ($\lesssim 0.1$ $km\,s^{-1}$) to characterize streamer motion, given the narrow lines observed.

In Chapter 3, I investigated the kinematics of the filamentary structure ($\approx$ 1500 au

resolution) of Barnard 5 (B5), a mostly quiescent region in Perseus, and within the inner envelope ($\approx$ 100 au scales) of B5-IRS1, the sole embedded protostar within the filaments. The goal was to connect the flow of material between different physical scales. Using HC_3N observations, I found that chemically fresh gas flows from outside the filaments toward their spines, meaning that the filaments' gas is replenished while star formation is ongoing. At $\sim$ 100 au scales, I employed a clustering algorithm to disentangle the multiple velocity components in H_2CO emission, through which I found a streamer and a candidate streamer flowing toward the protostellar disk. The velocity at the location of the protostar in the large scale HC_3N observations is consistent with the velocities observed in the streamer, but the difference in resolution between them (a factor $\approx$ 10) is too large to confirm these two molecules trace the same gas flow. Nevertheless, the results of this work suggest that chemically unprocessed gas coming from the larger molecular cloud can reach B5-IRS1 through the streamer. This work highlights the power of clustering algorithms together with multiple velocity component decomposition to separate the different gas components toward a protostellar system.

Chapter 4 presents the first systematic search for streamers within a star-forming region. Even as the number of discovered streamers has steadily increased in the last few years, they have been found mostly serendipitously (e.g. Kido et al. 2023; Aso et al. 2023), and it is unclear if they are a frequent feature around protostars or they are a rare phenomenon. Based on the previous chapters and recent publications (e.g. Garufi et al. 2022; Thieme et al. 2022; Hsieh et al. 2023b), I observed that most streamers have two properties in common: first, they are usually detected in carbon-chain molecules (such as HC_3N), and second, the gas that traces their structure shows acceleration with respect to protostars' velocities with decreasing distance. To prove this method, I used HC_3N and N_2H^+ observations from the ProPStar survey (PI: J. Pineda), taken with NOEMA and the 30-m telescope. These observations cover a filament within NGC 1333, an active star-forming region in Perseus. I used a clustering algorithm to aid in the interpretation of the large scale gas, recovering the fiber structure in both molecules. From a total of 16 protostars within the observed area, I found HC_3N emission consistent with asymmetric infall toward 7 of them (a frequency of about 40%). Additionally, the gas that feeds the streamers seems to come from outside the fiber structure (traced by N_2H^+), infalling from the larger molecular cloud toward the fibers. This result shows that asymmetric features are a more common feature toward protostars that previously thought, and should therefore be included in the current picture of star and planet formation.

5.2 Future work

Streamers are a relatively new phenomenon discovered in regards to star and planet formation. Even so, numerical simulations already suggest that streamers could have a deep impact in the star and planet formation process (e.g. Kuznetsova et al. 2022). However, **these have remained mostly unobserved, in particular for embedded protostars.** As such, there are several open possibilities for future research into streamer observations.

Here, I describe a few projects that are of interest for future work.

A major avenue for exploration is the effect of streamers in the physical and chemical conditions of protostellar disks. Planet formation likely starts during the embedded star formation stages, as observations of Class II disks have suggested there is not enough mass to form exoplanets (e.g. Manara et al. 2018; Tychoniec et al. 2020). Notably, substructures linked to planet formation such as rings have been observed in a few embedded disks around Class I protostars (Sheehan & Eisner 2018; Segura-Cox et al. 2020; Sheehan et al. 2020). Thus, it is of great interest to analyze the effect of streamers in embedded disks.

Recent works have shown that asymmetric infall into protoplanetary disks can cause shocks which change the temperature at the landing site, but this effect remains largely unexplored, being measured only for a couple of Class I/II disks (Garufi et al. 2022) and only one embedded protostar (Artur de la Villarmois et al. 2022). Depending on the strength of the shock and how much the temperature increases, streamers could release volatile molecules like water in parts of the outer disk, changing the assumed chemical abundances at the time of planet birth. The challenge is to resolve the asymmetric shock front within the disk, which requires high resolution that can only be achieved with interferometers. I plan to use data currently available as part of the PRODIGE large program, which are able to resolve the streamers and locations of shock tracing molecules within the gas disks. I have additionally observed Per-emb-50 with the most extended NOEMA configuration, improving the image resolution from $1.2''$ to $0.8''$, to pinpoint the shocks produced by each infall mechanism (Ch. 2). To see the effect of streamers in planet-forming disks, I will leverage on the detection of shock tracers, such as sulfur dioxide (SO_2), and also on kinematic tracers of the disk and the inner envelope, such as sulfur monoxide (SO), formaldehyde (H_2CO) and carbon monoxide (CO) isotopologues. I will analyze the temperature and density profile of disks and streamers, both with LTE and non-LTE models (e.g. RADEX, van der Tak et al. 2007) depending on the column densities of the regions.

Simulations suggest that streamers can produce significant changes in the dynamic properties of protoplanetary disks. For instance, Kuznetsova et al. (2022) showed that streamers produce rings and gaps that last long after the streamer has vanished, structures which are usually attributed to planets carving the disk in several works (e.g., Zhang et al. 2018a). Also, Kuffmeier et al. (2021) showed that misaligned disks can result from late asymmetric infall. However, there are only three streamers that have been detected toward ringed disks (Alves et al. 2020; Yen et al. 2019; Flores et al. 2023), two of which are embedded protostars, and only one case of a misaligned disk correlated with a streamer (Ginski et al. 2021). Future observations can discover more streamers toward disks that have these kind of structures. Very high resolution (~ 10 au) observations capable thanks to the extended ALMA configurations are expected to discover more disks with substructures in the future. For instance, the recently published eDisk campaign (Ohashi et al. 2023) reveals that substructure in very young disks is uncommon, but there are a few disk with candidate rings and spirals (Yamato et al. 2023; Sai et al. 2023). I will lead proposals for ALMA observations of protostars with streamers, to understand if the presence of substructure in early disks can be more easily observed for sources with asymmetric infall.

Another compelling direction for streamer research is to measure their effects on the

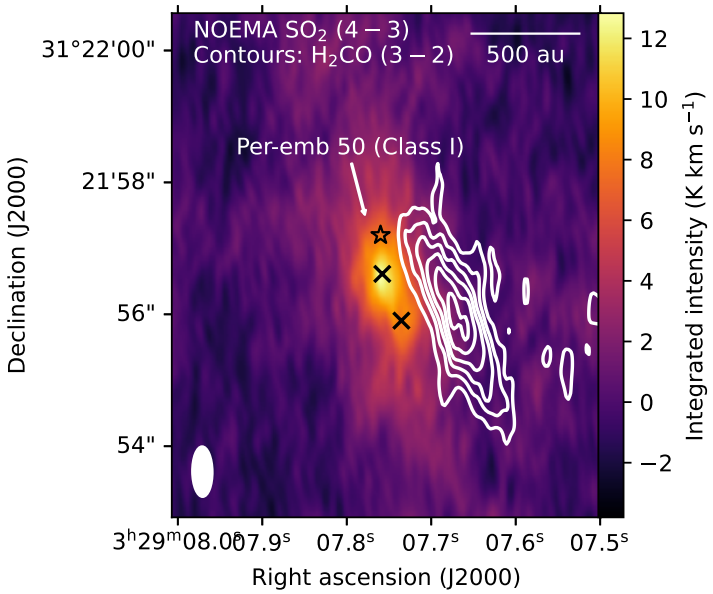

Figure 5.1: Recent NOEMA observations of SO_2 toward Per-emb-50 (Ch. 2) that resolve two distinct peaks, each possibly associated with a different streamer.

evolution of the star-disk system. In the few cases where the mass infall rate from streamer to disk ($\dot{M}_{\rm in}$) is compared with the protostellar accretion rate (disk-to-protostar, $\dot{M}_{\rm acc}$), it has been found that $\dot{M}_{\rm in} \gtrsim \dot{M}_{\rm acc}$ (Chou et al. 2016; Yen et al. 2019; Pineda et al. 2020; Thieme et al. 2022; Valdivia-Mena et al. 2022; Flores et al. 2023). Simulations show that infall onto the disk can produce gravitational instabilities (Kuffmeier et al. 2018), which in turn can lead to accretion outbursts (Bae et al. 2014) and trigger binary or planet formation at early, embedded stages (Kratter et al. 2010b,a). Yet as there are only six streamers where the mass has been measured, our current understanding of the mass accumulation via streamers suffers from small-number statistics. To determine if streamers can produce accretion bursts in protostars, it is necessary to compare more streamers' $\dot{M}_{\rm in}$ in protostars with a wide range of $\dot{M}_{\rm acc}$. With this purpose, I successfully applied for ALMA observing time in Cycle 10 to survey a sample of protostars with known $\dot{M}_{\rm acc}$ to find streamers and estimate their infall rate. The plan is to form the first statistically significant sample of streamer $\dot{M}_{\rm in}$ to determine the impact of streamers in the mass accretion process toward the disk and the protostar.

Currently, the few estimations of infall rate show that streamers can deliver a significant amount of mass to the protostellar disk, but it is still unclear if this mode of mass transport is dominant over envelope infall. Recent simulations suggest that this should be the case (Tu et al. 2024; Heigl et al. 2024), but no observational comparison has been made up to date. Our campaign accepted for ALMA Cycle 10 also opens the possibility to compare both types of infall. I plan to estimate the envelope infall rates using the inverse P-Cygni line profile characterization, extensively used for both low- and high-mass protostars (e.g., Di Francesco et al. 2001; Wyrowski et al. 2016), where observed. For the streamers, I can

use optically thin line emission to measure the mass and and the timescales obtained from their free-fall model to obtain the infall rates (as in Chapter 2). If streamers are a dominant mass infall mechanism, then this have to be considered in physico-chemical models of star and planet formation. In the case they are not as dominant as suggested by numerical simulations, it validates the axisymmetric assumption as a good approximation to be used in the planet formation models.

5.3 Final remarks

The subject of streamers in star and planet formation is a nascent niche that has garnered growing interest. This thesis added several new streamers and candidates to the literature and demonstrated that their origins lie in chemically unprocessed gas from beyond their natal cores. These results have helped to shift the understanding of low-mass star and planet formation to a process influenced by the environment and its dynamics. However, this area of research is still in its infancy, garnering increased interest in the protostar and protoplanetary disk community. I hope that my future endeavors in streamer research will help to clarify their true role in star and planet formation.

Appendix A

Appendices for Chapter 2 (Valdivia-Mena et al. 2022)

A.1 Continuum at 220 GHz

Figure A.1 shows the continuum imageat 1.3 mm (220 GHz) resulting from the LI continuum window of our dataset. The noise level of this image is 0.2 mJy beam^{-1}.

A.2 Gaussian component fitting

We fit a single Gaussian component to all the spectra in the $H_2CO(3_{0,3}–2_{0,2})$ and the $C^{18}O(2–1)$ cubes, using the Python `PySpecKit` library (Ginsburg & Mirocha 2011). We left out of the analysis all spectra with a peak signal-to-noise ratio lower than four. After fitting, we selected for further analysis the fitted spectra that met all of the following requirements:

- the parameter uncertainties were all smaller than 50%,
- the Gaussian component had a central velocity in the observed emission velocity range (between 5.5 and 9.5 km s^{-1} for H_2CO and $C^{18}O$), and
- the fitted amplitude had a S/N > 4.

The results of the fit for $H_2CO(3_{0,3}–2_{0,2})$ are shown in Fig. 2.2, and for $C^{18}O(2–1)$ the results are shown in Fig. 2.5.

We fit one, two, and three Gaussian components to the SO spectra near the protostar using the same criteria as above, similar to the multifit approach by Sokolov et al. (2019). After fitting, we kept the pixels where for each Gaussian, all of the above criteria were met,

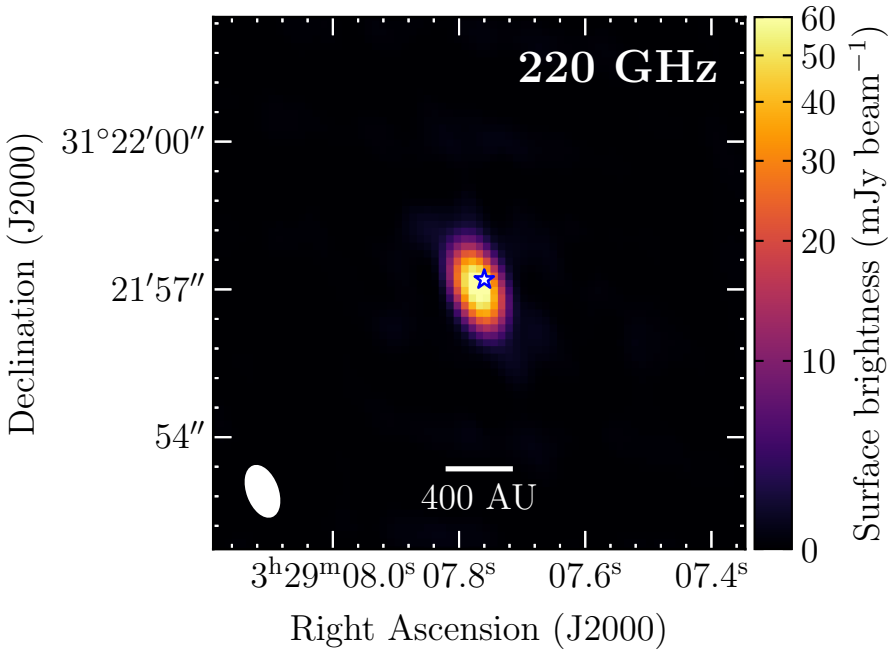

Figure A.1: Continuum image at 220 GHz (1.3 mm) of Per-emb-50 obtained with NOEMA. The continuum is done only with the LI continuum window of the observations. The blue star represents the position of Per-emb-50. The white ellipse in the lower left corner represents the beam size.

except for the central velocity, where the emission range changes from $5.5 - 9.5$ km s^{-1} to $-1.0 - 14.0$ km s^{-1}.

We used the Akaike information criterion (AIC) to decide whether one, two, or three Gaussian components reproduced best each SO spectra. This criterion uses the AIC value AIC to determine which model minimizes information loss:

$$AIC = 2k + \chi^2 + C, \tag{A.1}$$

where k is related to the number of free parameters of the model (see below), χ^2 is the classical chi-squared statistic, and C is a constant defined by the number of independent channels and the uncertainties (Choudhury et al. 2020). For k, each Gaussian component has three free parameters, so $k = 3g$, where g is the number of Gaussian components in each model. For C, we assumed that each channel in the spectra had a constant normal error, which corresponds to the rms of the SO cube, and we used the same data to test the three models. C was the same for all models and did not play a role in choosing the best model, so we set $C = 0$. The fit with the lowest AIC value was the preferred one for each spectrum.

We evaluated the probability that the model with the minimum information loss was a considerable improvement from the other two models for each spectrum. The difference between the minimum AIC, AIC_{min} (which comes from the "best" model) and the AIC value of model i, AIC_i, is proportional to the probability that model i is as good as the minimum to minimize information loss as:

$$P \propto \exp\left(\frac{AIC_{min} - AIC_i}{2}\right). \tag{A.2}$$

For SO(5_5-4_4), all of the fitted spectra have less than 5% probability that the competing models fit better the spectra than the model with minimum AIC. This means that, for those spectra that are well fitted by three Gaussians, the improvement from two Gaussians is significant. The same can be said for the improvement in those spectra that are best fitted with two Gaussians instead of only one. Therefore, we conclude that each spectra is well described by one, two, or three Gaussian components, depending on each case. Figure A.2 shows four spectra fitted with either one, two or three Gaussians.

A.3 Envelope mass calculation

We obtained the envelope mass upper and lower limits using the flux in our continuum obtained with NOEMA (see Appendix A.1) and the Bolocam 1.1 mm image from Enoch et al. (2006). First, we obtained the flux in the Bolocam 1.1 mm continuum within a beam-sized aperture ($\theta_{FWHM} = 31''$), centered at the location Per-emb-50, $F_{\rm Bolocam} = 324 \pm 46$ mJy, together with the peak value within this aperture $I_{\rm Bolocam} = 573 \pm 55$ mJy beam^{-1}. Then, we obtained the total flux and peak value within the primary beam of the continuum obtained with NOEMA ($22''$), $F_{\rm NOEMA} = 89 \pm 2$ mJy and $I_{\rm NOEMA} = 72.9 \pm 1$ mJy beam^{-1}, respectively. We assumed that the NOEMA continuum contains disk emission only, as it

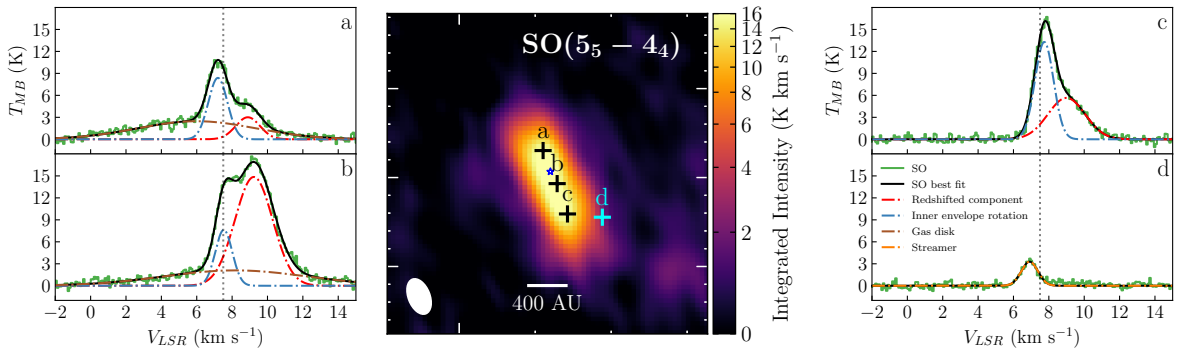

Figure A.2: Sample spectra of SO in four selected locations in Per-emb-50's inner envelope and disk region. **Left and right:** Beam averaged SO spectra (green line) at positions a to d. The black solid curve represents the best fit Gaussian function. The dashed-dotted lines represent the individual Gaussians that, added together, correspond to the best fit function. Each individual color in the dashed-dotted lines represents one of the kinematic components found in Sect. 2.3.8: blue corresponds to the inner envelope rotation, red matches the redshifted component, brown corresponds to the gas disk, and orange matches the streamer. **Middle:** Integrated intensity map of SO between -1 and 14 km s^{-1}, as shown in Fig. 2.1, zoomed into the inner 1000 au closest to the protostar. Crosses (black and cyan) mark the locations of each spectrum, labeled a to d from highest to lowest, from right to left.

does not contain zero-spacing information, whereas the Bolocam 1.1 mm image includes emission from the disk and envelope. We subtracted the flux in the NOEMA continuum from the flux obtained from Bolocam, thus obtaining the flux of the envelope only $\Delta S_{1\mathrm{mm}} = S_{\mathrm{Bolocam}} - S_{\mathrm{NOEMA}}$, and used Equation 4 of Enoch et al. (2009) to calculate the envelope mass:

$$M_{env} = \frac{D^2 \Delta S_{1\mathrm{mm}}}{B_{1\mathrm{mm}}(T_D)\kappa_{1\mathrm{mm}}}. \tag{A.3}$$

We assumed that the continuum at 1 mm consists of optically thin emission and used $\kappa_{1mm} = 0.0114$ cm^2 g^{-1}, $T_D = 15$ K as stated in Enoch et al. (2009), and a distance $D = 293$ pc (Ortiz-León et al. 2018). Using the flux difference, we obtained an envelope mass of 0.18 $M_\odot$. On the other hand, using the peak difference, we obtained 0.39 $M_\odot$.

A.4 Determination of column density

We first obtained the integrated intensity map of the primary beam corrected $C^{18}O(2-1)$ emission in the spatial region where the streamer is defined for the streamline model (see Fig. 2.5). We integrated the map between 5.5 and 9.5 km s^{-1}. This velocity range covers the spectral emission of the streamer in $C^{18}O(2-1)$ completely. Then, we calculated the total column density of the $C^{18}O$ molecule using Equation 80 of Mangum & Shirley (2015)

in each pixel of the integrated intensity map. We used a line strength $S = \frac{J^2}{J(2J+1)} = 2/5$ in relation to the dipole moment of the $C^{18}O$ molecule $\mu = 0.11079$ Debye $= 1.1079 \times 10^{-19}$ esu cm, the rotor rotation constant for $C^{18}O$ $B_0 = 54891.420$ MHz, the upper state energy for the $C^{18}O(2$ –1) transition $E_u = 15.81$ K, and the degeneracy of the $C^{18}O$ (2 – 1) transition $g_J = 2J + 1 = 5$. We assumed a beam filling factor $f = 1$, as emission was resolved. The resulting equation for $N(C^{18}O)$ in cm^{-2}, T_{ex} in K and $\int T_R\, dv$ in K $km\,s^{-1}$ is

$$N(C^{18}O) = 1.63 \times 10^{15} \frac{Q_{rot}(B_0, T_{ex})}{5} \frac{\exp(\frac{15.81}{T_{ex}})}{\exp(\frac{10.54}{T_{ex}}) - 1} \frac{\int T_R\, dv}{J_\nu(T_{ex}) - J_\nu(T_{bg})}, \quad \text{(A.4)}$$

where

$$Q_{rot} = \frac{k_B T_{ex}}{hB_0} + \frac{1}{3} \quad \text{(A.5)}$$

is the first order Taylor approximation of the partition function of a rigid-rotor diatomic molecule, and

$$J_\nu(T) = \frac{\frac{h\nu}{k_B}}{\exp(\frac{h\nu}{k_B T}) - 1} \quad \text{(A.6)}$$

is the Rayleigh-Jeans equivalent temperature in K. We used $T_{bg} = 2.7$ K and $\nu = 219.560$ GHz (the frequency of the $C^{18}O(2$ –1) line). We used a constant $T_{ex} = 15 \pm 5$ K.

A.5 SO_2 spectra and image

Figure A.3 shows the integrated intensity map of $SO_2(11_{1,11}$ – $10_{0,10})$ between 5 and 12 $km\,s^{-1}$, and to the left and right, spectra of SO, SO_2, and H_2CO in the same selected positions as in Fig. A.2.

A.6 SO decomposition

Figure A.4 shows the velocity dispersion σ_v of each kinematic element found in Sect. 2.3.8 (see Fig. 2.8) through the Gaussian fitting described in Appendix A.2. It should be noted that all images have different colorscales.

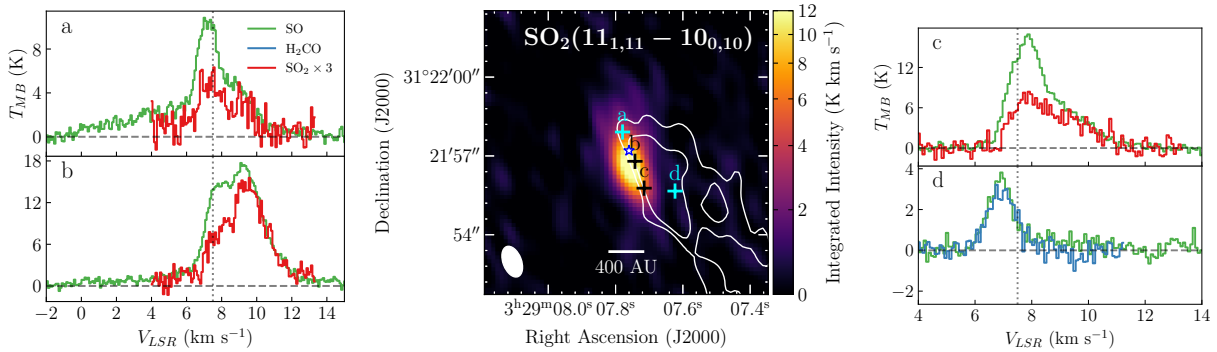

Figure A.3: Velocity integrated $SO_2(11_{1,11} - 10_{0,10})$ together with sample spectra of SO_2, SO, and H_2CO at positions a to d. **Left and right:** Beam averaged spectra at positions a to d. Each color represents the spectrum of a molecule: blue corresponds to H_2CO, green to SO and red to SO_2. The dotted vertical line marks the central velocity of the protostar $V_{LSR} = 7.5$ km s^{-1}. The dashed horizontal line represents the 0 K level. If a molecule does not appear at a panel, its because emission from that molecule has a S/N < 5. **Middle:** Velocity integrated image of the $SO_2(11_{1,11} - 10_{0,10})$ molecular transition. The crosses represent the places where each spectrum was extracted, labeled from a to d. The white contours represent the three and five times the rms of the integrated map contours of H_2CO (0.25 K km s^{-1}). The white ellipse in the bottom left corner represents the beam size. The blue star marks the position of Per-emb-50.

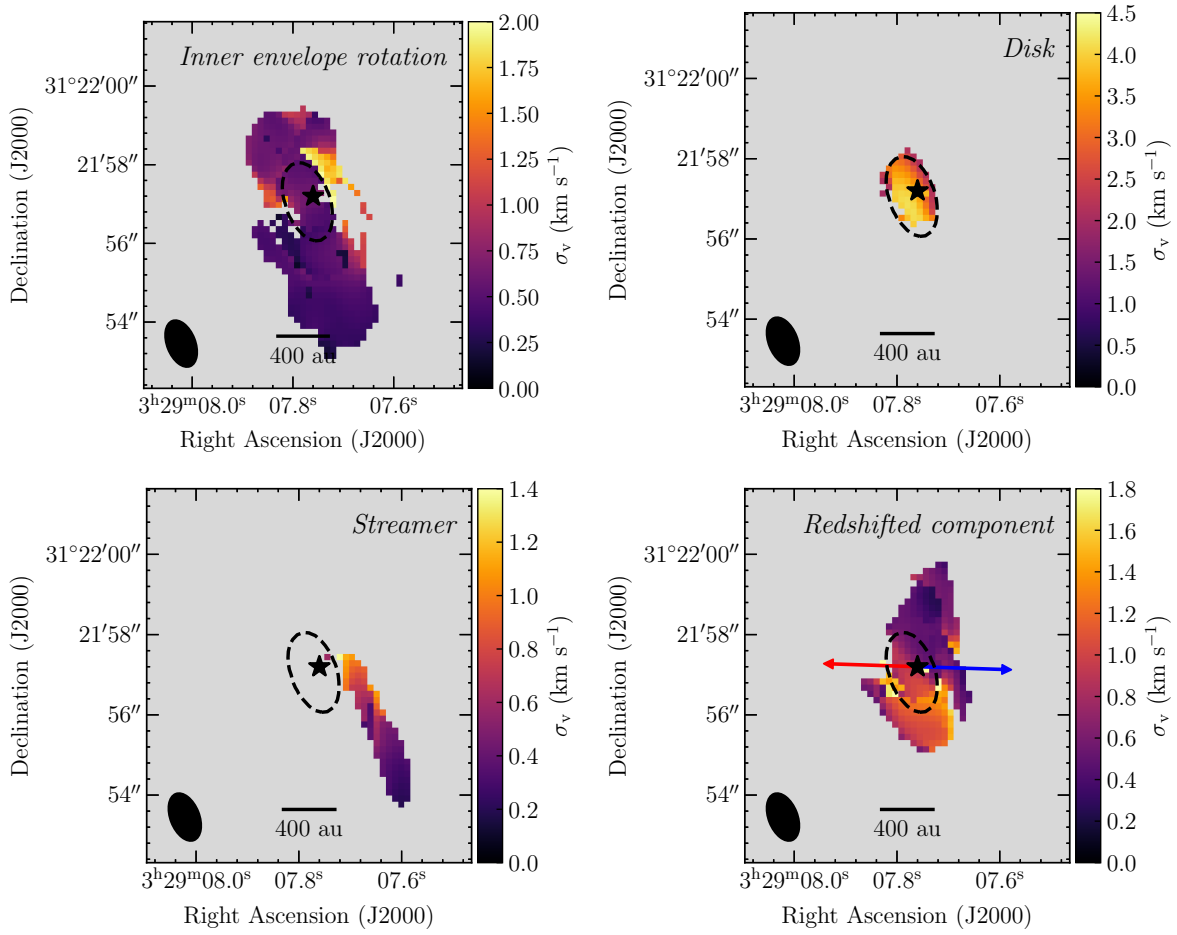

Figure A.4: σ_v of the inner envelope rotation, disk, streamer and redshifted components in SO($5_5 - 4_4$) found in Sect. 2.3.8. The dashed contour represents the 220 GHz continuum emission at the 7 mJy beam^{-1} level. The black ellipses in the lower left corners represent the beam size.

Appendix B

Appendices for Chapter 3 (Valdivia-Mena et al. (2023)

B.1 Very Large Array and Green Bank Telescope observations

We used the NH_3 (1,1) inversion transition data from P15 to define the filaments and cores and compare them to our NOEMA and 30m observations. The details of the reduction can be found in P15 and S21. In summary, VLA observations using the K-band were taken using D and CnD configuration (project number 11B-101), and GBT observations were included to recover the zero-spacing information in the UV plane (project number 08C-088). The data were reduced and imaged using CASA (McMullin et al. 2007), with multiscale CLEAN and a Briggs weight (robust parameter of 0.5).

Figure 3.1 shows the contours of the dense filaments and condensations found in NH_3 (1,1) emission from P15 as defined in S21, which used dendogram analysis to define the filaments and condensations. We use their nomenclature to name the filaments and cores throughout this work. Figure B.1 shows the central velocities $v_{\rm LSR}$ obtained in P15 from a line fit to the NH_3 (1,1) hyperfine components using the `cold-ammonia` model implemented in `pyspeckit` (Ginsburg & Mirocha 2011; Ginsburg et al. 2022). The central velocities range from 10 to approximately 10.5 $\mathrm{km\,s^{-1}}$ and vary smoothly across the map. The central velocities' uncertainties are on average 7×10^{-5} $\mathrm{km\,s^{-1}}$ and range from 3×10^{-5} $\mathrm{km\,s^{-1}}$ within the condensations and 2×10^{-4} $\mathrm{km\,s^{-1}}$ at the edges of the filaments. Fil-1 shows a velocity gradient from 10.1 to 10.5 $\mathrm{km\,s^{-1}}$ approximately from north to south, and Fil-2, from 10 to 10.3 $\mathrm{km\,s^{-1}}$ from south to north, except near the protostar.

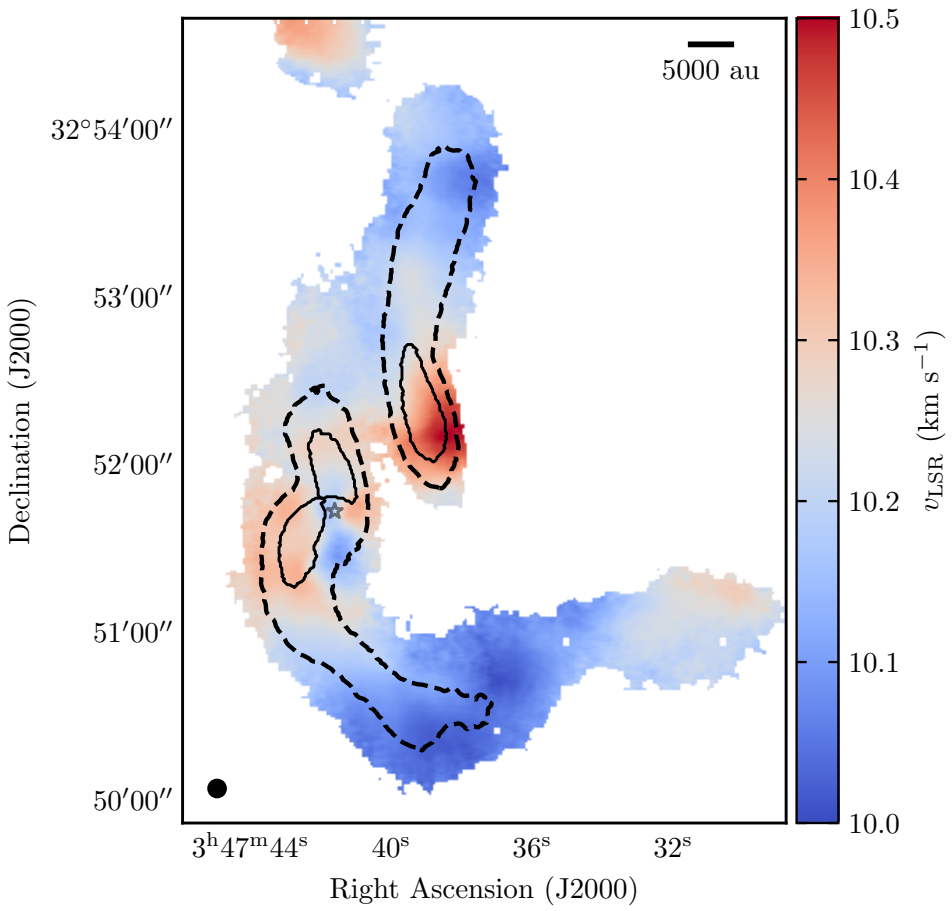

Figure B.1: Central velocities of the NH_3 (1,1) spectra from P15. The dashed lines outline the filaments seen in NH_3 (1,1). The solid lines outline the condensations seen through the same molecule emission. The star marks the position of B5-IRS1.

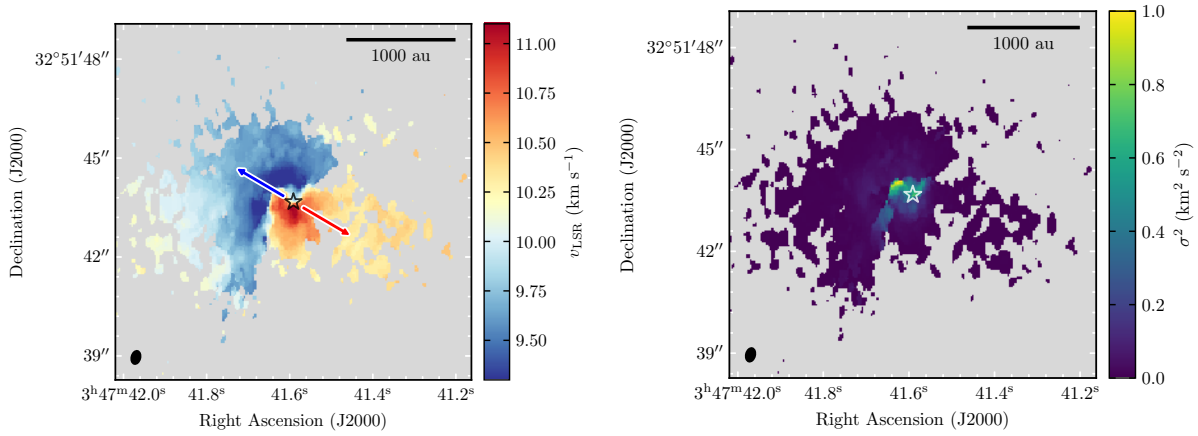

Figure B.2: Moments 1 (left) and 2 (right) of the ALMA H_2CO ($3_{0,3} - 2_{0,2}$) line emission. The black (left) and white (right) stars represent the position of the protostar. The blue and red arrows indicate the directions of the blue and redshifted outflow lobes from Zapata et al. (2014). The scalebars indicate a length of 1000 au. The black ellipse in the bottom left corner represents the beam size.

B.2 H_2CO moment maps

Figure B.2 shows moments 1 (weighted velocity) and 2 (weighted velocity dispersion) for H_2CO emission with $S/N > 5$. The moment maps show that emission has different velocities in the east-west direction. Emmision toward the east of the protostar has a larger extension and is blueshifted with respect to B5-IRS1's v_{LSR} (10.2 km s^{-1}, P15). Emission toward the west covers less area and is mostly redshifted with respect to the protostar. The moment 1 map shows a curved boundary within a beam of the protostar for the blue and redshifted sides.

The moment 2 map shows that most H_2CO emission has a variance σ^2 of about 0.1 km s^{-1}, except within a radius of approximately 0.5″ from the protostar and toward the south of it as well. Most notably, the peak of σ^2 is within a resolved distance (one beam) of B5-IRS1, toward the east.

B.3 $C^{18}O$ line emission images

Figure B.3 shows the integrated emission of $C^{18}O$ from 7.8 to 12.4 km s^{-1}. Figure B.4 shows the channel maps of $C^{18}O$ between 7.8 and 12.3 km s^{-1} in 0.3 km s^{-1} steps. $C^{18}O$ traces both the envelope and the natal cloud and is more extended than H_2CO. Channels between 9.6 and 10.4 km s^{-1} are affected by strong bowls of negative emission due to missing short-spacing data, but $C^{18}O$ is more affected by the missing scales than H_2CO, as it has larger regions with negative emission artifacts. $C^{18}O$ shows point-like emission between 7.8 and 9.0 km s^{-1} and from 11.1 to 12.3 km s^{-1}, which we suggest comes from

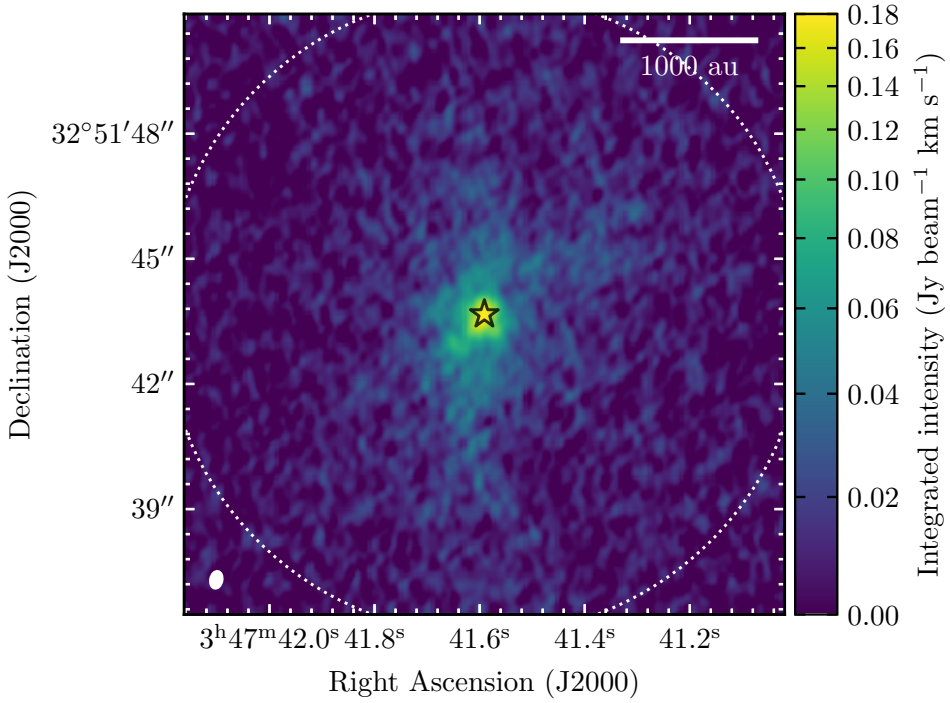

Figure B.3: Velocity integrated image of $C^{18}O$ emission from 7.8 to 12.4 km s^{-1}. We note that the area covered in the $C^{18}O$ map is larger than for the H_2CO image, shown in Fig. 3.3. The black star represents the position of the protostar. The scalebar indicates a length of 1000 au. The white ellipse in the bottom left corner represents the beam size. The primary beam of the image is drawn with a white dotted circle.

the gas disk surrounding the protostar.

B.4 Gaussian fit to the spectra and selection criterion

We fit a single Gaussian component to the spectra in the HC_3N (10–9) cube and one, two, and three Gaussian components in the H_2CO ($3_{0,3}$–$2_{0,2}$) cube, using the Python `pyspeckit` library (Ginsburg & Mirocha 2011). We leave out of the analysis all spectra with a peak S/N lower than 5 for the case of HC_3N and lower than 3 for H_2CO.

We created a mask with the pixels to fit. First, we select all pixels with $S/N > 5$. Then, we did a series of morphological operations on the mask using the `morphology` library from `scikit-image` python package (van der Walt et al. 2014). For HC_3N we did the following operations in order: first, we removed islands with fewer than 100 pixels using the function `remove_small_objects`. Secondly, we filled the holes smaller than 100 pixels with the function `remove_small_holes`. Finally, we did a morphological closing of the mask to fill cracks in the mask, using the `closing` function with a circular footprint with radius of 6 pixels.

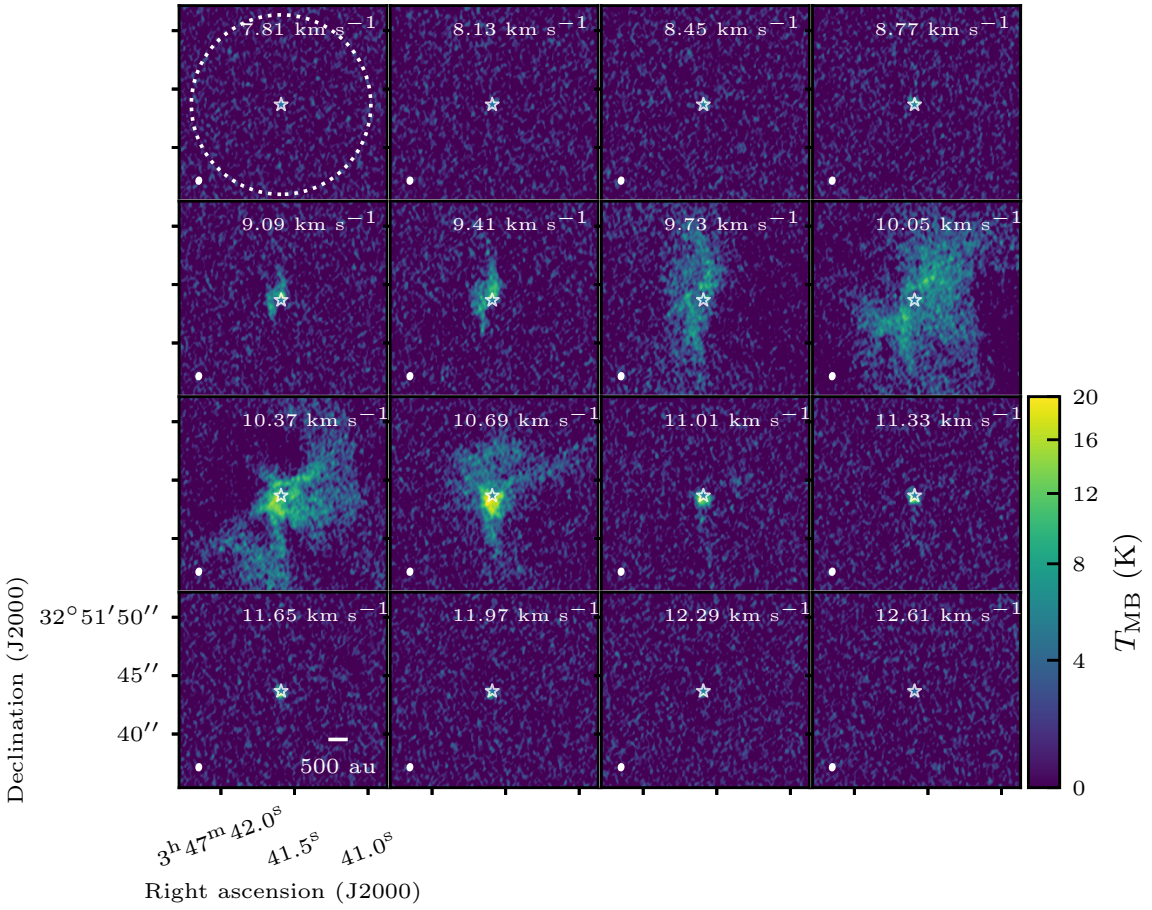

Figure B.4: Channel maps between 7.81 and 12.61 km s^{-1} for the ALMA C^{18}O (2 – 1) spectral cube. The white star represents the location of the protostar. The white dotted circle marks the extent of the primary beam. The white ellipse at the bottom left corners represents the beam size. The scalebar shows a 500 au length in the map.

For H_2CO, we built the mask with the following sequence: first, we removed islands with fewer than 50 pixels using the function `remove_small_objects`. Secondly, we filled the holes smaller than 50 pixels with the function `remove_small_holes`. Then, we did a morphological closing of the mask to soften cracks in the edges, using the `closing` function with a circular footprint with radius of 3 pixels. Afterwards, we filled the holes with fewer than 200 pixels. Finally, we did a morphological opening of the mask to round the edges using a disk footprint of radius 4 pixels. This mask allowed us to capture pixels with significant H_2CO emission, larger than $S/N > 3$, that are connected to significant areas of emission and not in disconnected islands that are associated to artifacts.

The initial guesses are fundamental in all of our fits to obtain reasonable results. For HC_3N, we first obtained the moments of the cube, as described in the Minimal Gaussian cube fitting example from pyspeckit[1]. Then, we checked the initial guesses to replace any value that is not within acceptable ranges, as follows. If the initial peak is negative, we replace it with a value of 0 K. If the initial central value was not within the range of observed velocities (between 9 and 11.3 $\mathrm{km\,s^{-1}}$), we replaced it with 9 $\mathrm{km\,s^{-1}}$ if the value was lower than 9 $\mathrm{km\,s^{-1}}$ and with 11.3 $\mathrm{km\,s^{-1}}$ if the value was higher than 11.3 $\mathrm{km\,s^{-1}}$. We replaced all initial velocity dispersions larger than 2.3 $\mathrm{km\,s^{-1}}$ to 2.3 $\mathrm{km\,s^{-1}}$, which is the difference between the observed velocity boundaries. In the pixels where the initial guesses were not a number (NaN), we replaced the peak intensity for 1 K, the central velocity for 10.2 $\mathrm{km\,s^{-1}}$ and the dispersion for 1 $\mathrm{km\,s^{-1}}$.

The initial guesses for H_2CO fit were different in the cases we fit one, two and three Gaussians. For one Gaussian, we used the same initial guesses for all pixels: a peak temperature T_{peak} of 10 K, central velocity v_{LSR} of 10.2 $\mathrm{km\,s^{-1}}$ and dispersion σ_{v} of 0.8 $\mathrm{km\,s^{-1}}$. For two Gaussians, we use the same initial guesses for most of the pixels except for select regions where we input different guesses manually. For most of the pixels, the first component had initial guesses of $T_{\mathrm{peak}} = 10$ K, $v_{\mathrm{LSR}} = 10.5$ $\mathrm{km\,s^{-1}}$ and $\sigma_{\mathrm{v}} = 0.3$ $\mathrm{km\,s^{-1}}$, and the second, $T_{\mathrm{peak}} = 10$ K, $v_{\mathrm{LSR}} = 9.2$ $\mathrm{km\,s^{-1}}$ and $\sigma_{\mathrm{v}} = 0.3$ $\mathrm{km\,s^{-1}}$. For three Gaussians, our initial guesses were $T_{\mathrm{peak}} = 10$ K, $v_{\mathrm{LSR}} = 11.3$ $\mathrm{km\,s^{-1}}$ and $\sigma_{\mathrm{v}} = 0.3$ $\mathrm{km\,s^{-1}}$ for the first component, $T_{\mathrm{peak}} = 10$ K, $v_{\mathrm{LSR}} = 10.7$ $\mathrm{km\,s^{-1}}$ and $\sigma_{\mathrm{v}} = 0.3$ $\mathrm{km\,s^{-1}}$ for the second, and $T_{\mathrm{peak}} = 5$ K, $v_{\mathrm{LSR}} = 9.5$ $\mathrm{km\,s^{-1}}$ and $\sigma_{\mathrm{v}} = 0.3$ $\mathrm{km\,s^{-1}}$ for the third, except for selected regions where we input different guesses manually.

After fitting once, we did a second fit, using the resulting output from the first fit as initial guesses. To do this, we selected for further analysis the fitted spectra that met all of the following requirements and the rest are replaced with NaNs: the parameter uncertainties had to be all smaller than 50%; the amplitude of the Gaussian was a positive value; the Gaussian component had a central velocity in the observed emission velocity range (between 8 and 12 $\mathrm{km\,s^{-1}}$ for H_2CO, and between 9 and 11.3 $\mathrm{km\,s^{-1}}$ for HC_3N); and finally, the fitted amplitude had $S/N > 2$ for the case of H_2CO and $S/N > 5$ for HC_3N. Then, we interpolated the parameters obtained that passed this filter to fill in the pixels where the fit did not converge to a solution with the initial guesses, or where the first fit did not pass the filter described above. For the interpolation we used the `griddata` function

[1]https://pyspeckit.readthedocs.io/en/latest/example_minimal_cube.html

from the `scipy.interpolate` python library (Virtanen et al. 2020). Afterwards, we input the interpolated values as initial guesses for the fits.

To mitigate the effects of the missing short- and zero-spacing information in our interferometric data for the H_2CO fit, we fit one, two and three Gaussian components using the spectra with the values between 9.7 and 10.3 km s^{-1} masked, following the same procedure above. This only has a positive net effect on the final results for the spectra within a 500 au radius from the protostar. For the rest of the spectra, masking the channels has no net positive effect on the final results and misses Gaussian components that peak within the masked channels. Therefore, we only used the fit with masked central channels for the spectra within a 500 au radius.

We kept the second fit results and did a further quality assessment. For HC_3N, the assessment included the requirements mentioned above. For H_2CO, we added the following criteria after evaluating the previous requirements: first, the fitted amplitudes selected all had $S/N > 3$; the uncertainty in the central velocity for each fit had to be less than the channel size (0.08 km s^{-1} for the H_2CO ALMA cube, Table 3.1); and finally, for pixels where the fit was done with masked channels, there could not be a peak located at the masked channels. After this evaluation, we also filtered islands of pixels in the image space that had fewer than 50 pixels for the one Gaussian fit, and fewer than 15 pixels for the two Gaussian fitting, as this would only add noise to the clustering.

We used the Akaike information criterion (AIC) to decide how many Gaussian components reproduced best each spectra, in a similar manner as applied in Choudhury et al. (2020) and Valdivia-Mena et al. (2022), for the case where we fit up to 3 Gaussians in H_2CO. This criterion uses the AIC value AIC to determine which model minimizes information loss:

$$AIC = 2k + \chi^2 + C, \tag{B.1}$$

where k is the number of free parameters of the model, χ^2 is the classical chi-squared statistic and C is a constant defined by the number of independent channels and the uncertainties (Choudhury et al. 2020). Because each Gaussian component has three free parameters, $k = 3g$, where g is the number of Gaussian components in each model. For C, we assumed that each channel in the spectra has a constant normal error, which corresponds to the rms of each cube. As we used the same data to test the three models, C is the same for all models and does not play a role in choosing the best, so we set $C = 0$.

We evaluated the probability that the model with the minimum information loss, which is the one with the minimum AIC, is a considerable improvement from the other models for each spectrum. The probability that model i is as good as the model with minimum AIC to minimize information loss is proportional to the differencce between the minimum AIC, AIC_{min} and the AIC value of model i, AIC_i:

$$P = \exp\left(\frac{AIC_{min} - AIC_i}{2}\right). \tag{B.2}$$

For each spectrum, the fit with the lowest AIC value is the preferred one. We also checked that the best fit has at least a 95% probability of minimizing the information loss

better than when compared with any other of the models applied: this translates to a value of $P < 0.05$. For the case of H_2CO, there are very few spectra (around 0.1%) where the probability is less than 95% for the best model, so we leave the fit with the lowest AIC value.

B.4.1 HC_3N two Gaussian fit

The best fit parameters for the HC_3N emission spectra are in Figure 3.5. Figure B.5 shows the spectrum at the position of the protostar and its Gaussian fit with a dashed line. We also did a two Gaussian fit to the central $4''$ around the protostar in the HC_3N map. This possible second feature is hinted at in the residuals of the one Gaussian fit at the position of the protostar, seen in Fig. B.5, where some residuals reach $S/N \gtrsim 3$. We fit two Gaussians and compare the results using the Akaike Information Criterion (AIC). The resulting fit at the location of the protostar is shown in Fig. B.5 with solid lines. The residuals from both fits show that two Gaussians fit the spectrum better than one at the position of the protostar. However, as too few spectra were actually better fitted with two Gaussians that with one when evaluated with AIC (less than 10% of the pixels, Fig. B.6), we decided to leave all spectra with only one Gaussian.

B.5 Core and filament volume density traced by HC_3N

We obtained the volume density of H_2 gas $n(H_2)$ using the HC_3N line ratio between the 10 – 9 and 8 – 7 level transitions and the non-LTE radiative transfer code RADEX (van der Tak et al. 2007), with the goal of calculating the infall rate of material from the core to the filaments in Barnard 5.

B.5.1 HC_3N (8 – 7) integrated image

Figure B.7 shows the integrated intensity of HC_3N $(8-7)$ emission. We integrated the line cube between 9.2 and 11.2 $\mathrm{km\,s^{-1}}$, the same range as for HC_3N $(10-9)$. The morphology is similar to the HC_3N $(10-9)$ integrated map, but the peak in integrated intensity is located within Cond-2 instead of the protostar.

B.5.2 HC_3N line ratio

We used the integrated line intensity maps for both HC_3N transitions to obtain a line ratio map. First, we smoothed the $HC_3N\,(10-9)$ integrated image with a Gaussian kernel in CASA to the reach the resolution of the $(8-7)$ transition map ($\approx 5''$, Table 3.1). Then, we regridded the resulting convolved image to match the $(8-7)$ line map pixel grid. Finally, we divided the regrid $HC_3N\,(10-9)$ integrated intensity map by the HC_3N $(8-7)$ integrated image:

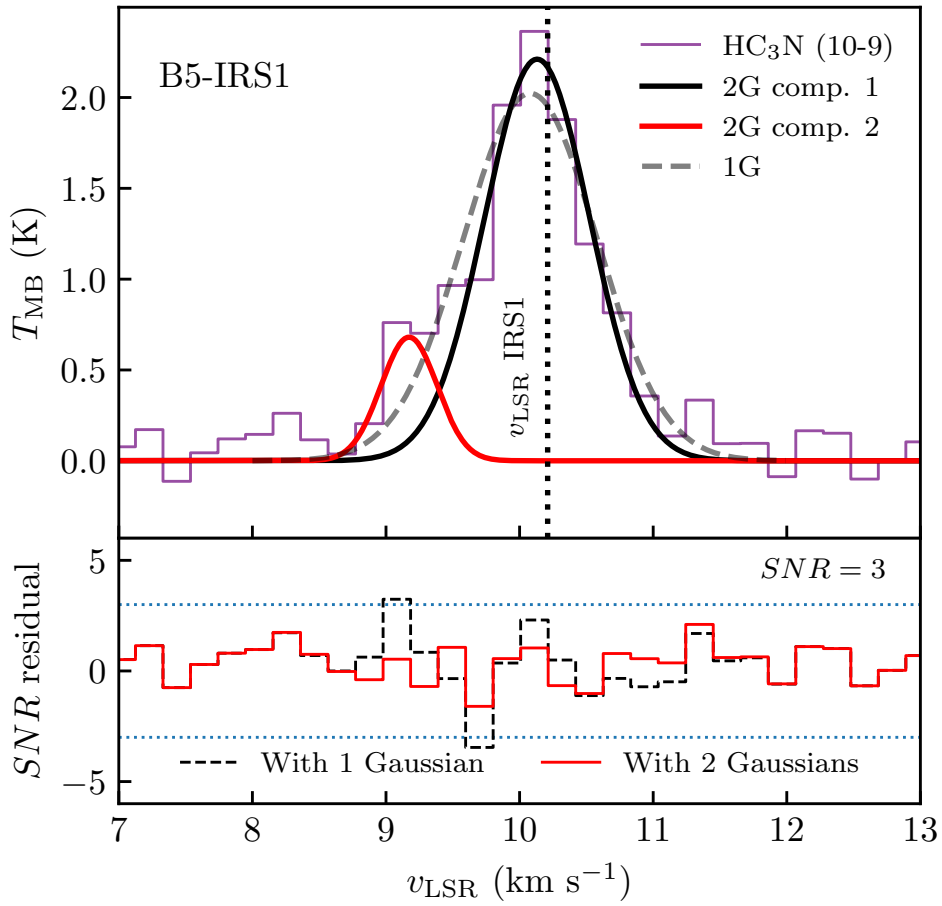

Figure B.5: Results from the one- and two-Gaussian fit to the HC_3N (10–9) emission at the position of the protostar B5-IRS1. Top: HC_3N (10–9) emission spectrum at the position of B5-IRS1, together with the best fit results using one and two Gaussian curves. The vertical dashed line represents the central velocity of the protostar from P15. Bottom: residuals from the fit in terms of S/N. The dashed purple line represents the residuals after the 1 Gaussian fit, whereas the solid purple line, the residuals after the 2 Gaussian fit. The horizontal blue dashed lines mark the $S/N = 3$ and -3 levels.

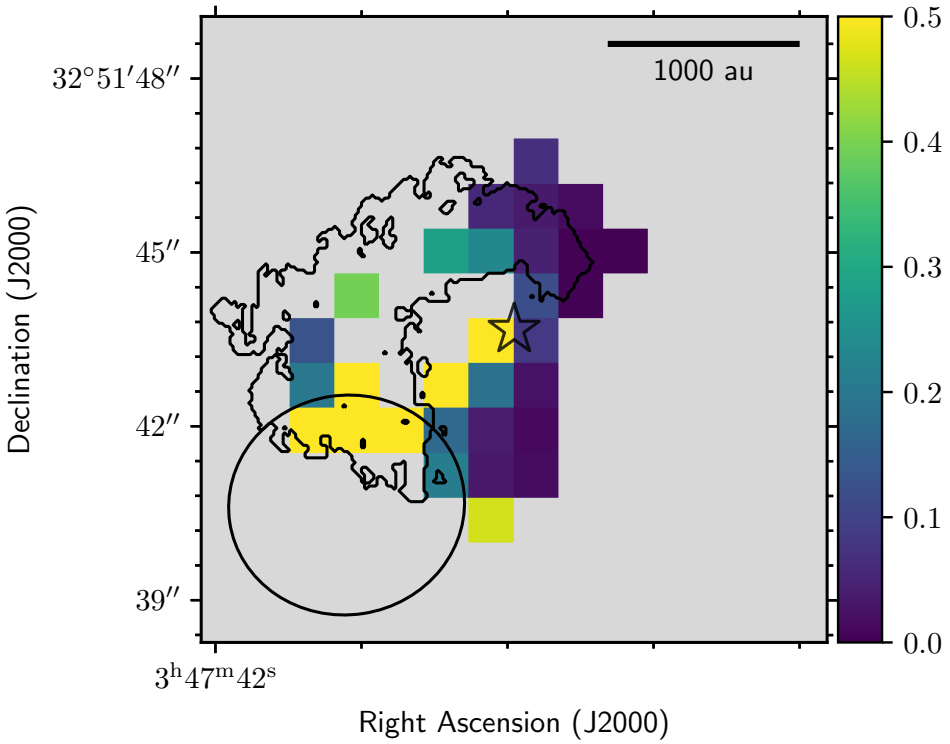

Figure B.6: Probability P (Eq. B.2) for two Gaussian components fit in HC_3N (10–9) around 4″ from the protostar. Contours indicate the location of the blue streamer found in Sect. 3.4.2.1.

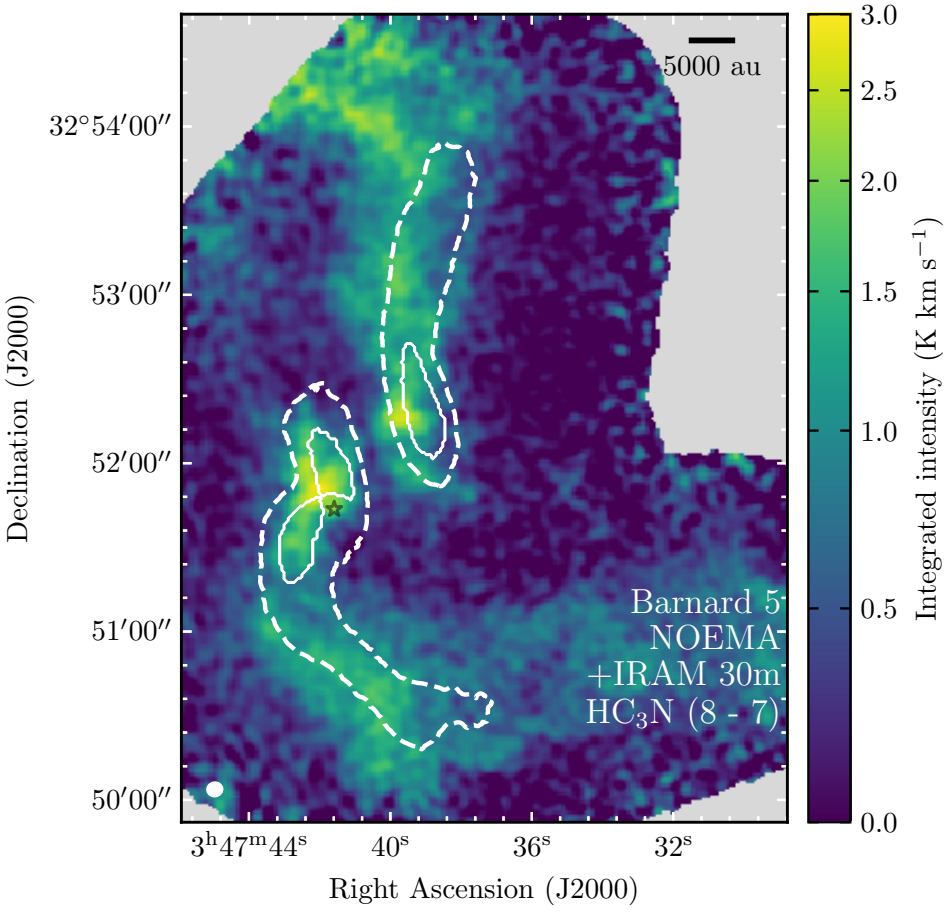

Figure B.7: Velocity integrated HC_3N $(8-7)$ line emission, from 9.2 to 11.2 km s^{-1}. White dashed contours correspond to the filaments identified in NH_3 emission by P15 and S21. White solid contours outline the edges of the condensations labeled as in P15. The gray star marks the position of the protostar B5-IRS1.

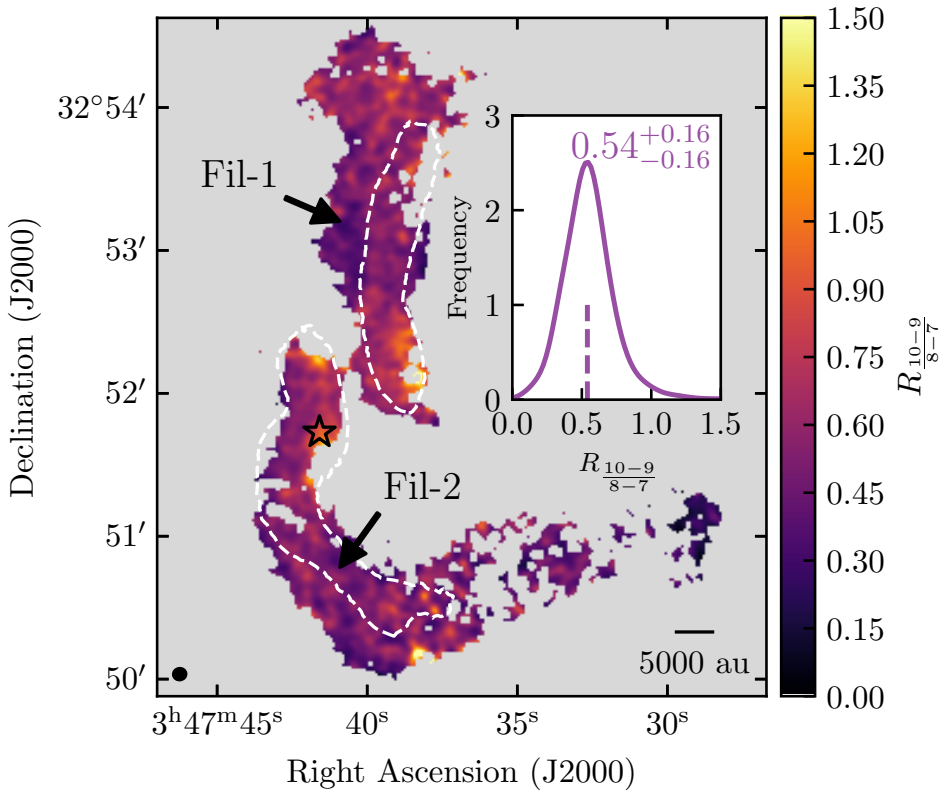

Figure B.8: Map of the line ratio between the HC_3N $(10-9)$ and $(8-7)$ transitions. White dashed contours correspond to the filaments identified in NH_3 emission by P15 and S21. The black star marks the position of the protostar B5-IRS1. Inset: KDE of the line ratios obtained. The dashed vertical line shows the median value of the distribution, and the uncertainties correspond to the distance to the 1st and 3rd quartiles.

$$R_{\frac{10-9}{8-7}} = \frac{\int T_{R,10-9} dv}{\int T_{R,8-7} dv}, \tag{B.3}$$

where $\int T_R dv$ is the integrated intensity of a spectrum in K km s^{-1}. The resulting map is in Fig. B.8 and includes pixels where $S/N > 5$ for both $10-9$ and $8-7$ transitions.

In general, $R_{\frac{10-9}{8-7}}$ does not present large systematic variations along the filaments, and variations are usually clumpy and reach differences of up to 0.2 within one beam. The distribution of line ratios of the whole map is shown in the inset of Fig. B.8: it has a median of 0.54 and its shape resembles a Gaussian. The ratio does reach values up to 1.0 in the vicinity of the protostar, which could occur due to higher temperatures and/or higher optical thickness in the region. Very low values of $R_{\frac{10-9}{8-7}}$, under 0.2, and very high values, over 1.1, are located in the edges of the filaments and are due to the detection edges of either HC_3N $(10-9)$ or HC_3N $(8-7)$. Near the condensations the ratio is also slightly higher, increasing from ≈ 0.55 to ≈ 0.65. This could be due to a higher temperature closer

to the condensation, caused by mass infall, which would then populate more the $(10-9)$ transition, and/or emission in the condensations becoming optically thick. As the map shows no considerable spatial variations, it is safe to take its mean to describe the volume density of the whole emission.

B.5.3 H_2 volume density traced by HC_3N

We took the mean value of the distribution, $< R >= 0.56 \pm 0.01$, to estimate the H_2 density $n(H_2)$ and the excitation temperature T_{ex} for the $HC_3N\,(10-9)$ transition. We compared this ratio with the results from the RADEX models run by Pineda et al. (2020), as their input parameters result in similar emission intensities T_R as the ones observed in this work and the line ratios resulting from their test (between 0.2 and 0.8) include our resulting line ratio. A line ratio $< R >= 0.56 \pm 0.01$ corresponds to a density of $\approx 10^5$ cm^{-3} (based on the Extended data fig. 1 from Pineda et al. (2020)) and results in an excitation temperature $T_{ex} \approx 6.4$ K for the $10-9$ molecular transition.

B.6 Clustering of H_2CO Gaussian components

We clustered the different Gaussian components found in Sect. 3.3.4 to aid in their physical interpretation. We applied the unsupervised learning tools from the `scikit-learn` Python library (Pedregosa et al. 2011) to the results of our 1, 2 and 3 Gaussian component fitting of the ALMA H_2CO emission. We used the right ascension (RA), the declination (DEC) and central velocities ($v_{\rm LSR}$) of each Gaussian component as features for clustering. Using all properties of the fits as features, or using the three mentioned parameters plus either amplitude or velocity dispersion, does not represent an improvement in the clustering of the Gaussian components. We first scaled all the features to a range from -1 to 1 using the `StandardScaler` class in the `preprocessing` Python library. By doing so, we assigned the same relative weight to all the features. Then, we used the algorithm DBSCAN (Ester et al. 1996), implemented in the `DBSCAN` class, with parameters `eps` = 0.248 and `min_samples` = 100. The rest of the parameters are left as default. This results in 5 clusters in (RA, DEC, $v_{\rm LSR}$) space. The resulting groups found by DBSCAN are shown in Fig. B.9.

There are a total of 11992 individual Gaussian components in the cube, out of which DBSCAN determined 3042 (25%) are outliers, and do not belong to any cluster. This does not imply that these Gaussians are fitting noise, only that the features could not be grouped. In particular, points within $1''$ to the east of the protostar could not be grouped. This region is dominated by emission with $v_{\rm LSR} \approx 9.25$ km s^{-1}. We suggest this emission is also part of the blueshifted streamer described in Sect. 3.4.2.2, as it follows the same apparent gradient. Adding these points to the blueshifted cluster does not affect the streamline model nor the resulting centrifugal radius, so we decided to follow the grouping resulting from the clustering algoithm. Out of all the clustered points, the largest group is a fully blueshifted cluster (consisting of 5529 individual points) and the second largest, a fully redshifted cluster (with 2557 individual points), with respect to the protostar's $v_{\rm LSR}$

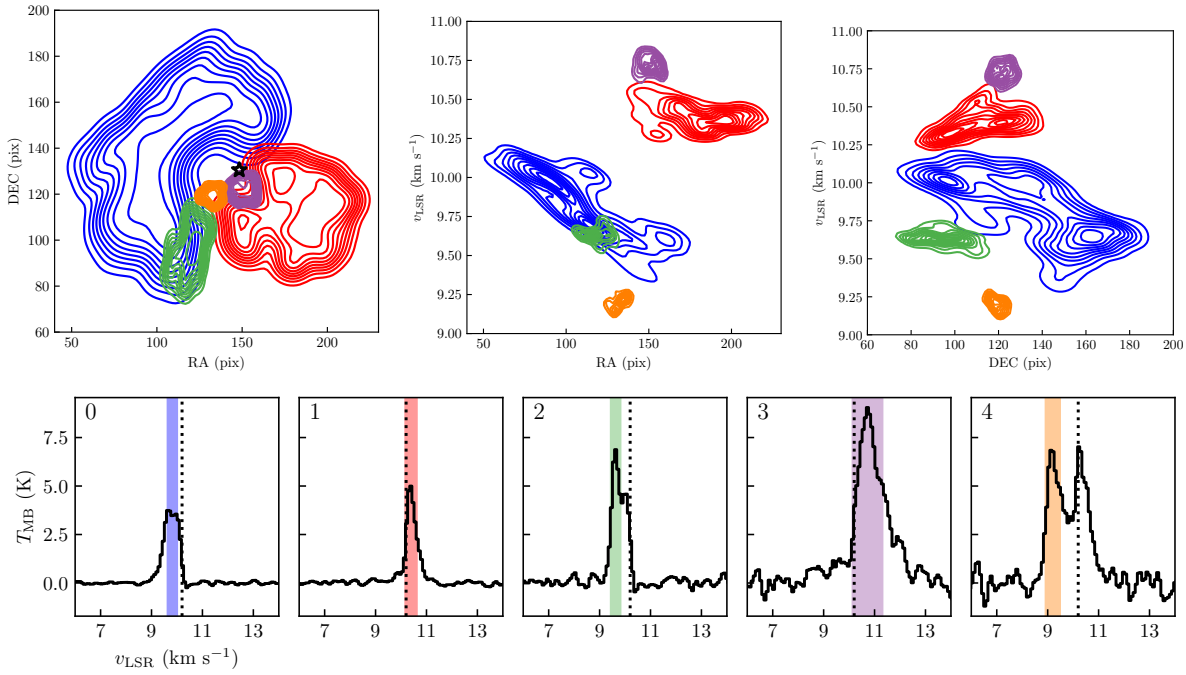

Figure B.9: Results from the clustering of the Gaussian components in the ALMA H_2CO spectra. Each cluster is labeled with a number from 0 to 4, in order of descending number of points. Blue and red points (labeled 0 and 1) represent the clusters named blueshifted and redshifted component, respectively. Orange, purple and green points represent the other three found clusters. **Top**: Density plots of the clustered groups using Gaussian KDEs, seen in the image plane (RA and DEC in pixels, left), in RA versus $v_{\rm LSR}$ (middle) and in DEC versus $v_{\rm LSR}$ (right). The black star marks the position of the protostar. **Bottom:** average spectra taken from the area covered by each group, labeled with the numbers from the Top Left panel. The ALMA H_2CO spectra are drawn with black solid lines. The colored vertical areas represent the location of average $v_{\rm LSR}$ and FWHM of each cluster. The vertical dotted line marks the protostar's $v_{\rm LSR}$.

(10.2 km s^{-1}).

B.6.1 Nonthermal velocity dispersion of H_2CO emission

We checked the velocity dispersion $\sigma_{\rm v,fit}$ of the Gaussians in the blueshifted and redshifted clusters and compared them to the thermal sound speed. Nonthermal velocity dispersion larger than the sound speed can be attributed to the outflow or to gas tracing rotation motions instead of infall.

First, we deconvolved the velocity dispersion with respect to the channel size of our data using

$$\sigma_{\rm v}^2 = \sigma_{\rm v,\,fit}^2 - \frac{2\Delta_{\rm ch}}{2.355}, \tag{B.4}$$

where $\Delta_{\rm ch}$ is the channel width (Table 3.1). Then, we subtracted in quadrature the thermal dispersion $\sigma_{\rm th}$ from the deconvolved velocity dispersion, thus obtaining $\sigma_{\rm v,\,nt}$:

$$\sigma^2_{\rm v,\,nt} = \sigma^2_{\rm v} - \sigma^2_{\rm th}. \tag{B.5}$$

The thermal dispersion is

$$\sigma_{\rm th} = \sqrt{\frac{k_B T}{\mu_{\rm H_2CO} m_{\rm H}}} = 0.052\,{\rm km\,s^{-1}}, \tag{B.6}$$

where k_B is the Boltzman constant, T is the kinetic temperature of the gas, which we assumed is 9.7 K from Pineda et al. (2021), $\mu_{\rm H_2CO} = 30.026$ is the molecular weight of the H_2CO molecule and $m_{\rm H}$ is the mass of a Hydrogen atom.

The resulting $\sigma_{\rm v,\,nt}$ for the two envelope components are in Fig. B.10. The dispersion increases when the distance to the protostar decreases for both components, but it is mostly subsonic for both parts of the envelope. H_2CO emission becomes transonic (larger than $c_{\rm s} = 0.18$ km s^{-1}) within $r \lesssim 600$ au approximately. This means that, for majority of the emission within both components, the H_2CO gas is unaffected by the outflow and is not caused by Keplerian rotation.

B.7 Estimate of the protostellar mass

We used the $C^{18}O$ $(2-1)$ ALMA data to estimate the protostellar mass of B5-IRS1. We first looked at the position-velocity (PV) diagram of $C^{18}O$ using the astropy package `pvextractor` (Ginsburg et al. 2016). We generated the PV diagram along a path centered on the protostar with a total length of 1600 au, with a position angle (PA) of 157.1° (with 0° pointing toward the north), obtained from the outflow PA (Zapata et al. 2014), and a width of 0.4″. The pixel size of the $C^{18}O$ cube is 0.054″, so we chose to take an integer number of pixels as the width of the PV sampling path that was as close to the beam width as possible (7 pixels, or 0.4″). The resulting PV diagram is in Fig. B.11 and shows the classical diamond shape that is attributed to a combination of Keplerian rotation and infall motion of the inner envelope (e.g., Lee et al. 2014; Sakai et al. 2014). When we compare the PV diagram with the Keplerian curve produced by a 0.1 $M_\odot$ protostellar mass (the previously reported protostellar mass in Brassfield & Bourke 2011) and for a disk with an inclination $i = 77°$ (obtained from the outflow inclination angle $i = 13°$, Yu et al. 1999), the PV diagram 5σ limit is above the curve, indicating the protostar's mass is possibly higher. We plotted over the PV diagram the Keplerian curve for 0.2 $M_\odot$ with the same disk i and we saw that it is closer to the 5σ edge than 0.1 $M_\odot$. From this simple observation, we suspect the central protostar's mass is higher. To confirm, we did a deeper analysis into the $C^{18}O$ data.

We obtained the central position of $C^{18}O$ emission in each velocity channel and determine if it is consistent with Keplerian motion. For this, we fit a two-dimensional Gaussian at each of the channels of the $C^{18}O$ $(2-1)$ cube between 7.9 and 9.2 km s^{-1} and between

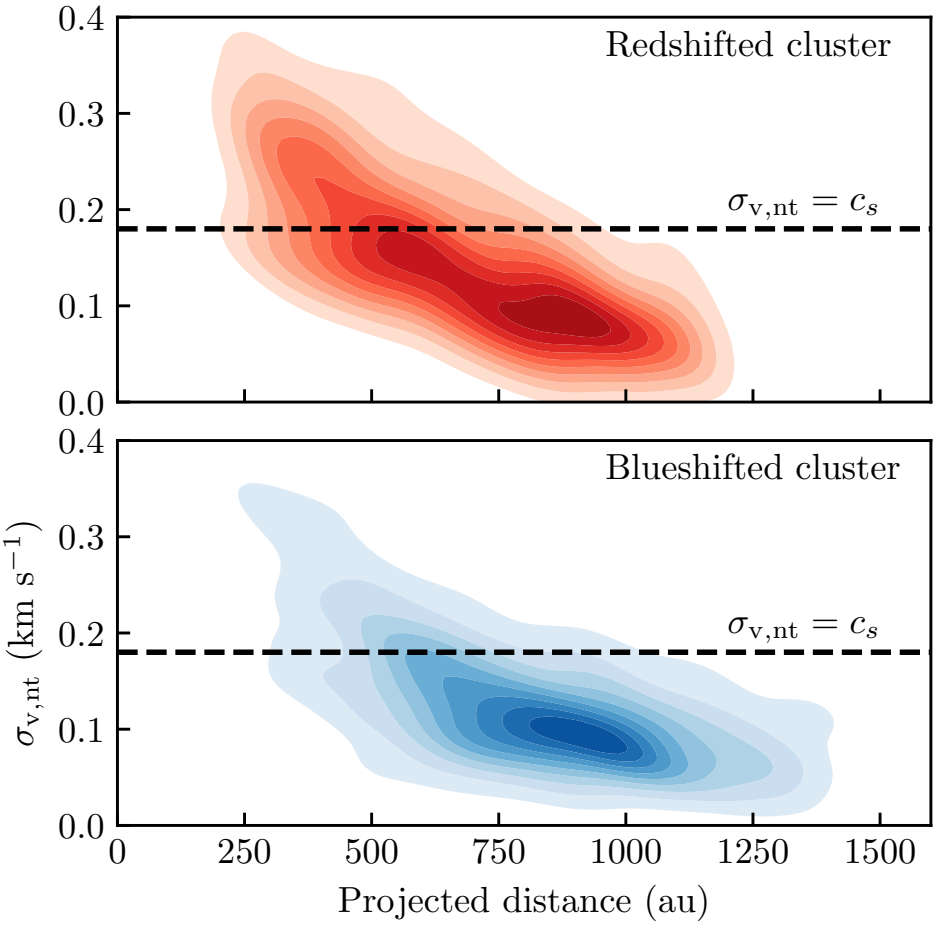

Figure B.10: KDE of the nonthermal velocity dispersion for the blueshifted and redshifted envelopes. The dashed line represents where $\sigma_{\rm v,\,nt}$ equals the sound speed for gas at 9.7 K (0.18 km s^{-1}).

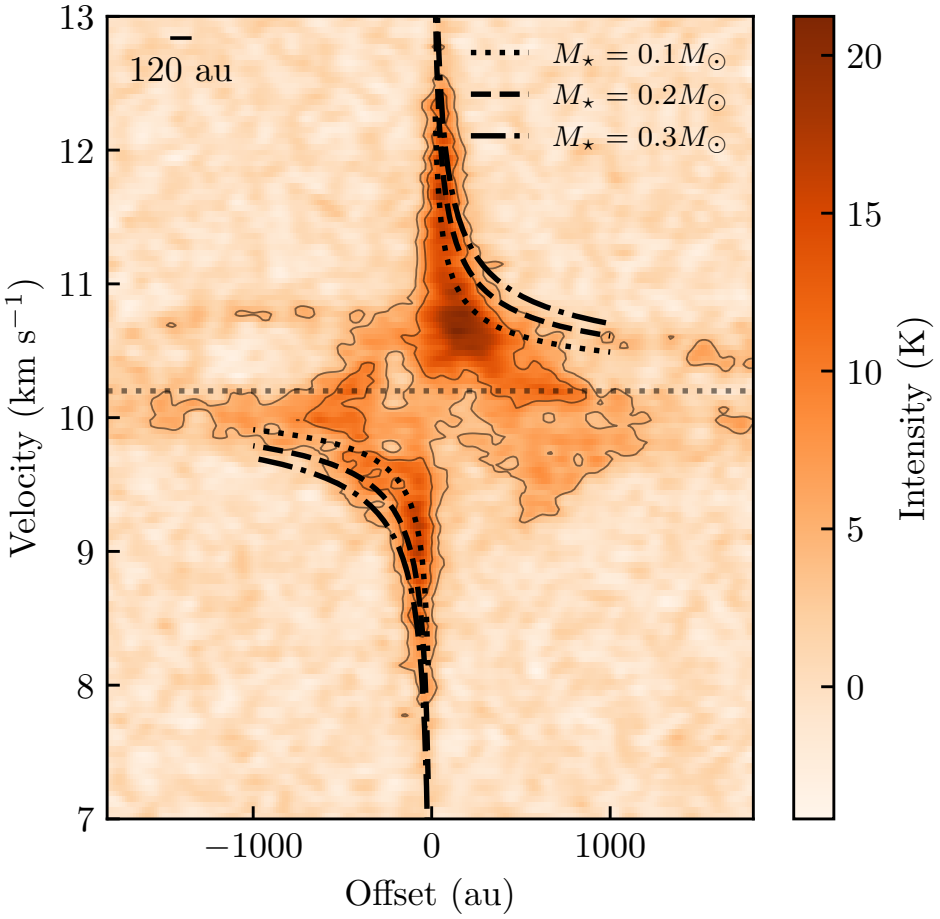

Figure B.11: Position-velocity diagram of the ALMA C^{18}O datacube, centered at the position of the protostar, with a PA of 157.1° and a width of 0.4″. The black curves show the Keplerian rotation profile produced by three protostellar massses: the dotted line shows the Keplerian curve for a protostar of 0.1 $M_\odot$ (Brassfield & Bourke 2011), the dashed line for 0.2 $M_\odot$, and the dash-dotted line for 0.3 $M_\odot$. The dotted horizontal line marks the protostar's $v_{\rm LSR} = 10.2$ km s^{-1}. The scalebar represents one beam width (120 au or 0.4″)

10.8 and 12.4 km s^{-1}. These ranges cover the velocities of C^{18}O emission that are the most blueshifted and redshifted with respect to the protostar, and miss the central channels seen in Fig. B.4, where emission is affected by missing short- and zero-spacings. We used the `models.Gaussian2D` class and fit the Gaussian model using least-squares minimization with the Levenberg-Marquardt algorithm, implemented in the `fitting.LevMarLSQFitter` class. Both classes are part of the `astropy` python package. We use the peak value of each channel, the position of the peak, and the beam width $\sigma_{\rm beam} = \theta_{\rm FWHM}/2.355$ (Table 3.1) as initial guesses for the amplitude, central position and dispersion of the Gaussian at each channel. We used the channels between $v_{\rm LSR} = 7.9 - 8.8$ km s^{-1} and $11.1 - 12.4$ km s^{-1} to calculate the barycenter (i.e. the rotation center) of the points blueshifted and redshifted with respect to the protostar's $v_{\rm LSR}$. Finally, we calculated the distance of each point to the calculated barycenter d and plot d against the corresponding channel's velocity with respect to the protostar's $v_{\rm LSR}$, $\delta v_{\rm LSR,IRS1} = v_{LSR} - 10.2$ km s^{-1}. Using the corrected center instead of the position from Tobin et al. (2016) returns a more precise velocity versus distance plot. Nevertheless, the distance between the barycenter and the protostar's coordinates is $\lessapprox 0.1''$.

The resulting C^{18}O central positions per velocity channel are in Fig. B.12 Left and the velocity versus distance plot is in Fig. B.12 Right. The faded blue and red points represent the fitted positions where there is extended emission in the velocity channel, which affected the Gaussian fit. For emission peaks located from 0 to about 70 au ($0.2''$), as distance from the protostar increases, $\delta {\rm v}_{LSR,{\rm IRS1}}$ tends to decrease. In the image plane, as $\delta {\rm v}_{LSR,{\rm IRS1}}$ decreases, the points tend to get away from the protostar in opposite directions along a northwest to southeast orientation, similar to the orientation of the disk used to obtain the PV diagram. These two behaviors are expected for Keplerian rotation. However, emission centered farther away than ~ 70 au show a change in direction: as $v_{\rm LSR}$ gets closer to the protostar's $v_{\rm LSR}$, the blueshifted points move toward the east instead of northwest, and the redshifted points move toward the west instead of southeast. These low $\delta {\rm v}_{LSR,{\rm IRS1}}$ "tails" have different behaviors in velocity versus distance: $\delta {\rm v}_{LSR,{\rm IRS1}}$ drops faster with distance for the redshifted points than for the blueshifted ones. Moreover, the blueshifted and redshifted points that are the farthest away from the protostar are at the edges of the blueshifted and redshifted envelope components, respectively. We note that these points come from the channels which have considerable extended emission. This suggest that C^{18}O emission is tracing part of the infall that we trace with H_2CO emission as C^{18}O extended emission.

We plotted the Keplerian velocity versus distance curve expected for a protostellar mass of 0.1, 0.2 and 0.3 M$_\odot$ over the velocity versus distance plot for C^{18}O positions (in Fig. B.12 Right). The uncertainty in central position is too large to fit a Keplerian rotation curve to these data, so we only overplot the expected Keplerian curves for the selected masses and do not attempt to obtain a radius from these data points. Most of the points less than 100 au away from the protostar fall between the 0.2 and 0.3 M$_\odot$ curves. However, the large uncertainty of the points that are closer to the protostar are too large to clearly distinguish between both cases, some also reaching values consistent with 0.1 M$_\odot$. We decide to use a protostellar mass of 0.2 M$_\odot$, as this is not far from the value presented in

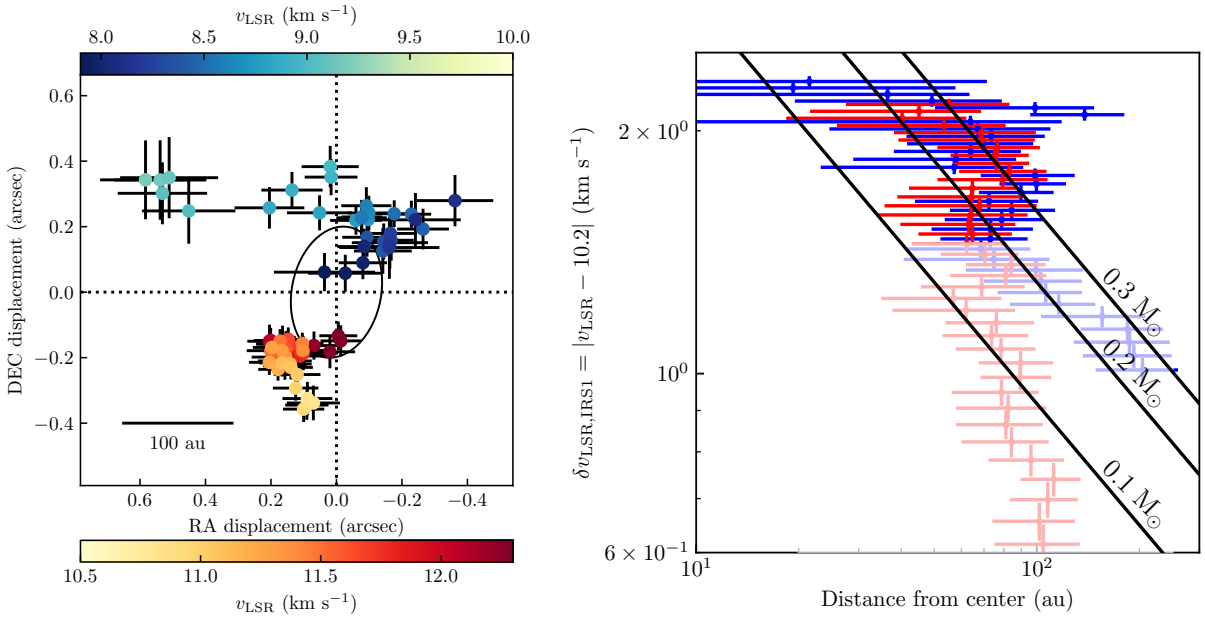

Figure B.12: Results from the two-dimensional Gaussian fit to the C^{18}O channel maps. **Left**: Best fit central positions with respect to the image plane, where their colors represent the velocity of the channel $v_{\rm LSR}$. The dashed lines represent the position of the barycenter. The ellipse centered at the barycenter represents the beam size (FWHM). **Right**: C^{18}O emission velocity with respect to the protostar's $v_{\rm LSR}$ versus distance from the protostar. Blue dots are obtained from the C^{18}O emission blueshifted with respect to the protostar and red dots from the redshifted emission. Faded dots come from velocity channels with considerable extended emission, and therefore their properties are affected by motions other than Keplerian. The solid black lines are the Keplerian rotation profiles for 0.1, 0.2 and 0.3 M$_\odot$.

Brassfield & Bourke (2011) but still looks consistent with most of the points obtained from our Gaussian fit and the 5σ contours of the PV diagram (Fig. B.11).

B.8 Comparison between H_2CO and $H^{13}CO^+$

We compared the emission coming from the blueshifted component from the DBSCAN analysis (Sect. 3.4.2.1) with the $H^{13}CO^+$ emission from van't Hoff et al. (2022) both in the image plane and in velocity space. We first looked at the location of emission. van't Hoff et al. (2022) show that $H^{13}CO^+$ emission has a ridge-like shape toward the west of B5-IRS1. $H^{13}CO^+$ peak emission ridge coincides with the area occupied by the blueshifted component, although emission with $S/N > 3$ is more extended than the blue streamer. Spatial coincidence does not mean both molecules trace the same part of the envelope, so we looked into the kinematics of $H^{13}CO^+$.

We fit a Gaussian curve to the $H^{13}CO^+$ spectra with the same procedure as for HC_3N (Appendix B.4) but first selecting all spectra with $S/N > 3$ to make the mask. The resulting central velocities are in Fig. B.13 Left. We note that all the velocities in the east side of B5-IRS1 are blueshifted with respect to the protostar. $H^{13}CO^+$ shows a velocity gradient from 10.1 to 9.4 $\mathrm{km\,s^{-1}}$ as distance to the protostar decreases. This gradient is similar to the gradient seen in the blueshifted component in Fig. 3.11, which suggest both molecules trace an infall motion. This also confirms that $H^{13}CO^+$ does not trace outflow motion, using the same arguments as in Sect. 3.4.2.2.

We calculated the difference between v_{LSR} for H_2CO and $H^{13}CO^+$ spectra to investigate if H_2CO has any additional movement with respect to $H^{13}CO^+$ or if differences are random. For this, we reprojected the spatial grid of H_2CO to the one of $H^{13}CO^+$ using the astropy package `reproject`. The KDE of the difference is in Fig. B.13 Right. Differences in velocity appear to be random; there appears to be no tendency for a preferential redshift of blueshift of H_2CO with respect to $H^{13}CO^+$ for any velocity. The median value of the difference is $0.02^{+0.07}_{-0.09}$ $\mathrm{km\,s^{-1}}$, smaller than the channel width for H_2CO data (Table 3.1). This means both molecules share the same velocities and velocity gradients. We therefore conclude that both H_2CO and $H^{13}CO^+$ trace the infall motion of the blueshifted streamer.

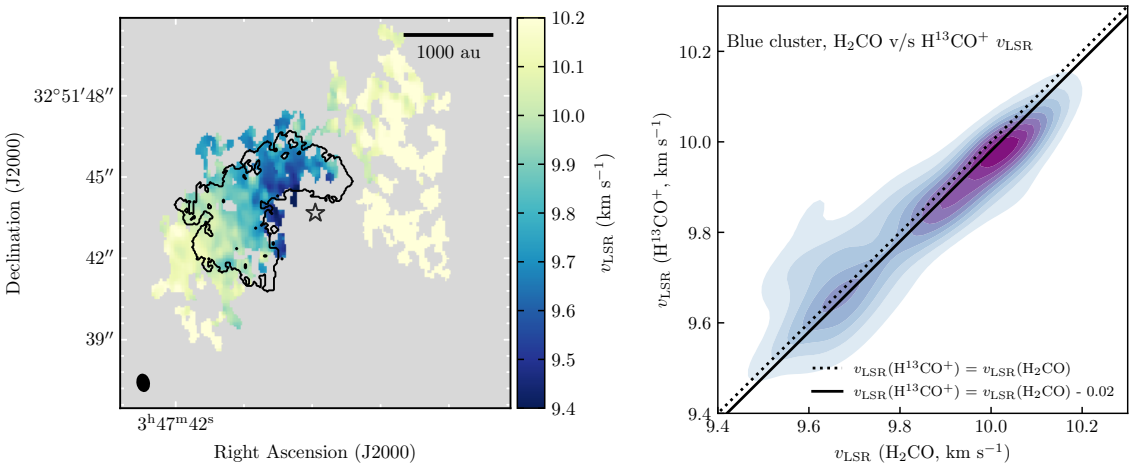

Figure B.13: Comparison between the $v_{\rm LSR}$ found for $H^{13}CO^+$ observations from van't Hoff et al. (2022) and our H_2CO $v_{\rm LSR}$ results. **Left:** Central velocities obtained through the Gaussian fit to $H^{13}CO^+$ observations from van't Hoff et al. (2022). The black ellipse represents the beam size. The black contour indicates the area covered by the H_2CO blueshifted cluster found using DBSCAN. The black star represents the position of B5-IRS1. **Right:** KDE of the difference between the central velocities of H_2CO and $H^{13}CO^+$ emission. The dotted line shows the one-to-one relation, and the solid line shows the same relation but displaced by 0.02 km s^{-1}

Appendix C

Appendices for Chapter 4

C.1 Channel maps

Figures C.1 and C.2 show the channel maps of HC_3N and N_2H^+ emission between approximately 5.6 and 9.7 $\mathrm{km\,s^{-1}}$, in steps of about 0.2 $\mathrm{km\,s^{-1}}$. We note that there is emission in HC_3N outside of this range, starting from -3 $\mathrm{km\,s^{-1}}$ and ending at approximately 13 $\mathrm{km\,s^{-1}}$.

C.2 Density-based clustering of molecular emission

In this section, we describe the steps taken to cluster the N_2H^+ and HC_3N velocity structures. We cluster the Gaussian points from each molecule based on their position in the plane of the sky and their v_{LSR}. Using the amplitude T_{peak} or their dispersion σ_{v} does not improve the clustering results, and as our goal is to disentangle the velocity structures of the filament, the analysis in the position-position-velocity space is sufficient (in particular after filtering out the Gaussians with high dispersion).

From the Gaussian fitting and the quality assessment, we have 94864 Gaussians in the N_2H^+ data cube and 56771 Gaussians in the HC_3N data cube. We did a finer selection of Gaussian components for both molecules before clustering, so as to ensure that we trace the bulk emission of the filament structure. We select only the points with low uncertainty in their parameters, that is, with an uncertainty less than 25% the value of the parameter. This criterion leaves out uncertain points that can add confusion to the clustering. We also filter out the Gaussian fits that show $\sigma_{\mathrm{v}} > 1$ $\mathrm{km\,s^{-1}}$, as these represent fits with outflows. We filter possible Gaussian components that represent random noise in the spectra by selecting only those components with velocities between 5 and 9 $\mathrm{km\,s^{-1}}$. This also helps to filter out HC_3N that corresponds to high-velocity outflow wings. We were left with 81657 Gaussians in the N_2H^+ data cube and 52019 Gaussians in the HC_3N data cube.

We cluster the Gaussian component results of N_2H^+ using Hierarchical Density-Based Spatial Clustering of Applications with Noise (HDBSCAN). HDBSCAN is an extension of the Density-Based Spatial Clustering of Applications with Noise (DBSCAN) algorithm. In

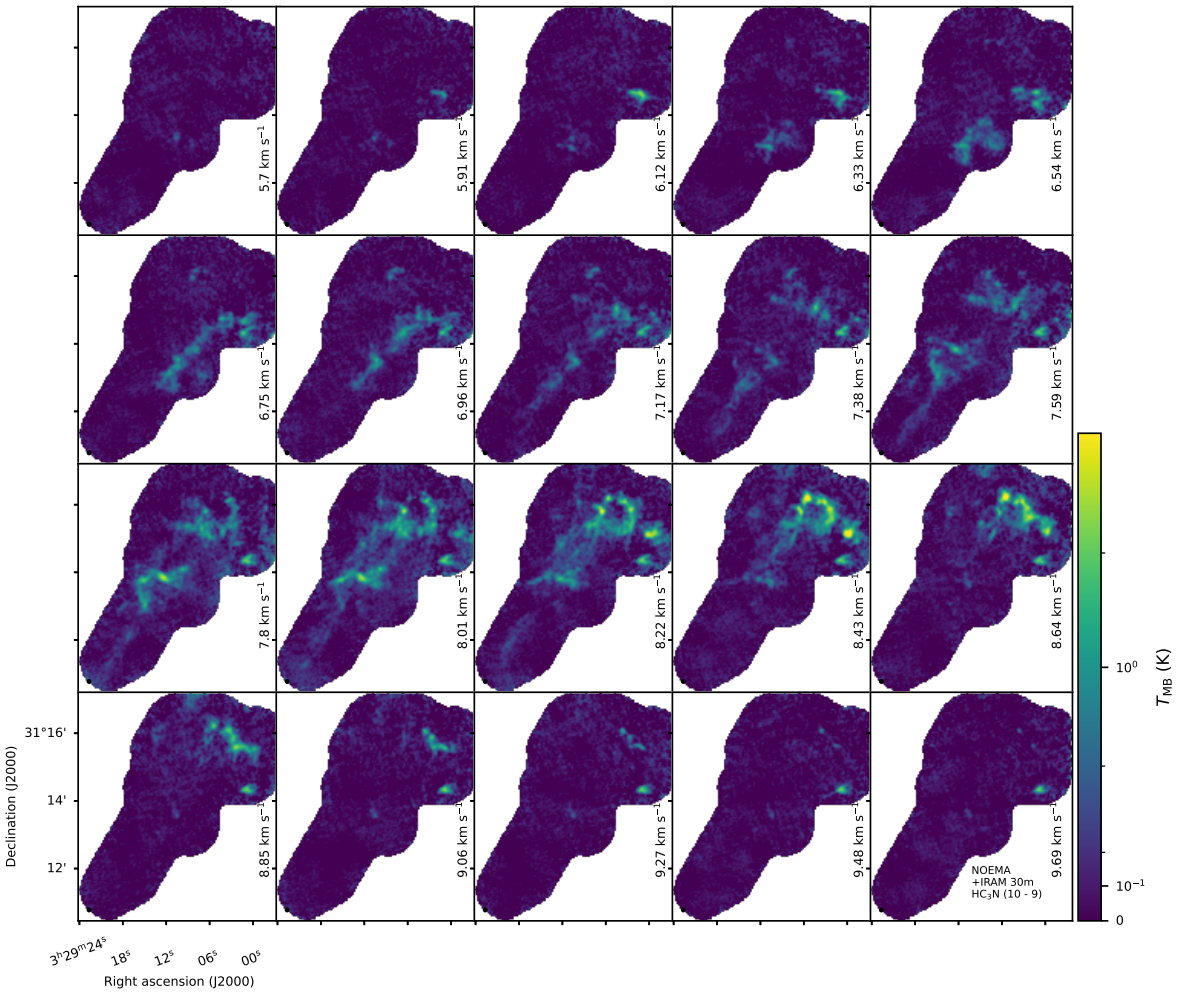

Figure C.1: Channel maps between 5.7 and 9.7 $\mathrm{km\,s^{-1}}$ for HC_3N $J = 10 - 9$ emission.

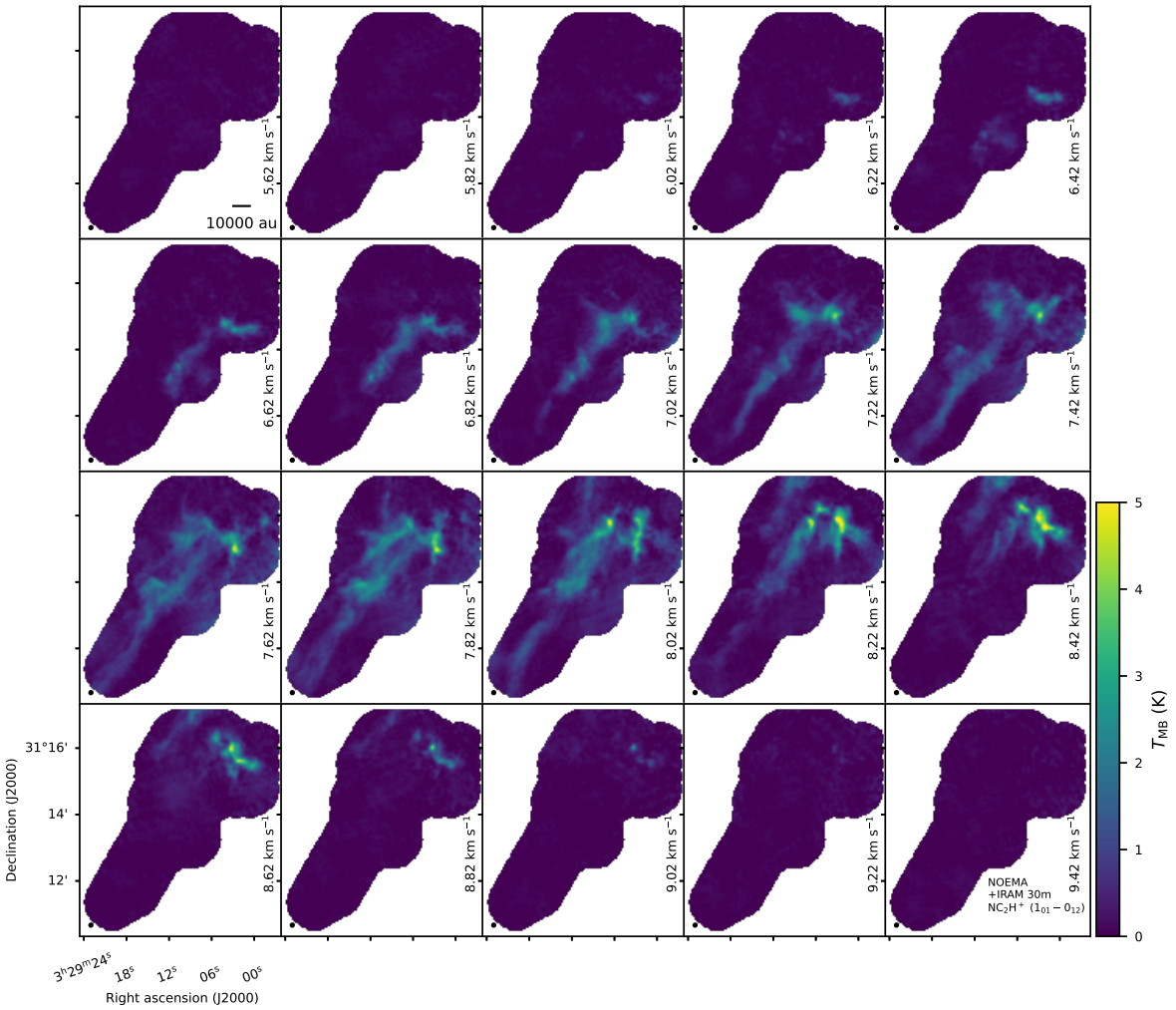

Figure C.2: Channel maps between 5.6 and 9.4 km s^{-1} for N_2H^+ $J = 1 - 0$, $F_1F = 01 - 12$ emission.

Parameter	HC_3N	N_2H^+
min_sample	200	240
min_cluster_size	500	900

Table C.1: HDBSCAN parameters used to cluster the HC_3N and N_2H^+ Gaussian peaks.

summary, DBSCAN defines clusters of points in the user-defined hyperspace as local point overdensities, and leaves sparsely distributed points as noise (Ester et al. 1996). A core is defined as an overdensity surrounding a core sample (a single point in the hyperspace) with a minimum of samples n within a radius of ϵ. HDBSCAN, instead of fixing the radius ϵ, selects clusters based on the minimum spanning tree of the mutual reachability graph[1], i.e. explores all possible values of ϵ (Campello et al. 2013; McInnes & Healy 2017). This process allows the algorithm to form clusters of different densities. We use the `hdbscan` package from the contributed packages to `scikit-learn`[2].

The best results for each molecule are obtained with the parameters shown in Table C.1, named according to the parameter names in the python implementation[3]. The parameters are different for each molecule because the number of Gaussian peaks for HC_3N (about 51000) is much smaller than the number of Gaussian peaks in N_2H^+ (more than 81000). The resulting clusters can be seen in Fig. 4.3.

Figure C.3 shows the peak temperature $T_{\rm peak}$, velocity $v_{\rm LSR}$ and dispersion $\sigma_{\rm v}$ of the HC_3N clusters, grouped according to their fiber, redshifted or blueshifted. resulting from the HDBSCAN analysis. Figure C.4 shows the same quantities but for the N_2H^+ clusters.

C.3 Close-up of N_2H^+ velocity profiles toward individual protostars

Figure C.5 shows the same two top panels ($T_{\rm peak}$ and $v_{\rm LSR}$) of Fig. 4.7 right for all other sources where we find a streamer candidate. Some show position-velocity cuts, and for those where a second component in N_2H^+ coincides roughly with the streamer's velocity, we plot the $v_{\rm LSR}$ KDE of the corresponding component instead of the position-velocity cut.

[1]https://scikit-learn.org/stable/modules/clustering.html
[2]https://hdbscan.readthedocs.io/en/latest/
[3]https://hdbscan.readthedocs.io/en/latest/parameter_selection.html

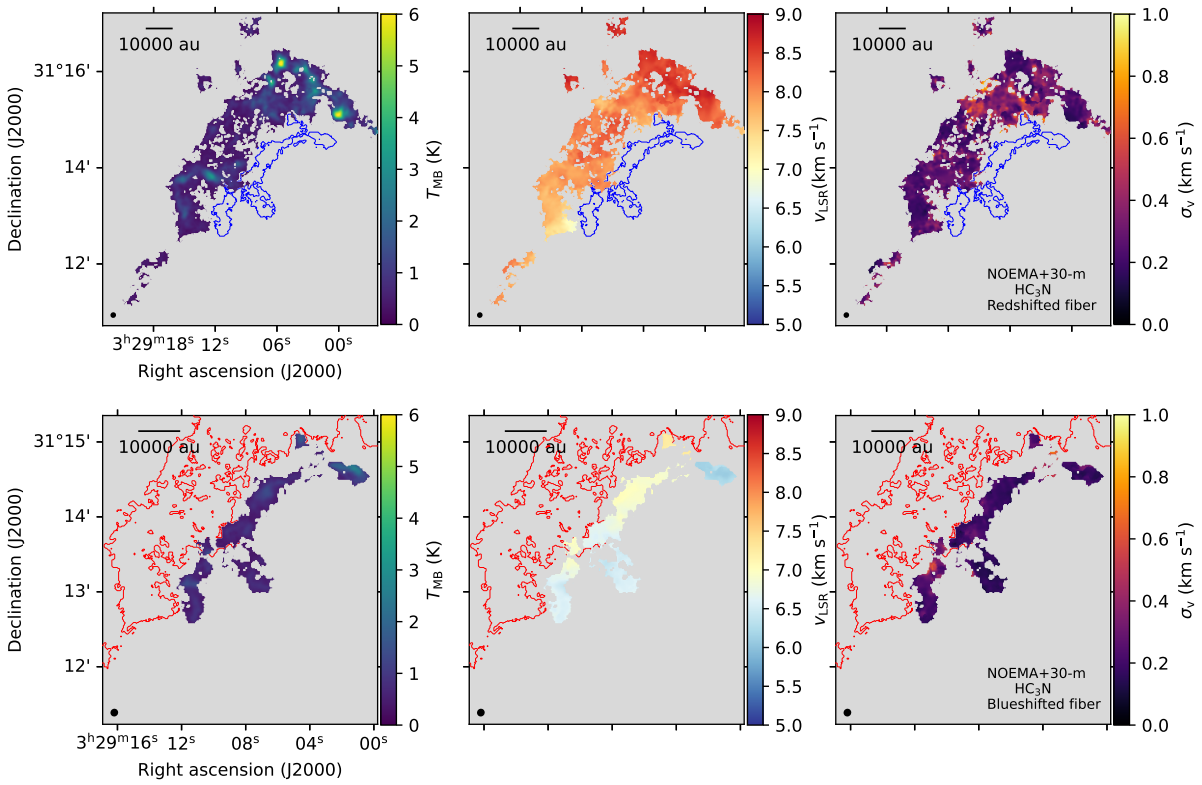

Figure C.3: Peak temperature, central velocity and velocity dispersion of the HC_3N clusters. Top: $T_{\rm peak}$, $v_{\rm LSR}$ and $\sigma_{\rm v}$ for the clusters belonging to the redshifted fiber. The blue contour indicates the position of the blueshifted fiber. Bottom: $T_{\rm peak}$, $v_{\rm LSR}$ and $\sigma_{\rm v}$ for the clusters belonging to the blueshifted fiber. The red contour indicates the position of the redshifted fiber.

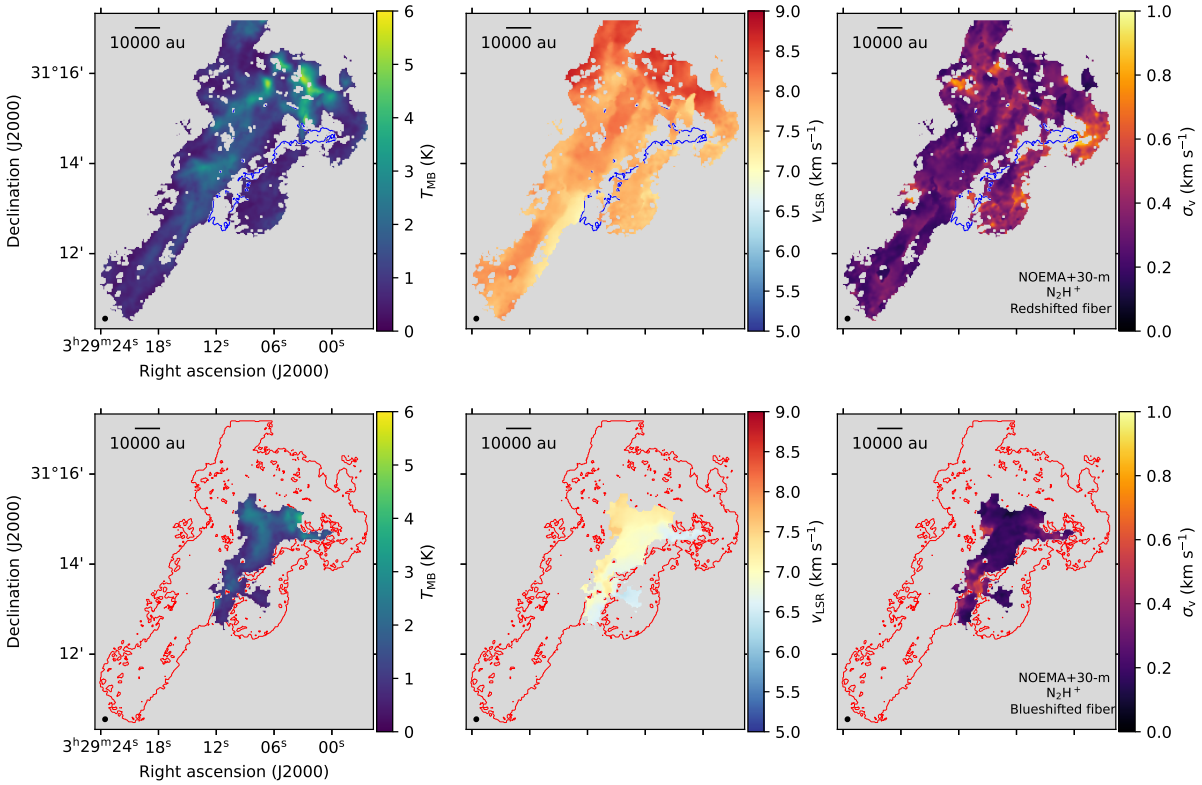

Figure C.4: Peak temperature, central velocity and velocity dispersion of the N_2H^+ clusters. Top: $T_{\rm peak}$, $v_{\rm LSR}$ and $\sigma_{\rm v}$ for the redshifted fiber. The blue contour indicates the position of the blueshifted fiber. Bottom: $T_{\rm peak}$, $v_{\rm LSR}$ and $\sigma_{\rm v}$ for the blueshifted fiber. The red contour indicates the position of the redshifted fiber.

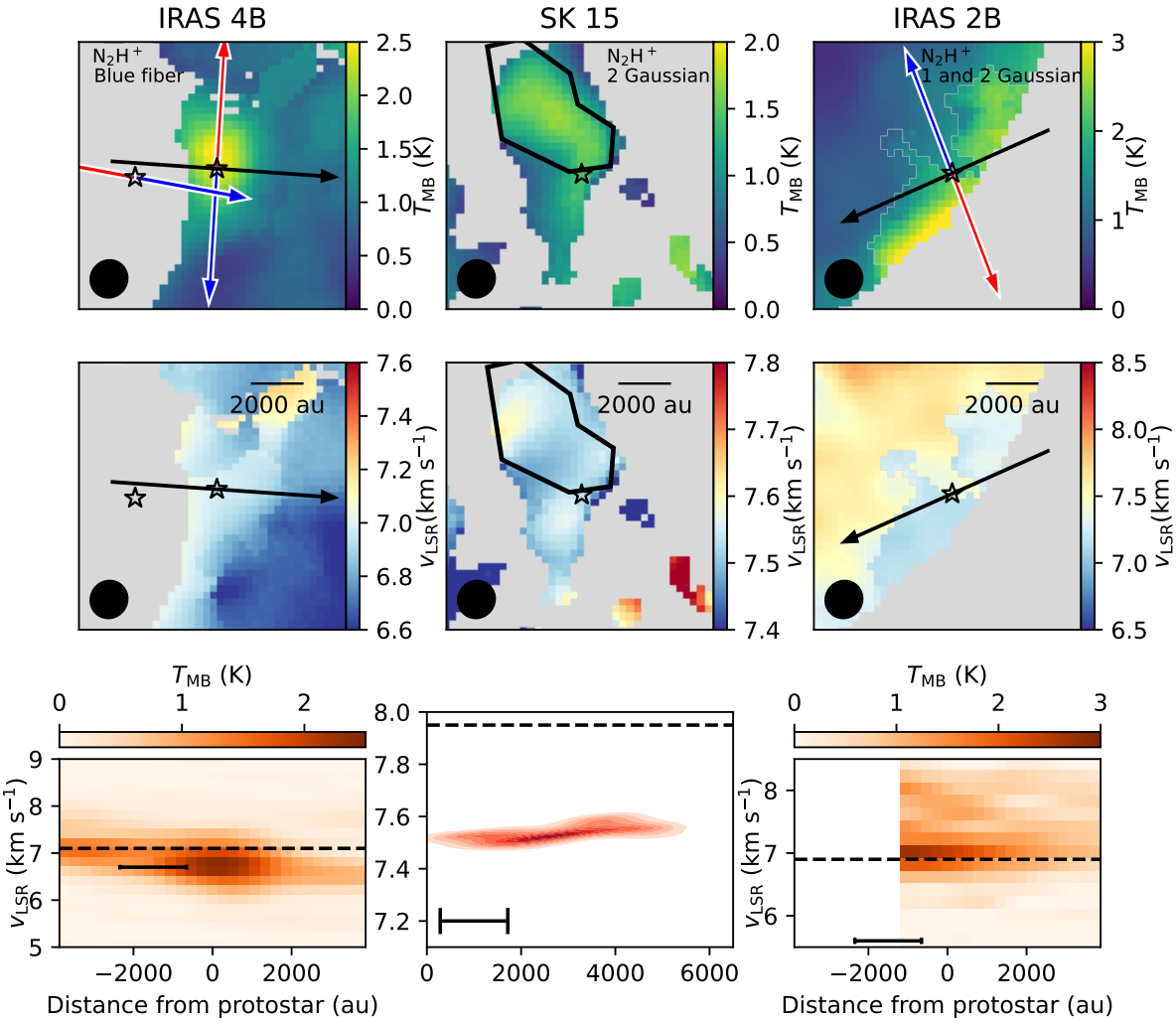

Figure C.5: Zoom-in plots of N_2H^+ emission for IRAS 4B (left), SK 15 (center) and IRAS 2B (right), with the same panels as shown in Fig. 4.7 right except for SK 15. The Gaussian component for each protostar is labeled accordingly. The black ellipse at the bottom left corner represents the beam. Top: Amplitude $T_{\rm MB}$ of the Gaussian component plotted. The blue and red arrows indicate the direction of the blueshifted and redshifted outflow lobes, respectively, for known outflows in the plotted area. Middle: Central velocity $v_{\rm LSR}$ of the Gaussian component selected. The scalebar represents a length of 2000 au. Bottom: For IRAS 4B and IRAs 2B, the position-velocity diagram along the path indicated in the top panel. For SK 15, KDE of the $v_{\rm LSR}$ within the selected region. The red density histogram representd the KDE of the velocities within the black polygon. The dashed lines mark the $v_{\rm LSR}$ of each protostar. The black scalebar represents a length equivalent to one beam.

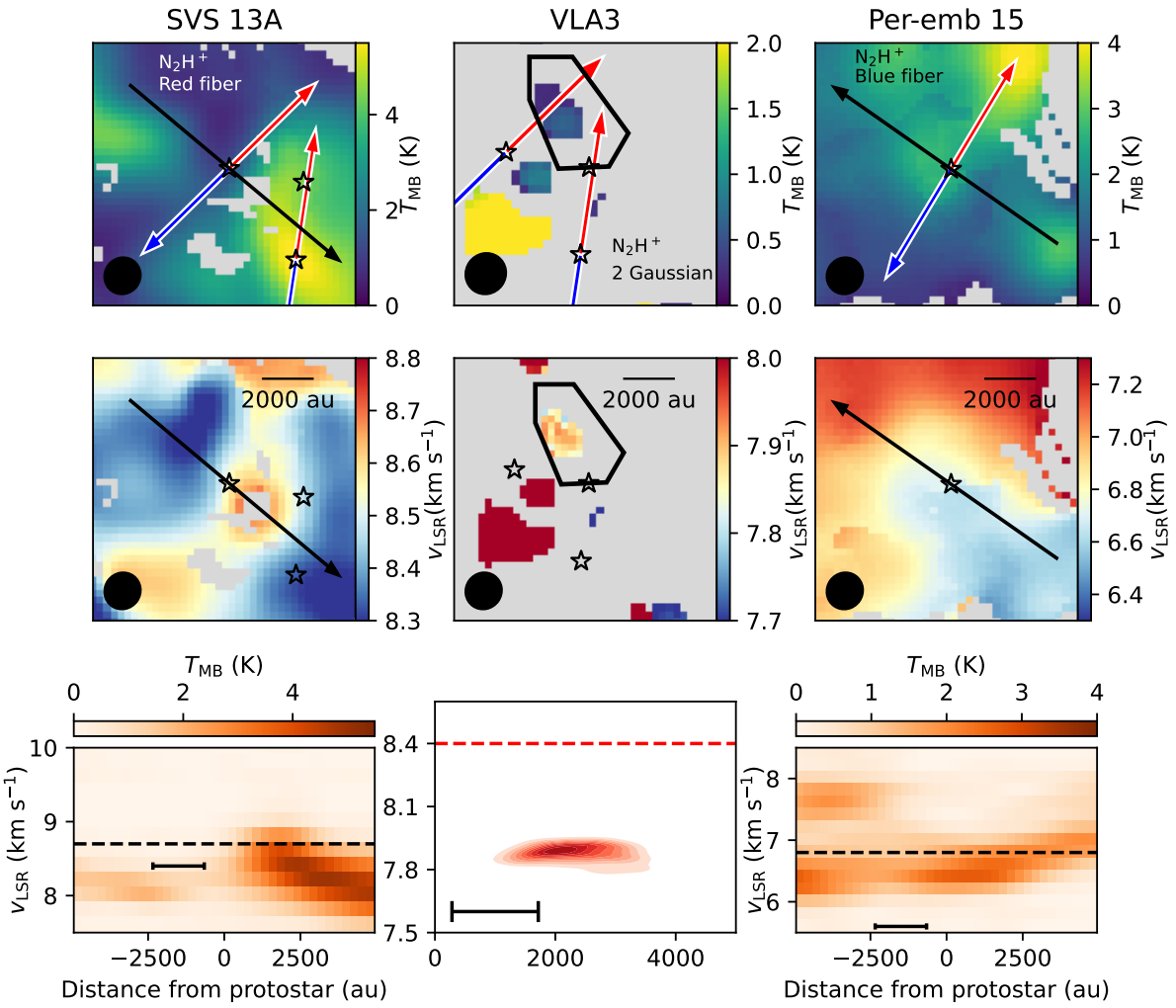

Figure C.5 (cont.): Zoom-in plots of N_2H^+ emission for SVS 13A (left), VLA 3 (center) and Per-emb 15 (right), with the same panels as shown in Fig. 4.7, except for VLA 3.

Bibliography

Adam, R., Adane, A., Ade, P. A. R., et al. 2018, A&A, 609, A115

Agurto-Gangas, C., Pineda, J. E., Szűcs, L., et al. 2019, A&A, 623, A147

Aikawa, Y., Ohashi, N., Inutsuka, S.-i., Herbst, E., & Takakuwa, S. 2001, ApJ, 552, 639

Akiyama, E., Vorobyov, E. I., Baobabu Liu, H., et al. 2019, AJ, 157, 165

Alves, F. O., Caselli, P., Girart, J. M., et al. 2019, Science, 366, 90

Alves, F. O., Cleeves, L. I., Girart, J. M., et al. 2020, ApJ, 904, L6

Andersen, B. C., Stephens, I. W., Dunham, M. M., et al. 2019, ApJ, 873, 54

André, P., Di Francesco, J., Ward-Thompson, D., et al. 2014, in Protostars and Planets VI, ed. H. Beuther, R. S. Klessen, C. P. Dullemond, & T. Henning, 27

André, P., Men'shchikov, A., Bontemps, S., et al. 2010, A&A, 518, L102

Andre, P., Ward-Thompson, D., & Barsony, M. 1993, ApJ, 406, 122

Andre, P., Ward-Thompson, D., & Barsony, M. 2000, in Protostars and Planets IV, ed. V. Mannings, A. P. Boss, & S. S. Russell, 59

Andrews, S. M. & Williams, J. P. 2005, ApJ, 631, 1134

Anglada, G., Rodríguez, L. F., & Torrelles, J. M. 2000, ApJ, 542, L123

Arce, H. G., Shepherd, D., Gueth, F., et al. 2007, in Protostars and Planets V, ed. B. Reipurth, D. Jewitt, & K. Keil, 245

Artur de la Villarmois, E., Guzmán, V. V., Jørgensen, J. K., et al. 2022, A&A, 667, A20

Artur de la Villarmois, E., Jørgensen, J. K., Kristensen, L. E., et al. 2019, A&A, 626, A71

Arzoumanian, D., André, P., Didelon, P., et al. 2011, A&A, 529, L6

Aso, Y., Kwon, W., Ohashi, N., et al. 2023, ApJ, 954, 101

Audard, M., Ábrahám, P., Dunham, M. M., et al. 2014, in Protostars and Planets VI, ed. H. Beuther, R. S. Klessen, C. P. Dullemond, & T. Henning, 387

Bae, J., Hartmann, L., Zhu, Z., & Nelson, R. P. 2014, ApJ, 795, 61

Ballesteros-Paredes, J., Hartmann, L. W., Vázquez-Semadeni, E., Heitsch, F., & Zamora-Avilés, M. A. 2011, MNRAS, 411, 65

Bally, J. 2016, ARA&A, 54, 491

Barnard, E. E. 1919, ApJ, 49, 1

Basu, S. & Mouschovias, T. C. 1994, ApJ, 432, 720

Bate, M. R. 2018, MNRAS, 475, 5618

Bate, M. R., Tricco, T. S., & Price, D. J. 2014, MNRAS, 437, 77

Belloche, A., Hennebelle, P., & André, P. 2006, A&A, 453, 145

Bergin, E. A. & Tafalla, M. 2007, ARA&A, 45, 339

Bianchi, E., López-Sepulcre, A., Ceccarelli, C., et al. 2022, ApJ, 928, L3

Bolatto, A. D., Wolfire, M., & Leroy, A. K. 2013, ARA&A, 51, 207

Brassfield, E. & Bourke, T. L. 2011, in American Astronomical Society Meeting Abstracts, Vol. 217, American Astronomical Society Meeting Abstracts #217, 340.09

Buchner, J., Georgakakis, A., Nandra, K., et al. 2014, A&A, 564, A125

Cabedo, V., Maury, A., Girart, J. M., & Padovani, M. 2021, A&A, 653, A166

Cabral, B. & Leedom, L. C. 1993, in Proceedings of the 20th Annual Conference on Computer Graphics and Interactive Techniques, SIGGRAPH '93 (New York, NY, USA: Association for Computing Machinery), 263–270

Cacciapuoti, L., Macias, E., Gupta, A., et al. 2023, arXiv e-prints, arXiv:2311.13723

Campello, R. J. G. B., Moulavi, D., & Sander, J. 2013, in Advances in Knowledge Discovery and Data Mining, ed. J. Pei, V. S. Tseng, L. Cao, H. Motoda, & G. Xu (Springer Berlin Heidelberg), 160–172

Carter, M., Lazareff, B., Maier, D., et al. 2012, A&A, 538, A89

Caselli, P., Benson, P. J., Myers, P. C., & Tafalla, M. 2002a, ApJ, 572, 238

Caselli, P., Myers, P. C., & Thaddeus, P. 1995, ApJ, 455, L77

Caselli, P., Walmsley, C. M., Zucconi, A., et al. 2002b, ApJ, 565, 344

Cassen, P. & Moosman, A. 1981, Icarus, 48, 353

Ceccarelli, C., Codella, C., Balucani, N., et al. 2023, in Astronomical Society of the Pacific Conference Series, Vol. 534, Protostars and Planets VII, ed. S. Inutsuka, Y. Aikawa, T. Muto, K. Tomida, & M. Tamura, 379

Chen, C.-Y., Mundy, L. G., Ostriker, E. C., Storm, S., & Dhabal, A. 2020a, MNRAS, 494, 3675

Chen, H., Myers, P. C., Ladd, E. F., & Wood, D. O. S. 1995, ApJ, 445, 377

Chen, M. C.-Y., Di Francesco, J., Pineda, J. E., Offner, S. S. R., & Friesen, R. K. 2022, ApJ, 935, 57

Chen, M. C.-Y., Di Francesco, J., Rosolowsky, E., et al. 2020b, ApJ, 891, 84

Chen, M. C.-Y., Di Francesco, J., Rosolowsky, E., et al. 2020c, ApJ, 891, 84

Chen, X., Launhardt, R., & Henning, T. 2009, ApJ, 691, 1729

Chevance, M., Krumholz, M. R., McLeod, A. F., et al. 2023, in Astronomical Society of the Pacific Conference Series, Vol. 534, Protostars and Planets VII, ed. S. Inutsuka, Y. Aikawa, T. Muto, K. Tomida, & M. Tamura, 1

Chou, H.-G., Yen, H.-W., Koch, P. M., & Guilloteau, S. 2016, ApJ, 823, 151

Choudhury, S., Pineda, J. E., Caselli, P., et al. 2020, A&A, 640, L6

Commerçon, B., Launhardt, R., Dullemond, C., & Henning, T. 2012, A&A, 545, A98

Crutcher, R. M. 2012, ARA&A, 50, 29

De Simone, M., Codella, C., Ceccarelli, C., et al. 2022, MNRAS, 512, 5214

Dhabal, A., Mundy, L. G., Chen, C.-y., Teuben, P., & Storm, S. 2019, ApJ, 876, 108

Dhabal, A., Mundy, L. G., Rizzo, M. J., Storm, S., & Teuben, P. 2018, ApJ, 853, 169

Di Francesco, J., Myers, P. C., Wilner, D. J., Ohashi, N., & Mardones, D. 2001, ApJ, 562, 770

Dobbs, C. L., Krumholz, M. R., Ballesteros-Paredes, J., et al. 2014, in Protostars and Planets VI, ed. H. Beuther, R. S. Klessen, C. P. Dullemond, & T. Henning, 3–26

Draine, B. T. 2003, ARA&A, 41, 241

Draine, B. T. 2004, in The Cold Universe, Vol. 32 (Springer), 213

Drążkowska, J., Bitsch, B., Lambrechts, M., et al. 2023, in Astronomical Society of the Pacific Conference Series, Vol. 534, Protostars and Planets VII, ed. S. Inutsuka, Y. Aikawa, T. Muto, K. Tomida, & M. Tamura, 717

Dullemond, C. P., Küffmeier, M., Goicovic, F., et al. 2019, A&A, 628, A20

Dunham, M. M., Allen, L. E., Evans, Neal J., I., et al. 2015, ApJS, 220, 11

Dunham, M. M., Stutz, A. M., Allen, L. E., et al. 2014, in Protostars and Planets VI, ed. H. Beuther, R. S. Klessen, C. P. Dullemond, & T. Henning, 195–218

Dutrey, A., di Folco, E., Guilloteau, S., et al. 2014a, Nature, 514, 600

Dutrey, A., Semenov, D., Chapillon, E., et al. 2014b, in Protostars and Planets VI, ed. H. Beuther, R. S. Klessen, C. P. Dullemond, & T. Henning, 317–338

Dutrey, A., Wakelam, V., Boehler, Y., et al. 2011, A&A, 535, A104

Endres, C. P., Schlemmer, S., Schilke, P., Stutzki, J., & Müller, H. S. 2016, Journal of Molecular Spectroscopy, 327, 95, new Visions of Spectroscopic Databases, Volume II

Enoch, M. L., Evans, Neal J., I., Sargent, A. I., & Glenn, J. 2009, ApJ, 692, 973

Enoch, M. L., Young, K. E., Glenn, J., et al. 2006, ApJ, 638, 293

Ester, M., Kriegel, H.-P., Sander, J., & Xu, X. 1996, in Proceedings of the Second International Conference on Knowledge Discovery and Data Mining, KDD'96 (AAAI Press), 226–231

Evans, Neal J., I., Allen, L. E., Blake, G. A., et al. 2003, PASP, 115, 965

Evans, Neal J., I., Dunham, M. M., Jørgensen, J. K., et al. 2009, ApJS, 181, 321

Fernández-López, M., Arce, H. G., Looney, L., et al. 2014, ApJ, 790, L19

Fernández-López, M., Girart, J. M., López-Vázquez, J. A., et al. 2023, ApJ, 956, 82

Feroz, F. & Hobson, M. P. 2008, MNRAS, 384, 449

Feroz, F., Hobson, M. P., & Bridges, M. 2009, MNRAS, 398, 1601

Ferrière, K. M. 2001, Reviews of Modern Physics, 73, 1031

Field, G. B., Goldsmith, D. W., & Habing, H. J. 1969, ApJ, 155, L149

Fiorellino, E., Manara, C. F., Nisini, B., et al. 2021, A&A, 650, A43

Flores, C., Ohashi, N., Tobin, J. J., et al. 2023, ApJ, 958, 98

Foster, J. B., Cottaar, M., Covey, K. R., et al. 2015, ApJ, 799, 136

Frerking, M. A., Langer, W. D., & Wilson, R. W. 1982, ApJ, 262, 590

Friesen, R. K., Medeiros, L., Schnee, S., et al. 2013, MNRAS, 436, 1513

Friesen, R. K., Pineda, J. E., co-PIs, et al. 2017, ApJ, 843, 63

Frimann, S., Jørgensen, J. K., Dunham, M. M., et al. 2017, A&A, 602, A120

Fukui, Y., Iwata, T., Mizuno, A., Bally, J., & Lane, A. P. 1993, in Protostars and Planets III, ed. E. H. Levy & J. I. Lunine, 603

Fuller, G. A., Myers, P. C., Welch, W. J., et al. 1991, ApJ, 376, 135

Garufi, A., Podio, L., Codella, C., et al. 2022, A&A, 658, A104

Ginsburg, A. & Mirocha, J. 2011, PySpecKit: Python Spectroscopic Toolkit

Ginsburg, A., Robitaille, T., & Beaumont, C. 2016, pvextractor: Position-Velocity Diagram Extractor

Ginsburg, A., Sokolov, V., de Val-Borro, M., et al. 2022, AJ, 163, 291

Ginski, C., Facchini, S., Huang, J., et al. 2021, ApJ, 908, L25

Goodman, A. A., Benson, P. J., Fuller, G. A., & Myers, P. C. 1993, ApJ, 406, 528

Greene, T. P., Wilking, B. A., Andre, P., Young, E. T., & Lada, C. J. 1994, ApJ, 434, 614

Guilloteau, S., Reboussin, L., Dutrey, A., et al. 2016, A&A, 592, A124

Gupta, A., Miotello, A., Manara, C. F., et al. 2023, A&A, 670, L8

Gutermuth, R. A., Myers, P. C., Megeath, S. T., et al. 2008, ApJ, 674, 336

Hacar, A., Clark, S. E., Heitsch, F., et al. 2023, in Astronomical Society of the Pacific Conference Series, Vol. 534, Protostars and Planets VII, ed. S. Inutsuka, Y. Aikawa, T. Muto, K. Tomida, & M. Tamura, 153

Hacar, A. & Tafalla, M. 2011, A&A, 533, A34

Hacar, A., Tafalla, M., & Alves, J. 2017, A&A, 606, A123

Hacar, A., Tafalla, M., Forbrich, J., et al. 2018, A&A, 610, A77

Hacar, A., Tafalla, M., Kauffmann, J., & Kovács, A. 2013, A&A, 554, A55

Hanawa, T., Garufi, A., Podio, L., Codella, C., & Segura-Cox, D. 2024, arXiv e-prints, arXiv:2402.02706

Harada, N., Tokuda, K., Yamasaki, H., et al. 2023, ApJ, 945, 63

Hatchell, J., Richer, J. S., Fuller, G. A., et al. 2005, A&A, 440, 151

Heigl, S., Hoemann, E., & Burkert, A. 2024, arXiv e-prints, arXiv:2401.03779

Hennebelle, P., Commerçon, B., Lee, Y.-N., & Charnoz, S. 2020, A&A, 635, A67

Hennebelle, P., Lesur, G., & Fromang, S. 2017, A&A, 599, A86

Herbst, E. & Leung, C. M. 1989, ApJS, 69, 271

Heyer, M. & Dame, T. M. 2015, ARA&A, 53, 583

Heyer, M. H. & Brunt, C. M. 2004, The Astrophysical Journal, 615, L45

Higuchi, A. E., Sakai, N., Watanabe, Y., et al. 2018, ApJS, 236, 52

Högbom, J. A. 1974, A&AS, 15, 417

Houghton, H. E. 1942, Monthly Notes of the Astronomical Society of South Africa, 1, 107

Hsieh, C.-H., Arce, H. G., Li, Z.-Y., et al. 2023a, ApJ, 947, 25

Hsieh, T.-H., Murillo, N. M., Belloche, A., et al. 2019, ApJ, 884, 149

Hsieh, T.-H., Murillo, N. M., Belloche, A., et al. 2018, ApJ, 854, 15

Hsieh, T. H., Segura-Cox, D. M., Pineda, J. E., et al. 2023b, A&A, 669, A137

Huang, J., Bergin, E. A., Öberg, K. I., et al. 2021, ApJS, 257, 19

Huang, J., Ginski, C., Benisty, M., et al. 2022, ApJ, 930, 171

Hunter, C. 1977, ApJ, 218, 834

Imai, M., Sakai, N., López-Sepulcre, A., et al. 2018, ApJ, 869, 51

Johnstone, D., Rosolowsky, E., Tafalla, M., & Kirk, H. 2010, ApJ, 711, 655

Jørgensen, J. K., Bourke, T. L., Myers, P. C., et al. 2007, ApJ, 659, 479

Jørgensen, J. K., Visser, R., Williams, J. P., & Bergin, E. A. 2015, A&A, 579, A23

Kennicutt, R. C. & Evans, N. J. 2012, ARA&A, 50, 531

Kenyon, S. J., Hartmann, L. W., Strom, K. M., & Strom, S. E. 1990, AJ, 99, 869

Kido, M., Takakuwa, S., Saigo, K., et al. 2023, ApJ, 953, 190

Kippenhahn, R., Weigert, A., & Weiss, A. 2013, Stellar Structure and Evolution (Springer Berlin Heidelberg)

Kirk, H., Myers, P. C., Bourke, T. L., et al. 2013, ApJ, 766, 115

Könyves, V., André, P., Men'shchikov, A., et al. 2015, A&A, 584, A91

Kounkel, M., Covey, K., Moe, M., et al. 2019, AJ, 157, 196

Kratter, K. M., Matzner, C. D., Krumholz, M. R., & Klein, R. I. 2010a, ApJ, 708, 1585

Kratter, K. M., Murray-Clay, R. A., & Youdin, A. N. 2010b, ApJ, 710, 1375

Kuffmeier, M., Calcutt, H., & Kristensen, L. E. 2019, A&A, 628, A112

Kuffmeier, M., Dullemond, C. P., Reissl, S., & Goicovic, F. G. 2021, A&A, 656, A161

Kuffmeier, M., Frimann, S., Jensen, S. S., & Haugbølle, T. 2018, MNRAS, 475, 2642

Kuffmeier, M., Goicovic, F. G., & Dullemond, C. P. 2020, A&A, 633, A3

Kuffmeier, M., Haugbølle, T., & Nordlund, Å. 2017, ApJ, 846, 7

Kuffmeier, M., Jensen, S. S., & Haugbølle, T. 2023, European Physical Journal Plus, 138, 272

Kuznetsova, A., Bae, J., Hartmann, L., & Mac Low, M.-M. 2022, ApJ, 928, 92

Kuznetsova, A., Hartmann, L., & Heitsch, F. 2019, ApJ, 876, 33

Lada, C. J. 1987, in Star Forming Regions, ed. M. Peimbert & J. Jugaku, Vol. 115, 1

Larson, R. B. 1969, MNRAS, 145, 271

Larson, R. B. 1981, MNRAS, 194, 809

Larson, R. B. 2003, Reports on Progress in Physics, 66, 1651

Le Gouellec, V. J. M., Hull, C. L. H., Maury, A. J., et al. 2019, ApJ, 885, 106

Lebreuilly, U., Hennebelle, P., Colman, T., et al. 2021, ApJ, 917, L10

Lee, C.-F., Hirano, N., Zhang, Q., et al. 2014, ApJ, 786, 114

Lee, C.-F., Li, Z.-Y., & Turner, N. J. 2020, Nature Astronomy, 4, 142

Lee, K. I., Dunham, M. M., Myers, P. C., et al. 2016, ApJ, 820, L2

Liu, H. B., Takami, M., Kudo, T., et al. 2016, Science Advances, 2, e1500875

Manara, C. F., Morbidelli, A., & Guillot, T. 2018, A&A, 618, L3

Mangum, J. G. & Shirley, Y. L. 2015, PASP, 127, 266

Masunaga, H. & Inutsuka, S.-i. 2000, ApJ, 531, 350

Masunaga, H., Miyama, S. M., & Inutsuka, S.-i. 1998, ApJ, 495, 346

Matsumoto, T., Machida, M. N., & Inutsuka, S.-i. 2017, ApJ, 839, 69

McGuire, B. A. 2022, ApJS, 259, 30

McInnes, L. & Healy, J. 2017, in 2017 IEEE International Conference on Data Mining Workshops (ICDMW), 33–42

McKee, C. F. & Ostriker, E. C. 2007, ARA&A, 45, 565

McKee, C. F. & Ostriker, J. P. 1977, ApJ, 218, 148

McMullin, J. P., Waters, B., Schiebel, D., Young, W., & Golap, K. 2007, in Astronomical Society of the Pacific Conference Series, Vol. 376, Astronomical Data Analysis Software and Systems XVI, ed. R. A. Shaw, F. Hill, & D. J. Bell, 127

Mendoza, S., Tejeda, E., & Nagel, E. 2009, MNRAS, 393, 579

Mestel, L. & Spitzer, L., J. 1956, MNRAS, 116, 503

Mignon-Risse, R., González, M., Commerçon, B., & Rosdahl, J. 2021, A&A, 652, A69

Miotello, A., Kamp, I., Birnstiel, T., Cleeves, L. C., & Kataoka, A. 2023, in Astronomical Society of the Pacific Conference Series, Vol. 534, Protostars and Planets VII, ed. S. Inutsuka, Y. Aikawa, T. Muto, K. Tomida, & M. Tamura, 501

Mouschovias, T. C. & Paleologou, E. V. 1980, ApJ, 237, 877

Murillo, N. M., van Dishoeck, E. F., Hacar, A., Harsono, D., & Jørgensen, J. K. 2022, A&A, 658, A53

Myers, P. C. & Ladd, E. F. 1993, ApJ, 413, L47

Narita, S., Hayashi, C., & Miyama, S. M. 1984, Progress of Theoretical Physics, 72, 1118

Norman, M. L., Wilson, J. R., & Barton, R. T. 1980, ApJ, 239, 968

Offner, S. S. R., Moe, M., Kratter, K. M., et al. 2023, in Astronomical Society of the Pacific Conference Series, Vol. 534, Protostars and Planets VII, ed. S. Inutsuka, Y. Aikawa, T. Muto, K. Tomida, & M. Tamura, 275

Ohashi, N., Tobin, J. J., Jørgensen, J. K., et al. 2023, ApJ, 951, 8

Ortiz-León, G. N., Loinard, L., Dzib, S. A., et al. 2018, ApJ, 865, 73

Padoan, P., Haugbølle, T., & Nordlund, Å. 2014, ApJ, 797, 32

Palla, F. & Stahler, S. W. 1993a, ApJ, 418, 414

Palla, F. & Stahler, S. W. 1993b, ApJ, 418, 414

Paneque-Carreño, T., Pérez, L. M., Benisty, M., et al. 2021, ApJ, 914, 88

Pedregosa, F., Varoquaux, G., Gramfort, A., et al. 2011, Journal of Machine Learning Research, 12, 2825

Pelkonen, V. M., Padoan, P., Haugbølle, T., & Nordlund, Å. 2021, MNRAS, 504, 1219

Penston, M. V. 1969, MNRAS, 144, 425

Phuong, N. T., Dutrey, A., Diep, P. N., et al. 2020, A&A, 635, A12

Pineda, J. E., Arzoumanian, D., Andre, P., et al. 2023, in Astronomical Society of the Pacific Conference Series, Vol. 534, Protostars and Planets VII, ed. S. Inutsuka, Y. Aikawa, T. Muto, K. Tomida, & M. Tamura, 233

Pineda, J. E., Caselli, P., & Goodman, A. A. 2008, ApJ, 679, 481

Pineda, J. E., Goodman, A. A., Arce, H. G., et al. 2010, ApJ, 712, L116

Pineda, J. E., Offner, S. S. R., Parker, R. J., et al. 2015, Nature, 518, 213

Pineda, J. E., Schmiedeke, A., Caselli, P., et al. 2021, ApJ, 912, 7

Pineda, J. E., Segura-Cox, D., Caselli, P., et al. 2020, Nature Astronomy, 4, 1158

Pineda, J. E., Zhao, B., Schmiedeke, A., et al. 2019, ApJ, 882, 103

Planck Collaboration, Ade, P. A. R., Aghanim, N., et al. 2016, A&A, 586, A138

Plunkett, A. L., Arce, H. G., Corder, S. A., et al. 2013, ApJ, 774, 22

Podio, L., Tabone, B., Codella, C., et al. 2021, A&A, 648, A45

Protassov, R., van Dyk, D. A., Connors, A., Kashyap, V. L., & Siemiginowska, A. 2002, ApJ, 571, 545

Ray, T., Dougados, C., Bacciotti, F., Eislöffel, J., & Chrysostomou, A. 2007, in Protostars and Planets V, ed. B. Reipurth, D. Jewitt, & K. Keil, 231

Rufat, D. S. 2017, PhD thesis, California Institute of Technology

Rybicki, G. B. & Lightman, A. P. 1985, Radiative processes in astrophysics (John Wiley & Sons, Ltd)

Sai, J., Yen, H.-W., Ohashi, N., et al. 2023, ApJ, 954, 67

Saigo, K. & Hanawa, T. 1998, ApJ, 493, 342

Sakai, N., Sakai, T., Hirota, T., et al. 2014, Nature, 507, 78

Sakai, N. & Yamamoto, S. 2013, Chemical Reviews, 113, 8981

Sandell, G. & Knee, L. B. G. 2001, ApJ, 546, L49

Schmiedeke, A., Pineda, J. E., Caselli, P., et al. 2021, ApJ, 909, 60

Schneider, N., Bontemps, S., Simon, R., et al. 2011, A&A, 529, A1

Segura-Cox, D. M., Harris, R. J., Tobin, J. J., et al. 2016, ApJ, 817, L14

Segura-Cox, D. M., Looney, L. W., Tobin, J. J., et al. 2018, ApJ, 866, 161

Segura-Cox, D. M., Schmiedeke, A., Pineda, J. E., et al. 2020, Nature, 586, 228

Seifried, D., Banerjee, R., Pudritz, R. E., & Klessen, R. S. 2013, MNRAS, 432, 3320

Seifried, D., Banerjee, R., Pudritz, R. E., & Klessen, R. S. 2015, MNRAS, 446, 2776

Sheehan, P. D. & Eisner, J. A. 2018, ApJ, 857, 18

Sheehan, P. D., Tobin, J. J., Federman, S., Megeath, S. T., & Looney, L. W. 2020, ApJ, 902, 141

Shimajiri, Y., Sakai, T., Kitamura, Y., et al. 2015, ApJS, 221, 31

Shirley, Y. L. 2015, PASP, 127, 299

Shu, F. H. 1977, ApJ, 214, 488

Shu, F. H., Adams, F. C., & Lizano, S. 1987, ARA&A, 25, 23

Skilling, J. 2004, in American Institute of Physics Conference Series, Vol. 735, Bayesian Inference and Maximum Entropy Methods in Science and Engineering: 24th International Workshop on Bayesian Inference and Maximum Entropy Methods in Science and Engineering, ed. R. Fischer, R. Preuss, & U. V. Toussaint, 395–405

Skilling, J. 2006, Bayesian Analysis, 1, 833

Smith, R. J., Glover, S. C. O., Bonnell, I. A., Clark, P. C., & Klessen, R. S. 2011, MNRAS, 411, 1354

Smith, R. J., Glover, S. C. O., Klessen, R. S., & Fuller, G. A. 2016, MNRAS, 455, 3640

Sokolov, V., Pineda, J. E., Buchner, J., & Caselli, P. 2020, ApJ, 892, L32

Sokolov, V., Wang, K., Pineda, J. E., et al. 2019, ApJ, 872, 30

Soler, J. D., Alves, F., Boulanger, F., et al. 2016, A&A, 596, A93

Spitzer, L. 1978, Physical Processes in the Interstellar Medium, A Wiley-Interscience publication (Wiley)

Stahler, S. W. & Palla, F. 2004, The Formation of Stars (Wiley)

Stahler, S. W., Shu, F. H., & Taam, R. E. 1980, ApJ, 241, 637

Stephens, I. W., Bourke, T. L., Dunham, M. M., et al. 2019, ApJS, 245, 21

Stephens, I. W., Dunham, M. M., Myers, P. C., et al. 2017, ApJ, 846, 16

Suri, S., Sánchez-Monge, Á., Schilke, P., et al. 2019, A&A, 623, A142

Suzuki, H., Yamamoto, S., Ohishi, M., et al. 1992, ApJ, 392, 551

Swade, D. A. 1989, ApJ, 345, 828

Takakuwa, S., Saigo, K., Matsumoto, T., et al. 2017, ApJ, 837, 86

Takakuwa, S., Saito, M., Saigo, K., et al. 2014, ApJ, 796, 1

Tang, Y. W., Guilloteau, S., Piétu, V., et al. 2012, A&A, 547, A84

Taylor, G., Carilli, C., Perley, R., & (U.S.), N. R. A. O. 1999, Synthesis Imaging in Radio Astronomy II, Astronomical Society of the Pacific conference series (Astronomical Society of the Pacific)

Terebey, S., Shu, F. H., & Cassen, P. 1984, ApJ, 286, 529

Thieme, T. J., Lai, S.-P., Lin, S.-J., et al. 2022, ApJ, 925, 32

Thompson, A. R., Moran, J. M., & Swenson, George W., J. 2017, Interferometry and Synthesis in Radio Astronomy, 3rd Edition (Springer)

Tobin, J. J., Hartmann, L., Bergin, E., et al. 2012, ApJ, 748, 16

Tobin, J. J., Hartmann, L., Looney, L. W., & Chiang, H.-F. 2010, ApJ, 712, 1010

Tobin, J. J., Looney, L. W., Li, Z.-Y., et al. 2016, ApJ, 818, 73

Tobin, J. J., Looney, L. W., Li, Z.-Y., et al. 2018, ApJ, 867, 43

Tsukamoto, Y., Maury, A., Commercon, B., et al. 2023, in Astronomical Society of the Pacific Conference Series, Vol. 534, Protostars and Planets VII, ed. S. Inutsuka, Y. Aikawa, T. Muto, K. Tomida, & M. Tamura, 317

Tu, Y., Li, Z.-Y., Lam, K. H., Tomida, K., & Hsu, C.-Y. 2024, MNRAS, 527, 10131

Tychoniec, Ł., Manara, C. F., Rosotti, G. P., et al. 2020, A&A, 640, A19

Tychoniec, Ł., van Dishoeck, E. F., van't Hoff, M. L. R., et al. 2021, A&A, 655, A65

Ulrich, R. K. 1976, ApJ, 210, 377

Unno, M., Hanawa, T., & Takasao, S. 2022, ApJ, 941, 154

Valdivia-Mena, M. T., Pineda, J. E., Segura-Cox, D. M., et al. 2022, A&A, 667, A12

Valdivia-Mena, M. T., Pineda, J. E., Segura-Cox, D. M., et al. 2023, A&A, 677, A92

van der Tak, F. F. S., Black, J. H., Schöier, F. L., Jansen, D. J., & van Dishoeck, E. F. 2007, A&A, 468, 627

van der Walt, S., Schönberger, J. L., Nunez-Iglesias, J., et al. 2014, PeerJ, 2, e453

van Dishoeck, E. F. 2014, Faraday Discussions, 168, 9

van Gelder, M. L., Tabone, B., van Dishoeck, E. F., & Godard, B. 2021, A&A, 653, A159

van't Hoff, M. L. R., Harsono, D., van Gelder, M. L., et al. 2022, ApJ, 924, 5

Virtanen, P., Gommers, R., Oliphant, T. E., et al. 2020, Nature Methods, 17, 261

Vorobyov, E. I. & Basu, S. 2015, ApJ, 805, 115

Walch, S., Naab, T., Whitworth, A., Burkert, A., & Gritschneder, M. 2010, MNRAS, 402, 2253

White, J. A., Kóspál, Á., Rab, C., et al. 2019, ApJ, 877, 21

Williams, J. P. & Cieza, L. A. 2011, ARA&A, 49, 67

Wilson, T., Rohlfs, K., & Huettemeister, S. 2008, Tools of Radio Astronomy, Astronomy and Astrophysics Library (Springer Berlin Heidelberg)

Wurster, J., Bate, M. R., & Price, D. J. 2019, MNRAS, 489, 1719

Wyrowski, F., Güsten, R., Menten, K. M., et al. 2016, A&A, 585, A149

Yamamoto, S. 2017, Introduction to Astrochemistry: Chemical Evolution from Interstellar Clouds to Star and Planet Formation, Astronomy and Astrophysics Library (Springer Japan)

Yamato, Y., Aikawa, Y., Ohashi, N., et al. 2023, ApJ, 951, 11

Yang, Y.-L., Sakai, N., Zhang, Y., et al. 2021, ApJ, 910, 20

Yen, H.-W., Gu, P.-G., Hirano, N., et al. 2019, ApJ, 880, 69

Yen, H.-W., Takakuwa, S., Ohashi, N., et al. 2014, ApJ, 793, 1

Yu, K. C., Billawala, Y., & Bally, J. 1999, AJ, 118, 2940

Zamponi, J., Maureira, M. J., Zhao, B., et al. 2021, MNRAS, 508, 2583

Zapata, L. A., Arce, H. G., Brassfield, E., et al. 2014, MNRAS, 441, 3696

Zhang, S., Zhu, Z., Huang, J., et al. 2018a, ApJ, 869, L47

Zhang, Y., Higuchi, A. E., Sakai, N., et al. 2018b, ApJ, 864, 76

Zhao, B., Caselli, P., Li, Z.-Y., & Krasnopolsky, R. 2018, MNRAS, 473, 4868

Zucker, C., Schlafly, E. F., Speagle, J. S., et al. 2018, ApJ, 869, 83

Acknowledgements

They say it takes a village to raise a child: I would say it takes a group to coach a PhD student, and I had the most amazing group push me throughout this process. Undertaking a PhD has been an adventure, with ups and downs, specially considering it started during a worldwide pandemic. Thus, all the people that have helped, accompanied and pushed me through this process are also responsible for the fact that I can stand today with this thesis.

I first want to thank my advisors, Paola Caselli and Jaime Pineda, for giving me the opportunity to develop these interesting projects. You were not only great scientific advisors, but you have also fostered a great working environment, re-enchanting me with science. Paola, you introduced me to the fascinating world of astrochemistry, and everything I learned has definitely motivated me to research beyond the dynamics of gas. You have and continue to be an inspiration for me. Jaime, you received me as a naïve master student and built my image of what academia is and what it can be. Thank you for all your patience when I busted into your office (sometimes several times a day) with scientific or personal inquiries and for teaching me how to navigate through the world of radioastronomy. Beyond research, together with your family, Karen and Dante, you opened the doors to your home to receive my husband and me: I will always be thankful to you three for your aid, specially in the first weeks of our arrival in Germany, and for all the board games we played together.

Secondly, thanks to Dominique Segura-Cox and to Maria Jose Maureira, my mentors throughout this journey. Dominique, your guidance in this new subject of streamers helped me develop the picture in my head that I needed to really understand this new phenomenon, but more than anything, you showed me that working in academia does not imply leaving your own personality behind and that there is space for fun and creativity in research. Cote, thank you so much for all your advice, friendship, and for receiving me as a fellow expat in a new country. You taught me that what might be the best for others is not necessarily the best for me, and reminded me to care for myself as much as for other people.

Thank you to all CAS members, for all the lunches, after-hours and good times all around. The lively environment in the CAS group turned this PhD from a challenging new experience to amazing 3 and 1/2 years. Thanks to Katarina and Caroline, my Deutche Freunde, for all the coffees, drinks, homemade bread and food we shared, that made me feel welcome in a country that does not feel so foreign anymore. Thanks to Judit,

Hayley, Shreya, Farideh, Anika, Birgitta, Pavol, Michaela, Elena, Marta, Wiebke, Davide, Jelke and many more CAS office mates, for all the lunches, dinners, coffees and laughter. Special thanks to Angelika (our personal angel) for all the help you gave us, specially at the beginning when everything was so new and confusing. Oh how you always received me with a smile in your office and you always made the time to help with aaaaaall these German forms until I was crystal clear with them! I will miss hearing your laughter from down the hallway.

I want to thank my husband, Jaime, who followed me on this dream of studying abroad. Words cannot begin to describe how much I love you. You have been my pillar that supports me against all difficulties, my counselor for hard situations, my faithful ally in all battles in life. You have encouraged me throughout all my career and beyond, without asking anything in return. I wish for many more years filled with adventures with you.

I want to thank my family and friends, who have supported me throughout all this academic journey from near and far. Thanks Mamá and Papá, for supporting me in this wish of becoming a scientist, even though you might not understand exactly what I do, but read my publications regardless and celebrate every achievement, no matter small. To my extended family, all my cousins that are like siblings to me, my godmother, nephews and nieces, thanks for all the calls and messages that shortened the 12,500 km from Chile to a single phone ring. Thanks to the friends that by coincidence ended up close, Teresa (#lasTeres), Pola and Chichi, for bringing a bit of Chile to Munich. Thanks to my high-school friends (the *copuchapalooza*), specially Anto, Bachler, Sofi, Kirk, Cami, I am so proud of the "adults" we have become. Thanks to the Astroniñas, for pushing a beautiful project and allow me to participate from afar.

And finally, I wish to thank my cats Wendy and Sally for the emotional support since your arrival. Meow meow.